Progress in Materials Science 117 (2021) 100752

Contents lists available at ScienceDirect

Progress in Materials Science

journal homepage: www.elsevier.com/locate/pmatsci

Friction stir welding/processing of metals and alloys: A comprehensive review on microstructural evolution

A. Heidarzadeh [a,*], S. Mironov [b], R. Kaibyshev [b], G. Çam [c], A. Simar [d], A. Gerlich [e], F. Khodabakhshi [f], A. Mostafaei [g], D.P. Field [h], J.D. Robson [i], A. Deschamps [j], P. J. Withers [k]

[a] Department of Materials Engineering, Azarbaijan Shahid Madani University, Tabriz, Iran
[b] Belgorod National Research University, Pobeda 85, Belgorod 308015, Russia
[c] Iskenderun Technical University, Faculty of Engineering and Natural Sciences, Department of Mechanical Engineering, 31200 Iskenderun-Hatay, Turkey
[d] Institute of Mechanics, Materials and Civil Engineering, UCLouvain, 1348 Louvain-la-Neuve, Belgium
[e] Department of Mechanical and Mechatronics Engineering, University of Waterloo, Waterloo, ON, Canada
[f] School of Metallurgy and Materials Engineering, College of Engineering, University of Tehran, P.O. Box: 11155-4563, Tehran, Iran
[g] Department of Mechanical, Materials and Aerospace Engineering, Illinois Institute of Technology, 10 W 32nd Street, Chicago, IL 60616, USA
[h] School of Mechanical and Materials Engineering, Washington State University, Pullman, WA 99164-2920, USA
[i] Department of Materials, The University of Manchester, Manchester M13 9PL, UK
[j] Univ. Grenoble Alpes, CNRS, Grenoble INP, SIMaP, F-38000 Grenoble, France
[k] Henry Royce Institute, Department of Materials, The University of Manchester, Manchester M13 9PL, UK

ARTICLE INFO

Keywords:
Friction stir welding/processing
Stacking fault energy
Metal matrix composites
Recovery
Microstructure
Recrystallization

ABSTRACT

The unique combination of very large strains, high temperatures and high strain rates inherent to friction stir welding (FSW) and friction stir processing (FSP) and their dependency on the processing parameters provides an opportunity to tailor the microstructure, and hence the performance of welds and surfaces to an extent not possible with fusion processes. While a great deal of attention has previously been focused on the FSW parameters and their effect on weld quality and joint performance, here the focus is on developing a comprehensive understanding of the fundamentals of the microstructural evolution during FSW/P. Through a consideration of the mechanisms underlying the development of grain structures and textures, phases, phase transformations and precipitation, microstructural control across a very wide range of similar and dissimilar material joints is examined. In particular, when considering the joining of dissimilar metals and alloys, special attention is focused on the control and dispersion of deleterious intermetallic compounds. Similarly, we consider how FSP can be used to locally refine the microstructure as well as provide an opportunity to form metal matrix composites (MMCs) for near surface reinforcement. Finally, the current gaps in our knowledge are considered in the context of the future outlook for FSW/P.

* Corresponding author.
E-mail address: ac.heydarzadeh@azaruniv.ac.ir (A. Heidarzadeh).

https://doi.org/10.1016/j.pmatsci.2020.100752
Received 10 March 2019; Received in revised form 23 September 2020; Accepted 5 October 2020
Available online 8 October 2020

1. Introduction

Friction stir welding (FSW) has attracted growing interest because it has the potential to overcome common issues associated with conventional fusion welding processes such as large distortions, solidification cracking, macro and micro segregation, coarse dendritic structures, gas and shrinkage porosities, solid inclusions, surface oxidation or discoloration, the formation of brittle intermetallics between dissimilar materials, a wide heat affected zone (HAZ), high energy consumption, environmental pollution, and so on [1,2]. Furthermore, the ability to control microstructure and to obtain microstructures not easily obtained through other routes mean that it is critical to understand the relationship between FSW conditions and microstructure so as to better tailor weld properties. Alongside this, friction stir processing (FSP) can generate near surface microstructures not easily achieved in other ways. Accordingly, FSW and FSP are being exploited across a broad range of industrial applications as illustrated in Fig. 1a-h.

The general principles underlying FSW are shown in Fig. 2a: in essence, a rotating tool is inserted into the interface between two workpieces, which is then traversed along the welding line. The tool normally comprises a pin and shoulder (Fig. 2b). The deformation and heat induced by the rotating tool lead to the formation of a solid-state weld. By contrast, FSP can be used either to modify the surface microstructure (Fig. 2c), or to incorporate a second phase (Fig. 2d). In the latter case, the second phase particles are inserted into the surface of the material by cutting a groove or drilling holes such that the rotating tool incorporates the particle into the materials creating a composite structure. As indicated in Fig. 2, many FSW/P parameters influence the final microstructure of the processed zone.

Several excellent reviews of the FSW literature have already been published [6-14]. In particular the reader is pointed towards the reviews by Mishra and Ma [2] with regard to microstructural aspects and Meng et al. [15] with respect to strategies for controlling weld quality. The former is probably the most complete analysis of the state of the art to date. Particular attention has been paid to the microstructural changes in the key structural materials including aluminum, copper, magnesium and titanium alloys as well as various steel grades. However, the field has advanced significantly since the publication of this classical work, both in terms of the range of systems and processing parameters studied, and in terms of our understanding of FSW-induced microstructural behavior. This review aims to build on the platform established by Mishra and Ma [2] to draw together our current understanding of, and gain a new perspective on, microstructural evolution during FSW/P. It commences with a focus on the important mechanisms underlying microstructural and textural evolution during FSW/P of metals and alloys before considering the factors associated when processing specific metals and alloys in turn. The review also considers the challenges associated with joining a wide range of dissimilar materials combinations. Finally, it considers the microstructural evolution during FSP; particularly in relation to the surface modification of alloys and the production of metal matrix composites (MMCs). The review is of value both to beginners and to experienced engineers and scientists interested in understanding microstructure development during FSW/P with the aim of improving our ability to further improve and control the properties of welds and surface treatment.

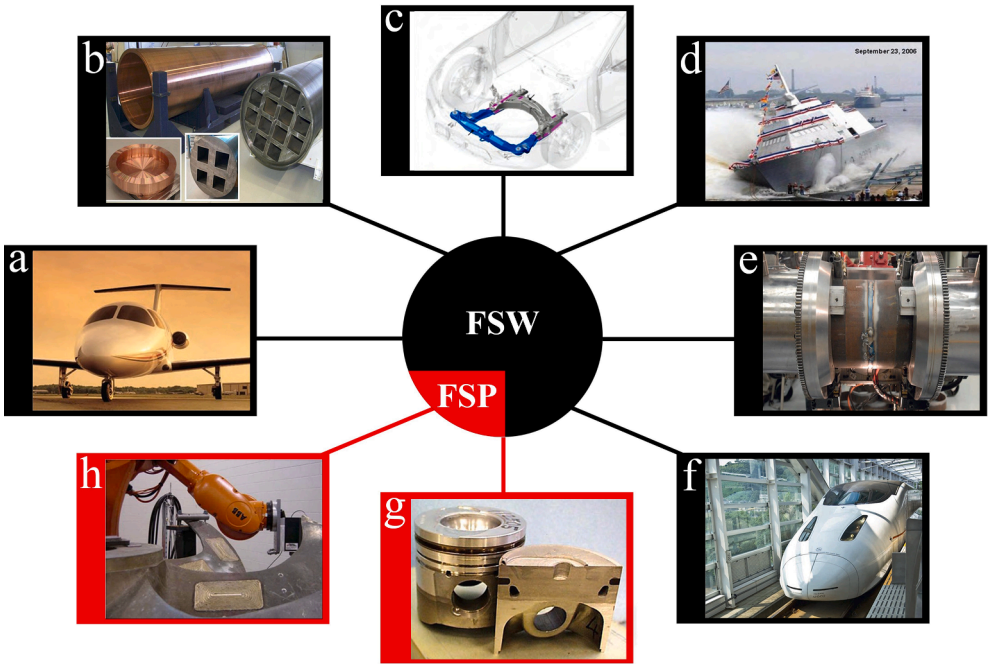

Fig. 1. Examples of the industrial application of friction stir welding and processing [3-5]: (a) the Eclipse 500 business jet, the first to use FSW, (b) 50 mm thick copper nuclear waste storage canisters, (c) dissimilar FSW of aluminum to steel in Honda front subframe, (d) deckhouse structure of Littoral Combat ship, (e) orbital FSW of steel pipes, and (f) floor panels of Shinkansen train, FSP surface modification of h) the Nibral propeller and g) automotive piston. This figure is reproduced from cited investigations with permission from Elsevier.

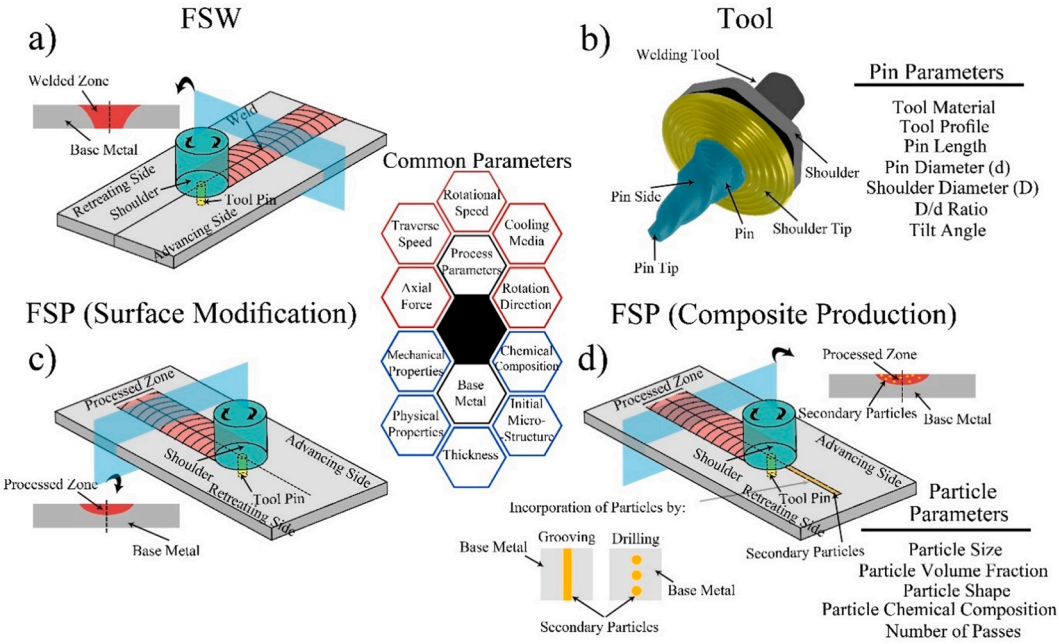

Fig. 2. Schematics of (a) the FSW process, (b) the FSW/P tool, (c) FSP for surface modification, and (d) FSP for composite production. The common process control parameters are represented in the center of the figure while those specific to the tool design and FSP are listed in (b) and (d), respectively.

2. Mechanisms of grain structure evolution

Due to the unique features of the FSW process, the weld zone material experiences severe thermomechanical excursions [16] which drive recrystallization and recovery processes [2]. The tool rotation results in stirring and mixing of material around the rotating pin by plastic flow, while friction between the tool and the workpiece provides the main contribution to heat generation [2]. In addition, a large fraction (~80% [17]) of work relating to plastic flow is dissipated as heat giving rise to local adiabatic heating. As a result, the

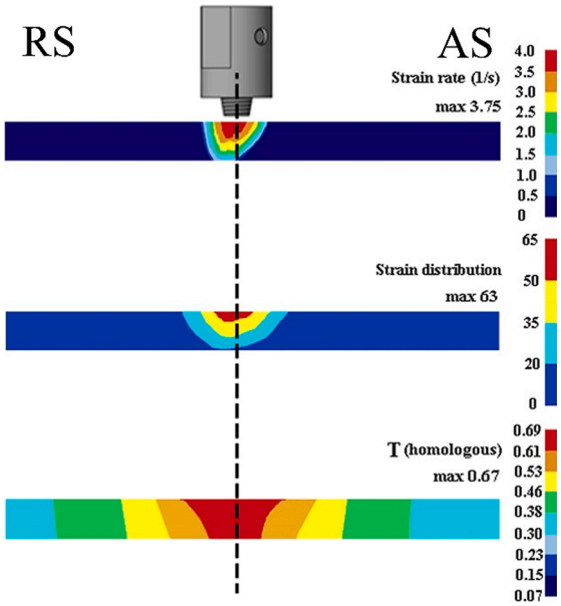

Fig. 3. Generalized presentation of the distributions of temperature (top), strain (middle) and strain rate (bottom) across a transverse cross-section of a AA2024-T4 alloy weld. These fields are slightly asymmetric between the retreating (RS) and advancing (AS) sides. The illustration is drawn based on information provided in [2,17-20].

thermal field, the imposed strain and strain rate are highly non-uniform as shown in Fig. 3 and vary with distance from the rotating pin and shoulder according to the tool shape, the rotational and traverse speeds, the axial force of the tool shoulder on the workpiece, the pin tilt and the properties of the processed materials such as the thermal conductivity, the temperature-dependent flow stress, etc. [16].

Broadly speaking, as depicted in Fig. 4, the weld zone can be divided into four zones distinguished by their distinct thermo-mechanical characteristics, namely, the stir zone (SZ), thermomechanically affected zone (TMAZ), heat affected zone (HAZ) and base material (BM). Unsurprisingly, as shown in Fig. 3, the highest peak temperature, strain, and strain rate are the near surfaces of the pin and shoulder and tend to decrease sharply toward the BM. In the SZ, the peak temperature ranges from 0.9 to 0.75 T_m (melting temperature) decreasing away from the shoulder contact surface and in the transverse direction away from the pin surface [16]. The SZ exhibits a basin-like shape significantly widening towards the upper surface and is not symmetric with respect to the weld line (Fig. 4a) [2,18-24]. In the TMAZ, the peak temperature decreases with distance from the weld line from ~0.7 to 0.6 T_m [18,19,21-23]. The TMAZ is a transition zone, in which the temperature varies sharply across it. In the HAZ the peak temperature decreases gradually from ~0.55 T_m to ambient temperature from the TMAZ to the BM. Pre-weld heating may cause the HAZ to extend out further towards the BM.

The strain and strain rate gradients tend to be much steeper than the temperature gradients (Fig. 3). In the SZ, the true strain and strain rate can be as high as $\geq 10^2$ and $>10\ s^{-1}$, respectively decreasing downwards from the shoulder surface and in the transverse direction away from the pin surface [18-21,24]. In the TMAZ, the strain and strain rate decrease towards zero at the boundary with the HAZ; however, even here the strain is sufficient for a noticeably deformed microstructure.

The markedly different deformation and thermal histories associated with the SZ, TMAZ, HAZ and BM mean that microstructure evolution varies sharply with position (Fig. 4a). Further, this can take place dynamically during processing and statically after processing. To aid the interpretation of the grain-structure development occurring during FSW the underlying mechanisms of microstructural evolution are outlined below.

2.1. Static recovery

According to the definition given by Humphreys, the recovery refers to microstructural changes, which occur in a deformed material prior to recrystallization [25]. However, the recovery can also occur independently of any recrystallization and some materials may undergo only recovery; this is because recovery and recrystallization are competing processes since both are driven by the stored energy associated with the increased dislocation density [25-27].

It is widely accepted that the static recovery (SRV) results in a decrease in strength through changes in dislocation structure due to (i) dislocation annihilation, (ii) dislocation rearrangement into lower energy configurations (i.e., dislocation boundaries), and (iii) subgrain growth [25]. Dislocation annihilation and rearrangement into stable configurations occur simultaneously and are followed by subgrain coarsening. All the recovery processes are driven by glide, climb, and cross-slip of dislocations that may result in the formation of low angle boundaries (subgrains). Accordingly, the extent of this phenomenon is very sensitive to dislocation mobility and

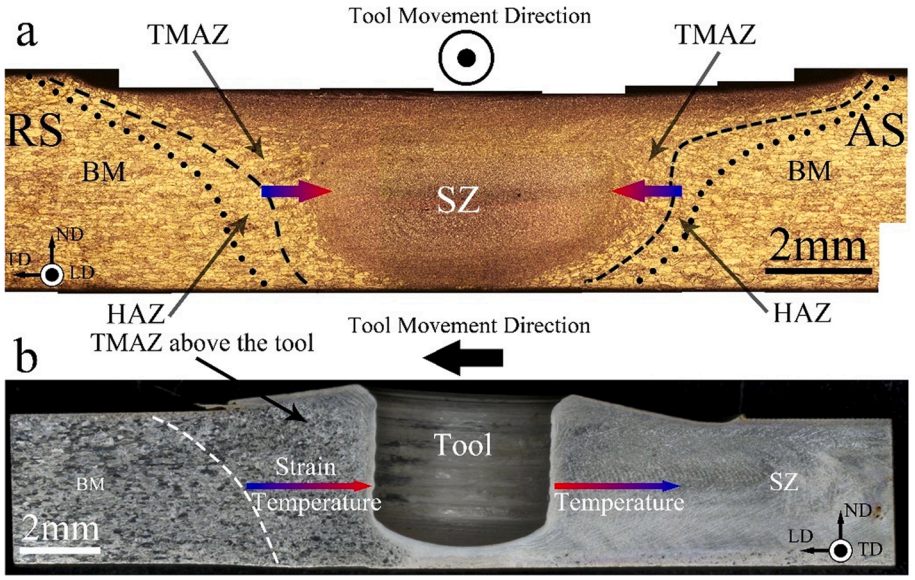

Fig. 4. (a) A typical optical cross-section showing SZ, TMAZ, HAZ and BM. Dotted and dashed lines show outer boundaries of TMAZ and HAZ. Colored arrows indicate gradients of temperature, strain and strain rate from low (purple) to high (red) values. (b) Optical metallograph of a longitudinal cross-section obtained using the "stop-action" technique (pin was moving from left to tight). The dotted line indicates the outer boundary of TMAZ. Colored arrows indicate gradients of temperature, strain, and strain rate from low (purple) to high (red) values. (For interpretation of the references to color in this figure legend, the reader is referred to the web version of this article.)

accumulated dislocation density. Generally, in pure metals, SRV may occur at $T > 0.3\ T_m$, while recrystallization processes operate at $T > 0.4\ T_m$. However, both temperature ranges are essentially dependent on the thermo-mechanical history of material and may be shifted towards either lower or higher temperatures depending on the density and arrangement of accumulated dislocations. Other important issues include the stacking fault energy (SFE), the solute content and dispersoids. Specifically, high-SF metals normally exhibit extensive cross-slip and dislocation climb, thus, the microstructural behavior in such materials is often dominated by recovery, even at relatively high temperatures. In contrast, low-SFE materials typically experience almost no recovery. The solutes can affect the structural behavior through alteration of the SFE, affecting diffusion properties as well as dislocation pinning via the formation of Cottrell atmospheres and typically inhibiting both recovery and recrystallization. Dispersoids with dimensions $\leq$200 nm may also effectively pin lattice dislocations shifting the occurrence of SRV and recrystallization toward higher temperatures.

2.2. Static recrystallization

In a classical sense, static recrystallization (SRX) involves the nucleation of new strain-free grains and their subsequent growth to consume the deformed microstructure [16]. During this process, the microstructure at any time is divided into two distinctly different regions (i.e. the recrystallized and non-recrystallized areas); the recrystallized fraction gradually increases from 0 to 1 as the transformation process proceeds. Such a process fits the definition of a *discontinuous* annealing phenomenon [16], and is sometimes referred to as discontinuous static recrystallization (DSRX). In some cases, however, the recrystallization may develop in a quite different manner, being sometimes referred as the *continuous* static recrystallization (CSRX) or "recrystallization *in situ*." Both these mechanisms are briefly considered in this section.

DSRX takes place in materials having low SFE at $T > 0.5\ T_m$ [25,27]. Nucleation occurs due to the migration of a portion of pre-existing HAGBs into the deformed matrix in a heterogeneous manner (Fig. 5) [25,28-30]. The driving force is the decrease in energy arising from the dislocations consumed by the migrating portion of the HAGBs countered by the increase in energy due to increased grain boundary area caused by bulging (Fig. 5) [25,28,29]. Subsequently, growing grains consume the deformed or recovered microstructure until the material is fully recrystallized. The microstructure is heterogeneous at any time and distinctly divided into recrystallized and non-recrystallized regions. Nucleation is energetically favored once the bulging cap reaches a critical radius determined by the grain boundary energy and the dislocation density [25,28,29].

CSRX, in which a sub-grain bounded partly by LAGBs and partly by HAGBs serves as a nucleus, occurs in materials with high SFE [25,27]. This type of SRX is usually accompanied by extensive particle coarsening which decreases the Zener drag force (Fig. 6) [25,27]. Nucleation by CSRX is attributed to subgrain structure produced by preceding SRV and may occur by two distinctly different mechanisms [25]. The first nucleation mechanism is associated with the migration of LAGBs. It causes the growth of subgrains in the presence of an orientation gradient that originated from geometrically necessary dislocations, which provide compatible deformation for inhomogeneous deformation [25,31]. LAGBs comprising two or more sets of such dislocations are feasible for the transformation to HAGBs. It occurs by the continuous increase in their misorientation during migration due to trapping lattice dislocations [25,27]. The second nucleation mechanism is the coalescence of neighboring subgrains through the decomposition of a low misorientation LAGB (Fig. 7). These LAGBs comprise statistically stored dislocations, which accumulate under uniform plastic deformation, and are termed incidental boundaries [31]. Rearrangement of lattice dislocations from an incidental LAGB to a geometrically necessary one provides an increase in its misorientation (Fig. 7) [25,28,29,31-33]. The coalescence occurs with little boundary migration, the driving force arising from a reduction in boundary energy [25,32,33].

The migration of LAGBs and their coalescence (Fig. 7) leads to subgrain coarsening [25,32,33]. A decrease in stored energy occurs during annealing due to the removal of individual dislocations and their rearrangement to lower energy LAGB configurations [25]. A moving sub-boundary absorbs dislocations leading to increasing misorientation and, therefore, energy and the final transformation of this LAGB to a HAGB [25]. As a result, subgrains delimited by LAGBs produced by SRV are continuously replaced by subgrains and, finally, grains delimited by HAGBs from all sides [25,29].

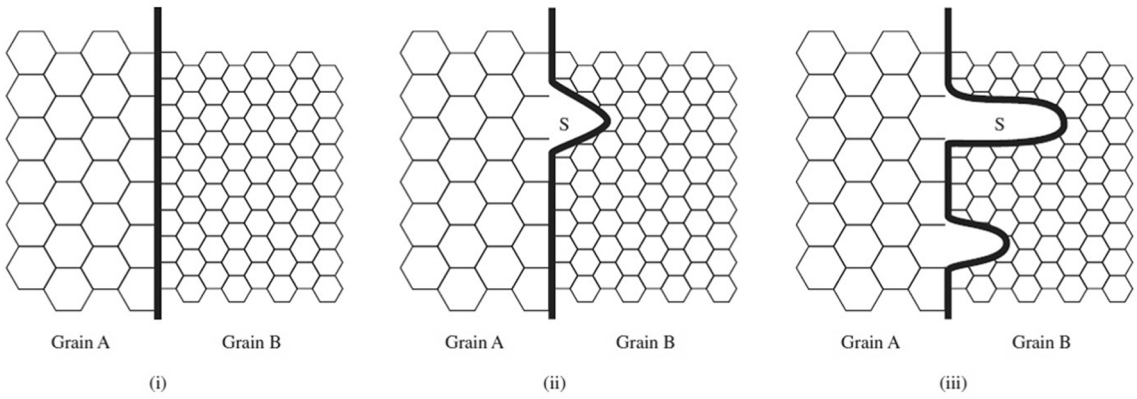

Fig. 5. Schematic showing the migration of a pre-existing grain boundary toward the subgrain structure by SRV [29].

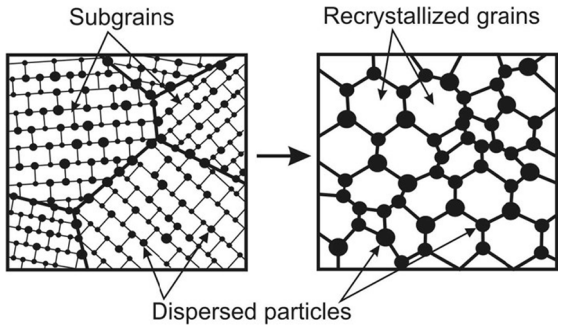

Fig. 6. Schematic representation of the CSRX. Reprinted from [27] with permission from Elsevier.

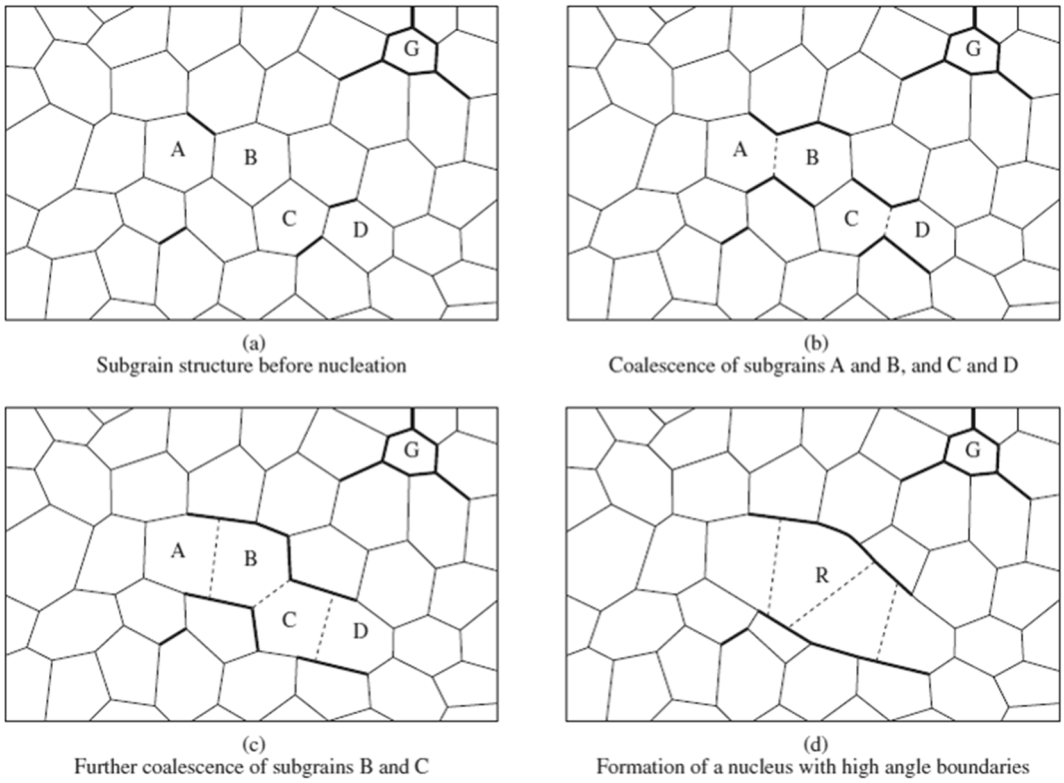

Fig. 7. Schematic showing the formation of a nucleus by coalescence and subgrain coarsening: (a) subgrain structure produced by SRV with a grain G, (b) coalescence of pairs by decomposition of transverse LAGBs between subgrains A-B and C-D, (c) coalescence of the A/B and C/D (sub) grains by decomposition of B-C LAGB, (d) the formation of the coarse nucleus by boundary migration. The thick and thin lines indicate HAGBs and $LAGB_S$, respectively. Reprinted from [29].

2.3. Dynamic recrystallization

Dynamic recrystallization (DRX) is the dominant mode of microstructural evolution in the SZ and TMAZ. The dynamic restoration mechanisms differ considerably from those operating during static annealing of a deformed material [25,27]. The homogeneity of the resulting structure is essentially independent of the DRX mechanism and dictated by the applied strain. Increasing deformation temperature and/or decreasing the strain rate enhances the homogeneity of the recrystallized microstructure. A uniform microstructure evolves in the SZ, while a partially recrystallized structure appears in the TMAZ [34-37]. There are two types of DRX: discontinuous DRX (DDRX) and continuous DRX (CDRX). The former is a two-step recrystallization phenomenon, involving distinct nucleation and subsequent grain growth steps [25,27,36-43]. It occurs in materials with low to medium SFE in which DRV is slow after reaching a critical strain ($T > 0.5\ T_m$) [25,27,41-43]. CDRX is a one-step process that occurs in all materials at $T < 0.5\ T_m$ [25,27,42-47] and also in materials with medium to high SFE at $T > 0.5\ T_m$. The new grains appear because of the increase in sub-boundary misorientation brought about by the continuous accumulation of the dislocations introduced by plastic deformation [25,27,42-47].

The 3D network of LAGBs evolves due to prior DRV. The occurrence of DDRX requires high temperatures and low strains, while CDRX occurs at intermediate temperatures and high strains [43,46].

There are two main features of DRX. Firstly, new grains continuously undergo deformation and so contain many lattice dislocations [25,27]. Secondly, at intermediate recrystallized stages, DRX produces a necklace microstructure consisting of a recrystallized mantle along the initial boundaries with unrecrystallized remnants in the core (Fig. 8). A distinctive feature of CDRX is the presence of a well-defined subgrain structure in the remnants of unrecrystallized grains [25,27]. DRV and CDRX can occur concurrently in the core and mantle regions of the initial grains (Fig. 8), respectively [25,27,46,47]. DRV produces a network of incidental LAGBs having a misorientation of ~1° and takes place in grains belonging to transition texture orientations and associated with multiple slips. Conversely, CDRX usually occurs in stable orientations (e.g. α or β–fibers in cubic materials), in which single or double slip is operative [25,34,35,47]. This structure is typical of the periphery of the TMAZ. The proportion of recrystallized grains in the necklace structure increases from the periphery to the inner edge of the TMAZ [34-37].

The DDRX mechanism involves local grain boundary bulging, growth of the DRX nucleus (driven by stored energy in the neighboring deformed grains), and stagnant grain growth resulting from DRX grain impingement and a diminished driving force for growth (because of work hardening of the growing recrystallized grains) [43,48]. The principal nucleation mechanism of DDRX is similar to the Bailer-Hirsh mechanism suggested for DSRX [27,41,43,48]. In this mechanism, a network of subgrains readily develops near the grain boundaries leading eventually to boundary corrugations or serrations (Fig. 9). The bulged DRX nuclei become separated from the highly dislocated structures by a LAGB or annealing twins (depending on the value of Zener–Hollomon parameter (Z)) such that the DDRX nucleus is partially bounded by a bulged portion of initial HAGB and by a LAGB (Fig. 9) [25,27,39]. Both of these boundaries are able to migrate toward the high dislocation density in parent grains.

The difference in local dislocation densities is commonly considered to be the driving force for the grain boundary migration toward high dislocation density and corresponding growth of DRX nuclei (Fig. 9) [25,27]. Absorption of dislocations by grain boundaries, which serve as sink sites for dislocations, and rearrangement of dislocations followed by their mutual annihilation and/or the formation of subgrain boundaries occur at relatively high rates and strongly decrease the driving force [25]. These processes accelerate with increasing temperature [49,50]. Concurrently, DRV promotes inhomogeneities in dislocated structures between neighboring grains of different orientations thereby facilitating the bulging of a grain boundary portion [25,27,43,48]. Dislocation density gradients are developed near the original grain boundaries because of the incompatibilities in plastic deformation between grains and the strong dependence of DRV rate upon the orientation of the crystalline lattice [31,41,43,48]. This point is most important for DDRX nucleation. As a result, the critical strain for DDRX decreases with increasing temperature and/or decreasing strain rate [27].

A high density of incoherent particles or the presence of coherent dispersoids may suppress DDRX. If the sum of the Zener drag pinning force and the drag force, which relates to the curvature of the HAGB, exceeds the driving force for boundary bulging due to stored dislocations [25], DDRX cannot occur. Finer DDRX grains may be formed at larger strains due to the larger driving force [25,27,43].

Grain boundary shearing (GBS) along initial boundaries commonly takes place during hot working at a low strain rate [27,43,48-52]. GBS induces additional inhomogeneous strains increasing the driving force for recrystallization and promoting the rotation of the bulged DRX nuclei increasing the misorientation between the nucleus and parent grain (Fig. 9) [27,43,48,51,52]. As a result, the DDRX nuclei evolve rapidly at grain boundaries of initially coarse grains resulting in the evolution of necklace-like microstructure, in which the chains of fine DDRX grains decorate original boundaries (Figs. 8 and 9) [25,27,43,46,48,52,53]. The DRX mantle propagates with increasing strain, ultimately resulting in a homogeneous microstructure consisting of fine grains (Fig. 8) [25,27,39,43,46,48]. An increase in deformation temperature promotes the recovery-assisted nucleation and diffusion-controlled growth of new grains and, thus, accelerates the DRX kinetics [25,39,42,43,53].

CDRX involves the formation of stable three-dimensional (3D) arrays of strain-induced LAGBs due to dislocation rearrangement, followed by their gradual transformation to HAGBs (Fig. 10) [25,27,43-47,54]. The progressive evolution of the subgrains occurs continuously and ultimately leads to their conversion to fine grains, when the sub-boundary misorientation exceeds 15° [25,27,43-47,54]. The rotation of subgrains is accompanied by boundary migration (Fig. 10). As a result, the size of the resulting grains is higher than the preceding subgrains by ~30%. [45,47,54]. CDRX may occur in materials with low SFE subjected to intense straining at intermediate temperatures [46,53]. Such conditions may appear in the inner half of the TMAZ and the SZ in which $T > 0.6T_m$ and true

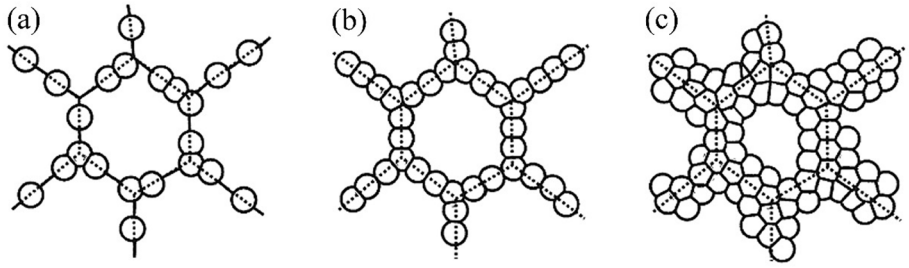

Fig. 8. The progressive development of a recrystallized mantle during DRX; (a) The formation of separate DRX grains, (b) the formation of the first recrystallization layer, (c) the formation of a mantle of recrystallized grains. The dotted lines show the prior grain boundaries and solid lines the boundaries of recrystallized grains. Reprinted from [25] with permission from Elsevier.

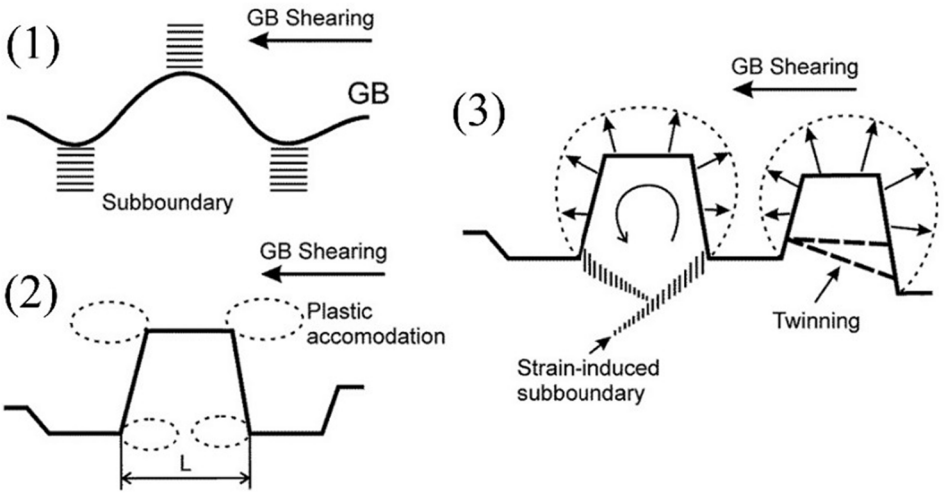

Fig. 9. Schematic representation of the DDRX mechanism; (1) at low strains, the corrugation and the evolution of sub-boundaries occur concurrently, (2) GB shearing along the original boundary leads to the development of local strain gradients during further straining, and (3) the bulging of parts of the serrated grain boundaries is accompanied by the formation of sub-boundaries at high Z or twin boundaries at low Z. Reprinted from [27] with permission from Elsevier.

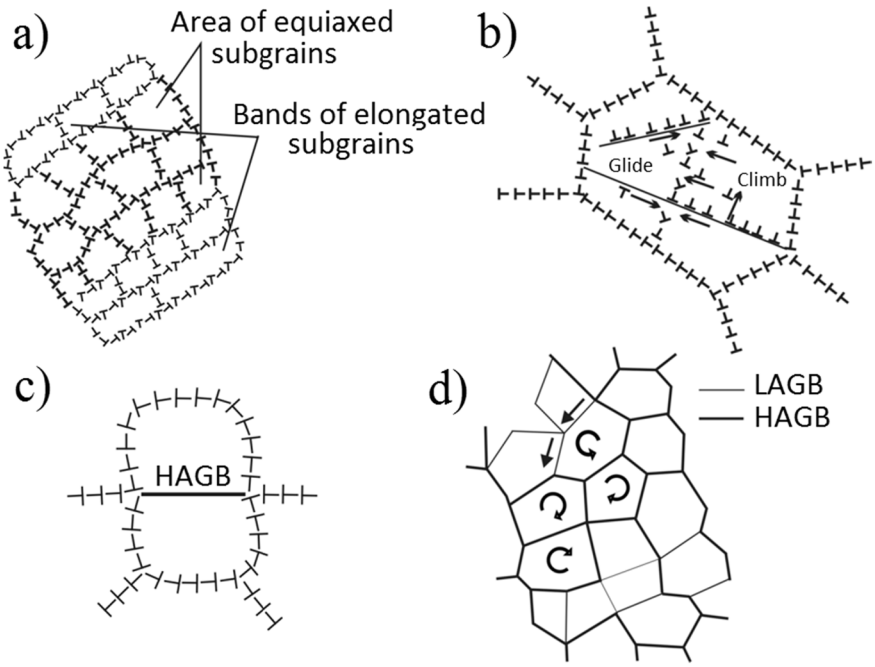

Fig. 10. Schematic representation of CDRX; (a) the formation of 3D arrays of subgrains; (b) interaction of LAGBs with lattice dislocations resulting in progressive increase in their misorientation; (c) subgrain as a nucleus; (d) rotation of subgrains and grains facilitate the transformation of LAGBs to HAGBs. Reprinted from [45] with permission from Elsevier.

strain ranges from ~1 to 20. CDRX is characterized by much slower kinetics than those associated with DRX because the continuous evolution of strain-induced grains requires very large strains [25,27]. CDRX produces a necklace microstructure at an intermediate stage due to the rapid development of strain gradients near grain boundaries (Fig. 8).

Geometric DRX (GDRX) is a kind of CDRX observed in pure Al or low alloy Al belonging to 1XXX series deformed in torsion or by extensive rolling [25,55-58]. New grains evolve due to the impingement of wavy boundaries of initial grains that leads to the subdivision of the fibrous grains to crystallites bounded by HAGBs after large strain. The GDRX mechanism requires some boundary mobility for the bulging process followed by their pinch off. The last process occurs due to boundary tension and is driven by minimizing boundary energy [25,58,59]. GDRX occurs when the boundary spacing and wavelength typically become similar to the

subgrain size due to the extensive concurrent elongation of initial grains and the formation of subgrain structure with no orientation gradients due to DRV [25,36,58]. The interpenetration of the scalloped boundaries occurs, thus transforming a severely compressed grain into a chain of fine nearly-equiaxed grains. Therefore, a fine-grained microstructure having a large proportion of high-angle boundaries may evolve without the activation of any microscopic recrystallization mechanism. The presence of pinning agents hinders GDRX shifting the formation of fine grains to higher strains. Analyzing experimental results [36,60,61] suggests that GDRX is unlikely to occur under FSW because the strain rate in the SZ is very high while the strain in the TMAZ is insufficient for severe grain elongation.

2.4. Post-dynamic recrystallization

In the conventional FSW, the weld region remains hot for some time behind the tool after FSW with the nugget cooling at a rate ranging from 10 to 60 K/s depending on the material, plate thickness, FSW parameters, and location [60,62-64]. As a result, post deformation annealing [25,27] occurs in the SZ until the weld has cooled completely [60,62-64]. This phenomenon is known as metadynamic recrystallization (MDRX) [25,27,65] and the nature of microstructural evolution is dependent on zone. Three types of DRX structures are susceptible to MDRX [27,65]. First, the recrystallized grains containing a moderate dislocation density may grow under static post-FSW annealing. Secondly, MDRX may occur in heterogeneous DRX regions by extensive growth of small pre-existing nuclei, which are almost dislocation-free [25,27,65]. Thirdly, SRV or even SRX may take place in unrecrystallized material having a high dislocation density.

3. Texture evolution

Friction stir welded joints are characterized by textural variations through the thickness and across the width of the weld, but they can also occur along the length of the processed zone [66-68]. The SZ, TMAZ, and HAZ all have very different thermomechanical histories and hence, have different textural features. In addition, there are local textures that develop within various regions of the SZ that derive from the final deformation state of each specific location. These are a function of tool design and weld parameters that alter flow in the SZ [67-70].

3.1. Textures arising from shear deformation

Depending upon the processing parameters, the local textures that develop within the SZ are associated with DRX during compressive deformation and shearing. Those in the TMAZ are dependent upon bending and recrystallization (or grain growth) of the base metal texture, while those in the HAZ develop by recrystallization or grain growth of the base material. The predominant deformation mode during FSW/P is that of shear deformation. Textures during shearing are described by alignment of the crystallite lattices with the shear plane normal (SPN) and the shearing direction (SD). For example, face-centered-cubic structures (FCC) deformed by shearing typically produce partial fiber textures of $\{1\,1\,1\}\ \langle uvw\rangle$ where the $\langle 1\,1\,1\rangle$ poles align with the shear plane normal and the crystallites are distributed randomly about that axis, and $\{hkl\}\ \langle 1\,1\,0\rangle$ where the $\langle 1\,1\,0\rangle$ directions are aligned with the shearing direction and the distribution about that direction is unspecified. These are referred to as the A and B fibers, respectively. In addition, a C texture component, $\{1\,0\,0\}\ \langle 0\,1\,1\rangle$, occurs during shearing of FCC metals [71]. Fig. 11 shows a $\{1\,1\,1\}$ pole figure that contains the

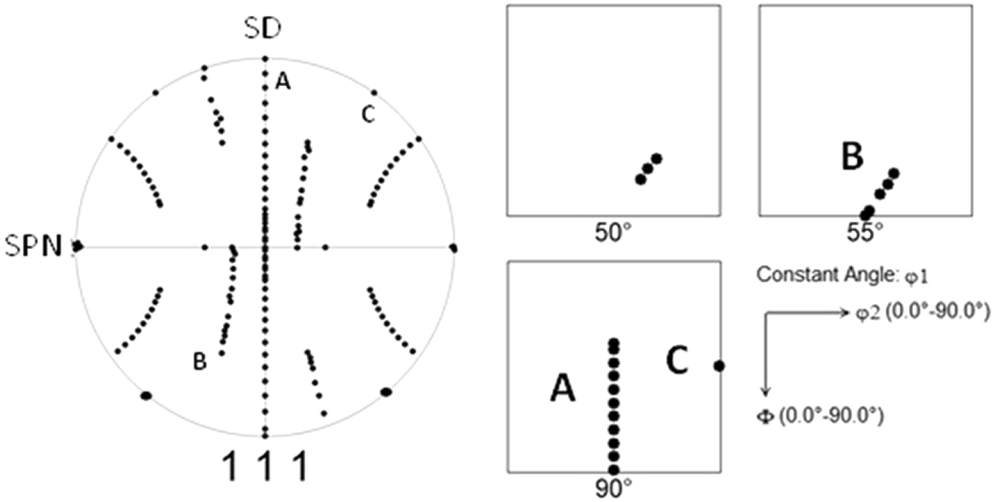

Fig. 11. Ideal partial A and B fiber textures and the C texture component shown as (a) a pole figure, and (b) Euler space plots with A and C seen in the constant sections of $\varphi_1 = 90^\circ$ and the partial B fiber spread through the $\varphi_1 = 50^\circ$ and 55° sections. SD and SPN stand for shear direction and shear plane normal, respectively.

ideal A and B partial fibers and the C component alongside discrete Euler space. In this convention, φ_1, Ø and φ_2 represent consecutive rotations about the x-axis, the new z-axis, and the new x-axis, respectively [72,73]. It should be noted that the orientation distribution function (ODF) is actually a probability density function, but it is conventionally referred to as a distribution function.

For hexagonal close-packed (HCP) materials, shear textures comprise a series of fiber textures, including B $\{0001\}\langle uvtw\rangle$, and two C fibers with the basal plane rotated to orientations 30° from the shearing direction and a random distribution of the lattice rotated about that direction [74].

Dynamic recrystallization can cause difficulties in interpretating the local textures in terms of the deformation state of the metal. Fortunately, the textures of dynamically recrystallized metals tend to follow those of the deformed metals closely. This is because the recrystallization nuclei are formed from the deformed and deforming grains, giving a structure of fine grains having a similar texture to the deformed ones.

During FSW/P, certain alloys may undergo phase transformations. For example, α-titanium (HCP), transforms to β-titanium (BCC) at temperatures above about 0.6 T_m. If the temperature rises above the transformation temperature, shear textures form in the higher temperature β-phase that exists during processing. These microstructures transform as the processed material cools, and the transformation microstructures exhibit textures distinct from those that developed during processing. Nevertheless, due to orientation relationships that exist in transformation microstructures, it is often possible to determine the texture that developed during processing and to back-out material flow during processing. In steels, the transformation between the high temperature austenitic phase (ɣ, FCC) and the lower temperature ferritic phase (α, BCC) is understood to be $\{111\}_\gamma||\{110\}_\alpha$ and $\langle 110\rangle_\alpha||\langle 111\rangle_\gamma$ (Kurdjomov-Sachs relationship [75]) or others [76,77]. If titanium is stirred under hot conditions, it is processed as BCC β-titanium, resulting in shear textures indicative of a BCC shear deformation. Upon cooling, the structure transforms to HCP α-titanium with an orientation relationship understood to be $\{0001\}\alpha||\{011\}\gamma$ and $\langle 11-20\rangle\alpha\ ||\langle 111\rangle\gamma$. If random variant selection occurs, the resulting textures are identifiable, but are more random than for materials processed similarly without the phase transformation.

3.2. Local textures and metal flow during FSW/P

As alluded to in the previous sections, crystallographic textures vary dramatically from point to point within and near the zone produced by FSW/P. Because of this, local anisotropies exist that result in spatial variations in strength, hardness, corrosion susceptibility, etc. Local textures that develop during FSW/P have been evaluated for alloys of aluminum [78-83], magnesium [84-90], titanium [91-95], steels [96-101], copper [102,103], nickel [104,105] and metal matrix composites [106,107], as well as for dissimilar metal joints [108-112]. An example is shown in Fig. 12 showing bands of distinct textures across the width of the FSW region. This occurs because the shear direction of the last in time material to be processed in the plate is aligned with the tangent of the weld tool as it passes through the metal. This direction changes from point to point across the weld as the profile of the tool shoulder creates a semicircle that follows behind the tool. The shear plane normal in this region depends upon the FSW/P parameters such as tool rotation rate, the welding speed, and the design of the weld tool.

In order to properly interpret the local textures observed in friction stir welded/processed metals, the reference coordinate frame must be rotated to a suitable orientation to represent the textures as ideal components and fibers. Given that the dominant textures derive from the shear deformation, it is necessary only to identify the positions of the shear plane normal and the shearing direction from the observed textures. Rotation of the ideal textures to the FSW coordinate frame requires minimization of the norm of a calculated difference ODF; $\Sigma_I \sqrt{[f_{ideal}(g_i) - f_{actual}(g_i)]^2}$; where g_i is the orientation of the crystallite lattice through the space of the ODF,

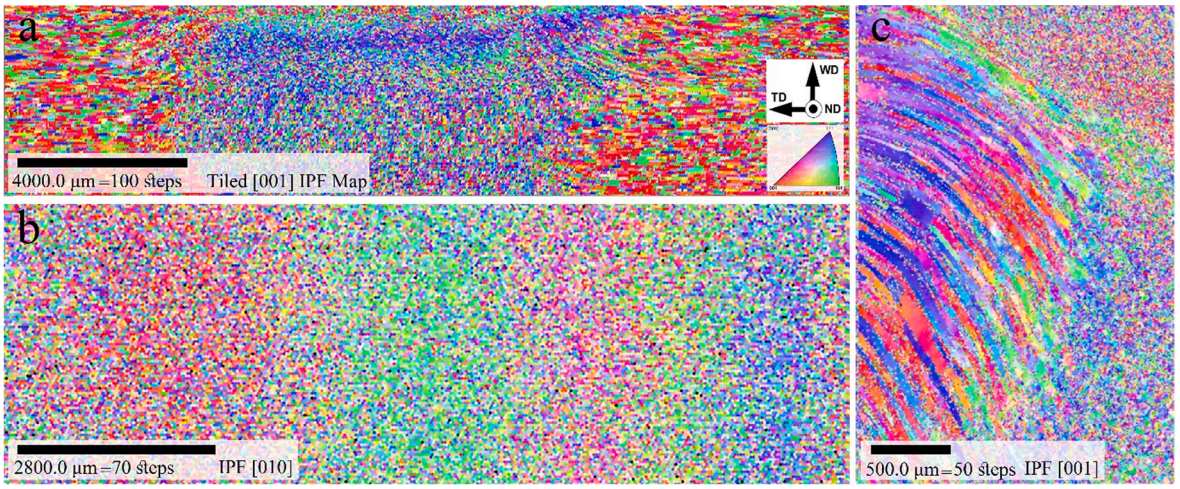

Fig. 12. (a) EBSD IPF map across a cross-section of a friction stir weld in commercial purity aluminum, (b) corresponding plan view (weld moves from bottom to top) for region under the 25.4 mm diameter weld tool shoulder. The advancing side (AS) is on the right. Crystallographic poles aligned with the transverse direction (left to right in the image). (c) Enlarged cross-sectional view of the transition region from the BM to the SZ on the AS. Reproduced from [66] with permission from Springer Nature. The coordinate system and color codes are the same in (a-c) as shown in (a).

f_{ideal} represents the ideal ODF for shear deformation and f_{actual} is the measured function. The actual function is rotated through all possible coordinate frames until it best matches that of the ideal function, thus revealing the orientation of the shear plane normal and the shearing directions. If the resulting structure is a transformation microstructure, the Euler angles must be operated upon by the appropriate orientation relationships before searching for the minimum ODF difference function. Fig. 13 shows an example of a texture for a FSP AZ31 magnesium alloy in both the specimen reference frame and after rotation by 35° about the plate normal direction. The latter is in good agreement with the ideal shear texture in the recognized SD/SPN coordinate frame (Fig. 13c). Local texture determination aids in understanding material failures and inhomogeneous corrosion behavior in and around friction stirred regions. Analysis of material flow fields using crystallographic texture as a tool, can provide important insights into material flow for optimization of weld parameters and tool design. The textures occurring in metals deformed by simple shear, as reviewed by Fonda and Knipling [68], are combined with contributions from elsewhere in Table 1 [74,113-116].

4. Microstructural evolution during FSW

Thermomechanically, FSW represents a unique combination of very large strain, high temperature, and relatively high strain rate. The present section attempts to summarize the current state of understanding of the microstructural processes occurring under such extreme conditions. In view of the severe processing conditions, experimental investigation of the concomitant microstructural evolution is challenging. At present, two approaches are typically employed for this purpose, namely the stop-action technique and the mapping of the transient region, as shown in Fig. 14.

As the name suggests, the stop-action technique (Fig. 14a) involves an emergency stop of the FSW machine and subsequent immediate quenching of the welded material in an attempt to "freeze" the evolving microstructure near the welding tool [36,78,119]. In some cases, rapid extraction of the tool is used instead [79,120,121] and liquid CO_2 is applied to enhance the quenching effect [103,122-124]. Such a "stop-action" technique is believed to allow the direct observation of the FSW-induced microstructure evolution in-situ during the process. It should be noted, however, that a rotating tool cannot be stopped instantly due to inertia of the FSW system. Moreover, mechanical relaxation of this system results in shifting of the tool from the position of the actual weld termination [125,126]. In other words, tool stoppage (or tool extraction) will inevitably affect the microstructure near the final tool position. Therefore, the "stop action" approach is perhaps applicable only for relatively slow FSW and caution should be exercised in interpreting the experimental results.

The second technique (Fig. 14b) is based on the microstructural examination of the transient region from the BM to the SZ. Across this region, the material transforms from the parent state to the final one providing insight into the microstructural changes occurring during FSW (see yellow arrow in Fig. 14b). This method is very simple and is often used in practice. However, considering the complex nature of the microstructural changes taking place during and after, FSW this approach may not give a full picture.

Recently researchers have exploited the flux of synchrotron X-ray sources to obtain information in real-time using 'portable' FSW systems, for example, to follow precipitation by Small-Angle X-ray Scattering (SAXS) [127]. Real-time measurements have been complemented by high spatial resolution post mortem synchrotron X-ray mapping of the phases or residual stress (by X-ray diffraction) as well as the precipitate size and volume fraction (by SAXS) across the weld region [128-131]. Laboratory SAXS can also provide similar information on excised cross-sections, although at slightly lower spatial resolution [132], complemented by Differential Scanning Calorimetry (DSC) [133].

4.1. Development of grain structure

For the reasons discussed in section 2, microstructure evolution is a strong function of crystal structure and SFE. The literature has therefore been categorized here into three broad groups, i.e., (*i*) cubic metals with relatively high SFE ($\geq$100 MJm^{-2}), (*ii*) cubic metals with low-to-moderate SFE ($<$80 MJm^{-2}), and (*iii*) HCP metals.

4.1.1. Cubic metals with high stacking fault energy

Grain structure evolution during FSW of high-SFE cubic metals has been studied primarily in aluminum alloys [36,62,78-80,118,120,124,134-154]. However, some interesting observations have also been made in pure iron [34] and β-titanium [155]. In most cases, the microstructural evolution follows a number of common trends. At the colder periphery of the TMAZ, microstructural changes tend to be dominated by the formation of regular arrays of LAGBs, which rapidly accumulate misorientation and gradually

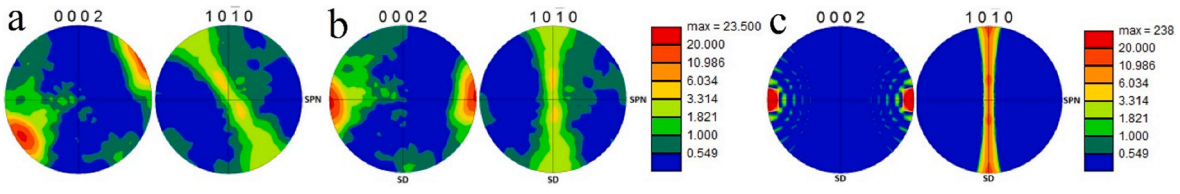

Fig. 13. Pole figures for the mid-plane position in SZ near the TMAZ on the retreating side (RS) of an AZ31 Mg alloy treated by FSP showing (a) a shear texture measured in the coordinate frame of the specimen coordinates, (b) the same texture after rotation to an orientation that aligns with the ideal shear texture, and (c) a representation of the ideal shear texture in HCP Mg. The color bars are in units of times random. Reprinted from [117].

Table 1
Texture components and definitions for common shear textures in FCC, BCC, and HCP metals. TD refers to the transverse direction (mutually orthogonal to SD and SPN). Partial fibers A and B for FCC crystal structures, are sometimes designated as specific texture components instead of partial fibers. Hence, A_1* and A_2* are also shown. Symmetrical equivalents of the Euler angle triplets are always assumed to be present in addition to those listed and are not explicitly included in this table.

Crystal Structure	Texture Name	Miller Indices	φ_t	Φ	φ_2
FCC	A-fiber	{1 1 1}||SPN			
	A_1*	$\left(\bar{1}\ 1\ 1\right)\left[\bar{1}\ 1\ \bar{2}\right]$	35.3	45	0
	A_2*	$(1\,1\,1)\left[1\ 1\ \bar{2}\right]$	125.3	90	45
	A	$\left(1\ \bar{1}\ 1\right)\left[\bar{1}\ \bar{1}\ 0\right]$	144.7	45	0
	B-fiber	SD||⟨1 1 0⟩			
	B	$\left(\bar{1}\ 1\ \bar{2}\right)\left[\bar{1}\ \bar{1}\ 0\right]$	0	54.7	45
	C	(0 0 1)[1 1 0]	90	45	0
BCC	D or D_1	$\left(\bar{1}\ \bar{1}\ 2\right)[1\ 1\ 1]$	54.7	45	0
	E	$(1\,1\,0)\left[1\ \bar{1}\ 1\right]$	90	35.3	45
	J	$(1\,1\,0)\left[1\ \bar{1}\ 2\right]$	90	54.7	45
	F	(1 1 0)[0 0 1]	0	45	0
HCP	B-fiber	{0 0 0 1}||SPN			
	P-fiber	SD||⟨1 1 $\bar{2}$ 0⟩			
	P_1	{1 1 0 0}⟨1 1 $\bar{2}$ 0⟩	0	0	0
	Y-fiber	{0 0 0 1}||±30° from TD to SPN			
	C_1-fiber	{0 0 0 1}|| −30° from SD to SPN			
	C_2-fiber	{0 0 0 1}|| 30° from SD to SPN			
	h5-fiber	{0 0 0 1}|| −5° from SD to SPN			
	h6-fiber	{0 0 0 1}|| 50° from SD to SPN			

transform into HAGBs [34,36,78,80,118,136]. From a broad perspective, the observed microstructural pattern is reminiscent of the grain subdivision process (Fig. 15a), which is often reported to occur during cold deformation of cubic metals with relatively high SFE [156-158].

Close to the welding tool, the concomitant increase in strain and temperature means that the parent grains become substantially elongated due to the geometrical requirements of the imposed FSW strain, thus transforming into thin, fibrous grains [34,36,78,80,118,136]. On the other hand, the increased heat input gives rise to grain-boundary bulging which may result in either GDRX [36,139] or nucleation of recrystallized grains [36,118], as shown in Fig. 15b. During the FSW cooling cycle, the SZ may additionally undergo microstructural coarsening [36,62,80,124] or even SRX [80], which may increase the grain size [62,80].

As expected, microstructural evolution is found to be sensitive to the weld heat input [62,118]. Specifically, an increase in FSW temperature may result not only in substantial grain growth, but also in a fundamental change in morphology from a lamellar type to an equiaxed one [118]. The latter effect alters the strain compatibility requirements at grain boundaries and thereby may principally affect the FSW-induced texture [118]. Moreover, the high welding temperatures reduce dislocation density and thus slow down the development of deformation-induced boundaries; as a result, the evolved microstructures may contain a relatively low HAGB fraction [118]. This effect presumably reflects an increased competition between DRV and DRX processes at high deformation temperatures in line with commonly accepted arguments discussed in Section 2.

It is also noteworthy that the grain structure evolution is also sensitive to the initial material condition [118,138,140,141]. In particular, for materials supplied in a cold-worked state the HAZ may undergo SRX (Fig. 15c) [118,138,140,141].

Despite the complexity of the microstructural processes shown above, the dominant mechanism is often believed to be the CDRX, as shown in Fig. 15d [34,36,78,118,134-136,138-141]. This is due to the relatively high dislocation mobility in high SFE materials, meaning they rapidly rearrange into deformation-induced boundaries, thus promoting CDRX. On the other hand, such rearrangement reduces the density of free dislocations and therefore eliminates a driving force for DDRX.

It should be noted, however, that grain structure evolution in 7xxx aluminum alloys as well as in pseudo-β titanium alloy (Fig. 15e) has been interpreted in terms of the discontinuous recrystallization [79,120,137,155]. The reason for the exceptional behavior of these materials is not clear. One of the possible explanations may be the influence of constituent second-phase particles on the recrystallization mechanism.

4.1.2. Cubic metals with low-to-moderate stacking fault energy

Microstructural development during FSW has been examined in the following low-to-moderate SFE materials; austenitic steels [125,126,159-172], Cu-30Zn brass [38,122,173-182], commercial purity copper [102,103,121,123,183], and nickel-based alloys [184,185]. The low-SFE metals are often supplied in a well-annealed temper, thus, their initial microstructure is characterized by a significant proportion of annealing twins. Accordingly, FSW-induced microstructural changes in these materials often initiate from a gradual transformation of Σ3 twin boundaries into random (non-twin) ones [163,172,173], as shown in Fig. 16. This is usually

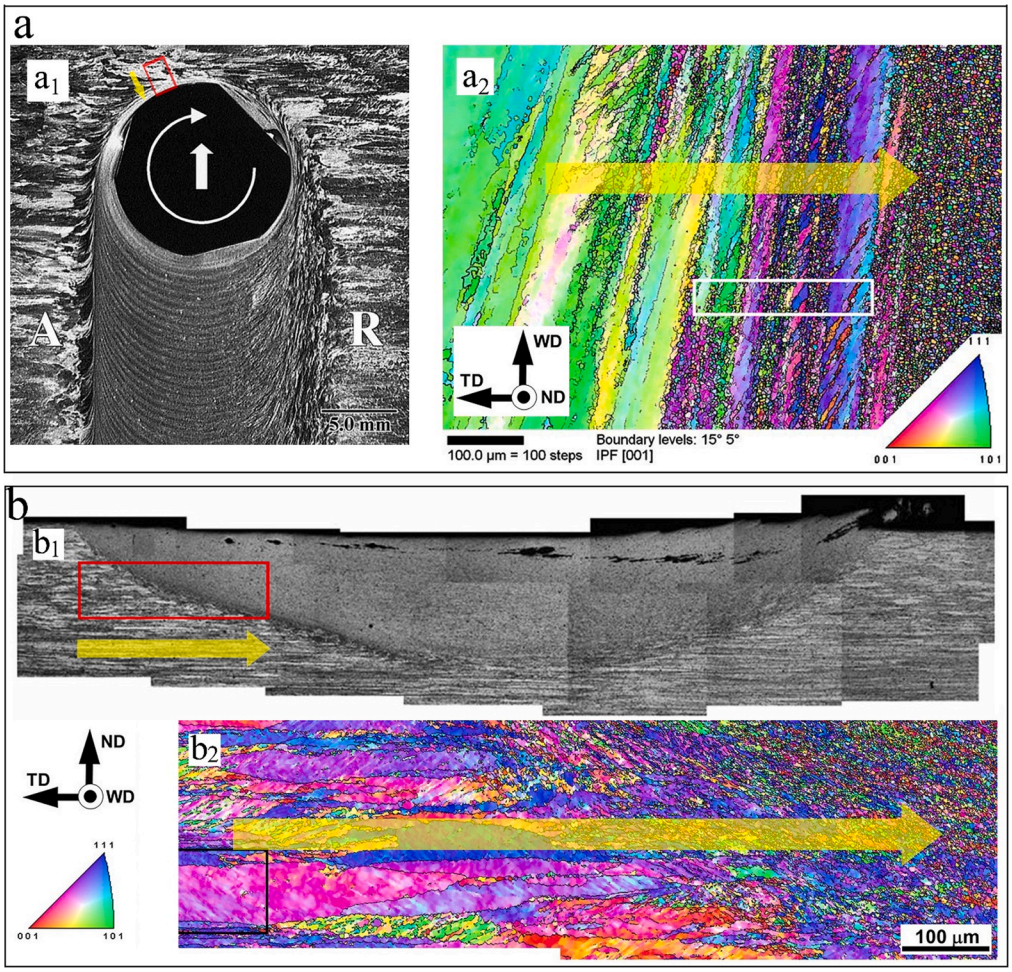

Fig. 14. Methods for investigating microstructural evolution during FSW; (a) stop-action technique [78]. (a_1) Macrostructure of the stop-action friction stir welded Al–Li 2195, (a_2) inverse pole figure (IPF) map of the area indicated by red rectangle in (a_1). (b) mapping of the transient region between base material and SZ [118]; (b_1) macrostructure of friction-stir welded Al alloy 1050 at a rotational speed of 500 rpm and a traverse speed of 10 mm/s, (b_2) IPF map of the area indicated by red rectangle in (b_1). The yellow arrows indicate the transition direction from the colder and lower strain periphery (far from the tool) towards the higher temperature and strain area (close to the tool). In (b) RS is on the left. Reproduced with permission from Elsevier and Springer Nature. All rights reserved. (For interpretation of the references to color in this figure legend, the reader is referred to the web version of this article.)

explained in terms of a slip imbalance between the twin and the adjacent matrix, which leads to diverging crystallographic rotations of both crystals, destroying the ideal Σ3 orientation relationship [186,187].

Closer to the welding tool the higher strains give rise to deformation-induced LAGBs in the grain interior, perhaps reflecting activation of the DRV process. In contrast to the high-SFE materials, however, the LAGBs are much less regular in appearance, do not form a clear subgrain structure, and tend to cluster near original grain boundaries [163,172,173] as illustrated in Fig. 17 for a variety of materials.

As shown in Fig. 18, an increase of the welding temperature promotes grain-boundary bulging and subsequent nucleation of recrystallized grains. This activates DDRX and results in a bimodal grain structure [38,102,126,162-164,167,169,172-174,184]. As expected, the grain-boundary migration is accompanied by annealing twinning; accordingly, the recrystallized grains are typically LAGB-free but contain annealing twins with nearly perfect Σ3 boundaries [38,102,126,162-164,167,169,172-174,184].

As seen in Fig. 19, close to the tool, surviving remnants of the parent grains are severely sheared due to the very large strains imposed during FSW [162,173]. This often results in the activation of CDRX. Accordingly, grain structure evolution becomes a competition between DDRX and CDRX [38,162-164,167,169,173,174,184].

Remarkably, annealing twins in the final SZ microstructure typically exhibit a nearly ideal misorientation Σ3, i.e. they show no signs of accumulated plastic strain [102,126,162-164,167,169,172-174]. For instance, the grain boundary map showing the Σ3 boundaries in the SZ in the friction stir welded super austenitic stainless steel in Fig. 20a. Therefore, it has been suggested that a significant portion of the DDRX occurs during the weld cooling cycle [163]. In copper, this has been confirmed by "stop-action"

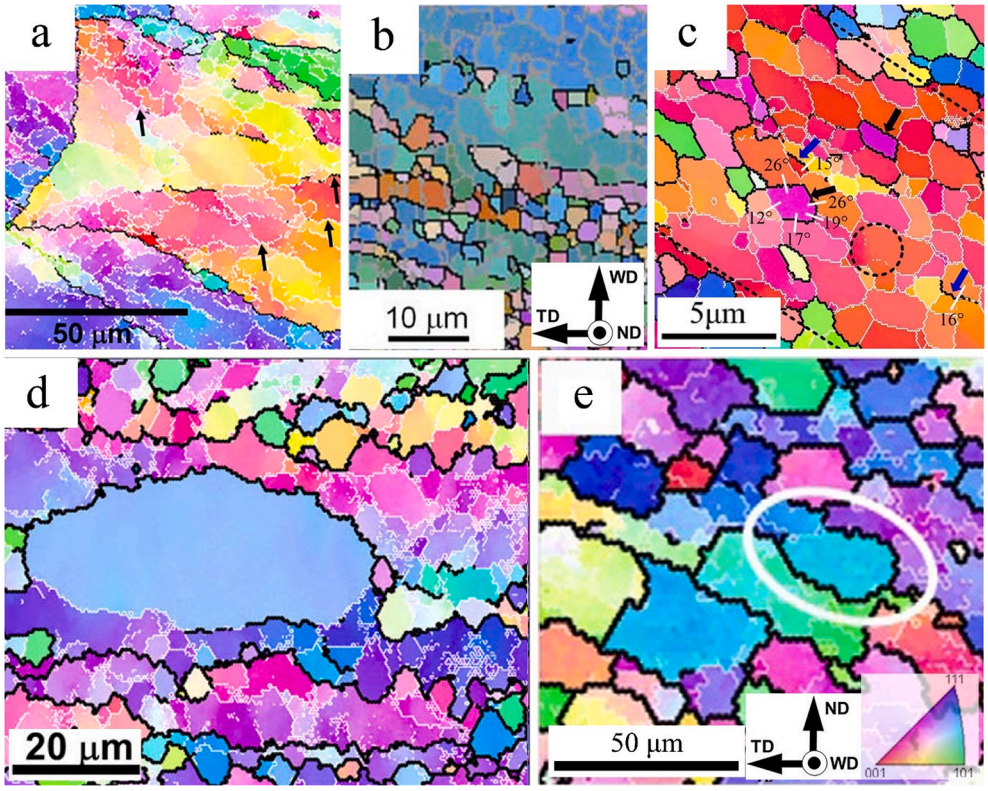

Fig. 15. IPF maps showing microstructural evolution during FSW of cubic metals with high SFE. (a) the grain subdivision process and the formation of regular LAGBs at the TMAZ during FSW of pure iron [34], (b) occurrence of GDRX during FSW of an Al-2195 plate [36], (c) LAGBs and HAGBs in TMAZ for FSW Al 1050-H24 sheets [124] where CDRX (transformation of LAGBs (white colored lines) to HAGBs (black colored lines)) is the dominant mechanism, (d) HAZ in the friction-stir welded Al 1050 plates in which a SRX grain is formed [118], (e) TMAZ in FSW Ti–15V–3Cr–3Al–3Sn alloy [155]. The area inside the white ellipse refers to a DDRX grain formed by building mechanism. (a) and (c-e) have the same coordinate system. The color code shown in (e) can be used for all cases. HAGBs and LAGBs are shown by black (darker) and white (lighter) colors, respectively. Reproduced with permission from Elsevier and Springer Nature.

experiments [79,102,103,122,123,126].

It is important to note that the FSW processing window for the low-to-moderate SFE materials is relatively narrow, thus, a systematic investigation into the effect of welding temperature and/or cooling rate on microstructure evolution is difficult. Nevertheless, limited experimental data evidence points to an enhancement of CDRX (Fig. 20b) [102,162,164,171,174] and even the activation of mechanical twinning (Fig. 20c) [173] and/or micro-banding [121] at low FSW temperatures. In this context, it is worth noting that recent microstructural examinations of friction-stir welded TWIP steels revealed no significant twinning [172]. This observation is believed to be due to the limited weldability of this material, which naturally restricts microstructural examination to welds at the relatively high-temperature range, as mentioned above. It is clear from the above that a characteristic of the microstructural evolution of low-to-moderate SFE materials during FSW is the significant role played by the DDRX in agreement with the accepted structural behavior of such materials under hot deformation discussed in Section 2.4. In austenitic steel joints, precipitation of sigma-phase [159,161,168] or δ-ferrite [156,160,165,170] is sometimes observed (Fig. 20d). Moreover, FSW of these materials often leads to extensive tool wear, which results in pronounced tool debris in the SZ [170-172]. The processes can lead to local grain refinement but the mechanism has not been studied.

4.1.3. Hexagonal close-packed metals

Microstructural evolution during FSW of HCP alloys has been studied for magnesium alloys [87,89,188-201], commercial purity titanium [35,202,203], and zirconium [204].

The process of grain structure development within the TMAZ in these materials is found to be broadly similar to that in the low-SFE metals discussed above. Specifically, the initial stage of microstructural evolution at the relatively cold periphery of the TMAZ may involve pronounced mechanical twinning [87,89,190,194], as shown in Fig. 21a) and b). In contrast to the cubic crystals, however, it is a result of the limited number of available slip systems. Since the mechanical twinning is sensitive to grain size as well as to the crystallographic texture, this process can be greatly influenced by the initial material condition [193]. The boundaries of the mechanical twins are also unstable against the ongoing strain; thus, the twins gradually transform into irregularly shaped grains (Fig. 21a and b) [87]. In common with the low-SFE metals, a further increase in strain and temperature result in the concurrent development of

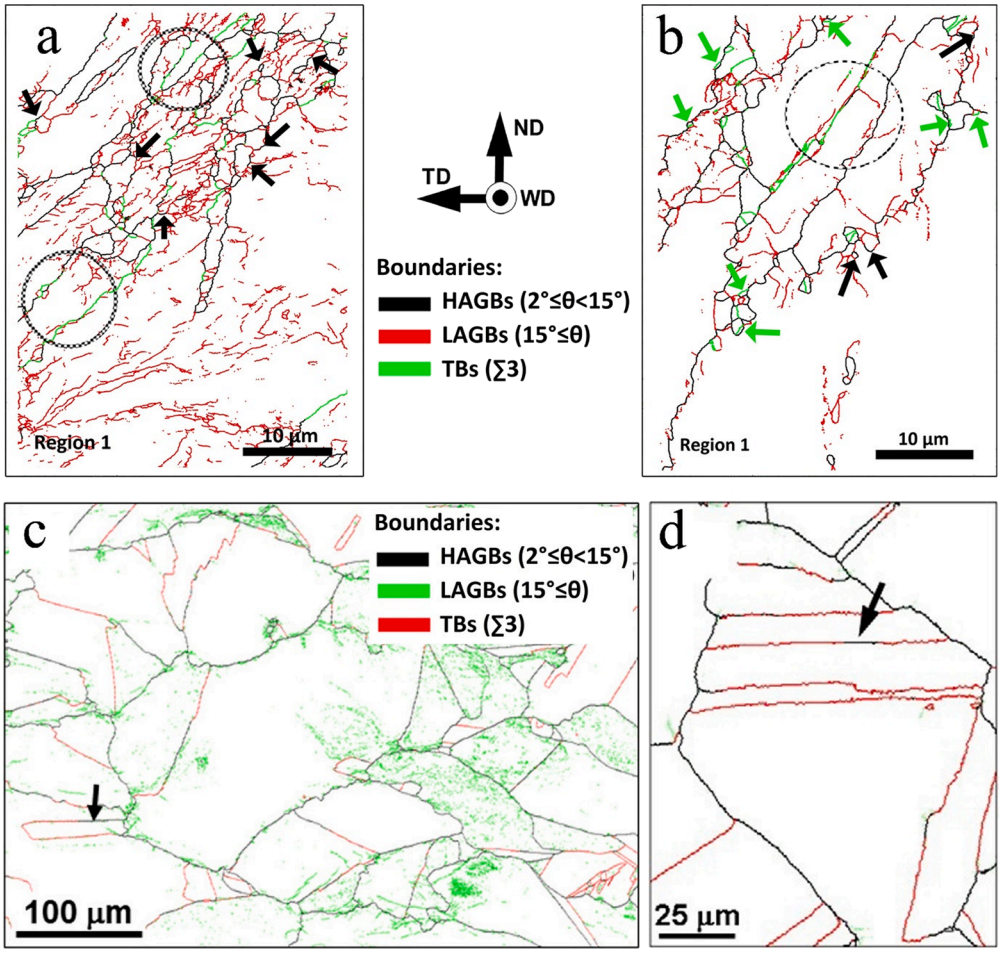

Fig. 16. Gradual transformation of Σ3 twin boundaries to random boundaries in the colder periphery of FSW-induced deformation zone: (a) grain boundary map of TMAZ in pure copper [38], (b) in Cu-30Zn brass alloy [38], (c) in a TWIP steel with a chemical composition of Fe-12.6Mn-0.49C-0.3Si-1.62Al [172], and (d) in a S31254 super austenitic stainless steel [163]. All maps have the same coordinate system. (a) and (b) have the same color codes as shown between them. (c) and (d) have the same color codes as shown in (c). Reproduced with permission from Elsevier.

CDRX and DDRX (Fig. 21c) and d)), often leading to a bimodal grain structure [35,87,89,189-191,195,196].

As shown in Fig. 22, FSW of HCP metals is characterized by exceptionally strong texture in the SZ [35,87,89,190-192], which can be in excess of 100x random in magnesium alloys [192]. Strong textures impose strict limitations on the grain-boundary misorientations and thus may exert a considerable influence on grain-structure evolution. Specifically, the development of an extremely sharp {0 0 0 1} ⟨u v t w⟩ *B*-fiber texture during FSW of magnesium alloys restricts the maximal allowable misorientation angle to 30° [87,190-192]. As a result, an extensive lowering of grain-boundary misorientations may occur [87,190-192]; this effect has been called "grain convergence" [35,87]. It is believed that this mechanism significantly contributes to the formation of the SZ microstructure in HCP metals [35,87,190-192]. As for cubic materials, microstructural coarsening can occur as the weld cools, which may affect the final grain size, texture strength and misorientation distribution [87,192].

The grain-structure evolution during FSW of HCP metals appears to be sensitive to the weld heat input with lower welding temperatures promoting mechanical twinning, but suppressing DDRX [87]. For instance, a high fraction of twins in the final SZ microstructure has been reported [194,202]. It is also noteworthy that FSW of commercial purity titanium may lead to pronounced tool wear [203], which may influence the formation of grain structure on a local scale.

4.1.4. Multiphase alloys

The microstructural behavior of alloys containing a significant (≥10 vol%) fraction of a second phase during FSW has been examined for duplex stainless steels [100,205,206], Ti-6Al-4V alloy [91,207-233] and Cu-Zn brass [234].

For duplex steels, FSW was found to result in substantial grain refinement in both the ferritic and austenitic phases [100,205]. In the ferrite, crystallographic measurements have revealed a typical simple-shear texture; thus, grain-refinement has been attributed to CDRX [100]. On the other hand, the texture evolved in the austenite was found to contain a significant fraction of Cube {0 0 1} ⟨1 0 0⟩ component, in addition to the typical simple-shear orientations [100]. It has been suggested, therefore, that CDRX in this phase was

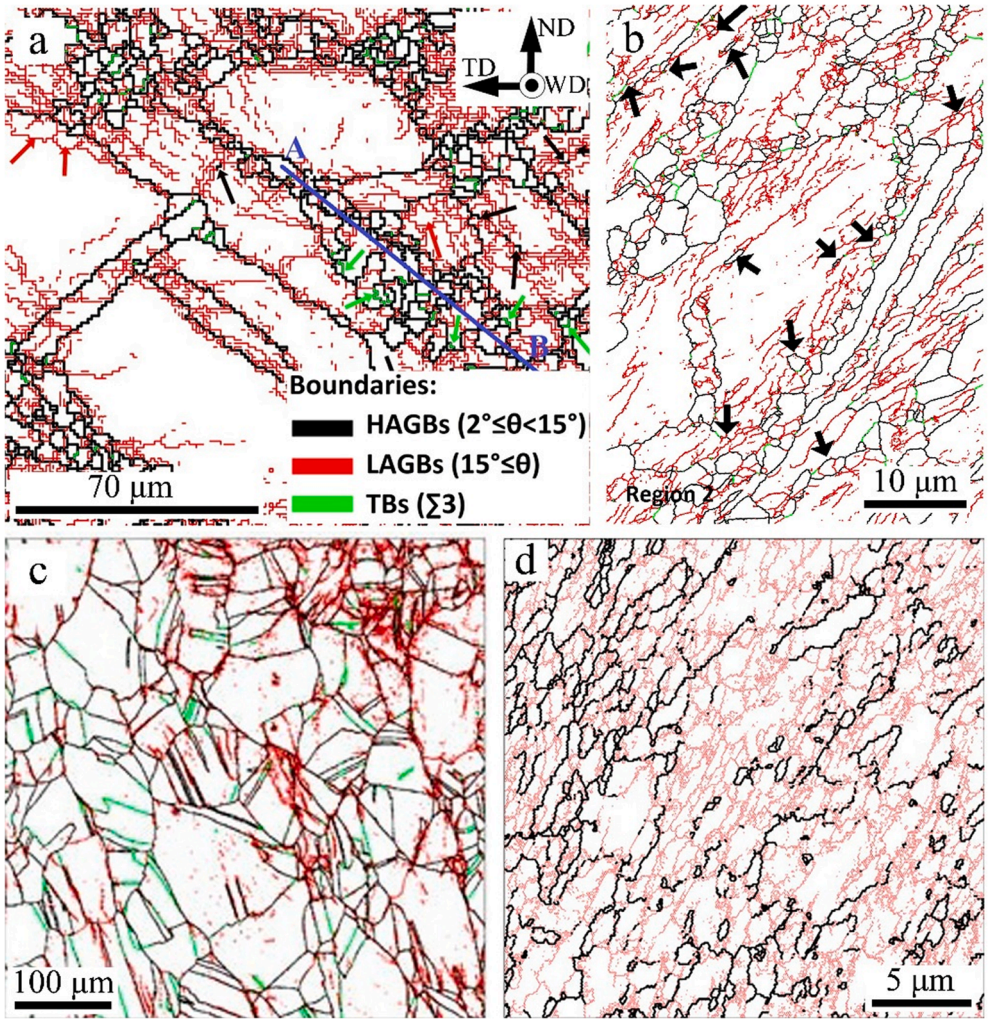

Fig. 17. Irregular formation of clusters of LAGBs near the original HAGBs and grain interiors in the TMAZ of moderate to low SFE materials for (a) Cu-30Zn brass [174], (b) pure copper [38], (c) Cu-30Zn brass [173], and (d) single-crystal austenitic stainless steel [162]. All maps have the same coordinate system and color codes as shown in (a). Reproduced with permission from Elsevier and Taylor & Francis.

followed by the SRX during the weld cooling cycle [100].

In Ti-6Al-4V, microstructure evolution is influenced principally by the welding temperature. Below the β-transus, the microstructural changes are dominated by a substantial increase in the β phase fraction [207] and globularization occurring in the α phase, as shown in Fig. 23a [208-211]. The latter process has been reported to be driven by the CDRX, which involves a progressive development of LAGBs in the α phase and subsequent diffusional penetration of the β phase along these deformation-induced boundaries [211,212]. Despite the fact that the globularization mechanism has been found to be broadly similar to that operating during conventional thermo-mechanical processing of Ti-6Al-4V, the SZ microstructure is rather distinctive. The α phase is usually dominated by ultrafine grains [207,209,210,213-222] containing no remnants of the original structure (thus being completely globularized), being characterized by a nearly-random texture [213-216,222], as well as an exceptionally fraction of high HAGBs [213,226], however, the mechanism is unclear. It is also notable that the tool wear during FSW of Ti-6Al-4V may result in local precipitation of the β phase [207], since the typical tool materials (i.e., tungsten or cobalt) are β-stabilizing elements.

During FSW of Cu-Zn brass, coarse β particles have been reported to promote PSN [234]. On the other hand, nano-scale dispersoids of this phase efficiently retard grain-boundary migration leading to an ultrafine-grained structure, as illustrated in Fig. 23b [234].

4.1.5. Effect of phase transformations

FSW of titanium alloys above the β-transus normally results in the β-transformed structure in the SZ. This typically consists of relatively fine (~10 μm) prior-β grains decorated by grain-boundary α and containing either α colonies with sandwiched α and β lamellae [91,93,212,220,222,225,228,235-243], or a basket-weave microstructure [91,220,231,239,244]. Usually, the phase transformation is believed to be governed by a diffusion mechanism, but sometimes development of α' martensitic phase is reported

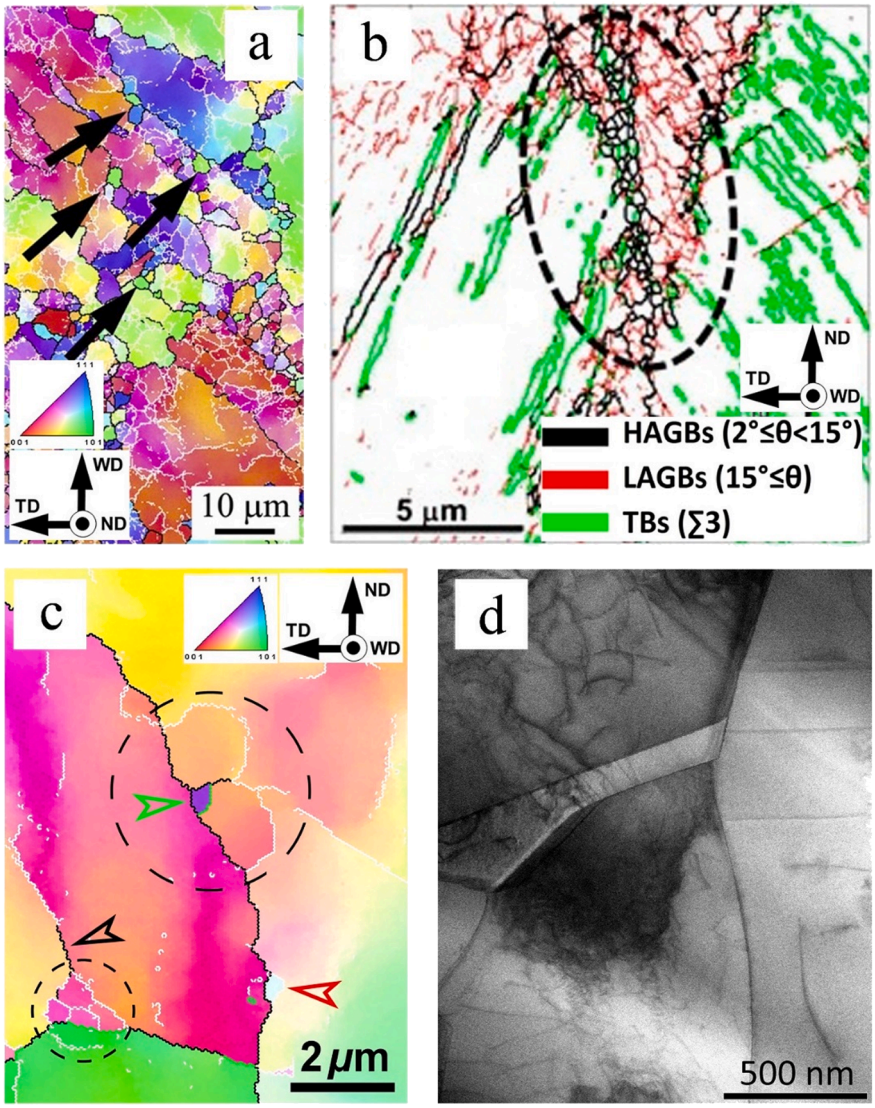

Fig. 18. Occurrence of DDRX and formation of bimodal grain structures during FSW of metals with low and medium SFEs: (a) IPF map of TMAZ in a friction stir welded 304 L austenitic stainless steels [126] showing grains formed by bulging mechanism (arrowed), (b) grain boundary map of the TMAZ in FSW Cu–30Zn brass [173] showing fine and equiaxed DDRX grains formed by bulging accompanied by Σ3 annealing twins (ellipse), (c) IPF map of the TMAZ in FSW Monel alloy, showing the formation of subgrains and transformation of LAGBs to HAGBs by CDRX (black arrow) and a DDRX grain (green arrow) formed by bulging accompanied by Σ3 twin boundary (green colored boundary) [184], other DDRX grains (red arrow) are formed by bulging accompanied by LAGBs (white colored boundary), (d) TEM image of TMAZ in a Cu-30Zn joint in which a bulged grain boundary and a Σ3 twin boundary form a new DDRX grain [38]. The grain boundary color codes are the same in (a-c) as shown in (b). Reproduced with permission from Elsevier and Taylor & Francis. (For interpretation of the references to color in this figure legend, the reader is referred to the web version of this article.)

[223,235,245]. The size of the β grains and α colonies are sensitive to FSW parameters; coarsening with an increase in the rotational speed or reduction in traverse speed [91,210,220,222,223,225,228,231,235,236,238,239,242,243,245-248]. This effect is usually explained in terms of a higher FSW temperature and longer exposure above the β transus [91]. On the other hand, an increase in the traverse speed enhances the cooling rate and thus results in the narrowing of α lamellae [210,235,239,245] and may even activate the martensitic transformation mechanism [223,235,245].

The α and β phases are normally found to be related via the Burgers orientation relationship, viz. $\{0\ 0\ 0\ 1\}_{\alpha}//\{1\ 1\ 0\}_{\beta}$ and $<1\ 1\ \bar{2}\ 0>_{\alpha}//<1\ 1\ 1>_{\beta}$ [91,94,211,241,244,249]. As a result, a very distinctive misorientation distribution forms in the α phase [239,244]. It is noteworthy that the phase transformation is sometimes reported to involve a relatively strict variant selection [94,244,249,250], but the origin of this effect is not completely clear. Orientation measurements in the α phase revealed the formation of a transformation D_1/D_2 $\{1\,1\,2\}$ $\langle 1\,1\,1\rangle$ texture inherited from the severely deformed β phase [91,94,249,251].

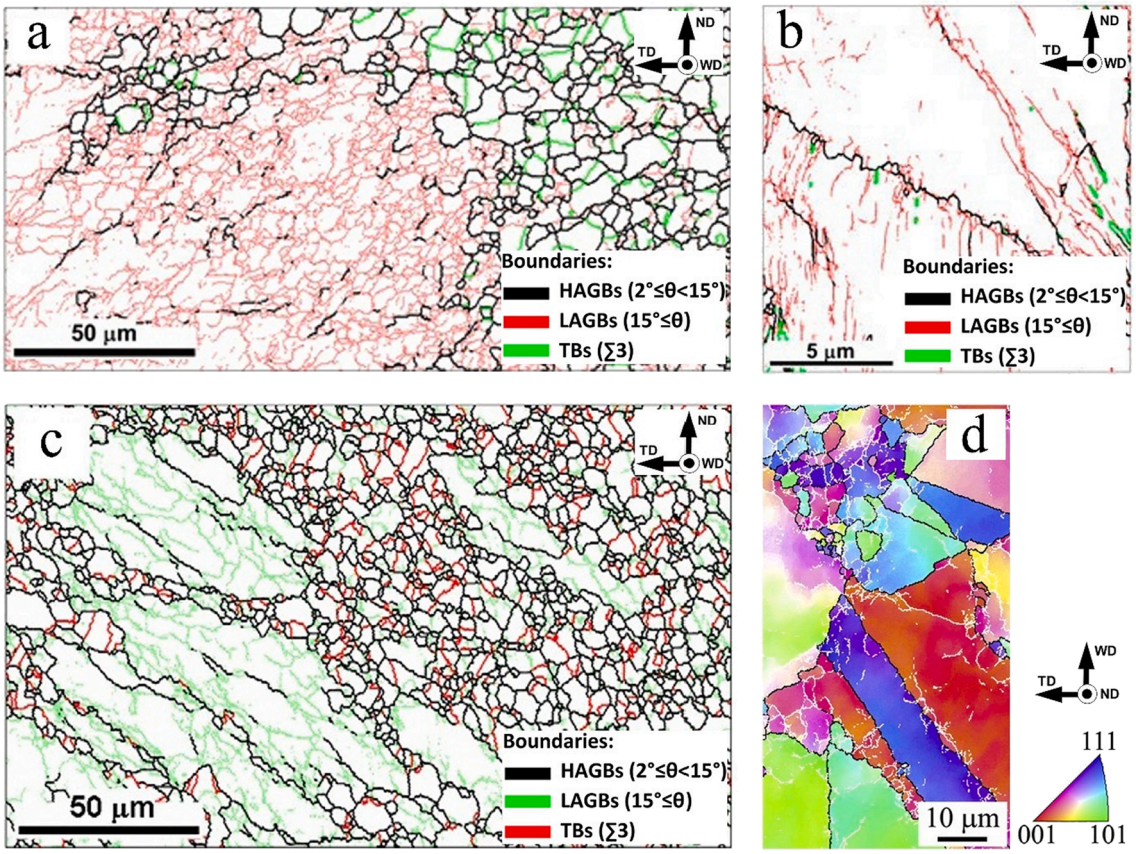

Fig. 19. The occurrence of CDRX by the transformation of LAGBs to HAGBs in the TMAZ during FSW of metals with low and medium SFEs; (a) single-crystal austenitic stainless steel [164], (b) Cu-30Zn brass alloy [173], (c) S31254 super austenitic stainless steel [163], and (d) commercial 304L austenitic stainless steel joint [126]. The LAGBs and HAGBs are shown by red and black colors, respectively, in (a) and (b). In (c) and (d), LAGBs are indicated by green and white colors, respectively. HAGBs and LAGBs are shown by black and white colors, respectively in (d). Reproduced with permission from Elsevier and Springer Nature. (For interpretation of the references to color in this figure legend, the reader is referred to the web version of this article.)

To investigate microstructure evolution occurring directly during FSW, several attempts have been made to reconstruct the grain structure of the high-temperature β phase [91,94,211,241]; however, the results are somewhat contradictory. Specifically, Mironov et al. [241] have suggested that the grain structure evolution is governed by the geometrical effect of strain and grain subdivision. This is in line with the work by Davis et al. [94], where a prevalence of CDRX has been proposed. On the other hand, Pilchak et al. [91] have concluded that the β grains undergo a form of severe plastic deformation leading to little change in shape or size.

The reconstruction of the texture of the high-temperature β phase usually reveals a D_1/D_2 $\{1\,1\,2\}$ $\langle 1\,1\,1\rangle$ simple shear texture [91,94]. In some cases, however, the formation of a recrystallized Cube $\{0\,0\,1\}$ $\langle 1\,0\,0\rangle$ texture has been reported [211]. The welded material may experience a secondary deformation in the α phase (perhaps, induced by the tool shoulder), which may give rise to P1 $\{\bar{1}\ 1\ 0\ 0\} < \bar{2}\ 1\ 1\ 0 >$ simple shear texture [249].

The FSW of carbon steels often leads to a martensitic transformation in the SZ [252-268]. In some cases, however, bainitic- [252,261,264,269-273] or even pearlitic transformations [258] have been reported. The martensite laths produced in the SZ are characterized by a relatively large orientation spread and thus the martensitic transformation is difficult to quantify in terms of a particular orientation relationship [266,267]. This effect is sometimes attributed to the severe deformation experienced by the austenitic phase during FSW [266,267]. Similar to Ti-6Al-4V, the martensitic reaction in steels has been reported to involve a relatively strict variant selection [266,267]. The origin of this effect is not clear but one of the possible explanations may be a crystallographic texture evolved in the high-temperature austenite. Sometimes, a relatively high fraction of retained austenite is found in the SZ microstructure; this effect is also associated with the heavily strained nature of the austenitic phase [273,274]. A remarkable characteristic of the SZ microstructure is a ferrite layer at the former faying surfaces of the welded sheets [255,266].

It is interesting to note that recent microstructural examinations of TRIP steel friction stir welded joints have revealed no evidence of strain-induced martensitic transformation [266,275,276]. This has been attributed to the limited weldability of such steels, which naturally restricted the observations of strain-induced microstructures to the relatively high-temperature range.

As for titanium alloys, tool wear can affect microstructure evolution during FSW of carbon steels [257,261,274,277] as can

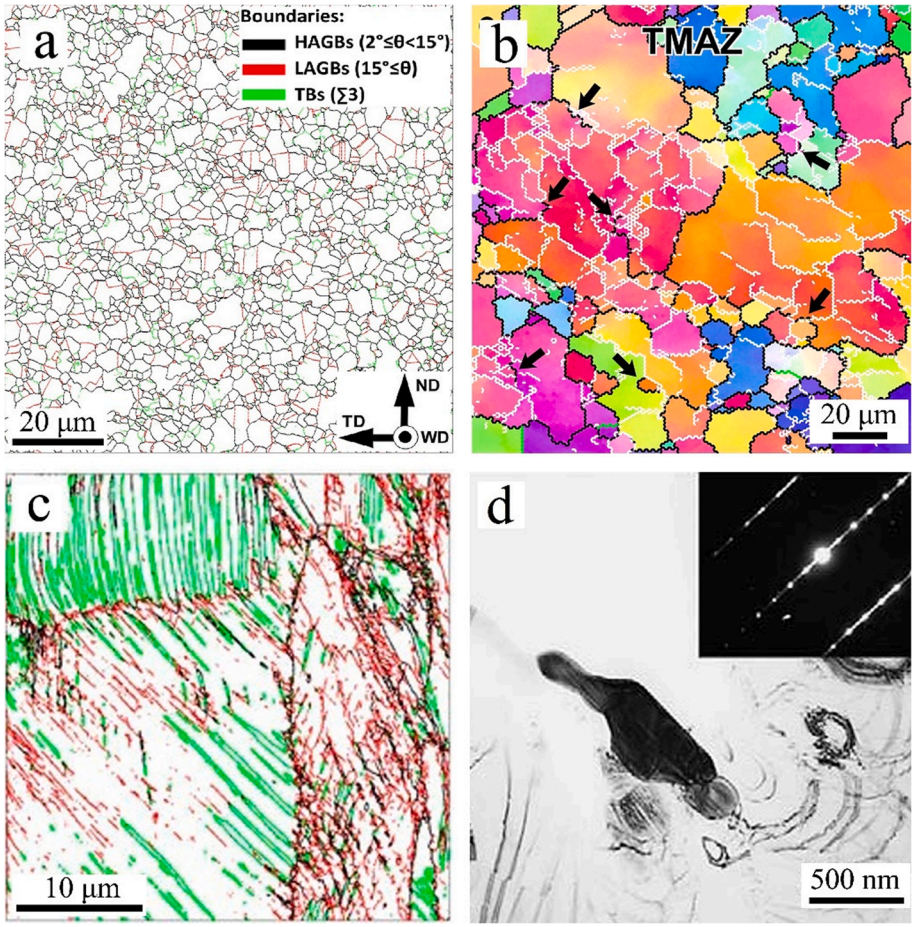

Fig. 20. (a) Grain boundary map of the SZ in the super austenitic stainless steel FSW [163], in which the annealing twins (green lines) exhibit a nearly-ideal ∑3 misorientation, (b) CDRX is promoted by increasing the heat input during FSW of Monel alloy [184]. Black arrows show the transformation of LAGBs to HAGBs, (c) formation of mechanical twins in Cu-30Zn brass (indicated by green colored boundaries) [173], (d) TEM image of the Cr rich carbides or sigma phases formed during FSW of 304 stainless steel [159]. The selected area diffraction (SAD) pattern of sigma phase is inset. The coordinate system and grain boundary color codes are the same in (a-c) as shown in (a). Reproduced with permission from Elsevier and Taylor & Francis. (For interpretation of the references to color in this figure legend, the reader is referred to the web version of this article.)

extensive oxidization [257,261]. However, these effects have not been studied yet.

A reconstruction of the prior-austenite grain structure has revealed a complex texture produced in this high-temperature phase during FSW, as shown in Fig. 24 [278]. It has been found to consist of a mixture of A_1^* $(111)[\overline{1}\overline{1}2]$ and $B/\overline{B}\{1\ 1\ 2\} < 1\ 1\ 0 >$ simple-shear components as well as of a rotated-cube recrystallization texture; this has been attributed to recrystallization occurring in the austenitic phase [278]. Moreover, evidence of the simple-shear texture has also been found in the martensitic phase; this effect has been explained in terms of secondary deformation experienced by the welded material during the weld cooling cycle [278].

4.2. Precipitation phenomena

Most industrial alloys contain dispersed phases. Due to the very large strains, as well as high temperatures generated during FSW, the second-phase particles may undergo significant changes. FSW-induced precipitation phenomena have been studied primarily in heat-treatable aluminum and magnesium alloys.

4.2.1. Aluminum alloys

Many precipitation hardening Al alloys, especially Cu-rich ones, are difficult to weld by conventional fusion welding processes, mainly due to excessive microcracking caused by hot tearing in the molten zone, porosity and residual stresses [279-284]. As a result, FSW is an attractive joining technique for these materials.

As indicated in Fig. 25, if the parent plate is in the high strength T6 state or the slightly overaged T7 state then precipitation effects are likely to lead to significant softening. Even for alloys in the naturally aged state (T3 or T4) coarse precipitates can form during

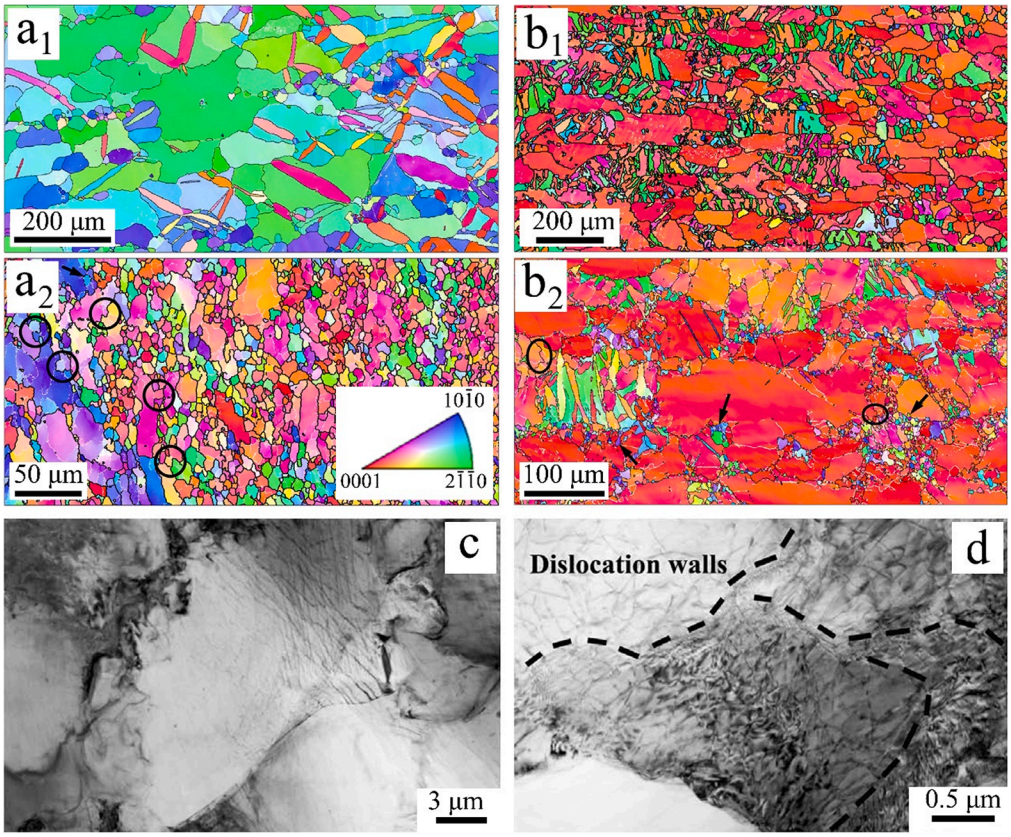

Fig. 21. Microstructural characteristics during FSW of HCP metals; IPF maps of TMAZ in AZ31 alloy joints for a) high and b) low heat input conditions [87]. (a_1, and b_1) show the formation of mechanical twins towards the edge of the deformation zone, (a_2, and b_2) transformation of deformation twins to grains through CDRX (black arrows) and DDRX (black circles). TEM images of Mg–Al–Zn alloy joints [89] showing (c) DDRX (bulging mechanism), and (d) CDRX by the formation of dislocation walls. The coordinate system and IPF color codes are the same in (a) and (b) as shown in (a_2). Reproduced with permission from Elsevier. All rights reserved.

welding in some locations, leading to local softening. More alloy-specific effects are discussed in detail below.

4.2.1.1. 2xxx series aluminum alloys. Alloys of the 2xxx series are based on the Al-Cu system. Depending on the additional solutes added to this binary alloy, they can be divided into three main sub-series showing different precipitation sequences: essentially binary Al-Cu such as AA2219, containing up to 6 wt% Cu and no other solute addition except the dispersoid-forming elements, Al-Cu-Mg based alloys such as AA2024, and Al-Cu-Li based alloys such as AA2050, AA2198, and AA2196.

In binary Al-Cu alloys, the sequence of precipitation from the supersaturated solid solution (SSSS) involves the progressive formation of phases of increasing stability and decreasing coherence with the Aluminum matrix (for recent work see e.g. [285,286]):

SSSS → GP I zones → GP II zones (θ″) → θ′ → θ (Al_2Cu)

Progression through this sequence depends strongly on time and temperature. GP I zones form preferentially at room temperature, while T6 and T8 peak-aging tempers mainly contain the θ′ phase, formed after artificial aging at temperatures around 150–200 °C. The formation of θ′ phase is significantly enhanced by former plastic deformation due to heterogeneous nucleation on dislocations [287].

As shown in Fig. 26, when FSW in the T6 or T8 temper, these alloys undergo a combination of precipitate dissolution and coarsening [288]. In the highest Cu-containing alloys, coarse θ particles remain in the SZ due to incomplete solutionizing, while this effect is suppressed with lower solute content. In the HAZ and TMAZ, the initial θ′ precipitates experience progressive dissolution, coarsening and transition to the stable θ phase, leading to a loss of hardness. This cannot be recovered by a post-weld heat treatment, which leads to further coarsening of the precipitates formed in the affected zones [289].

In Al-Cu-Mg alloys, the sequence of precipitation is modified by the strong attractive interaction between Cu and Mg:

SSSS → clusters / GPB zones → S (Al_2CuMg)

In this alloy system, the formation of clusters / Guinier-Preston-Bagaryatsky (GPB) zones account for a large part of the hardening

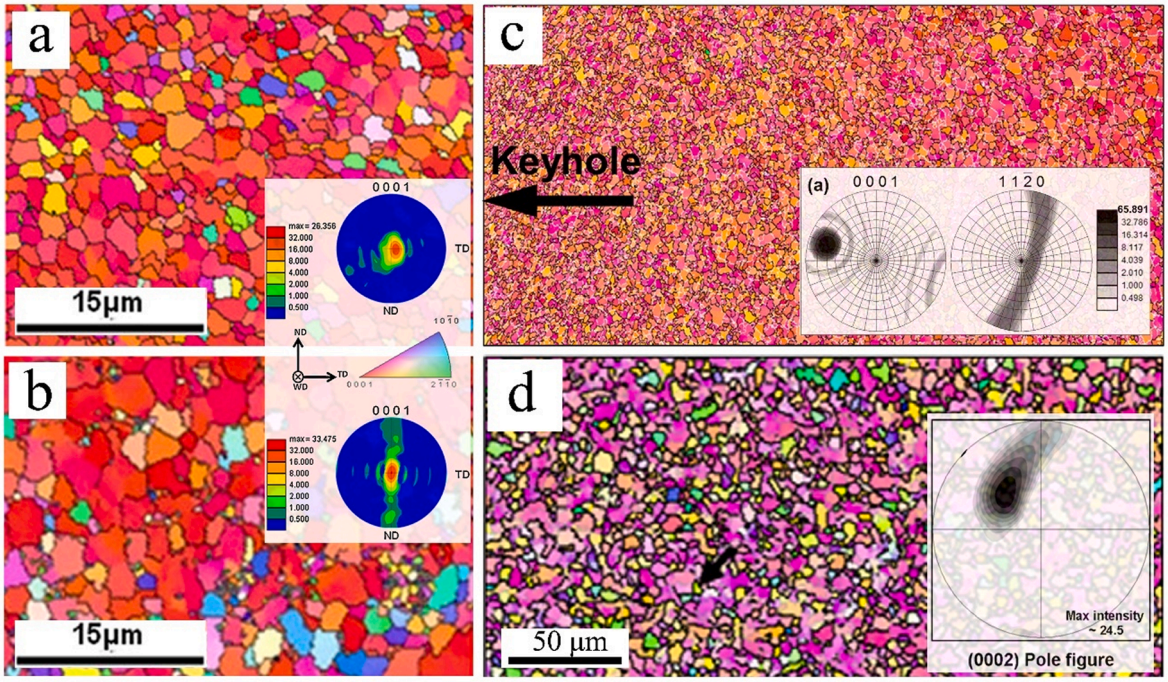

Fig. 22. Grain convergence phenomena in the SZ of HCP metals. IPF maps and corresponding pole figures for SZs in AMX602 magnesium joints welded under a) low heat input and b) high heat input [193], (c) AZ31 magnesium joint [87], and (d) pure titanium joint [35]. This figure is reproduced from cited references. The coordinate system and IPF color codes are the same in (a-d). Reproduced with permission from Elsevier. All rights reserved.

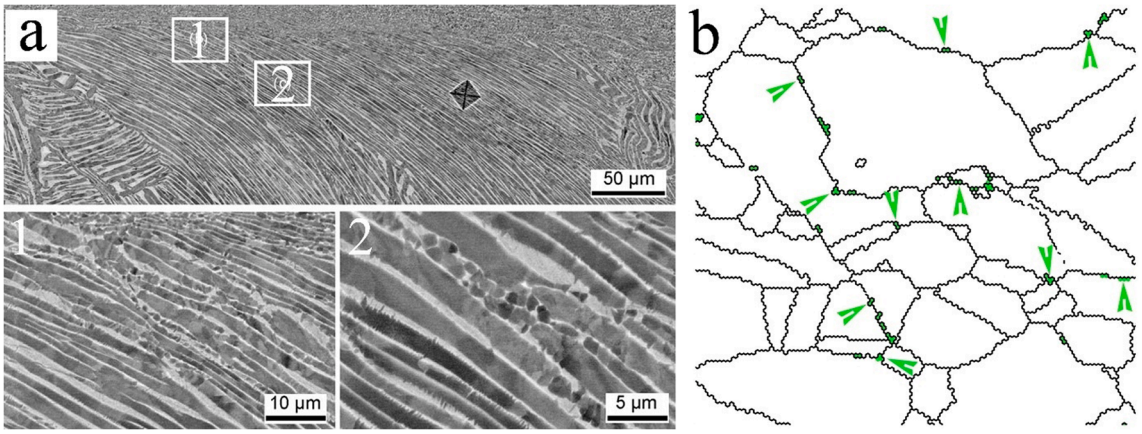

Fig. 23. FSW of multiphase alloys; (a) backscattered electron images of the transition region between BM and SZ in Ti-6Al-4V FSW [211], (b) EBSD phase map from the SZ of a two phase brass, showing nano-sized secondary phases (green arrows) remaining on the grain boundaries after FSW [234]. Reproduced with permission from Springer Nature. (For interpretation of the references to color in this figure legend, the reader is referred to the web version of this article.)

potential (~70%). During artificial aging at 150–200 °C, the hardness, therefore, rises very quickly (so-called rapid hardening effect) [290] while the formation of S-phase requires more time and leads to limited further hardening. The S-phase formation kinetics can be enhanced by a factor of 2–10 by plastic deformation realized either before, or during, aging [291].

Since these alloys are generally used in a T3 (naturally aged) temper for applications requiring a high toughness and fatigue resistance, the resulting FSW hardening profile (Fig. 25) shows a minimum on the HAZ/TMAZ boundary, with higher hardness in the BM and SZ [133]. The BM is efficiently hardened by the initial clusters / GPB zones, while the SZ is subjected to (almost) full dissolution and thus forms new GPB zones and hence a comparable hardness level. In the HAZ/TMAZ, S phase forms during welding due to the intermediate temperature, helped by the concurrent plastic deformation [133,291]. When welded in the T6 temper, the microstructure is similar in the SZ and HAZ/TMAZ, while the BM has a higher hardness, so that the contrast in mechanical properties

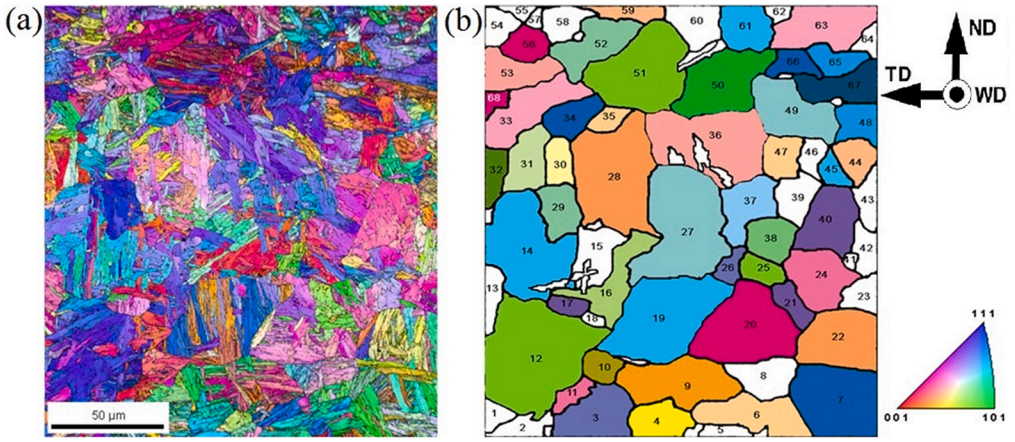

Fig. 24. EBSD maps showing microstructure of SZ produced during FSW of API X80 pipeline steel; (a) the final martensitic phase, and (b) reconstructed austenitic phase. Reprinted from [278]. Reproduced with permission from Springer Nature.

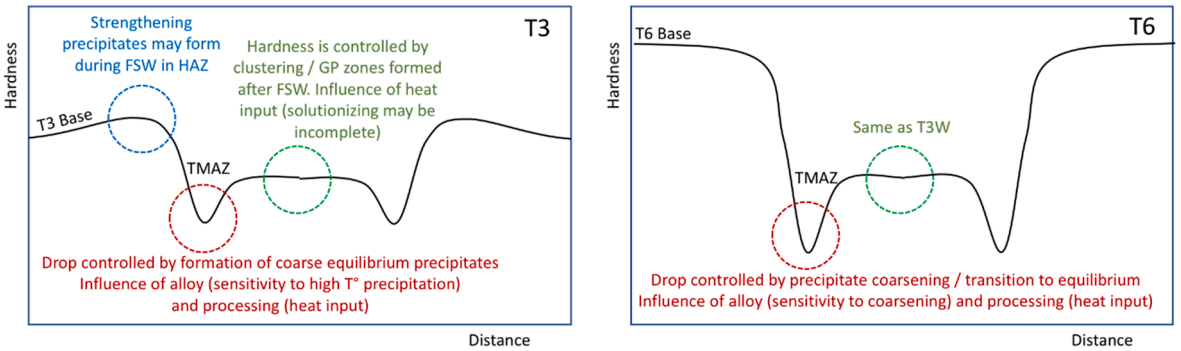

Fig. 25. Schematic showing the effect of FSW on the hardness profile for precipitation hardened aluminium alloy plates originally in the T3 and T6 tempers.

along the weld is more pronounced [133].

Al-Cu-Li alloys are more complex. In addition to these three main elements, other minor solutes are generally added, such as Mg, Ag and/or Zn [292,293]. The precipitation sequence potentially includes phases from the two preceding alloy families (from the GP zone → θ sequence and from the GPB zone → S sequence), as well as two additional phases: the metastable δ′ (Al_3Li) phase, and the stable T_1 (Al_2CuLi) phase. Other phases such as T_2, T_B, may form at relatively high temperatures in conditions relevant to FSW. The competition between the formation of all these phases depends both on the alloy composition, level of prior deformation, and aging temperature [294].

It is beyond the scope of this review to discuss the parameters that control the formation of these phases, however a few simple rules can be given. The most desirable phase in these alloys is the T_1 phase. At an artificial aging temperature (~150 °C), T_1 precipitates preferentially on dislocations and is favored by minor additions of Mg, Ag and Zn. Under favorable conditions, T_1 plates are slightly above 1 nm thick (1 unit cell) and their length can reach 100 nm [295]. At higher temperatures, they start to thicken and their contribution to strength is diminished. Precipitates of Al-Cu (GP zones, θ′) are generally found along with the T_1 precipitates; their proportion is enhanced when the material lacks Mg [293], or lacks the dislocation density needed for the formation of T_1 [296], resulting generally in slower precipitation kinetics and lower maximum strength. S-type precipitates also form in these alloys due to the presence of Mg and Cu [297]. Precursors of S phase are believed to precede the nucleation of T_1 on dislocations [292], and in fully aged tempers S and T_1 are often found together. The contribution of these S phases to strength is unclear, it may provide a significant contribution. δ′ precipitates are found when the Li content is higher than ~1.3 wt% [298]. They are spherical and coherent with the matrix up to large sizes. Their contribution to strength is generally considered as moderate, but they may have an influence on other properties such as fatigue propagation.

The microstructure of AA2050 alloy, which has a relatively low Li content, has been thoroughly investigated. When in the T8 temper, the FSW process results in precipitate dissolution and coarsening [130]. In the HAZ/TMAZ, precipitates initially of 1 unit cell experience thickening and the hardness drops. In the SZ, depending on the welding parameters, the initial precipitates are fully dissolved, and a new population of sub-nanometer sized clusters forms during post-welding natural aging (Fig. 27); their hardening effect is significantly lower than that of T_1 precipitates in the BM.

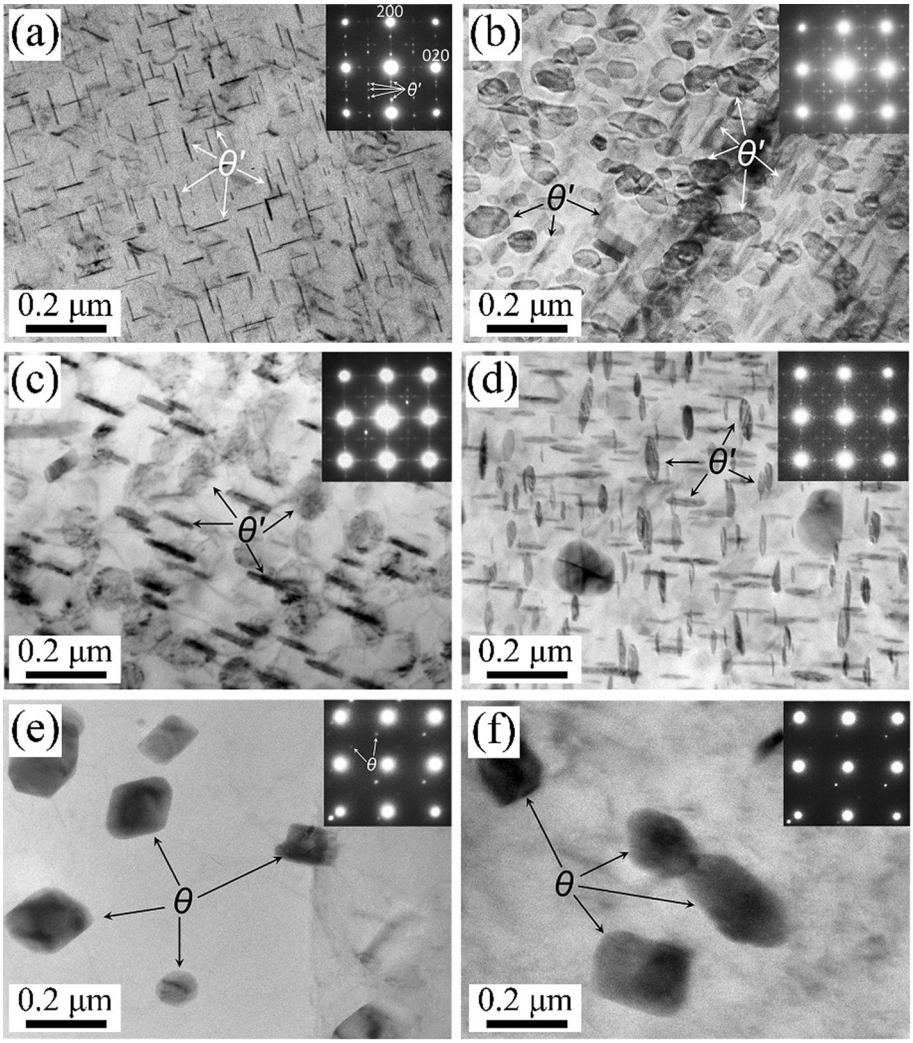

Fig. 26. TEM micrographs and associated SAD patterns along [100] zone axis across an AA2219-T8 FSW joint; (a) base metal; (b) HAZ-12 mm; (c) HAZ-10 mm; (d) HAZ-8 mm; (e) TMAZ; (f) SZ [288]. Reprinted with permission from Springer Nature.

When welded in the T3 temper, the microstructure may remain relatively homogeneous after welding, consisting of a distribution of sub-nanometer sized clusters [131]. This can be related to the relatively sluggish precipitation kinetics of the T_1 phase as compared to the S phase. If the welding is realized under conditions where the time at high temperature is sufficiently short, precipitation of coarse phases during welding can be avoided almost completely. Thus, it is of interest to evaluate whether a homogeneous precipitate microstructure can be obtained from this T3W (T3 temper welded) state by post-weld heat treatment. It has been found, however, that classical precipitation treatments were ineffective in forming T_1 precipitates in the SZ, due to the absence of sufficient dislocations after dynamic recrystallization [131]. This problem could be solved by applying a deformation after welding in the T3 state, resulting in a fully homogeneous hardness distribution, although this solution may not be very practical. When welding is performed during two passes, the microstructure resulting from the first pass is further modified by the second thermo-mechanical treatment applied, resulting in an even more complex distribution of precipitates [132].

4.2.1.2. 6xxx series aluminum alloys. Alloys of the 6xxx series, i.e. Al-Mg-Si alloys, form metastable precursors and the stable β(Mg_2Si) or the Q($Al_5Cu_2Mg_8Si_6$) phase. Two types of 6xxx series alloys should be distinguished as far as their precipitation sequence is concerned: low Cu content alloys and high Cu content alloys. Alloys presenting an excess Si may also form a pure Si phase. In low Cu alloys, the supersaturated solid solution (SSSS) decomposes in the following sequence [299,300]:

SSSS → clusters → GP zones → β'' → β' → $\beta(Mg_2Si)$

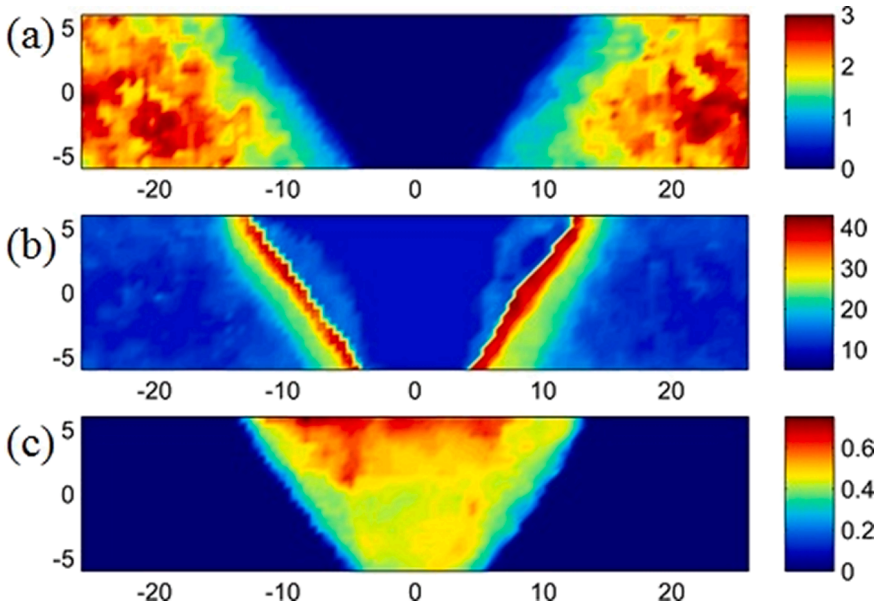

Fig. 27. Distribution of precipitates in the cross-section of an AA2050-T8 weld determined by SAXS mapping; (a) volume fraction (in A.U.) of T1 precipitates (b) thickness of T1 precipitates (in Å) (c) volume fraction of sub-nanometer scale clusters (in A.U.). Adapted from [130]. Reproduced with permission from Taylor & Francis.

where β'' precipitates are needle-shaped oriented along $\langle 1\,0\,0\rangle_{Al}$ with a monoclinic structure. β' precipitates are rod-shaped also oriented along $\langle 1\,0\,0\rangle_{Al}$ with a hexagonal crystal structure. β is a platelet with a face cubic centered structure incoherent with the Al matrix. In the high strength T6 state, these alloys contain a large density of β'' precipitates [300,301] typically ~25 nm in length and ~6 nm in diameter in a 6005A-T6 alloy [300].

When FSW is performed on alloys in the T6 temper, fine β'' precipitates are dissolved in the HAZ, while the larger precipitates are transformed to large β' precipitates. Thus, the precipitate density is significantly reduced [299,301-304]. Simar et al. [303] have shown that in a hot 6005A-T6 weld (low traverse speed) the precipitates in the HAZ are twice the size of those in a colder weld (high speed). After a post-weld T6 heat treatment (PWHT), new β'' precipitates are formed from the supersaturated solid solution due to the prior welding process [305].

In the SZ, the precipitates have dissolved and the dispersoids can only be observed by TEM [303]. Differential scanning calorimetry (DSC) reveals that a large number of GP zones form after post-weld natural aging in the SZ [303]. Rodrigues et al. [306] discussed the effect of the higher dislocation density in the SZ on the possibility of heterogeneous precipitation.

In the Al-Mg-Si-Cu alloys (i.e. Cu rich 6xxx series alloys), the supersaturated solid solution (SSSS) decomposes in the following sequence [299,300]:

$$\text{SSSS} \rightarrow \text{clusters} \rightarrow \text{GP zones} \rightarrow \beta'' \rightarrow \beta' + Q \rightarrow \beta(Mg_2Si) + Q$$

where Q precipitates are hexagonal lath-like precipitates with their long direction along $\langle 1\,0\,0\rangle_{Al.}$ The 6056 alloy is a common alloy presenting Q phase precipitation. The precipitate evolution in these alloys during FSW has been extensively studied [61,307,299].

In the Al6056-T4 alloy parent material, only coarse dispersoids may be observed by classical TEM [307], but the alloy contains GP zones formed during the room temperature aging following the solution treatment of the alloy. The HAZ comprises two distinct zones, as revealed by the hardness profile in Fig. 28a [299]. As the weld line is approached, there is initially a drop in hardness due to the partial dissolution of GP zones. Closer to the weld line, the hardness rises due to the heterogeneous precipitation of fine β'' precipitates on dislocations, see Fig. 28b [299]. At the border between the TMAZ and the HAZ, a more significant drop in hardness is observed due to the heterogeneous precipitation of coarse (65 nm long/15 nm in diameter) Q phases on dislocations or dispersoids [307] being somewhat finer on the retreating side of the weld [61]. Towards the inner region of the TMAZ, the hardness rises sharply as more and more dissolution of alloying elements enables a reprecipitation of GP zones during post-weld natural aging [299] thereby recovering the base material T4 hardness.

In the T6 initial state, Al6056 alloy contains a large amount of fine (hardening) β'' precipitates. In the TMAZ, (65–90 nm long/ 10 nm diameter) Q-type precipitates are observed [307]. Similarly to the 6056-T4 SZ, the 6056-T6 SZ only presents remaining dispersoids [61,307]. However, after a T6 post-weld heat treatment, fine β'' are retrieved, but tend to precipitate heterogeneously on dislocations in the SZ [307].

In the initial T78 state, Al6056 contains a homogeneous precipitation of β'' and (68 nm in length/5 nm in diameter) Q. [299]. In the HAZ, the hardness drops (Fig. 28a) due to the growth of the base material precipitates and their dissolution. A few new precipitates

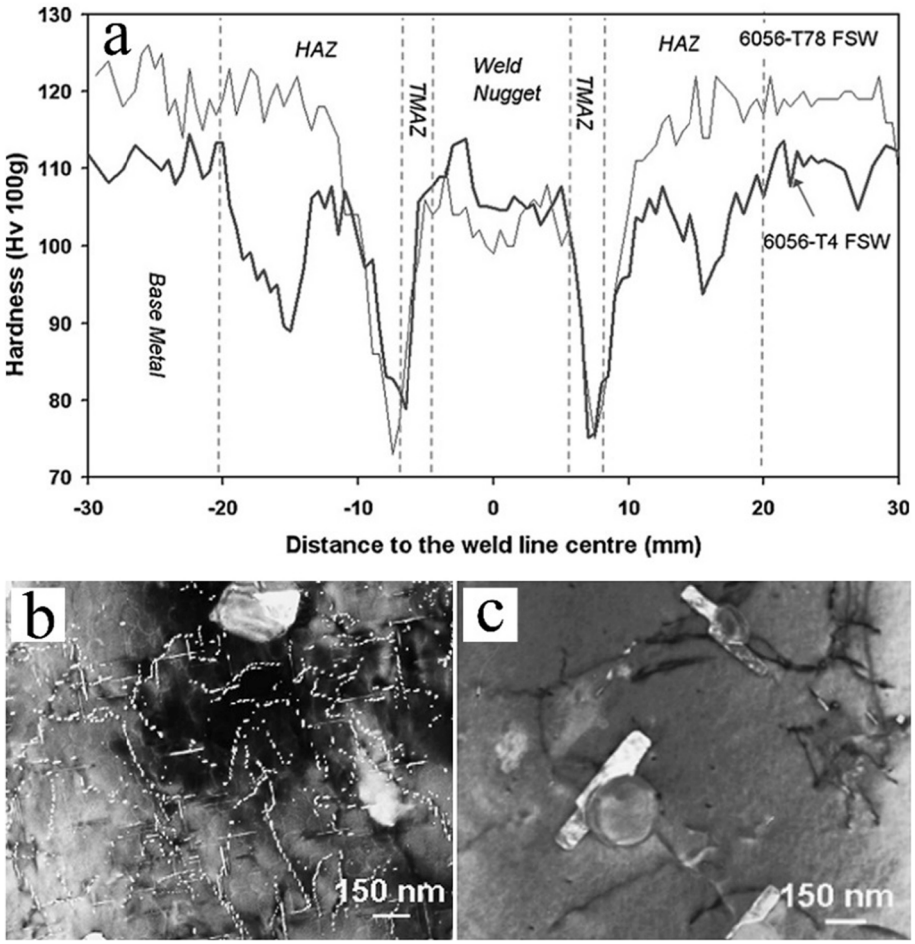

Fig. 28. (a) Mid-thickness hardness profiles obtained on the cross-section of 6056 T4 and T78 welds. (b) TEM observation of the fine heterogeneous β''precipitation on dislocations in the HAZ of a 6056-T4 weld, (c) TEM observation of the coarse heterogeneous Q-phase precipitation on dispersoids in the TMAZ of a 6056-T78 weld [299]. Reproduced with permission from Elsevier. All rights reserved.

form on dispersoids. In the TMAZ a few huge precipitates have grown on dispersoids (Fig. 28c), but most precipitates have dissolved and form GP zones upon room temperature aging [299]. In the SZ, the precipitates have entirely dissolved and GP zones have formed, recovering the T4 hardness (Fig. 28a).

4.2.1.3. 7xxx series aluminum alloys. 7xxx series alloys, i.e. Al-Zn-Mg alloys, are strengthened by metastable precursors and the stable η phase. In these alloys, the supersaturated solid solution (SSSS) decomposes in the following sequence [308]:

SSSS → GP zones (I or II) → η' ($MgZn_2$) → η ($MgZn_2$)

GP (I) and GP (II) zones dissolve at 100 °C and 125 °C, respectively [281]. Above these temperatures, η' and η precipitates may form [282]. Both are hexagonal phases being semi-coherent and incoherent with the Al matrix, respectively. In these alloys, the equilibrium precipitation grows favorably at grain boundaries. This leads to the depletion in Mg and Zn alloying elements near the grain boundary [309], resulting in a precipitate free zone (PFZ) a few tens of nm in width [135,310]. Heterogeneous rod-shaped grain boundary precipitates are also formed typically being 50 nm or smaller [135,311], see Fig. 29a. Base materials are generally in either T3, T6 or T7 states [309,310]. The T3 state is characterized by a high density of GP zones [128]. In the peak aged T6 state, typically 10 nm size intragranular strengthening precipitates (GP(II) zones [281,135]) are observed in addition to the larger intergranular grain boundary precipitates [281,310,311], see Fig. 29a. In the slightly over-aged state (typically T79), fine precipitates are also observed identified by TEM as mainly η precipitates with some coexisting η' precipitates [128].

The HAZ is characterized by peak temperatures of ~250–475 °C [311] causing small intragranular precipitates to dissolve and larger ones to grow [135,312,313], see Fig. 29b. The fine precipitates have been identified as η' and η by TEM diffraction pattern analysis [281,135]. Using SAXS mapping, Dumont et al. [128] did not find a significant increase in precipitate size in the HAZ, but did find that the volume fraction of precipitates tends to gradually drop in the HAZ of a 7449-T79 weld. The grain morphology is unchanged in that region of the weld, i.e. similar to the base material elongated grains. Increasing the heat input (lower advancing speed and larger rotational speed) leads to a wider HAZ [128] and larger precipitates [309] as more time is spent at high temperature. The

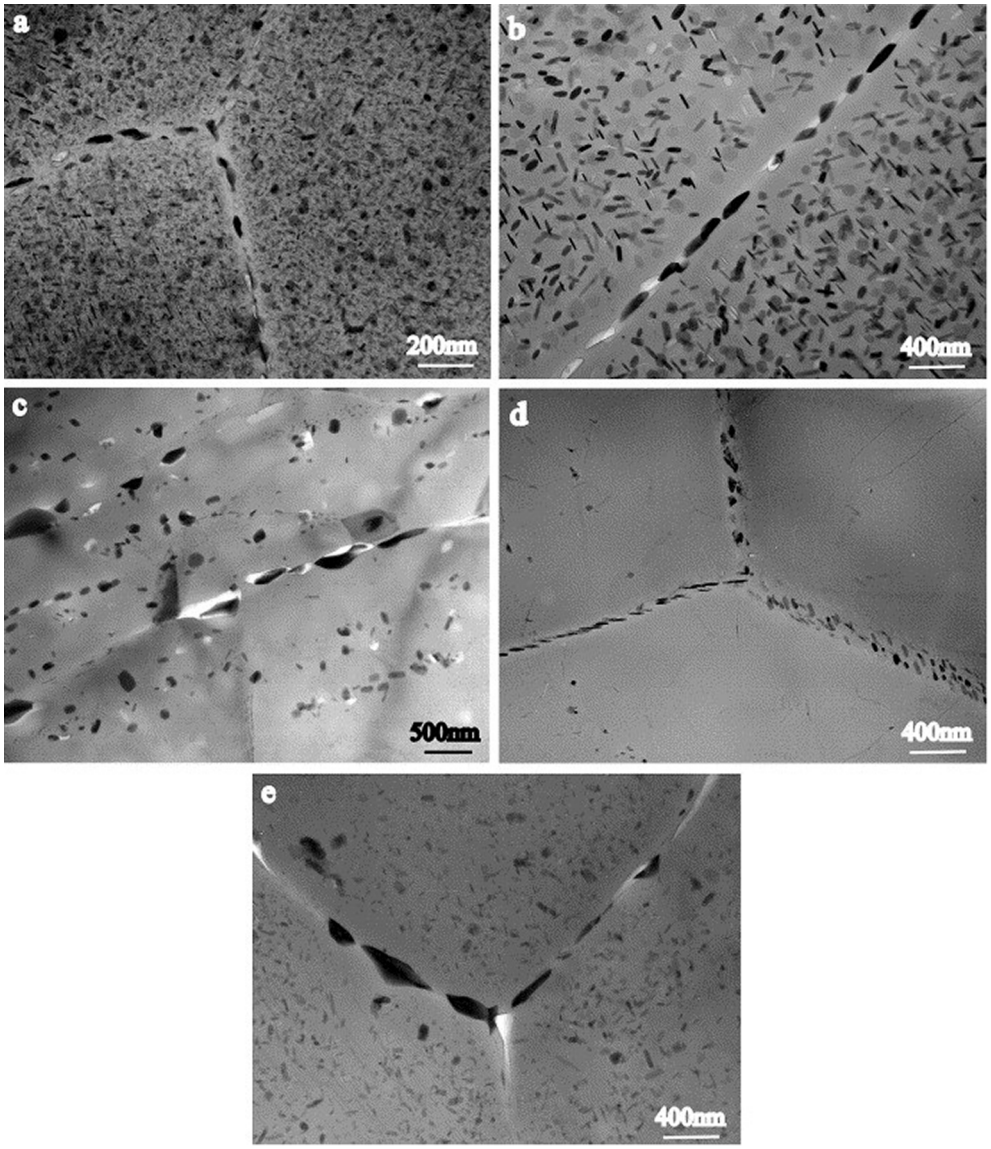

Fig. 29. Precipitate distribution across the zones of a 7050-T651 FSW; (a) BM, (b) HAZ, (c) TMAZ close to HAZ, (d) TMAZ close to SZ and (e) the SZ [135]. The homogenously distributed precipitates inside the grains are η' or η precipitates while the larger grain boundary precipitates are equilibrium precipitates (S, η or T). Reprinted with permission from Elsevier. All rights reserved.

larger grain boundary precipitates also tend to grow, increasing the precipitate free zone to more than 100 nm [135,281,310], see Fig. 29b. If the base material is in the T3 state, the HAZ is characterized by newly formed precipitates, most probably η precipitates [128].

The TMAZ presents mainly precipitate growth and a suppression of η' precipitates in favor of only equilibrium precipitates [128,135], Fig. 29c. Yuqing et al. [282] have shown by high-resolution TEM that the fine precipitates in the TMAZ of a 7075-T6 weld are S(Al_2CuMg), η and T($AlMgZn_2$). The high dislocation density due to the large plastic deformation in this region of the weld [135,281,310] favors the nucleation of additional precipitates. Dumont et al. [128] demonstrated by SAXS that this region does not show any additional precipitate dissolution compared to the HAZ. Closer to the SZ, only very few precipitates are found inside the grains, while grain boundary precipitation is enhanced [128,135], see Fig. 29d.

The SZ comprises bands of fine (5–10 μm) and very fine (3–5 μm) recrystallized grains of low dislocation density [311]. Grain boundary precipitates are even larger than in the TMAZ [135], see Fig. 29e. Scarce 100 nm-400 nm size $MgZn_2$ precipitates are found but no small η' and η strengthening precipitates are evident from SAXS or TEM as the peak temperature exceeds the solvus temperature of these precipitates [128,310,311,313]. The supersaturated solid solution resulting from the precipitate dissolution results in the subsequent formation of fine GP(I) zones during room temperature aging [128,135,281]. In a 7449-T79 weld these precipitates reach 0.9 nm in size and 4% in volume fraction [128]. After very long room temperature aging times (years) GP(II) precipitates and a few η'

precipitates may even form [281].

4.2.2. Magnesium alloys

Similar to aluminum alloys, many commercially important magnesium alloys depend on the controlled precipitation of second phase particles to achieve their properties. However, the effect of FSW on precipitation in magnesium alloys has been less well characterized than that in aluminum alloys, but shows many common features despite the differences in the crystal structure (e.g. hcp rather than fcc): in particular, rapidly nucleating GP zones giving way to metastable phases and finally stable precipitates as the microstructure approaches its equilibrium condition [314]. A notable exception to this is the commercially dominant Mg-Al system (e.g. AZ91) where the equilibrium precipitate forms directly from the solid solution, but is not a very effective strengthener [315].

A key difference between the behavior of precipitate forming aluminum and magnesium alloys is the far greater contribution that precipitates make to the strength of aluminum alloys compared to magnesium [314]. As a result, friction stir welding has a less severe effect on the strength of magnesium compared to aluminum. For example, the hardness in the softest region (in the HAZ) for magnesium alloys is rarely less than 70% of the parent hardness [316], whereas in 7xxx aluminum alloys it can be less than 50% of the parent. This is partly because the precipitates that form in magnesium alloys are generally larger and more widely spaced than in aluminum [314], and secondly, because the most powerful precipitate strengthening elements (i.e. the rare-earth elements in alloys such as WE43) are also highly effective strengtheners when in solid solution [317]. Furthermore, magnesium alloys are more effectively strengthened by grain refinement than aluminum alloys such that the grain refining effect of FSW in the SZ can overcome any loss in strength due to dissolution of strengthening precipitates.

Since precipitation is less important to the strength of magnesium alloys than aluminum alloys, industry pays far less attention to optimizing the precipitate distribution. In addition, magnesium alloy usage is dominated by cast alloys. Therefore, the microstructures of magnesium alloys prior to friction stir welding often contain high fractions of second phase at grain boundaries as eutectic formed on solidification.

Given that FSP and FSW can both have similar effects on the precipitates in magnesium, relevant literature from work on FSP will also be considered here. Examples of hardness profiles obtained after FSW of two different age hardenable commercial magnesium alloys are shown in Fig. 30a [316,318]. Although this alloy is precipitation strengthened, they have little effect on the overall hardness with the grain refinement in the SZ having a stronger effect than the precipitate dissolution. There is no significant loss of hardness in the TMAZ or HAZ due to precipitate dissolution or coarsening since the precipitates in the starting material are already large and widely spaced [315], providing only slightly more strength than the solute from which they form. In contrast, WE43 derives a much greater fraction of its strength from a fine precipitate distribution, so that the dissolution and coarsening of these precipitates leads to a marked reduction in hardness in the HAZ. The increase in hardness in the SZ is due to the grain refinement in this region.

Detailed analysis of the precipitation behavior across different weld zones has received little attention in magnesium alloys, however, in alloys where precipitation strengthening is particularly important (e.g. WE43) there have been a number of studies (e.g. [316,320,321]). A calculation of the equilibrium phase fractions in such an alloy and the range of maximum peak temperatures estimated for typical FSW parameters [316] are shown in Fig. 31a. It can be seen that the expected peak temperature lies below the solvus temperature for the equilibrium precipitate phase (Mg41RE5), therefore, full solutionization of this phase is not expected. Indeed, in common with most magnesium alloys originally developed for cast applications, there is often no temperature window where full precipitate dissolution can occur in the solid state. Therefore, the microstructures after FSW comprise a coarse equilibrium precipitate phase mostly located at the grain boundaries after dynamic recrystallization (see Fig. 31 b and c [316]).

There is now strong evidence that melting can play a significant role in the evolution of microstructure during FSW of some magnesium alloys [322,323]. This is particularly the case for the most widely used Mg-Al alloys (e.g. AM60, AZ91). Since these alloys are mainly used in cast form, they have a high fraction of eutectic phase on solidification. The temperature reached during FSW is sufficiently high to produce eutectic melting which has been confirmed by stop-action studies [322].

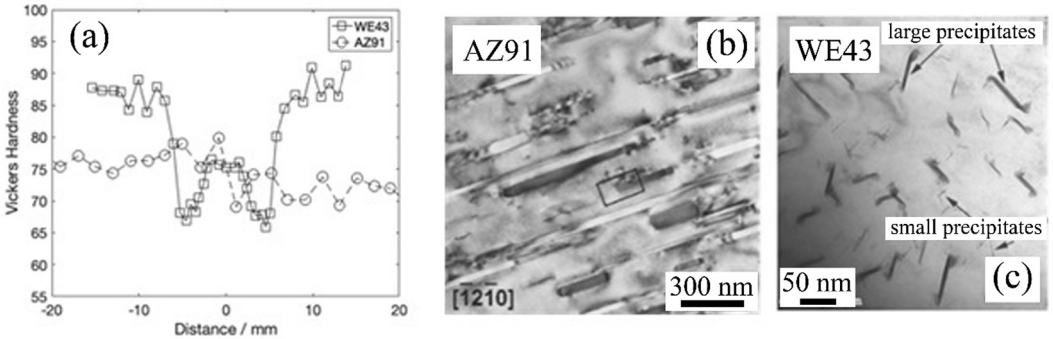

Fig. 30. Cross weld hardness profiles for (a) AZ91 [318] and WE43 [316]. Typical precipitate distributions in the parent material for (b) AZ91 [315] and (c) WE43 [319]. Reproduced with permission from Elsevier and Springer Nature. All rights reserved.

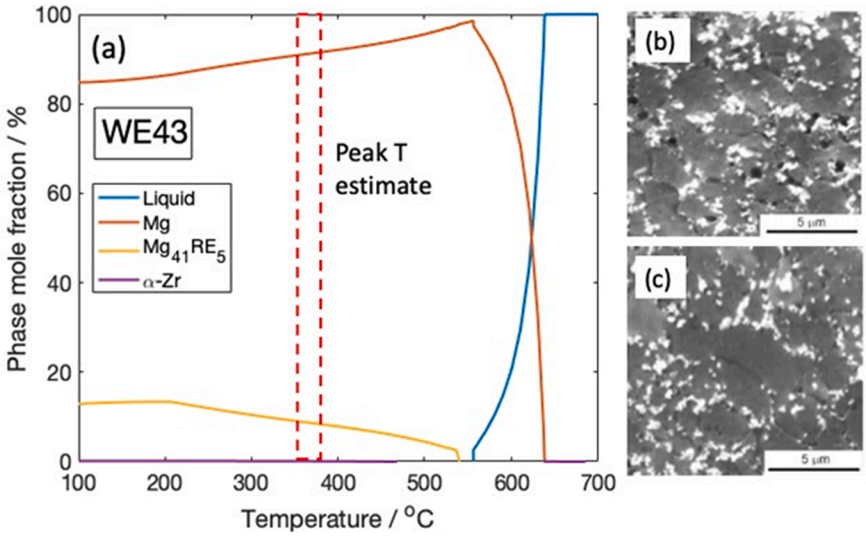

Fig. 31. (a) Calculated equilibrium phase fractions for WE43, indicating the estimated peak temperature reached during FSW (with rotation speeds 600–800 RPM and a welding speed of 102 mm/min) [316], the distribution of large second phase particles in (b) the SZ and (c) the TMAZ [316]. Reproduced with permission from Springer Nature.

4.3. Other materials

4.3.1. Metal matrix composites

Due to their unique mechanical properties, metal matrix composites (MMCs) attract significant industrial interest. However, they are difficult to join by conventional fusion techniques, due either to reaction between reinforcements and matrix, or to decomposition of the reinforcements in the molten pool. In this context, FSW is a promising option.

An important characteristic of friction-stir welded MMC is a relatively uniform reinforcement distribution. Indeed, FSW can even improve the distribution [324], perhaps due to the intrinsic stirring effect. On the other hand, local clustering of the reinforcement or even their alignment along the flow lines of the stirred material is sometimes reported [325,326]. Very often, a fragmentation of relatively coarse reinforcements is observed in the SZ [327-333]. As expected, no evidence of interface reaction is typically found, but local cracking in these locations may occur [324]. Drastic grain refinement in the metal matrix is normally observed [325,329,331-335]. In aluminum MMCs, this effect is often attributed to the CDRX [324]. In the age-hardenable alloys, FSW may lead to dissolution and/or coarsening of constituent particles as discussed in Section 4.2.1 [329,334,335].

4.3.2. High-entropy alloys

High-entropy alloys (HEA) represent an emerging class of structural materials. They contain a minimum of five principal alloying elements in near-equimolar composition but crystallize as a single phase. The feasibility of FSW high entropy alloys has been extensively studied over the last five years and the microstructural changes occurring during FSW are briefly summarized below.

Microstructural evolution as a result of FSW has been studied in CoFeNiCrMn alloys [336-340], CoFeNiCrMo alloys [341], AlCoCrFeNi alloys [342-347] as well as in the iron-based FeMnCoCrSi alloys [341,348-353]. In most cases, the final SZ microstructure has been found to be dominated by the FCC phase [336-347]. In the iron-based alloys, however, the final microstructure additionally included a minor fraction of HCP phase [348-353].

Typically, FSW leads to drastic grain refinement [336,338,340,342,343,345-354] and this is often explained in terms of DRX [336,346,347,354]. Zhu *et al.* [354] have suggested that the microstructural evolution is broadly similar to that observed in cubic metals of low SFE. In other words, there is a competition between DDRX and CDRX. These processes can also be affected by the wear of the welding tool [337,338,341,347,354], resulting in the formation of a particularly fine-grained microstructure attributed to the PSN [337,354]. In the iron-based FeMnCoCrSi alloys, microstructure evolution is additionally complicated by the extensive phase transformations [341,348-353], but details of this process are unclear.

5. Microstructural evolution during dissimilar FSW

Numerous industrial applications, particularly those in the transport industry, require joining of dissimilar materials to derive benefits in terms of low cost, design flexibility and weight reduction. FSW has great potential for obtaining sound joints for various dissimilar alloy systems, particularly where the metals have different physical or mechanical properties, which are very difficult, or impossible, to weld using conventional fusion welding techniques. Unsurprisingly while the FSW of dissimilar materials having similar physical and mechanical properties, such as Al-alloy to Al-alloy, are relatively easy to implement it becomes much more difficult to apply this technique to dissimilar materials combinations with sharply differing properties, such as Al-alloy to Mg-alloy or Al-alloy to

steel. Nevertheless, FSW of Al-alloys to steels has already been implemented for mass production of automotive structural components. Further expanding it to joining of dissimilar materials combinations such as Al-alloys to Mg-alloys or Mg-alloys to steels, may lead to further weight savings.

The recovery and recrystallization processes, phase transformations, and precipitation phenomena during dissimilar FSW are generally similar to the mechanisms discussed in Section 4. As a result, this section focuses primarily on the interfacial region and the formation of intermetallic compounds (IMCs). Alongside the usual FSW parameters, there are some important additional parameters to be considered when welding dissimilar systems, such as which material is placed on the advancing side (AS)/retreating side (RS), which can strongly affect the final microstructure of the SZ [355,356].

5.1. FSW of dissimilar alloys

5.1.1. Dissimilar aluminum alloys

A wide range of SZ microstructures can be obtained including complex intercalated lamellar structures (vortex-like cell structure or onion ring) [357-364] when the intermixing is good, whereas more asymmetric weld regions are observed if the intermixing is not sufficient (see Fig. 32). These comprise distinguishable zones typical of the respective similar aluminum alloy welds discussed in section 4.

At a finer scale, another interesting microstructural characteristic of dissimilar aluminum alloy joints is the formation of finer grains at the interface between the two materials in the SZ [365]. Fig. 33a and b show the finer grains in the interface of the dissimilar AA2024-AA7075 FSW joints. The origin of this behavior is not clear; however, it seems to be due to a large amount of deformation in this area. In the same joints, in the colder periphery of the deformed zone, many LAGBs or subgrains have been detected (Fig. 33c and d), which confirms the occurrence of DRV and CDRX.

5.1.2. Dissimilar magnesium alloys

There are relatively few reports looking at the FSW of dissimilar magnesium alloys [367-372]. For dissimilar FSW of AZ31/AZ80 [367] and ZG61/AZ91D [370] (see Fig. 34), it has been suggested that the material with superior plastic deformability (AZ31) should be placed on the RS. In contrast, in the case of AZ31-AZ91 dissimilar joints, defect-free joints have been produced by placing the lower high-temperature strength AZ31 Mg alloy on AS side [369]. In addition, it has been reported that fine grains are formed in the SZ containing distributed β ($Mg_{17}Al_{12}$) phases. In dissimilar FSW of ZK60-AZ31 [368] and AZ31-AM60 [371] magnesium alloys, it has been reported that the plate positioning had no significant effect on joint soundness.

Some microstructural characteristics of dissimilar magnesium alloys are illustrated in Fig. 35. It is evident from Fig. 35a-f, that sound joints without defects can be produced in dissimilar AM60-AZ31 magnesium alloys. The SZ of the joint exhibits a macroscopic "bowl-like" morphology. The grains in SZ are significantly refined by DRX. The grains in the SZ and TMAZ are favorably orientation for basal slip (grain convergence phenomena) and extension twinning, respectively. In addition, Fig. 35g shows that no intermetallic compound is formed at the interface of dissimilar FSWed magnesium alloy. In general, the texture and microstructural evolution were similar to what is observed in similar FSW of magnesium welds (see section 4).

5.1.3. Dissimilar copper alloys

Defect-free dissimilar Cu-joints can be readily fabricated [373-375]. Cu has successfully be joined to brass leading to both CDRX and DDRX in the SZ [373,375]. Brass contains finer grain sizes compared to copper in the SZ due to its lower SFE, which promotes DDRX [373]. Cu to bronze friction stir welds [374] also exhibit DRX in the SZ without welding defects.

The microstructural evolution in the interfacial region during dissimilar FSW of Cu-brass is shown schematically in Fig. 36. Initially, large pre-existing oxides on the surfaces of the base materials (Fig. 36a) fragment into small particles (Fig. 36b) due to the existence of compressive forces perpendicular to the interface and shear forces, which deforms material parallel to the interface. In this step, fresh surfaces, i.e. oxide-free surfaces, are generated (Fig. 36b). A joint then forms between the fresh copper and brass surfaces aided by the compressive force, while leaving the small oxide particles distributed on the interface local to which voids can persist (Fig. 36c). In the next step, the difference between the dislocation densities or internal energy between the opposing sides of the interface (Fig. 36d) results in a strain-induced migration of boundaries. Thus, the voids are distinguished and the dispersed oxides become enveloped by the growing grains (Fig. 36e). Finally, by further strain induced migration of grain boundaries, a sound interface

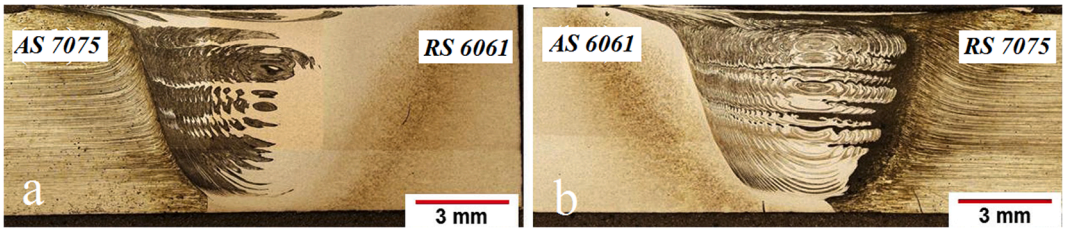

Fig. 32. Macrographs showing: a, and b) AA6061-AA7075 dissimilar joints welded at a rotational speed of 1200 rpm and a traverse speed of 180 mm/min with AA6061 placed on the RS and the AS, respectively. Reproduced from [359]. Reproduced with permission from Elsevier. All rights reserved.

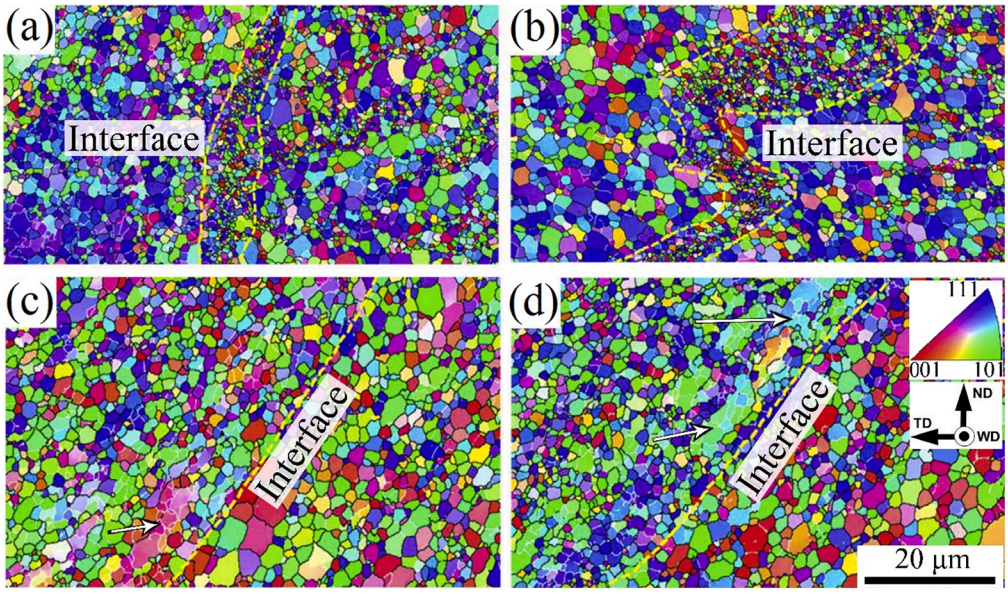

Fig. 33. IPF maps of the interface area in the dissimilar AA2024-AA7075 joints at different conditions at the center of SZ (a and b), and colder periphery of SZ (c and d). The yellow dashed lines indicate the interface between the dissimilar materials in the SZ. The arrows show the occurrence of DRV and CDRX. Reproduced from [366]. The coordinate system, scale bar, and IPF color codes are the same in (a-d) as illustrated in (d). Reproduced with permission from Elsevier. All rights reserved. (For interpretation of the references to color in this figure legend, the reader is referred to the web version of this article.)

without any oxide particles is achieved (Fig. 36f) [375].

5.1.4. *Dissimilar steels*

Joining of dissimilar steels having differing properties is required in many applications; however, significant challenges remain. The incompatibility can lead to solidification cracking, hydrogen cracking, and formation of brittle products and different residual stresses relative to similar metal welds. Several studies have examined the microstructures of dissimilar steel welds [111,376-393] and include structural steels such as St37 to St44 and St37 to St52 [376,377,394]. Neither of these combinations exhibited a distinct TMAZ and the characteristic onion rings were observed only in the SZ of St37-St44 joints since they have a similar microstructure. Moreover, the microstructure of the SZ for St37-St52 joints comprised complex structures such as Widmanstatten ferrite, ferrite + carbide aggregate and grain boundary ferrite. However, the fact that Widmanstatten ferrite is dominant in the SZ is due to the relatively low cooling rate of the welded region. Furthermore, very fine equiaxed grains (grain size being about 1 μm) were observed in the root region of the SZ [376].

A number of studies have examined the joining of structural steels to stainless steels [111,378-385]. These include joining of AISI type 304 austenitic stainless steel and St37 steel [378,379], welding of 2205 duplex stainless steel (DSS) and S275 low C-Mn structural steel [380], and welding of AISI 316 stainless steel and low C steel [381]. Typically, the conventional HAZ, TMAZ and SZ regions are evident on both sides of the joints, with the center of the welds having alternating bands of both materials, although no clear HAZ is seen on the austenitic steel side. In the case of dissimilar DSS-S275 joints, the fine and equiaxed grain structure in the SZ is due to the occurrence of DRX in ferrite and austenite phases. CDRX in ferrite phase of both DSS and S275 steels, and DDRX in austenite of S275 are the main mechanisms during grain structure formation [111]. The stirring process leads to the formation of complex interlocking features in the middle of the SZ. Moreover, the temperature in the center of the SZ lies between Ac_1 and Ac_3 during welding, resulting in a minor ferrite-to-austenite phase transformation in the S275 steel, and no changes in the fractions of ferrite and austenite in the DSS [111]. It is also reported for type 304 austenitic stainless - St37 steel joints that the SZ has a mixed microstructure containing different types of ferrite with colonies of ferrite and cementite, indicating DRX is taking place in the SZ of 304 stainless steel and phase transformation is occurring in that of St37 steel [378,379]. Moreover, in the case of 304 austenitic stainless - Q235 low carbon steel joints, FSW results in grain refinement in the SZ and TMAZ on the SS304 side [382]. The acicular ferrite and pearlite and some products of displacive transformations such as Widmanstatten ferrite and martensite are generated in the SZ on the Q235 steel side, which is due to the peak temperature exceeding Ac_3. It is also observed that the amount of acicular ferrite decreases in the TMAZ. Finally, the HAZ on the structural steel side shows partially and fully refined microstructures like those in fusion welding processes. In addition, compressive residual stress is formed in the SZ due to the difference in expansion coefficient between the two steels.

Friction stir butt welding of structural steel and ferritic stainless steel shows a characteristic onion ring structure comprising alternate bands of both steels [383]. No distinct TMAZ is exhibited by the joint, and the microstructure of the SZ on structural steel side exhibits fine ferrite, pearlite and martensite grains indicating that the peak temperature exceeds Ac_3 during FSW. UNS S31603 austenitic stainless steel - UNS S32750 super-duplex stainless steel joints have been produced by placing the higher strength super

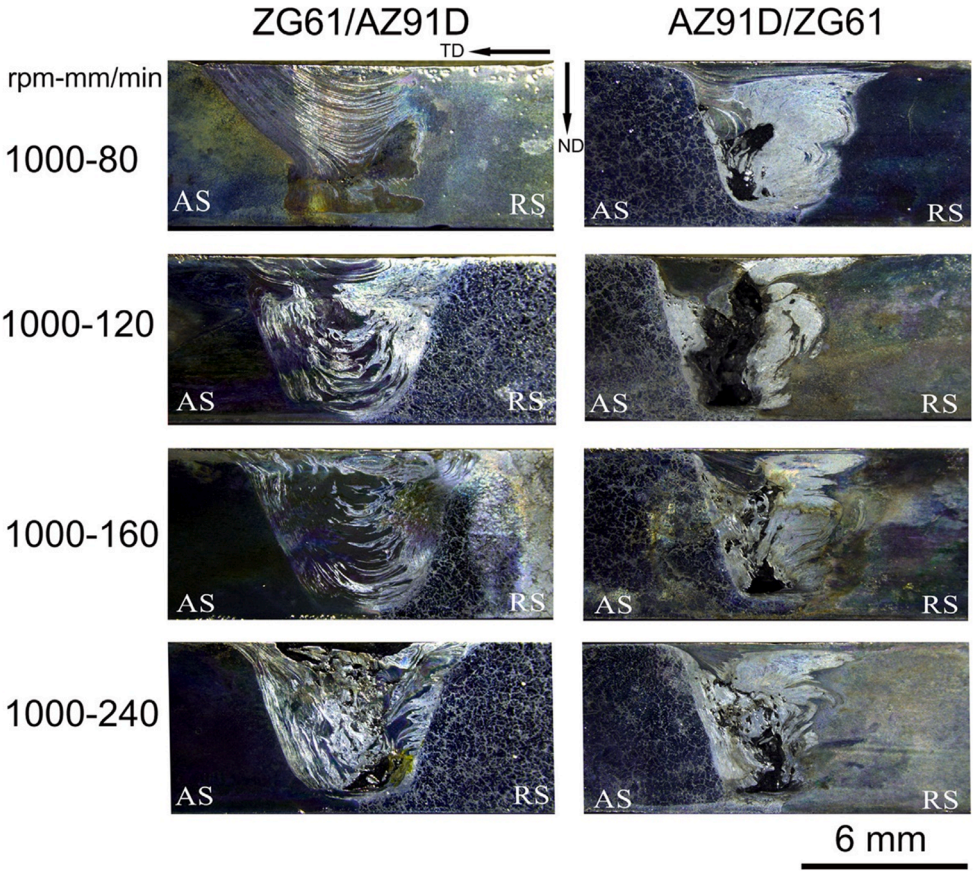

Fig. 34. Macrographs showing the cross-sections of dissimilar ZG61-AZ91 FSW joints as a function of rotation and traverse speeds [370]. All the joints obtained by placing AZ91 on the AS are defective due to poor plasticity of AZ91. Reprinted with permission from Elsevier. All rights reserved.

duplex steel on the AS [386]. The HAZ is indistinct while the SZ, TMAZ, and BM are well defined, with no bimetallic vortices in the SZ and a well-defined interface between both materials. Sound oxide-dispersion strengthened (ODS) alloy - F82H martensitic steel joints can be produced when the ODS plate is set on the AS and the FSW tool is plunged into the F82H [387]. During FSW, CDRX occurs in the ODS, while the F82H steel undergoes phase transformation [395].

5.2. FSW of dissimilar metals

5.2.1. Dissimilar welding of aluminum alloys to magnesium alloys

The conventional welding of Mg and Al alloys is very challenging, giving rise to the formation of coarse grains, massive brittle intermetallic compounds (IMCs), a large HAZ, solidification cracking, porosity, and evaporative loss of the alloying elements [396-398]. Among these difficulties, the formation of brittle Al-Mg based IMCs is particularly problematic due to the extensive intersolubility [399]. Al-Mg dissimilar welds are also highly susceptible to constitutional liquation [397,398,400-405] due to the formation of a low melting point eutectic phase at 450 °C. This leads to local hot cracking in regions where IMCs are formed affecting weld integrity [404,405]. This also favors the excessive formation of IMCs due to higher reactivity in the liquid state [401]. This is particularly evident in joints made with too much heat input [398,399,402]. Al_3Mg_2 and $Al_{12}Mg_{17}$ IMCs have been found during Al-Mg dissimilar FSW, and their amount and thickness depend on the heat input [396-398,406,407]. The macrostructure and microstructures of a dissimilar AZ31 Mg alloy and AA6061 Al alloy joint are illustrated in Fig. 37, showing the formation of IMCs in the interface of the dissimilar metals.

It is clear that the heat input during FSW should be kept as low as possible in order to limit the amount and thickness of IMCs formed and to improve the overall joint quality [399]. Furthermore, better intermixing is achieved when Al is placed on the RS and the tool offset is towards the Mg side [408,409]. This condition improves the joint quality [408-410], because it reduces the heat input and limits the formation of brittle IMCs [398,402,410]. A complex pin and shoulder geometry can also enhance material flow [398].

The weld parameters also affect the joint macrostructure giving rise to three types of bond [399], namely a distinct boundary (Type I); a lamellar structure with a distinct boundary (Type II), and a complex intercalated lamellar structure with a distinct boundary (Type III), as shown in Fig. 38 [399]. Inappropriate welding parameters causing inadequate heat input result in the formation of a Type I interface which displays negligible intermixing of Al and Mg alloys. Such joints will fracture at the interface due to the concentration of

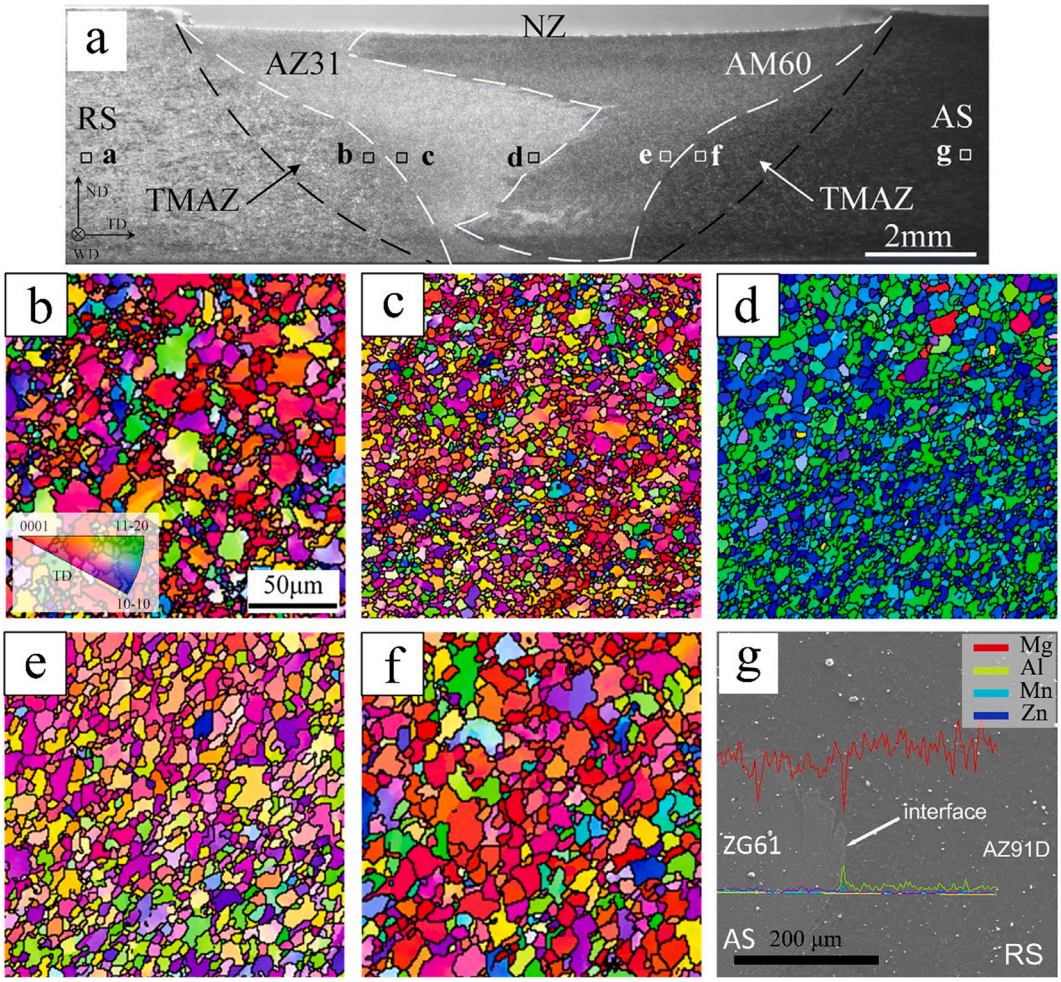

Fig. 35. Microstructural evolution during dissimilar FSW of AZ31-AM60 magnesium alloys. (a) macrograph of weld cross-section, (b-f) Corresponding IPF maps of the regions indicated in (a). (g) Backscattered electron SEM image of interface in ZG61-AZ91D joint with superimposed elemental EDS line scans of Mg, Al, Mn, and Zn. Reproduced from [370,371]. Reproduced with permission from Elsevier. All rights reserved.

brittle IMCs there [411-413]. Masoudian et al. [414] investigated AA6061 and AZ31 dissimilar welds and observed vortex flow-like intercalated microstructure in the SZ, which may be characterized as a Type III. Of the three types of interface, Type III is the most desirable for better joint performance as this complex interface structure will impede crack propagation [399].

Further welding strategies have also been applied to FSW of the Al-Mg system. One is the use of an interlayer (i.e., barrier sheet), for instance, a Zn interlayer during FSW of dissimilar AA6061 Al-alloy to AZ31 Mg-alloy, to improve joint quality [415]. Zn causes the formation of Zn-Mg IMC, which disperses in the interface of the joint instead of continuous Al-Mg IMCs, as shown in Fig. 39a and b. A Ni interlayer introduces less brittle Ni-based intermetallic phases in the SZ instead of $Al_{12}Mg_{17}$ [416]. Recently, a plasma electrolytic oxidation (PEO) interlayer has been used to improve the Al-Mg dissimilar FSW joints [417]. The PEO layer on the Mg prohibits and postpones the reaction between the Mg and Al, and hence it reduces the thickness of the Al-Mg IMCs in the interface area. In addition, during FSW, the PEO interlayer breaks up into particles, and then disperses in the interface. Another approach has been to limit the heat input so as to limit the formation of brittle IMCs; for example, by underwater FSW (UFSW) [418,419] or externally cooled FSW [420-422].

Several researchers [424-427] have also reported that joint performance can be improved when ultrasonic vibration assisted FSW (UAFSW) is used to join Al-alloy and Mg-alloys. The use of ultrasonic vibration during FSW is said to promote better material flow and the formation of homogeneous intercalated lamellae distributed in the SZ region (similar to Type III, Fig. 38) and significantly reduces the IMCs layer thickness [424-427]. Lv et al. [426,427] reported that the conventional FSW Al/Mg weld interface constitutes an intermetallic bi-layer of Al_3Mg_2 and $Al_{12}Mg_{17}$, whereas the application of ultrasonic vibration together with tool offset towards the Mg side reduced the bi-layer to a Al_3Mg_2 mono-layer of reduced overall thickness, thus enhancing joint strength. Combining ultrasonic vibration with a Zn interlayer has been reported to give rise to better microstructural features [423,428,429].

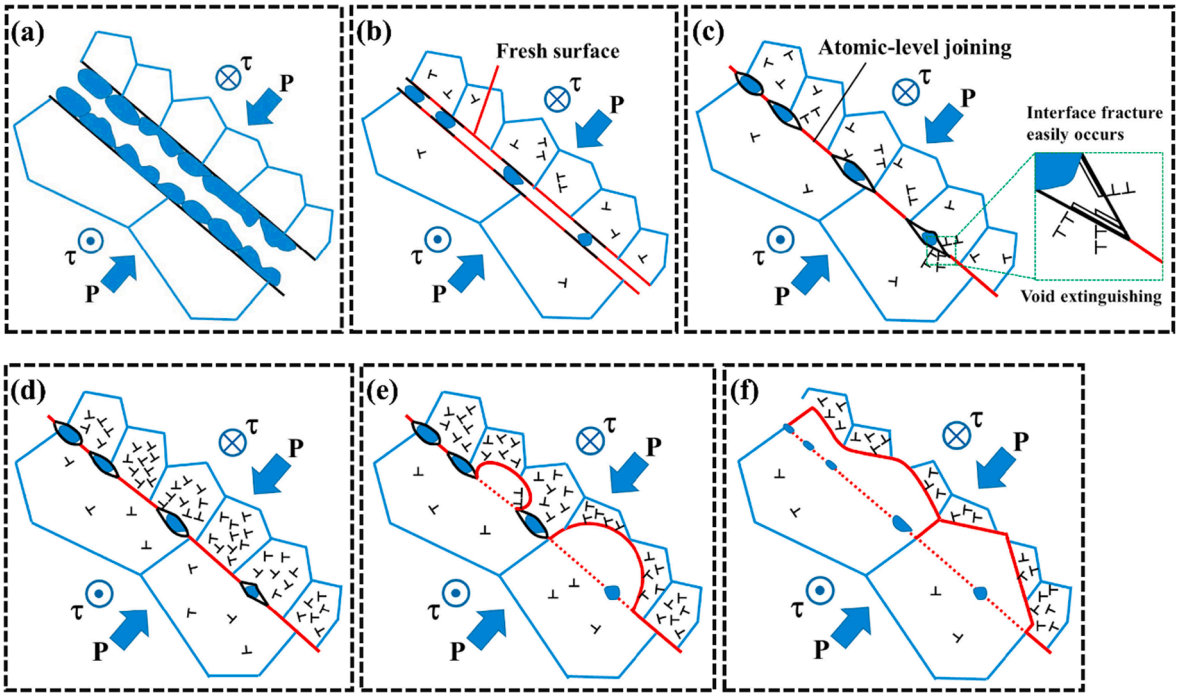

Fig. 36. Schematic of different steps of interfacial evolution during FSW of Cu-brass dissimilar joints. Reprinted from [375]. Reprinted with permission from Elsevier. All rights reserved.

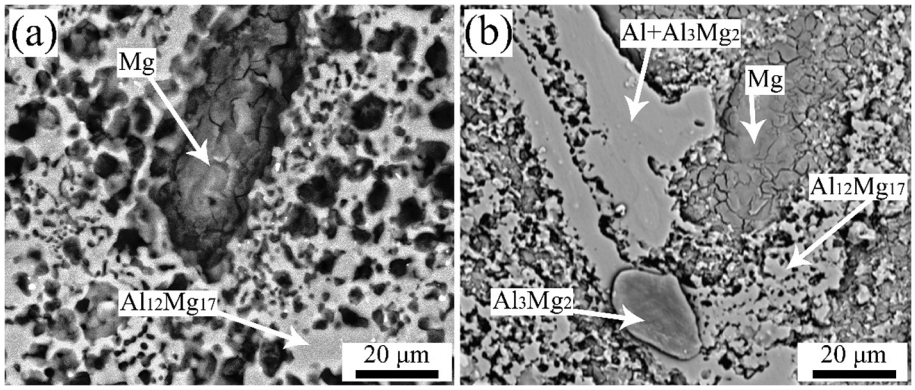

Fig. 37. Formation of IMCs in the SZ of an AA6061-AZ31 dissimilar FSW joint showing the presence of (a) $Al_{12}Mg_{17}$ IMC, and (b) Al_3Mg_2 + $Al_{12}Mg_{17}$ IMCs in the joint. Reproduced from [403] with permission from Elsevier. All rights reserved.

5.2.2. Dissimilar welding of aluminum alloys to copper alloys

The joining of Al to Cu has attracted much attention in the past decade because the low heat input compared to fusion welding avoids, or limits, IMC formation which can cause premature failure along the interface [156]. Many different IMCs have been observed but the most generally reported are Al_2Cu and Al_4Cu_9, although AlCu and Al_2Cu_3 have also been reported [23,355,430-467]. Care must be exercised because extremely low rotational speeds or excessively high traverse speeds produce defective joints due to insufficient heat input [441-445].

For joints from materials with such different thermomechanical properties as aluminum and copper, requires additional measures such as pin offset (i.e., tool insertion position) which can have a significant impact on the temperature distribution and material flow pattern, and thereby affect the microstructural evolution [2]. Among all the weld variables, the positioning (AS or RS) of the plates prior to FSW and the tool offset are the most critical factors in dissimilar joints of Al-Cu [430-432]. Indeed, without tool offset it is not possible to simultaneously plastically deform both Cu and Al [449-458], without which defective joints are generally formed [430,439,449-458]. For the Al–Cu FSW system, it is suggested that tool pin should be displaced toward the Al side in such a way that relatively few particles are detached from the Cu plate, which can easily flow and mix in the Al matrix [432,433] (see Fig. 40). This leads to an intercalated vortex type microstructure [454] comprising differently sized irregular Cu islands distributed within an Al

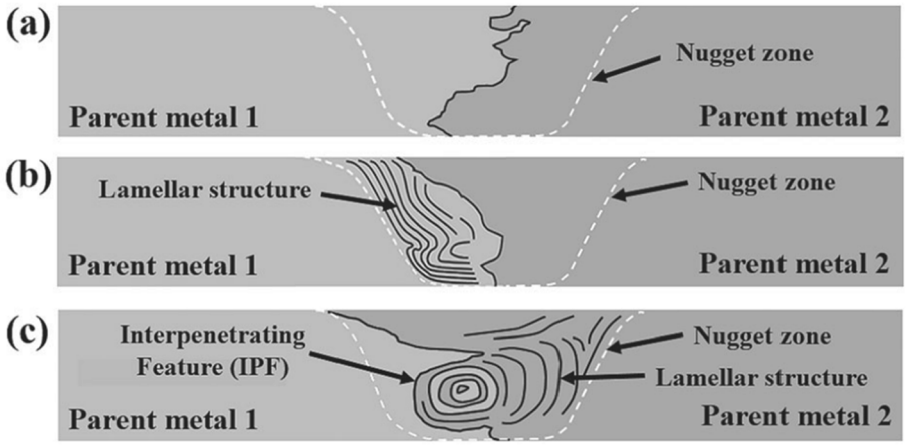

Fig. 38. Schematic showing the three characteristic joint microstructures observed in dissimilar Al-Mg joints; (a) Type I, distinct boundary, (b) Type II, lamellar structure with distinct boundary, and (c) Type III, complex intercalated lamellar structure. Reprinted from [399] with permission from Taylor & Francis.

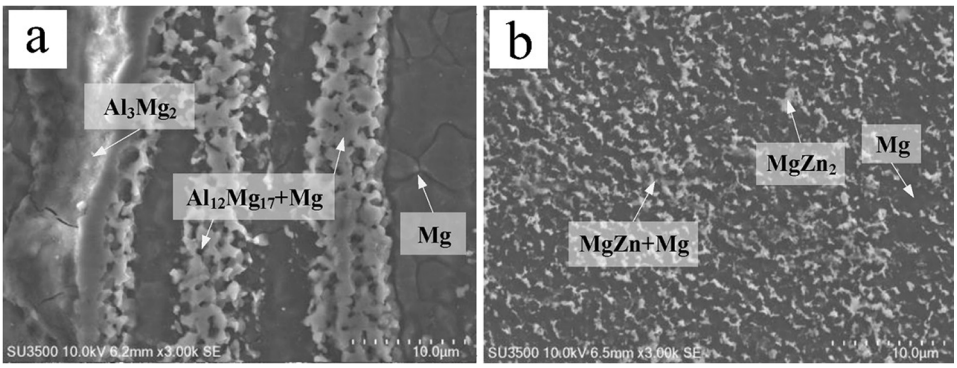

Fig. 39.. SEM micrographs showing the effect of interlayer on interfacial microstructure of dissimilar FSW joints: (a) AZ31B Mg/7075-T6 Al without any interlayer, and (b) AZ31B Mg/7075-T6 Al with a Zn interlayer. Reproduced form [423] with permission from Elsevier. All rights reserved.

matrix [456,457]. Then, the chemical reaction between Cu particles and Al matrix causes the formation of multilayer IMCs composed of Al_4Cu_9, Al_2Cu_3, and Al_2Cu. When the pin offset is too small brittle IMCs are formed and the surface morphology becomes poor [432,433]. However, it should be pointed out that the optimum value of tool offset depends upon the BM composition, thickness, tool design and process parameters [432,433].

Other approaches have also been applied to the FSW of Al-Cu joints, such as i) the use of barrier sheets [468], ii) friction stir diffusion bonding (FSDB) [469-471], iii) heat-assisted FSW (HAFSW) [433,466,472,473] and iv) UAFSW [474,475] all aiming to achieve thin or discontinuous IMCs at the interface.

5.2.3. Dissimilar welding of aluminum alloys to steels

Various IMCs form during fusion welding of Al-to-steel due to the low solubility of iron in aluminum at room temperature leaving welds prone to a thick brittle intermetallic layer, heavy cracking, and serious porosity, resulting in poor joint performance [476,477]. Depending on the heat input, FSW limits the formation of intermetallics at the Al-to-steel interface because it involves lower temperatures and avoids melting. It has been proposed that the IMC layer can be kept to less than 1 μm by keeping the heat input as low as possible through optimized weld parameters [418,477-502]. $AlFe_3$, AlFe, Al_3Fe_2, Al_2Fe, Al_5Fe_2, and Al_3Fe ($Al_{13}Fe_4$) have been reported in Al-steel joints [355,477,478,503-505]. A higher rotational speed and larger tool offset can be used to modify the overall temperature distribution in the weld and accordingly, influence the composition of the formed IMC layer. This may even promote the formation of FeAl instead of Fe_3Al in an Al6061 to TRIP 780/800 steel weld [486].

As for Al-Cu dissimilar FSW joints, a composite SZ structure, in this case comprising steel fragments in an Al matrix, is typically formed (Fig. 41) [506]. Here the shear forces induced by rotating tool results in the detachment of steel (Fe-rich) particles from the steel plate into the Al matrix. The accompanying severe shear deformation creates fine and elongated Fe grains having a shear type texture (Fig. 41g). The shear forces markedly refines the Al matrix in the SZ. Some of the fine steel particles dissolve in the Al matrix by

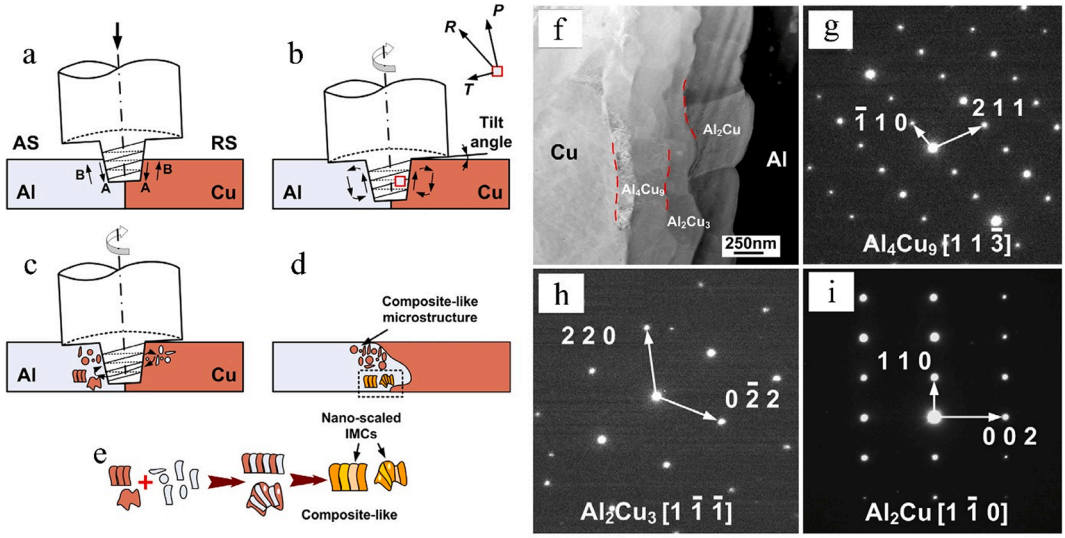

Fig. 40. Formation mechanism of composite-like structure in the SZ of dissimilar Al-Cu FSW joints; (a) Step 1: tool plunged into workpiece. (b) Step 2: shear deformation induced by rotating tool generating material flow, (c) Step 3: transfer of Al and Cu fragments into opposing sides, (d) final microstructure of the weld comprising Al matrix and reinforcements of nano-sized IMCs, (e) formation of multilayer IMCs in the SZ, (f) Bright field STEM micrograph of interface in dissimilar 5A02 aluminum alloy/pure copper FSW joint obtained using a high angle annular dark field (HAADF) detector with inset SAD patterns for the (g) Al_4Cu_9, (h) Al_2Cu_3, and (i) Al_2Cu phase regions. Reproduced form [456] with permission from Elsevier. All rights reserved.

Fe diffusion to form nano-sized Al_3Fe IMC. The steel fragments become coated with Al_5Fe_2 phase that forms instead of Al_3Fe phase due to the kinetics of the Al/Fe interface reaction giving rise to steel-Al_5Fe_2 coated fragments surrounded by Al-Al_3Fe composite structure dispersed in the Al matrix [506].

In this case novel FSW approaches include; i) FSDB [469,482,485] for which the rotational speed must be sufficient to generate enough heat to produce an intermetallic layer and induce bonding [469,482], ii) HAFSW which has been found to produce defect-free joints [419,472,507,508] through preheating which enhances the mechanical properties of the joints by increasing the peak temperature of the steel, and reducing the large temperature difference between the steel and the aluminum alloy, consequently promoting a better intermixing [472,507], iii) electrically assisted FSW [419] which is said to form a thin layer of IMC thereby improving weld efficiency in dissimilar AA6061 and TRI 780 steel welds and iv) water cooled FSW of AA5083 Al-alloy and AISI A441 steel [509], v) the use of UAFSW to incorporate fewer and smaller steel particles in the SZ as well as a thinner continuous intermetallic layer of $FeAl_3$ at the interface when joining AA6061 Al-alloy and mild steel [510], vi) the use of a Zn [511-513] or AlSi [513] coatings on the steel prior to FSW. In the last case, Zn produces a discontinuous, nanoscale IMC due to formation of Al-Zn eutectic compound, which helps to weld two parts by a liquid/solid reaction mechanism, while AlSi appears to improve the weld interfacial characteristics by a solid/solid reaction mechanism [513].

5.2.4. Dissimilar welding of aluminum alloys to titanium alloys

Al-Ti dissimilar joints are desirable in the aerospace and automobile industries; however, the large differences in physical and metallurgical properties of Al and Ti result in a poor weldability due to brittle IMCs that form at the interface. Another issue is the necessity for a protective atmosphere due to the high affinity of Ti to oxygen at temperatures above 500 °C. FSW can obviate these challenges with several reports of sound Al-Ti joints displaying acceptable mechanical properties with the IMC layer (generally $TiAl_3$ [514]) limited to less than 2 μm if optimized weld parameters are used, or special measures are taken during FSW [514-523].

The deformation in Al and Ti from the rotating FSW tool introduces dislocations which reorganize into energy dislocation structures such as dislocation cells and subgrains at larger strains and/or temperatures, aiding diffusion of Al and Ti atoms in the interface. Then, accompanied by DRX in the Al and Ti, they react to form $TiAl_3$ at the interface. Finally, the DRX grains grow, and a continuous (thin) layer of $TiAl_3$ forms at the interface due to its lower Gibbs free energy compared to supersaturated solid solution [524]. With increasing heat input, other compounds of Al and Ti can form in the interface, for example, upon increasing tool rotational speed from 700 to 900 rpm at constant tool traverse speed, offset, and tilt angle, $TiAl_3$, TiAl, and Ti_3Al are formed in the interface.

Some issues hinder the formation of a high-quality joint. While low heat input limits the formation of brittle IMC, this results in low plasticity of the Ti-alloy leading to intermixing problems giving rise to weak metallurgical bonding, or even a kissing bond. Generally, the tool is significantly offset towards the Al plate to avoid excessive tool wear [514,516,517] and to avoid great amounts of IMCs being formed at the joint interface, promoting brittle interface failure [516]. Sound dissimilar butt joints are produced if a proper range of offset distance is used, giving rise to a swirl-like structure comprising Ti particles in Al matrix [516]. Aluminum is usually placed on the RS [515-517,520,525,526]. By offsetting to 1 mm (i.e. only 1 mm of the pin lies in the Ti), better tensile properties are reached due to the suppression of Ti fragments and avoidance of a thick intermetallic compound layer at the weld interface [517]. Relatively large

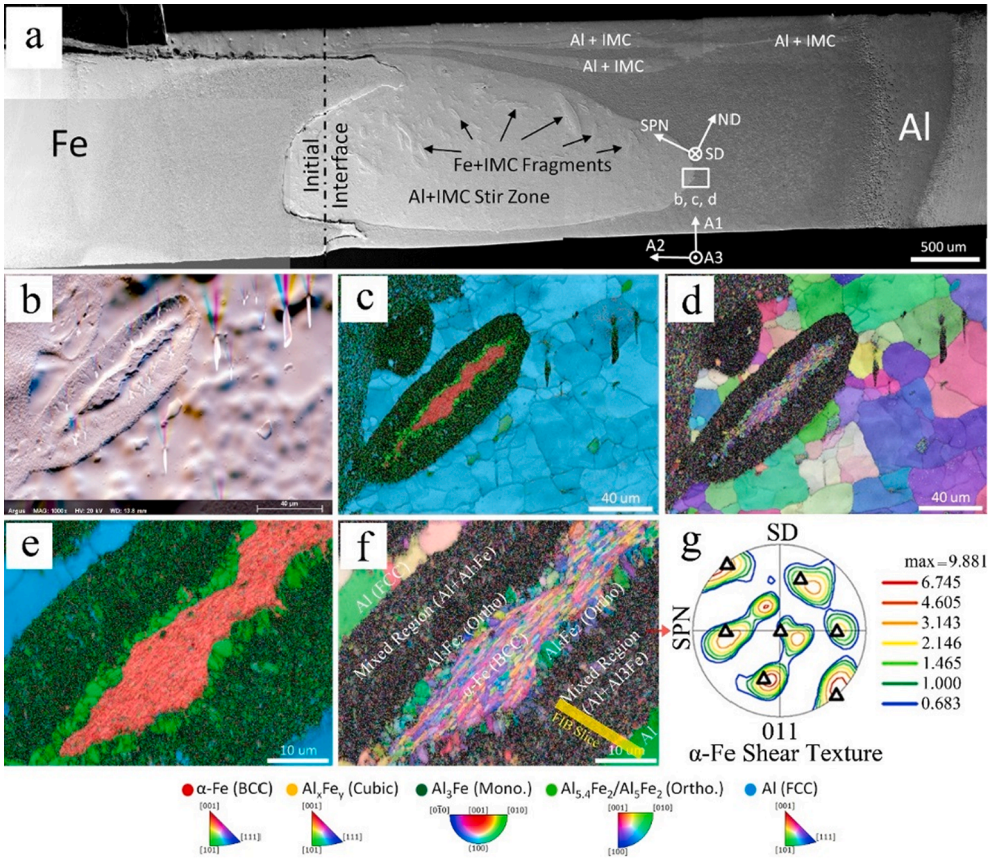

Fig. 41. Formation of IMCs in dissimilar Al-steel joints (a) SEM micrograph of cross-sectional macrostructure of AA5186-low carbon steel dissimilar FSW showing a composite SZ structure composed of Al matrix and Fe + IMCs fragments, (b) the forward scattered detector (FSD) image showing the surface topography, (c) IPF map, and (d) phase map of interfacial region indicated by white rectangle in (a). Higher magnifications of (c) and (d) are shown in (e) and (f), respectively, (g) (0 1 1) pole figure of steel fragments (α-Fe) in (f). The colour codes for each phase and their respective polefigure scales for each are shown at the bottom. Reproduced from [506] with permission from Elsevier. All rights reserved.

Ti fragments or particles are difficult to avoid in the SZ [516], as revealed by 3D X-ray micro-CT in Fig. 42a, however, the fragments of Ti are well distributed in Al matrix. The formation of a thick and continuous IMC (mainly $TiAl_3$) layer is suppressed, and nano-sized IMCs are formed in the joint interface by FSW in power control mode (Fig. 42b and c).

Approaches to control IMC formation include; i) a Nb or Zn interlayer ii) two-pass FSW, iii) preheating, and iv) UAFSW. A Nb interlayer retards the formation of brittle $TiAl_3$ at the interface. The Al matrix undergoes CDRX and DDRX, in which the DDRX takes place by PSN mechanism when an Nb interlayer is used [519]. Without the Nb interlayer, Al matrix is recrystallized by DRV and CDRX [528]. In both cases, the Ti close to the interface undergoes twinning. However, at the interface, due to adiabatic shear banding (ASB)

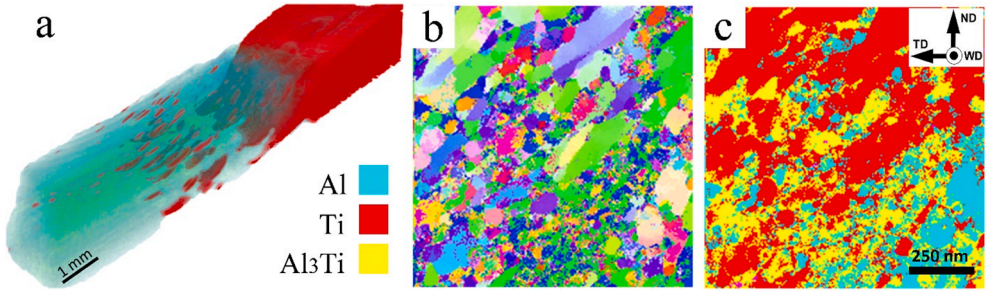

Fig. 42. Microstructural evolution during dissimilar FSW of AA2024-T3 aluminum alloy to Ti-6Al-4V titanium alloy, (a) 3D X-ray micro-CT image of the joint showing Ti fragments dispersed in the Al, (b) IPF and (c) phase maps of the interfacial area of the joint using the same colour code as (a). The scale bar and coordinate system are the same in (b) and (c) as shown in (c). Reproduced from [527] with permission from Elsevier. All rights reserved.

at higher strains and temperatures, Ti undergoes fragmentation and DRX. A significant improvement in the tensile ductility is observed due to the presence of finer particles; however, tensile strength is diminished. By contrast, a Zn interlayer renders the SZ more brittle due to the formation of ZnTi intermetallic phase in addition to $TiAl_3$ thus decreasing the tensile strength [529]. Two-pass FSW (AA2024 Al-alloy and Ti-6Al-4V [520]) and UAFSW (AA6061 Al-alloy and Ti6Al4V Ti-alloy [522,530]) refine the grains and break up the IMCs while preheating the Ti side eliminates the likelihood of a kissing bond [521].

5.2.5. Dissimilar welding of titanium alloys to steels

Ti and steel dissimilar joints are plagued by the formation of IMCs at the joint interface resulting from the limited solubility between Ti and Fe at room temperature, as well as excessive distortion and residual stresses due to their significantly different physical properties. As above, a protective atmosphere is required for Ti alloy. Very few investigations of dissimilar FSW of Ti to steels have been reported, but the basic microstructural concepts are summarized here. Dissimilar FSW of commercially pure titanium (CP-Ti) to 304 stainless steel (SUS304) shows that at 50 mm/min and 250 rpm welding conditions, the morphology of the interface comprises a flat (~1 μm thick) interfacial reaction layer. The interlay thickness and complexity increase with increasing pitch ratio (tool rotation/traverse speed) [531-533] which can result in an interface up to 300 μm thick comprising a macroscopically mixed and laminated structure consisting of multiple layers containing IMC [534].

5.2.6. Dissimilar welding of magnesium alloys to steel

The fusion welding of steel and magnesium is very difficult owing to their significantly different physical properties (e.g. T_m = 1538 °C for Fe and 650 °C for Mg) as well as the formation of IMCs at the joint interface. Despite the potential of FSW there have been very few studies. In the case of butt FSW of a mild steel to a Mg-alloy, defects can form in the Mg-matrix due to insufficient plasticization of the Mg at lower rotational speeds for a given traverse speed. However, excessive rotational speed causes the ignition of the Mg. With the pin footprint extending just 0.1 mm into the steel, steel fragments have been found to disperse in the magnesium matrix as small particles which have no influence on the joint strength. Offsets over 0.2 mm lead to a continuous dispersal of steel fragments into the magnesium matrix parallel to the weld interface, triggering brittle failure along the interface. The alloying elements in Mg alloys such as Al in AZ31, Y and Nd in WE43 have been found to contribute to the formation of IMCs [535,536] as have Al or Zn coatings on the steel [537]. However, during FSW of Mg alloys to galvanized steel, melted Zn was found to react with Mg to form a Mg-Zn layer [538]. The Mg-Zn layer was located out of the SZ, and hence it does not affect the mechanical properties.

5.2.7. Dissimilar welding of magnesium alloys to titanium alloys

Magnesium and titanium do not form a solid solution nor any compounds, meaning they are immiscible and thus extremely difficult to join. However, it has been suggested that Mg-alloys and Ti can be successfully joined by FSW if the Mg-alloy contains alloying elements of Al, Zn and Zr, which have a strong affinity with Ti, provided that appropriate welding conditions are used [539-541]. For instance, AZ-type magnesium alloys with various Al-contents (e.g. AZ31B, AZ61A and AZ91D) and AM-type magnesium alloy (AM60), have been successfully joined to pure titanium by FSW [539,540]. An Al-rich thin layer forms at the joint interface by reaction with Ti. Increasing the Al content of the Mg alloy increases the thickness of $TiAl_3$ layer, causing the tensile strength of the joint to decrease. Similar findings have been reported for dissimilar friction stir lap welding of AZ31 Mg alloy to Ti6Al4V alloy [542]. Similarly, during FSW of Zn and Zr-containing ZK60 Mg-alloy to titanium, Zn and Zr form a thin reaction layer with titanium at the joint interface [541].

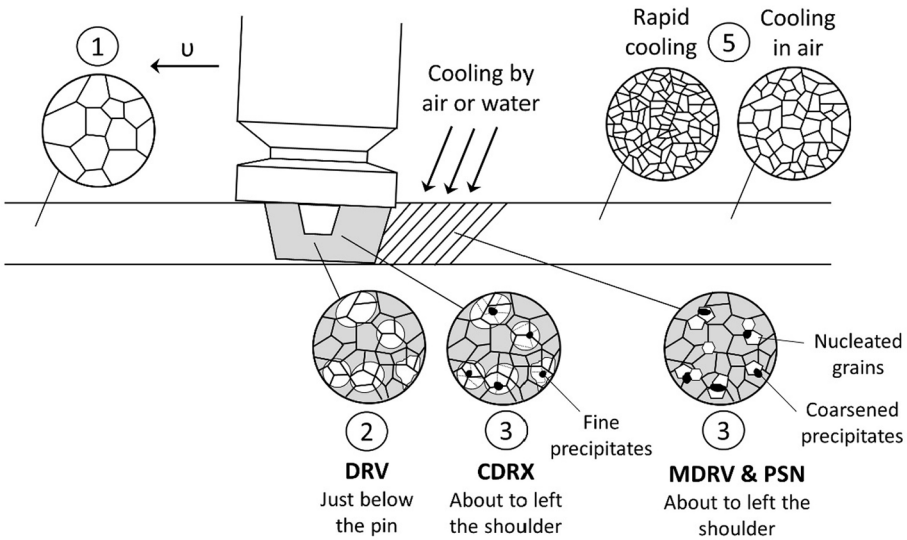

Fig. 43. Schematic illustrating microstructural evolution during FSP of a coarse-grained aluminum 5083 alloy [569]. Reprinted with permission from Elsevier. All rights reserved.

Incorporating an Al foil during dissimilar FSW of pure Mg to pure Ti refines the grain structure in the SZ, thereby improving the mechanical properties [543]. It has been reported that despite using higher heat inputs (lower traverse speeds), the average grain size of the Mg in the SZ decreases in the presence of Al foil. It is suggested that with increasing heat input more Al dissolves reducing the SFE of the Mg matrix, hence promoting the occurrence of DRX and finer grains.

6. Microstructural aspects of friction stir processing

6.1. FSP of autogenous plate

FSP can be utilized as a means of surface modification, surface alloying, or to reinforce the surface by forming a near-surface composite [523,544-562]. It has been used for grain refinement [563,564], and to recrystallize cast structures [565,566]. Ma et al. showed that the grain sizes could be reduced in Al 7075 to the point that it could promote superplasticity [120,567], and this phenomenon has been further explored in other alloys as well [568]. As illustrated in Fig. 43, the microstructural evolution during FSP is similar to FSW as discussed in sections 2–4; however, the processing occurs on a single workpiece. Nano-sized or micron-sized grains may form depending on whether forced rapid cooling is applied to the processed material. The scan pattern and the number of repeated passes affect the microstructural evolution in the SZ during FSP. One way of producing a larger SZ is to use a larger pin tool, which requires higher torque on the pin and thus more power. Multi-pass FSP is an alternative way of increasing the size of the SZ while maintaining some overlap between consecutive passes. Overlap ratios corresponding to the range of −1 to 1 has been suggested by Nascimento *et al.* [545]. As shown in Fig. 44, the first pass leads to a high strain region with dislocation walls, sub-grains, and CDRX grains. Upon applying the second pass, the low heat input, high total strain, and high strain rate generate additional sites for nucleation by DDRX, refining the grain size.

The typical FSP grain size and active dynamic restoration phenomena occurring for different alloys are summarized in Table 2. As discussed in section 2, it is well established that the SFE plays a leading role in determining the dynamic restoration mechanisms that control grain size during FSW/P. Aluminum and its alloys possess the highest SFE values (~160–200 $mJ.m^{-2}$) [570], and therefore the most important dynamic restoration phenomena during FSP of such alloys are DRV based on generation and rearrangement of the dislocation structures, combined with the opportunity to initiate DRX (both CDRX and GDRX variants). As a striking example of the drastic modification of microstructure, the influence of FSP modification on the grain structure in cast A369 aluminum alloy is shown in Fig. 45a. A wide range of examples of grain refinement via FSP are cited in a review by Mishra and Ma [2], however it is acknowledged that there are no clear models which correlate the tool geometry, processing parameters, and final level of grain refinement observed in the material after FSP. This is a considerable challenge due to the varying thermo-mechanical conditions which may be imposed, and the various refinement mechanisms noted above which depend on the alloy processed.

The microstructural modification of cubic metals with lower SFEs, such as austenitic stainless steels, copper alloys and brasses, is quite different, with dynamic restoration mechanisms based on the nucleation and growth of new and strain-free grains, i.e., DDRX. For typical BCC steels (carbon steels, ferritic and martensitic stainless steels), FSP is carried out in the FCC austenite phase temperature range. In other cases, such as austenitic stainless steels, the austenite phase would be stable down to room temperature conditions with an SFE value in the range of 20–40 $mJ.m^{-2}$ [570]. Iron-based metals in all cases can be considered as low SFE materials, and therefore microstructural modification is mainly by DDRX. HCP titanium and many Ti alloys present SFE values in the range of 300–350 $mJ.m^{-2}$ (even higher than aluminum and its alloys), however, they are processed in the BCC phase followed by transformation to HCP in the

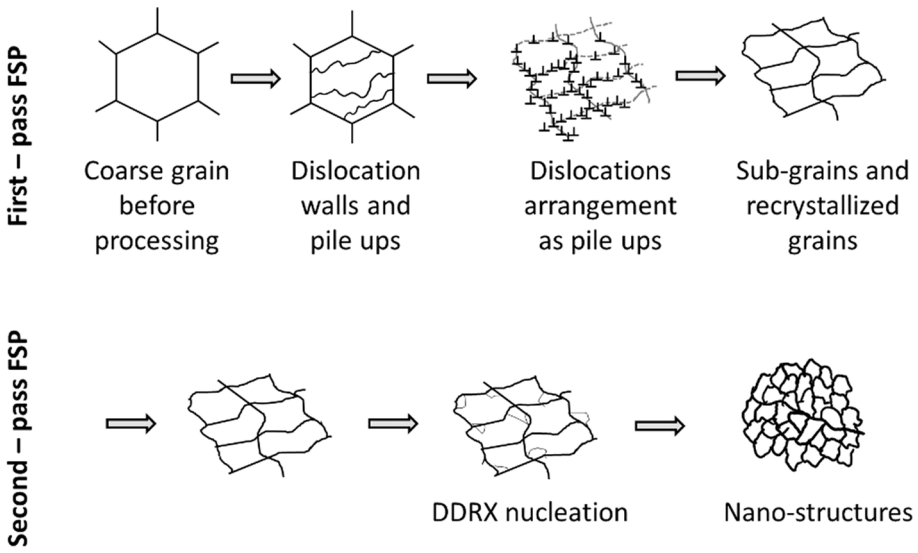

Fig. 44. Schematic showing the grain refinement process for one-pass and two-pass FSP.

Table 2
Grain size and operative dynamic restoration phenomena during FSP for different alloy types.

Alloy	Average grain size of BM	Average grain size of SZ	Restoration mechanisms	Refs.
AA1050	~65 μm	~0.5 μm	DRV/ DDRX/ GDRX	[573,574]
AA5052	~49.4 μm	~10.1 μm	DRV/ CDRX/ DDRX	[141]
AA5086	~48 μm	~6 μm	DRV/ CDRX/ DDRX	[575,576]
A356	~50–60 μm	~2 μm	DRV/ DDRX/ GDRX	[577,578]
Al-7Si-0.3Mg	~188 μm	~1.3 μm	DRV/ DDRX/ GDRX	[579,580]
AlSi9Mg	dendritic	~0.2 to 1 μm	DRV/ DDRX/ GDRX	[581]
Al-4Mg-0.8Sc-0.08Zr	~19 μm	~0.49 μm	DRV/ DDRX/ GDRX	[582,583]
Cu	~19 μm	~0.8 nm	DDRX	[584]
C12200 H02	~18 μm	~0.5 μm	DDRX	[585]
WE43	~35 μm	~2 μm	DDRX/ GDRX	[586,587]
AZ31	~75 μm	~100 nm	DDRX/ GDRX	[188,588]
AZ61	~75 μm	~100 nm	DDRX/ GDRX	[589,590]
AZ91	~150 μm	~4 μm	DDRX/ GDRX	[591,592]
Mg-Li-Al-Zn	~5–100 μm	~1.6 μm	DDRX/ GDRX	[593]
Steel 13Cr4Ni	~25 μm	~0.6 μm	DDRX	[594]
Steel D2	~40 μm	~1.6 μm	DDRX	[595,596]
CP-Ti	~100 μm	~1.7–2.0 μm	DDRX/ GDRX	[597]
Ti-6Al-4V	~500 μm	~1 μm	DDRX	[598]

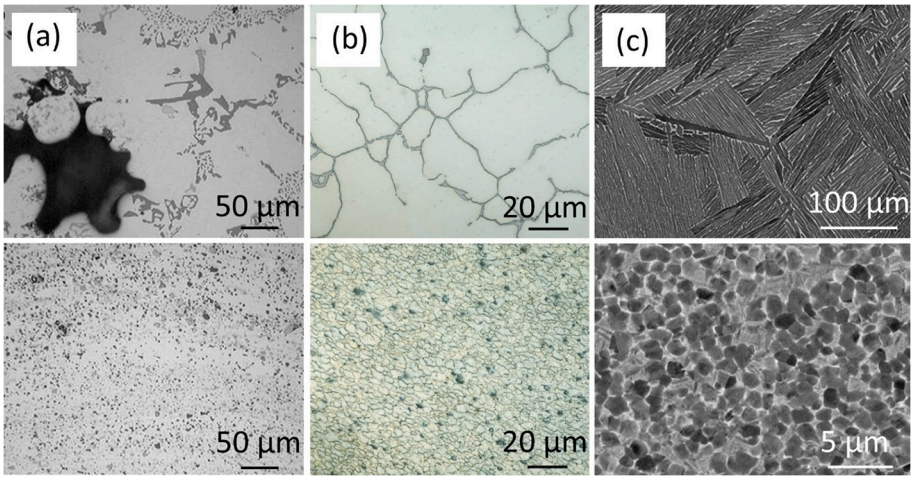

Fig. 45. The effect of FSP on the near surface microstructure for (a) cast A369 Al alloy [571], (b) cast magnesium alloy [572], (c) cast Ti-6Al-4V alloy [207] showing the as-cast structure (top) and after FSP (bottom). Reproduced with permission from Elsevier and Springer Nature. All rights reserved.

final microstructure [570]. In this context, microstructural refinement in HCP materials such as magnesium and titanium alloys are demonstrated in Fig. 45b, and c.

Finally, it is worth mentioning that the grain sizes displayed in Table 2 for the SZ in various alloys after FSP are the minimum values reported. The grain size is affected significantly by other processing parameters as well, such as; tool rotational speed, traverse velocity, number of FSP passes, cooling media employed (water, dry ice, liquid nitrogen, *etc*.), volume fraction of reinforcing agents, *etc*.

6.2. Surface modification of metal matrix composites (MMCs)

FSP is a highly effective way to surface treat metal matrix composites (MMCs) that were synthesized by other bulk production approaches such as casting and powder metallurgy (PM) [2,16]. In this context, FSP can refine and homogenize the microstructure, improve the reinforcement distribution, and remove porosity [16,599 565,577,600-621]. A wide variety of Al MMCs have been friction stir processed including Al/TiC [604], Al/TiB_2 [620], AA6061/SiC [618], A356/Al_3Ti [621], A413/Ni [608], AA6061/Al_2Cu [607], AA6061/Al_3Fe [565], AA6061/Al_3Zr [603], AA6061/Al_3Ti-Al_3Zr [606], A356/TiB_2-TiO_2 [611] and AA7075/SiC [612]. In this context, the following have been highlighted as the key outcomes during thermo-mechanical friction stirring action using a non-consumable rotating tool.

- breaking of coarse, secondary phase particles,
- closure of solidification micro-voids,

- acceleration of *in situ* solid-state chemical reactions in the case of *in situ* composites by enhancing the elemental diffusion,
- homogenization of composite structure by more uniformity in the dispersion of ceramic particles through the metal matrix,
- significant refinement of the grain structure

Some of these features are exemplified by the following examples. For the A356/Al_3Ti composite system [621], densification, homogenization, and refinement of the as-cast microstructure is evident in Fig. 46. As a result of the local forging and shear deformation introduced by FSP, the micro-voids arising from casting have been removed along with considerable grain recrystallization and refinement. In the case of A413/Al_3Ni *in situ* composite [608], the large, elongated Al_3Ni heterogeneously distributed within the dendritic aluminum matrix is broken up, more uniformly distributed and the cast structure homogenized by FSP as illustrated in Fig. 46b.

6.3. Production of MMCs by FSP

MMCs have been manufactured by FSP for various combinations of metal matrices and reinforcing particles or nanoparticles as summarised in Table 3. The minimum attainable near surface grain sizes (inside the SZ) with and without secondary phase reinforcements can be seen by comparing Table 2 and Table 3. To date, the main focus has been on the manufacture of aluminum-based MMCs, although numerous studies on other matrixes such as magnesium, titanium, copper, brass, nickel, and steel have also been reported [9,622-627], see Table 3. Here the differences between the microstructural evolution occurring in FSP when fabricating MMCs, as compared to conventional FSW/P, as described in sections 4 and 5 will be emphasized. Different strategies for dispersing the reinforcing phases through the metal matrix have been implemented for fabricating MMCs by FSP. The most common is to insert powder into a machined groove or into drilled holes on the surface of the plate to be reinforced before being distributed near-surface within the metal-matrix by multi-pass FSP.

Researchers have found that the relevant dynamic restoration phenomena occurring during FSP (as explained in more detail in section 2) are further enhanced in the presence of secondary phases or ceramic inclusions [27,652-654]. As a result, the stacking fault energy (SFE) of the matrix alloy plays a major role in controlling microstructural evolution.

6.3.1. Aluminum based MMCs

In the literature [606,610,623,655-724], the preparation of aluminum-based MMCs by FSP have been classified as "*ex-situ*", "*in situ*", and "*hybrid*". The impact of the FSP route on the microstructural features, mainly in the SZ of the processed Al-based MMCs, can be summarized for each class in turn.

***Ex situ* MMCs** –These composites are locally reinforced by various kinds of ceramic nanoparticles *ex situ*, such as; SiC [630,631,697,718], Al_2O_3 [628,640,725-728], B_4C [729], SiO_2 [730,731], TiC [682], fullerene [637], CNTs [633,634,657,703,713,732,733], graphene [635,636,667,701], as well as other ceramics [606,610,660,670,672,681,690] to form the MMCs. In addition, a range of aluminum alloys have been used as the matrix, including AA1050 [573,574,629], AA2024 [665], AA3003 [734], AA5052 [735,736], AA5083 [637,737,738], AA6061 [663,664,670], AA6082 [660,676,677], and AA7075 alloys [682]. Most of the MMCs prepared by FSP have employed the plate with pre-placed powder fabrication strategy. The nanoparticles have a major role effect on the dynamic restoration phenomena during FSP [630,631,633-636]. They can refine the grain size in the SZ according to the PSN mechanism described in section 2, by increasing the number of nucleation sites for new grains. In theory, nanoparticles (with average size $<$100 nm) are too small to stimulate nucleation [739], but depending on the degree of clustering/aggregation they may act collectively.

After the nucleation of new grains, the nanoparticles can also hinder the rate of grain boundary migration by Zener pinning [27]. Fig. 47 illustrates the formation of fine, equiaxed grains inside the SZ caused by the SiC particles in the Al matrix having a misorientation range tending towards the random orientation distribution described by the MacKenzie curve.

By conducting the FSP while under submerged cooling media such as water (chilled to low temperatures), dry ice, and liquid nitrogen it is possible to further refine the grain structure [509,632]. After grain nucleation, the influence of both nanoparticles and rapid cooling restrict the subsequent rate of grain growth. If the primary dynamic restoration phenomenon is DRV, CDRX, or GDRX, the main effect of the cooling medium will be the generation of more cells and confining their coalescence. The result of liquid nitrogen cooling medium during submerged FSP is shown in Fig. 48. The grain structure of the aluminum matrix consists of nano-scale cellular structures (with an average size of ~50 nm) as a result of cryogenic cooling.

Another important microstructural aspect is the distribution of reinforcing particles within the aluminum matrix. In general, it is not possible to achieve a completely homogenous distribution of nanoparticles by FSP fabrication [660,662,666,682,688,690], where the severity of agglomeration and the degree of heterogeneity is dependent on the processing parameters, matrix chemistry, and nanoparticle type [324,623,740]. The formation of an onion ring pattern in the dispersion of nanoparticles has been broadly reported for most systems [666,673,685,696,701,704,717,718]. Further, the number of rings and their sizes determine the overall microstructure and crystallographic texture of the final product [107,631,728,741].

Recently, significant interest has focused on using carbon-based compounds as the reinforcing agents to produce Al-based MMCs [635,667,687,700,701,703,713,733,743,744]. In this context, single-walled (SWCNTs) and multi-walled carbon nanotubes (MWCNTs), fullerene (C60), and graphene nano-platelets (GNPs) have been employed as the reinforcing agents, considering their unique physical and mechanical characteristics [745-751]. However, despite the great potential for reinforcing the soft metal matrix, most of these carbon-based structures are not stable during frictional heating and intense plastic deformation typical of FSP. As a result, there is a high chance that they may decompose, leading to a change or deterioration of their initial structures, or reaction with the aluminum

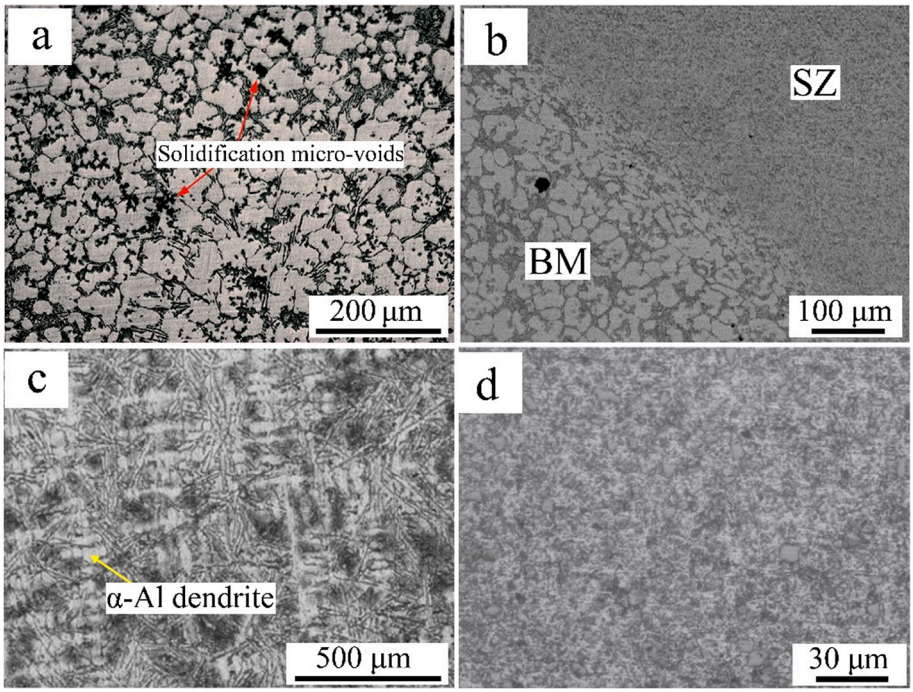

Fig. 46. Microstructure before (left) and after (right) FSP of a, and b) cast A356/Al_3Ti composite [621], and c, and d) cast A413/Al_3Ni *in situ* composite [608]. Reproduced with permission from Elsevier. All rights reserved.

Table 3
Grain size and operative dynamic restoration phenomena during FSP of different types of Al, Mg and Ti MMCs.

Strategy	System		Average grain size of BM	Average grain size of SZ	Restoration mechanisms	Refs.
	Base alloy	Reinforcement				
FSP of composites	AA5052	Al_2O_3	~25 μm	~0.94 μm	DRV/ DDRX	[628,629]
		SiC	~6.3 μm	~1.4 μm	DRV/ DDRX	[630,631]
		TiO_2	~49.4 μm	~2.9–0.05 μm	DRV/ DDRX	[107,632]
		MW-CNTs	~8.7 μm	~1.5 μm	DRV/ DDRX	[633,634]
		GNPs	~10.7 μm	~2.1 μm	DRV/ DDRX	[635,636]
	AA5083	Fullerene	~25.4 μm	~0.2 μm	DRV/ DDRX	[637]
	AA6061	Al_2O_3	~100 μm	~10 μm	DRV/ DDRX	[638]
	AA6082	Al_2O_3	~120 μm	~0.3 μm	DRV/ DDRX	[639,640]
	AA7075	TiN	~78 μm	~1.4 μm	DRV/ DDRX	[641]
	AZ31	SiC	~16.6 μm	~1.2 μm	DDRX	[642,643]
		Al_2O_3	~70 μm	~2.2 μm	DDRX	[644]
		n-HA	~54 μm	~2 μm	DDRX	[645,646]
	AZ61	SiO_2	~75 μm	~0.8 μm	DDRX	[647,648]
	AZ91	SiC	~150 μm	~7.2 μm	DDRX	[649,650]
	CP-Ti	*n*-HA	~100 μm	~1.4–14.8 μm	DDRX	[597,651]

matrix. Of course, this transformation may also create new products *in situ* such as the formation of aluminum carbide complex phases, which may act as reinforcing agents in some circumstances.

According to literature, the intensity of the crystalline texture depends on the type of reinforcing nanoparticles [107,631,634,636]. The preferred orientation can be modified considerably from the ideal shear component for FCC metals and alloys introduced in section 3. In the case of FSP Al-Mg/SiC MMC, the formation of Goss/Cubic and P1/P2 fiber components were reported [630,631]. For other Al-based MMCs containing MW-CNTs, GNPs, and TiO_2 nanoparticles, different texture components, such as orientations close to Cube, Brass, and silver components, respectively, have been reported [107,633-636,752]. These differences can be attributed to the differences in chemistry and aspect ratio of the inclusions, as well as their effects on the PSN and Zener-pinning mechanisms during DRX phenomena.

***In situ* MMCs** – Another interesting way of producing MMCs is to form the reinforcing particles *in situ* during FSP as a result of chemical reactions between the metal matrix and a second phase material [604,605,620,622,674,694,702,712,719,730,734,753-770]. In this context, metal oxide systems have attracted attention. Several *in situ* systems based on metallic oxides, including; TiO_2 [107,752,771-773], Fe_2O_3 [774], SiO_2 [730], CuO [702,766], and CeO_2 [755] have been examined as candidates for this means of

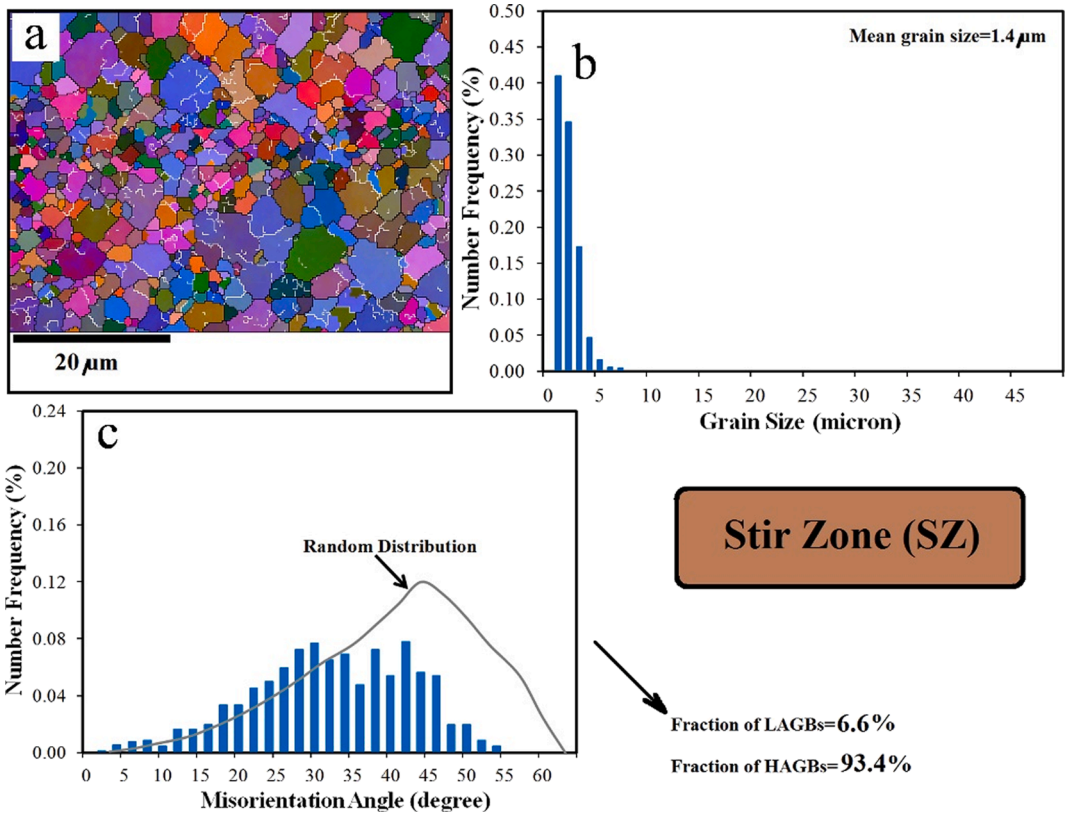

Fig. 47. EBSD analysis of an Al-SiC MMC processed by FSP in terms of (a) EBSD grain map, (b) grain size distribution, and (c) misorientation angle distribution histograms [630]. Reprinted with permission from Elsevier. All rights reserved.

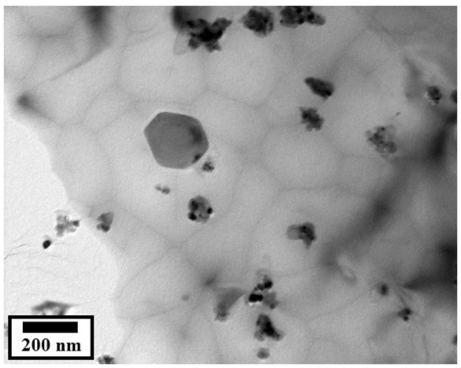

Fig. 48. TEM image showing the formation of a nano-scale cellular structure within the aluminum matrix of an Al-Mg/TiO_2 MMC as a result of FSP under cryogenic conditions [742]. Reproduced with permission from Elsevier. All rights reserved.

reactive FSP to promote *in situ* chemical reactions which enhance properties. In these systems, typically one new oxide phase and one aluminide phase is formed after the inserted phase is dissolved. Another alternative approach for *in situ* synthesis of Al-based MMCs is to insert an elemental powder mixture and promote solid-state reactions at the interfaces of these particles. For example, the addition of iron (Fe) [760], titanium (Ti) [694], nickel (Ni) [759,764], molybdenum (Mo) [761], and copper (Cu) [753,758] powders into the aluminum matrix will lead to the formation of Al_3Fe, Al_3Ti, Al_3Ni, and Al_2Cu aluminide particles by the reaction with the Al matrix.

In the case of the Al-Mg/TiO_2 system for instance, the occurrence of *in situ* solid-state reactions between the Al-Mg matrix and TiO_2 nanoparticles can result in the formation of nano-scale magnesium oxide (MgO) and titanium aluminide (Al_3Ti) phases [107,632,695,735,752,771-773]. The EBSD grain structural maps in Fig. 49 [107,771] show how by increasing the volume fraction of TiO_2 nanoparticles from 2% to 6%, the grain structure of the SZ is continuously refined down to an average size below 2 μm. This is caused by PSN and Zener pinning arising from the influence of nanoparticles on these dynamic restoration phenomena.

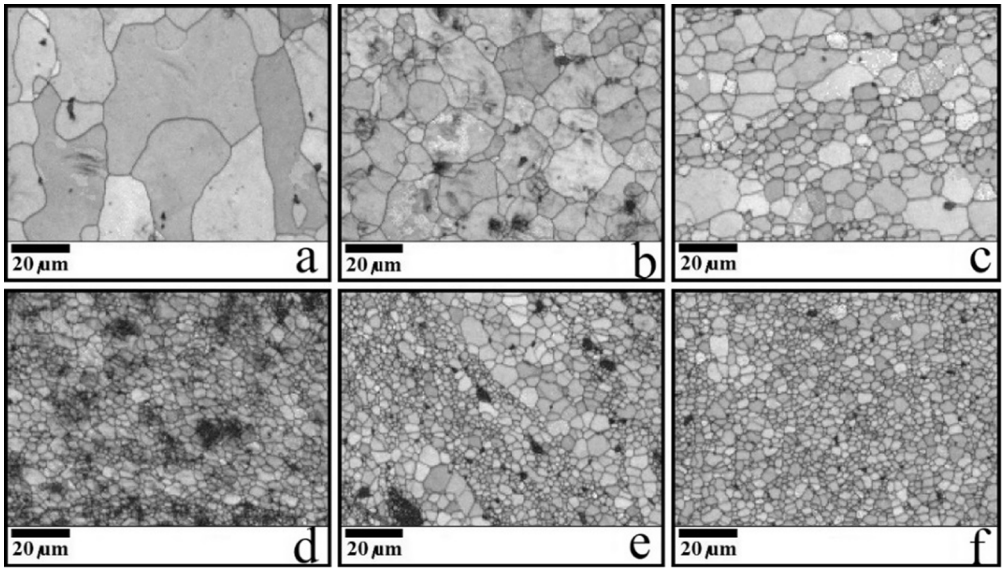

Fig. 49. Microstructure revealed by EBSD for the unreinforced alloy (a) before and (b) after FSP, compared to FSP *in situ* MMCs containing (c) 2 vol %, (d) 3 vol%, (e) 5 vol%, and (f) 6 vol% TiO_2 as the initial reinforcing agent [771]. Reprinted with permission from Elsevier. All rights reserved.

Hybrid MMCs – Hybrid systems incorporate mixtures of different reinforcing nanoparticles to combine the unique characteristics of different phases. FSP has been used to fabricate different hybrid systems containing combinations of several compounds such as; SiC-Al_2O_3 [706], TiC-B_4C [711], Al_2O_3-TiB_2 [775,776], B_4C-TiB_2 [777], $ZrSiO_4$-Al_2O_3 [778] as the reinforcing phases in an aluminum matrix. Combining two types of reinforcement, such as Al_2O_3 together with CNTs, or cerium oxide with CNTs can lead to higher strengthening than either of the particles alone, suggesting some possible interaction when multiple phases are present. The particular ratio of the two reinforcing phases also affects the properties achieved [743,779]. The microstructure of a hybrid nanocomposite fabricated by FSP material containing both Al_2O_3 and SiC nanoparticles is shown across multiple scales in Fig. 50. An equiaxed grain structure with an average size of ~1 μm is obtained, which is finer than the single-phase nanocomposite systems. A higher fraction of low-angle grain boundaries (LAGBs) is a result of more dislocation pile-up around the nanoparticles in the hybrid system versus the single particle system. In some cases, the two types of particles are selected for different purposes, for example one as a reinforcing phase, while other to improve other surface properties [708,709,780-782]. For instance, SiC [706,708,709,780] or Al_2O_3 [708,709,781] nanoparticles can be used as the reinforcing agent while graphite [706,708,709,780] or graphene [783] can be employed as the secondary agent to act as a lubricant.

6.3.2. *Magnesium based MMCs*

The incorporation of reinforcing nanoparticles by FSP into magnesium alloys has focused mainly on single-phase nanocomposites [605,624,646,673,694,784-807]. Reinforcing nanoparticles such as Al_2O_3 [787], SiC [798,799,802,803], TiC [790], SiO_2 [801], MW-CNTs [791,792] can locally strengthen the magnesium alloy matrix improving mechanical performance. Generally, the nanoparticles confer enhanced grain refinement in a similar manner to that observed in Al MMCS. Hydroxyapatite (HA) reinforcements have also been incorporated into bio-compatible Mg alloys as a secondary phase for medical implant applications [646,786,796]. Despite the fact that mechanical properties are not enhanced because the particles not bond well with the magnesium matrix, such near surface composites are very promising for biomedical applications due to the unique biodegradability and biocompatibility [624].

Fig. 51 shows boron nitride (BN) and HA nanoparticles incorporated in a magnesium alloy. Since magnesium has a hexagonal close-packed (HCP) structure with few active slip systems and a lower stacking fault energy (SFE), the effect of the severe plastic deformation arising from the tool is quite different compared to aluminum based composites. These induce DDRX (nucleation and growth) during FSP with the second phase activating PSN and Zener-pinning mechanisms thereby intensifying grain refinement.

6.3.3. *Titanium based MMCs*

Few reports are available regarding the production of titanium-based MMCs by FSP [597,651,741,809-813]. In preliminary work, Khodabakhshi *et al.* [597,651] incorporated hydroxyapatite (HA) particles into the surface of titanium during FSP for biomedical applications. Shafiei-Zarghani *et al.* [741,811] has focused on near-surface strengthening of commercial purity titanium (CP-Ti) by the addition of Al_2O_3 nanoparticles. As described earlier, the temperature required for the α to β phase transformation in pure titanium is around 882 °C [597] which is usually exceeded in the SZ during FSP treatment. Consequently, the grain refinement is influenced by nucleation of the β phase inside the α grains during FSP, along with heating and deformation of these grains during DRX. Moreover, some degree of β phase can remain in the structure during the reverse phase transformation upon cooling, which can be inferred from the shape of retained laths. The second phase inclusions such as Al_2O_3, SiC, and HA can act as preferred sites for nucleation of new β

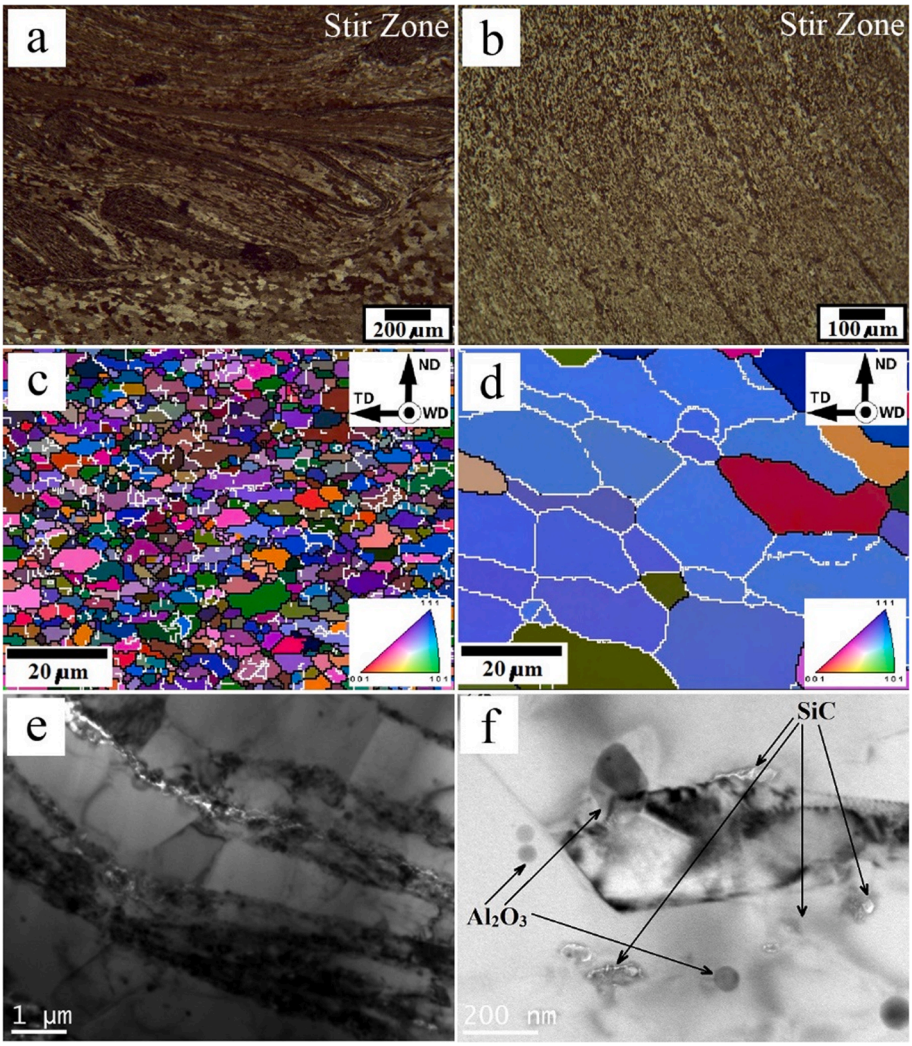

Fig. 50. Formation of a fine and equiaxed grain structure inside the SZ of FSP Al-Al_2O_3-SiC hybrid MMC; (a, b) optical, (c, d) EBSD mapping and (e, f) TEM images highlighting the simultaneous incorporation of Al_2O_3 and SiC nanoparticles into the Al matrix [574,629]. Reproduced with permission from Elsevier and Taylor & Francis. All rights reserved.

phase during FSP as well as enhancing the nucleation of new grains during DRX, and subsequently hinder grain growth by grain boundary pinning. The promotion of PSN and Zener-pinning mechanisms lead to a microstructure which tends to be randomly oriented, fine-grained, and equiaxed [597,651]. However, further below the surface layer but still within the SZ, a decreasing number of reinforcing nanoparticles are present and the role of the α to β phase transformation can be more significant, such that the microstructure changes toward a lath shape with enlarged grains.

6.3.4. Copper based MMCs

Copper-based MMCs prepared by FSP have garnered attention because of their potential for surface reinforcement for electrical applications [614,673,678,814-823], especially at high temperatures. As mentioned in section 4, twinning is a significant plastic deformation mechanism in copper and its alloys, due to the low SFE. This subsequently leads to reduced simultaneous activation of independent slip systems. However, during the high-temperature severe plastic deformation process in FSP, twinning can be restricted. Fig. 52 shows that for Cu- rice husk ash (RHA) composite that while there are annealing twins in the Cu substrate, the FSP refines the microstructure leading to equiaxed grains in the SZ free of micro-twins. It is worth noting that as a low SFE metal, dynamic restoration mechanisms such as DRV and CDRX are expected to be limited as discussed in section 4.2. As a result grain refinement in the SZ is usually by DDRX with grains refined to the submicron range [678,824].

6.3.5. Other MMCs

Only a few reports can be found in the literature relating to nickel-based [825,826] and steel-based MMCs [599,827,828], the main

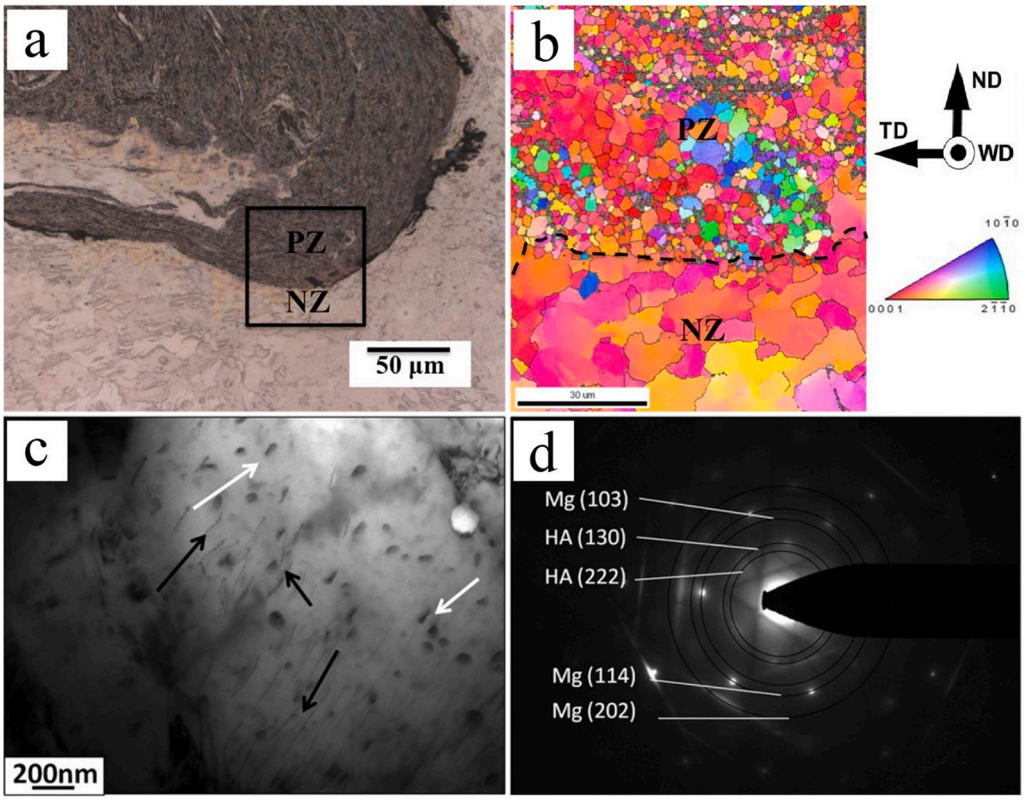

Fig. 51. Microstructural features of a Mg-based MMCs processed by FSP: (a) optical micrograph and (b) EBSD map for the SZ of AZ31-BN MMC [794], (c) TEM image and (d) SAD pattern for HA nanoparticles dispersed in a pure magnesium matrix in the SZ [808]. PZ and NZ refer to particle agglomerated zone and normal SZ, respectively. Reproduced with permission from Elsevier. All rights reserved.

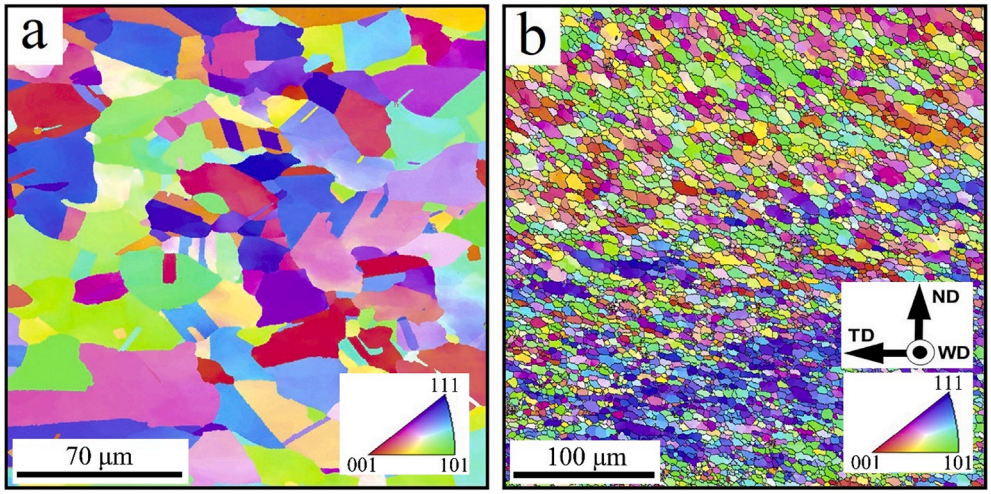

Fig. 52. EBSD maps of the grain structures for (a) the copper substrate and (b) the SZ of FSP prepared Cu-RHA MMC [824]. Reproduced with permission from Elsevier. All rights reserved.

feature being the refined grain structure of the SZ due to the incorporation of secondary phases by FSP. More detailed microstructural studies using EBSD and TEM analyses are required to reveal the distinct mechanisms of microstructural evolution. Since (low SFE) nickel does not undergo any solid-state phase transformation, microstructural refinement during the FSP process should be dynamic recrystallization via nucleation and growth with the nanoparticles stimulating the nucleation of new grains and hindering their growth by Zener pinning. For steel-based MMCs, the situation is complicated by the transformation of austenite and ferrite phases. The

potential for eutectoid phase transformation occurring during solid-state processing by FSP means the microstructures will depend significantly on the steel matrix alloy and processing parameters, which determine the cooling rate. If the peak temperature inside the SZ during FSP exceeds the eutectoid phase transition temperature, processing occurs in the solid-state within the austenite regime. It should also be bourne in mind that for some steels, it is possible to reach a state of considerable hard-facing using a simple heat treatment, and the incorporation of reinforcing nanoparticles in those cases may not be a sensible option.

7. Conclusions and outlook

The unique combination of very large strains, high temperatures and high strain rates inherent to FSW/P and their dependency on the processing parameters provides an opportunity to tailor the microstructure and hence the performance of welds and surfaces. In this review article, the current understanding of the relationship between processing conditions and microstructure has been considered for single phase, multiphase and dissimilar materials.

The evolution of grain structure during FSW/P is a complex process often involving several stages and several mechanisms including continuous recrystallization and discontinuous recrystallization. The principal mechanisms depend primarily on crystal structure and stacking fault energy (SFE). Specifically, the microstructural evolution of cubic metals with relatively high SFE is usually dominated by continuous recrystallization. In contrast, in FCC metals with low SFE, discontinuous recrystallization usually plays a primary role. In FCC materials of intermediate SFE, a transition from the continuous to discontinuous mechanism is observed with increased welding temperature. In hexagonal alloys, the microstructure evolution is strongly influenced by crystallographic texture. Specifically, the formation of a very sharp texture in the SZ may result in partial grain convergence.

The extreme thermomechanical excursions mean that materials containing second-phase precipitates normally undergo complex precipitation phenomena. In regions exposed to relatively low temperatures, coarsening and/or transition to more stable phases occurs. This can increase the strength if the initial temper is not aged, or lead to a reduction in strength when the material is initially at peak strength. In areas experiencing high temperatures, precipitates progressively dissolve together with their coarsening. Depending on the subsequent cooling rate, the dissolved solute may form new precipitates. Since the welded material normally contains a high density of crystal defects (i.e., dislocations, subgrain- and grain boundaries) as well as surviving second-phase particles, this new precipitation often develops in a heterogeneous manner.

FSW of dissimilar materials is of particular interest; many are either impossible or very difficult to weld by conventional fusion welding processes, particularly those having very different physical, chemical and mechanical properties or those in which brittle intermetallic phases form within the weld region. The main difficulties in FSW of dissimilar alloys with different properties is the lack of inhomogeneous mixing of materials and the formation of intermetallics in the joint area. Inhomogeneous mixing occurs due to the insufficient heat input and thus low plasticity of the materials to be welded. On the other hand, the reason for the formation of intermetallics is the high heat input applied to the material during welding. Measures such as external cooling can be employed to keep the heat input low. Thus, the joining of dissimilar materials is a very challenging task. The studies conducted on FSW of dissimilar materials to date have, however, shown that this joining technique can successfully be used for achieving defect-free joints with good properties between numerous dissimilar alloy combinations.

Generally, FSW offers distinct advantages over conventional fusion welding in terms of the materials that can be welded and the degree of microstructural control that can be exercised. As designs become more optimized for weight or performance there is an increasing need to weld dissimilar materials. We are likely to see increasing use of FSW to achieve hybrid structures involving multiple metals and alloys traditionally thought of as difficult or impossible to join. Much work needs to be done to optimize bond strength and the minimization of potentially harmful intermetallic reaction products.

The phase transformations occurring during/after FSW/P of titanium alloys and steels are influenced by the large deformations experienced by the high-temperature phase. Specifically, a significant grain refinement as well as a formation of a sharp simple-shear texture in the high-temperature phase often results in a pronounced variant selection during the subsequent phase transformation, which, in turn, gives rise to a transformation texture in the low-temperature phase. Moreover, the formation of a developed substructure in the high-temperature phase leads to local deviation from a characteristic orientation relationship between the phases.

In addition, FSP provides an opportunity to locally refine and homogenize the microstructure as well as to introduce nanoparticles into the near surface region to form metal matrix composites (MMCs). Here, the nanoparticles typically activate the particle stimulated nucleation (PSN) recrystallization mechanism and subsequently to pronounced Zener-pinning leading to an ultrafine-grained structure. FSP is perhaps underutilized at present as a means of surface treatment. Looking forwards, it is likely that a more diverse range of materials with locally tailored properties will be developed by combining new and existing alloys and ceramics to create materials having a diverse range of multi-functionalised surfaces.

In summary, significant progress in the understanding of the basic microstructural mechanisms of FSW/P has been achieved over the last two decades. This opens up new opportunities for a precise control of the final service properties of the welded/processed materials. Future progress in the field of FSW will be dependent on a continued exploration of the fundamental aspects underpining the key processing-microstructure-property relationships.

Declaration of Competing Interest

The authors declare that they have no known competing financial interests or personal relationships that could have appeared to influence the work reported in this paper.

Acknowledgments

A. Heidarzadeh would like to thank Mr. Amin Radi for his great help in preparing the images and schematics. A. Simar acknowledges the financial support of the European Research Council (ERC) for the Starting Grant ALUFIX project (grant agreement no. 716678). Philip J. Withers acknowledges a European Research Council advanced grant Correl-CT No. 695638 and acknowledges the support of the Henry Royce Institute for Advanced Materials, established through EPSRC grants EP/ R00661X/1, EP/P025498/1 and EP/P025021/1. S. Mironov would like to thank the Russian Science Foundation (grant No. 1949-02001) for financial support.

References

[1] Nandan R, DebRoy T, Bhadeshia HKDH. Recent advances in friction-stir welding–process, weldment structure and properties. Prog Mater Sci 2008;53:980–1023.
[2] Mishra RS, Ma ZY. Friction stir welding and processing. Mater Sci Eng: R: Reports 2005;50:1–78.
[3] Amini A, Asadi P, Zolghadr P. Friction stir welding applications in industry. Advances in friction stir welding and processing. Woodhead Publishing; 2014.
[4] Ronneteg U. Friction stir welding of copper and its NDT - From novelty to highly-developed! 12th European Conference on Non-Destructive Testing (ECNDT 2018). Gothenburg; 2018. p. 1–8.
[5] Murray DL. Friction stir processing of nickel-aluminum propeller bronze in comparison to fusion welds: Naval Postgraduate School; 2005.
[6] Gangwar K, Ramulu M. Friction stir welding of titanium alloys: A review. Mater Des 2018;141:230–55.
[7] Liu FC, Hovanski Y, Miles MP, Sorensen CD, Nelson TW. A review of friction stir welding of steels: Tool, material flow, microstructure, and properties. J Mater Sci Technol 2018;34:39–57.
[8] Padhy GK, Wu CS, Gao S. Friction stir based welding and processing technologies - processes, parameters, microstructures and applications: A review. J Mater Sci Technol 2018;34:1–38.
[9] Salih OS, Ou H, Sun W, McCartney DG. A review of friction stir welding of aluminium matrix composites. Mater Des 2015;86:61–71.
[10] Threadgilll PL, Leonard AJ, Shercliff HR, Withers PJ. Friction stir welding of aluminium alloys. Int Mater Rev 2009;54:49–93.
[11] Yang XW, Fu T, Li WY. Friction stir spot welding: A review on joint macro- and microstructure, property, and process modelling. Adv Mater Sci Eng 2014;2014.
[12] Çam G, İpekoğlu G. Recent developments in joining of aluminum alloys. Int J Adv Manuf Technol 2017;91:1851–66.
[13] Kashaev N, Ventzke V, Çam G. Prospects of laser beam welding and friction stir welding processes for aluminum airframe structural applications. J Manuf Processes 2018;36:571–600.
[14] Çam G, Mistikoglu S. Recent Developments in Friction Stir Welding of Al-alloys. J Mater Eng Perform 2014;23:1936–53.
[15] Meng X, Huang Y, Cao J, Shen J, dos Santos JF. Recent progress on control strategies for inherent issues in friction stir welding. Prog Mater Sci 2021;115:100706.
[16] Ma ZY. Friction Stir Processing Technology: A Review. Metall Mater Trans A 2008;39:642–58.
[17] He X, Gu F, Ball A. A review of numerical analysis of friction stir welding. Prog Mater Sci 2014;65:1–66.
[18] Jain R, Pal SK, Singh SB. A study on the variation of forces and temperature in a friction stir welding process: a finite element approach. J Manuf Processes 2016;23:278–86.
[19] Ahmad B, Galloway A, Toumpis A. Advanced numerical modelling of friction stir welded low alloy steel. J Manuf Processes 2018;34:625–36.
[20] Chen G-q, Shi Q-y, Li Y-j, Sun Y-j, Dai Q-l, Jia J-y, et al. Computational fluid dynamics studies on heat generation during friction stir welding of aluminum alloy. Comput Mater Sci 2013;79:540–6.
[21] Prakash P, Jha SK, Lal SP. Numerical investigation of stirred zone shape and its effect on mechanical properties in friction stir welding process. Welding World 2019;63:1531–46.
[22] Chen K, Liu X, Ni J. A review of friction stir–based processes for joining dissimilar materials. Int J Adv Manuf Technol 2019;1–23.
[23] Kadian AK, Biswas P. The study of material flow behaviour in dissimilar material FSW of AA6061 and Cu-B370 alloys plates. J Manuf Processes 2018;34:96–105.
[24] Su H, Wu CS, Pittner A, Rethmeier M. Thermal energy generation and distribution in friction stir welding of aluminum alloys. Energy 2014;77:720–31.
[25] Humphreys FJ, Hatherly M. Recrystallization and related phenomena. Elsevier; 2004.
[26] Kassner ME, Pérez-Prado MT. Five-power-law creep in single phase metals and alloys. Prog Mater Sci 2000;45:1–102.
[27] Sakai T, Belyakov A, Kaibyshev R, Miura H, Jonas JJ. Dynamic and post-dynamic recrystallization under hot, cold and severe plastic deformation conditions. Prog Mater Sci 2014;60:130–207.
[28] Cotterill P, Mould PR. Recrystallization and grain growth in metals. Krieger Pub Co; 1976.
[29] Rios PR, Siciliano Jr F, Sandim HRZ, Plaut RL, Padilha AF. Nucleation and growth during recrystallization. Mater Res 2005;8:225–38.
[30] Burke JE, Turnbull D. Recrystallization and grain growth. Prog Metal Phys 1952;3:220–92.
[31] Hughes DA, Hansen N, Bammann DJ. Geometrically necessary boundaries, incidental dislocation boundaries and geometrically necessary dislocations. Scr Mater 2003;48:147–53.
[32] Bailey JE. Electron microscopy and strength of crystals. Electron Microscope observations on recovery and recrystallization process in cold worked metals", ed Thomas G, Washburn J, New York, Interscience; 1963. p. 535–64.
[33] Hu H. Recrystallization by subgrain coalescence. Electron Microscopy Strength Cryst 1963:564.
[34] Mironov S, Sato YS, Kokawa H. Microstructural evolution during friction stir-processing of pure iron. Acta Mater 2008;56:2602–14.
[35] Mironov S, Sato YS, Kokawa H. Development of grain structure during friction stir welding of pure titanium. Acta Mater 2009;57:4519–28.
[36] Prangnell PB, Heason CP. Grain structure formation during friction stir welding observed by the 'stop action technique'. Acta Mater 2005;53:3179–92.
[37] Liu H, Fujii H. Microstructural and mechanical properties of a beta-type titanium alloy joint fabricated by friction stir welding. Mater Sci Eng, A 2018;711:140–8.
[38] Heidarzadeh A, Saeid T, Klemm V, Chabok A, Pei Y. Effect of stacking fault energy on the restoration mechanisms and mechanical properties of friction stir welded copper alloys. Mater Des 2019;162:185–97.
[39] Ponge D, Gottstein G. Necklace formation during dynamic recrystallization: mechanisms and impact on flow behavior. Acta Mater 1998;46:69–80.
[40] Montheillet F, Lurdos O, Damamme G. A grain scale approach for modeling steady-state discontinuous dynamic recrystallization. Acta Mater 2009;57:1602–12.
[41] Belyakov A, Miura H, Sakai T. Dynamic recrystallization under warm deformation of polycrystalline copper. ISIJ Int 1998;38:595–601.
[42] Huang K, Logé RE. A review of dynamic recrystallization phenomena in metallic materials. Mater Des 2016;111:548–74.
[43] Tikhonova M, Kaibyshev R, Belyakov A. Microstructure and mechanical properties of austenitic stainless steels after dynamic and post-dynamic recrystallization treatment. Adv Eng Mater 2018;20:1700960.
[44] Gourdet S, Montheillet F. A model of continuous dynamic recrystallization. Acta Mater 2003;51:2685–99.
[45] Kaibyshev R, Shipilova K, Musin F, Motohashi Y. Continuous dynamic recrystallization in an Al–Li–Mg–Sc alloy during equal-channel angular extrusion. Mater Sci Eng, A 2005;396:341–51.
[46] Dudova N, Belyakov A, Sakai T, Kaibyshev R. Dynamic recrystallization mechanisms operating in a Ni–20% Cr alloy under hot-to-warm working. Acta Mater 2010;58:3624–32.

[47] Malopheyev S, Kulitskiy V, Gazizov M, Kaibyshev R. Mechanism of grain refinement during equal-channel angular pressing in an Al-Mg-Sc alloy. Rev Adv Mater Sci 2016;47.
[48] Belyakov A, Miura H, Sakai T. Dynamic recrystallization under warm deformation of a 304 type austenitic stainless steel. Mater Sci Eng, A 1998;255:139–47.
[49] Kaibyshev OA. Superplasticity of alloys intermetallides and ceramics. Springer Science & Business Media; 2012.
[50] Yuzbekova D, Mogucheva A, Kaibyshev R. Superplasticity of ultrafine-grained Al–Mg–Sc–Zr alloy. Mater Sci Eng, A 2016;675:228–42.
[51] Kaibyshev R, Goloborodko A, Musin F, Nikulin I, Sakai T. The role of grain boundary sliding in microstructural evolution during superplastic deformation of a 7055 aluminum alloy. Mater Trans 2002;43:2408–14.
[52] Kaibyshev R, Sitdikov O, Goloborodko A, Sakai T. Grain refinement in as-cast 7475 aluminum alloy under hot deformation. Mater Sci Eng, A 2003;344:348–56.
[53] Tikhonova M, Belyakov A, Kaibyshev R. Strain-induced grain evolution in an austenitic stainless steel under warm multiple forging. Mater Sci Eng, A 2013;564:413–22.
[54] Gazizov M, Malopheyev S, Kaibyshev R. The effect of second-phase particles on grain refinement during equal-channel angular pressing in an Al–Cu–Mg–Ag alloy. J Mater Sci 2015;50:990–1005.
[55] McQueen HJ, Solberg JK, Ryum N, Nes E. Evolution of flow stress in aluminium during ultra-high straining at elevated temperatures. Part II Philos Mag A 1989;60:473–85.
[56] Solberg JK, McQueen HJ, Ryum N, Nes E. Influence of ultra-high strains at elevated temperatures on the microstructure of aluminium. Part I Philos Mag A 1989;60:447–71.
[57] Barnett MR, Montheillet F. The generation of new high-angle boundaries in aluminium during hot torsion. Acta Mater 2002;50:2285–96.
[58] Gholinia A, Humphreys FJ, Prangnell PB. Production of ultra-fine grain microstructures in Al–Mg alloys by coventional rolling. Acta Mater 2002;50:4461–76.
[59] Ferry M, Humphreys FJ. The deformation and recrystallization of particle-containing {011}<100> aluminium crystals. Acta Mater 1996;44:3089–103.
[60] Xu N, Song Q, Bao Y. Investigation on microstructure development and mechanical properties of large-load and low-speed friction stir welded Cu-30Zn brass joint. Mater Sci Eng, A 2018;726:169–78.
[61] Cabibbo M, McQueen HJ, Evangelista E, Spigarelli S, Di Paola M, Falchero A. Microstructure and mechanical property studies of AA6056 friction stir welded plate. Mater Sci Eng, A 2007;460:86–94.
[62] Yi D, Mironov S, Sato YS, Kokawa H. Effect of cooling rate on microstructure of friction-stir welded AA1100 aluminum alloy. Phil Mag 2016;96:1965–77.
[63] Zeng XH, Xue P, Wu LH, Ni DR, Xiao BL, Wang KS, et al. Microstructural evolution of aluminum alloy during friction stir welding under different tool rotation rates and cooling conditions. J Mater Sci Technol 2019;35:972–81.
[64] Yazdipour A, Dehghani K. Modeling the microstructural evolution and effect of cooling rate on the nanograins formed during the friction stir processing of Al5083. Mater Sci Eng, A 2009;527:192–7.
[65] Sakai T, Ohashi M, Chiba K, Jonas JJ. Recovery and recrystallization of polycrystalline nickel after hot working. Acta Metall 1988;36:1781–90.
[66] Field DP, Nelson TW, Hovanski Y, Jata KV. Heterogeneity of crystallographic texture in friction stir welds of aluminum. Metall Mater Trans A 2001;32:2869–77.
[67] Schneider JA, Nunes AC. Characterization of plastic flow and resulting microtextures in a friction stir weld. Metall Mater Trans B 2004;35:777–83.
[68] Fonda RW, Knipling KE. Texture development in friction stir welds. Sci Technol Weld Joining 2011;16:288–94.
[69] Field DP, Nelson TW. Tool geometry dependence of local texture in friction stir welds of 7050 aluminum plate. Materials Science Forum. Trans Tech Publ; 2002. p. 1507–12.
[70] Zhang J, Upadhyay P, Hovanski Y, Field DP. High-speed friction stir welding of AA7075-T6 sheet: microstructure, mechanical properties, micro-texture, and thermal history. Metall Mater Trans A 2018;49:210–22.
[71] Canova GR, Kocks UF, Jonas JJ. Theory of torsion texture development. Acta Metall 1984;32:211–26.
[72] Bunge H-J. Texture analysis in materials science: mathematical methods. Elsevier; 2013.
[73] Kocks UF, Tomé CN, Wenk H-R. Texture and anisotropy: preferred orientations in polycrystals and their effect on materials properties. Cambridge University Press; 1998.
[74] Beausir B, Tóth LS, Neale KW. Ideal orientations and persistence characteristics of hexagonal close packed crystals in simple shear. Acta Mater 2007;55:2695–705.
[75] Kurdjumow G, Sachs G. Über den Mechanismus der Stahlhärtung. Zeitschrift für Physik 1930;64:325–43.
[76] Nishiyama Z. X-ray investigation of the mechanism of the transformation from face centered cubic lattice to body centered cubic. Sci Rep Tohoku Univ 1934;23:637.
[77] Wassermann G. Ueber den Mechanismus der [alpha]-[gamma]-Umwandlung des Eisens. Verlag Stahleisen 1935.
[78] Fonda RW, Bingert JF, Colligan KJ. Development of grain structure during friction stir welding. Scr Mater 2004;51:243–8.
[79] Su J-Q, Nelson TW, Sterling CJ. Microstructure evolution during FSW/FSP of high strength aluminum alloys. Mater Sci Eng, A 2005;405:277–86.
[80] Suhuddin UFHR, Mironov S, Sato YS, Kokawa H. Grain structure and texture evolution during friction stir welding of thin 6016 aluminum alloy sheets. Mater Sci Eng, A 2010;527:1962–9.
[81] Gao C, Zhu Z, Han J, Li H. Correlation of microstructure and mechanical properties in friction stir welded 2198–T8 Al–Li alloy. Mater Sci Eng, A 2015;639:489–99.
[82] Fonda RW, Bingert JF. Texture variations in an aluminum friction stir weld. Scr Mater 2007;57:1052–5.
[83] Jin H, Saimoto S, Ball M, Threadgill PL. Characterisation of microstructure and texture in friction stir welded joints of 5754 and 5182 aluminium alloy sheets. Mater Sci Technol 2001;17:1605–14.
[84] Park SHC, Sato YS, Kokawa H. Basal plane texture and flow pattern in friction stir weld of a magnesium alloy. Metall Mater Trans A 2003;34:987–94.
[85] Woo W, Choo H, Brown DW, Liaw PK, Feng Z. Texture variation and its influence on the tensile behavior of a friction-stir processed magnesium alloy. Scr Mater 2006;54:1859–64.
[86] Woo W, Choo H, Prime MB, Feng Z, Clausen B. Microstructure, texture and residual stress in a friction-stir-processed AZ31B magnesium alloy. Acta Mater 2008;56:1701–11.
[87] Mironov S, Onuma T, Sato YS, Kokawa H. Microstructure evolution during friction-stir welding of AZ31 magnesium alloy. Acta Mater 2015;100:301–12.
[88] Liu D, Tang Y, Shen M, Hu Y, Zhao L. Analysis of Weak Zones in Friction Stir Welded Magnesium Alloys from the Viewpoint of Local Texture: A Short Review. Metals 2018;8:970.
[89] Feng AH, Ma ZY. Microstructural evolution of cast Mg–Al–Zn during friction stir processing and subsequent aging. Acta Mater 2009;57:4248–60.
[90] Yuan W, Panigrahi SK, Su J-Q, Mishra RS. Influence of grain size and texture on Hall-Petch relationship for a magnesium alloy. Scr Mater 2011;65:994–7.
[91] Pilchak AL, Tang W, Sahiner H, Reynolds AP, Williams JC. Microstructure evolution during friction stir welding of mill-annealed Ti-6Al-4V. Metall Mater Trans A 2011;42:745–62.
[92] Reynolds AP, Hood E, Tang W. Texture in friction stir welds of Timetal 21S. Scr Mater 2005;52:491–4.
[93] Ramirez AJ, Juhas MC. Microstructural evolution in Ti-6Al-4V friction stir welds. Materials Science Forum: Trans Tech Publications Ltd, Zurich-Uetikon, Switzerland 2003:2999–3004.
[94] Davies PS, Wynne BP, Rainforth WM, Thomas MJ, Threadgill PL. Development of microstructure and crystallographic texture during stationary shoulder friction stir welding of Ti-6Al-4V. Metall Mater Trans A 2011;42:2278–89.
[95] Knipling KE, Fonda RW. Texture development in the stir zone of near-α titanium friction stir welds. Scr Mater 2009;60:1097–100.
[96] Sato YS, Nelson TW, Sterling CJ. Recrystallization in type 304L stainless steel during friction stirring. Acta Mater 2005;53:637–45.
[97] Cho J-H, Boyce DE, Dawson PR. Modeling strain hardening and texture evolution in friction stir welding of stainless steel. Mater Sci Eng, A 2005;398:146–63.
[98] Young J, Field D, Nelson T. Material flow during friction stir welding of HSLA 65 steel. Metall Mater Trans A 2013;44:3167–75.

[99] Cho H-H, Hong S-T, Roh J-H, Choi H-S, Kang SH, Steel RJ, et al. Three-dimensional numerical and experimental investigation on friction stir welding processes of ferritic stainless steel. Acta Mater 2013;61:2649–61.
[100] Saeid T, Abdollah-Zadeh A, Shibayanagi T, Ikeuchi K, Assadi H. On the formation of grain structure during friction stir welding of duplex stainless steel. Mater Sci Eng, A 2010;527:6484–8.
[101] Mathon MH, Klosek V, De Carlan Y, Forest L. Study of PM2000 microstructure evolution following FSW process. J Nucl Mater 2009;386:475–8.
[102] Mironov S, Inagaki K, Sato YS, Kokawa H. Microstructural evolution of pure copper during friction-stir welding. Phil Mag 2015;95:367–81.
[103] Xu N, Ueji R, Fujii H. Dynamic and static change of grain size and texture of copper during friction stir welding. J Mater Process Technol 2016;232:90–9.
[104] Oh-Ishi K, Zhilyaev AP, McNelley TR. A microtexture investigation of recrystallization during friction stir processing of as-cast NiAl bronze. Metall Mater Trans A 2006;37:2239–51.
[105] Heidarzadeh A, Chabok A, Taherzadeh Mousavian R, Pei Y. High-resolution EBSD characterisation of friction stir welded nickel–copper alloy: effect of the initial microstructure on microstructural evolution and mechanical properties. Phil Mag 2019;1–16.
[106] Root JM, Field DP, Nelson TW. Crystallographic texture in the friction-stir-welded metal matrix composite Al6061 with 10 Vol Pct Al2O3. Metall Mater Trans A 2009;40:2109–14.
[107] Khodabakhshi F, Simchi A, Kokabi AH, Nosko M, Simančík F, Švec P. Microstructure and texture development during friction stir processing of Al–Mg alloy sheets with TiO2 nanoparticles. Mater Sci Eng, A 2014;605:108–18.
[108] Patterson EE, Hovanski Y, Field DP. Microstructural characterization of friction stir welded aluminum-steel joints. Metall Mater Trans A 2016;47:2815–29.
[109] Yu H, Hovanski Y, Field D. Observation of Local Texture in Friction Stir Welding of Mg Alloy AZ31B to Steel. Microsc Microanal 2011;17:418–9.
[110] Texier D, Zedan Y, Amoros T, Feulvarch E, Stinville JC, Bocher P. Near-surface mechanical heterogeneities in a dissimilar aluminum alloys friction stir welded joint. Mater Des 2016;108:217–29.
[111] Rahimi S, Konkova TN, Violatos I, Baker TN. Evolution of microstructure and crystallographic texture during dissimilar friction stir welding of duplex stainless steel to low carbon-manganese structural steel. Metall Mater Trans A 2019;50:664–87.
[112] Çam G. Friction stir welded structural materials: beyond Al-alloys. Int Mater Rev 2011;56:1–48.
[113] Tóth LS, Neale KW, Jonas JJ. Stress response and persistence characteristics of the ideal orientations of shear textures. Acta Metall 1989;37:2197–210.
[114] Li S, Beyerlein IJ, Bourke MAM. Texture formation during equal channel angular extrusion of fcc and bcc materials: comparison with simple shear. Mater Sci Eng, A 2005;394:66–77.
[115] Baczynski J, Jonas JJ. Texture development during the torsion testing of α-iron and two IF steels. Acta Mater 1996;44:4273–88.
[116] Li S. Orientation stability in equal channel angular extrusion. Part II: Hexagonal close-packed materials. Acta Mater 2008;56:1031–43.
[117] Young JP. The production of fine grained magnesium alloys through thermomechanical processing for the optimization of microstructural and mechanical properties. Washington State University; 2015.
[118] Mironov S, Inagaki K, Sato YS, Kokawa H. Effect of welding temperature on microstructure of friction-stir welded aluminum alloy 1050. Metall Mater Trans A 2015;46:783–90.
[119] Colligan K. Material flow behavior during friction welding of aluminum. Weld J 1999;75:229s–37s.
[120] Rhodes CG, Mahoney MW, Bingel WH, Calabrese M. Fine-grain evolution in friction-stir processed 7050 aluminum. Scr Mater 2003;48:1451–5.
[121] Su J-Q, Nelson TW, McNelley TR, Mishra RS. Development of nanocrystalline structure in Cu during friction stir processing (FSP). Mater Sci Eng, A 2011;528:5458–64.
[122] Xu N, Ueji R, Fujii H. Enhanced mechanical properties of 70/30 brass joint by rapid cooling friction stir welding. Mater Sci Eng, A 2014;610:132–8.
[123] Xu N, Ueji R, Morisada Y, Fujii H. Modification of mechanical properties of friction stir welded Cu joint by additional liquid CO2 cooling. Materials & Design (1980–2015) 2014;56:20–5.
[124] Liu XC, Sun YF, Fujii H. Clarification of microstructure evolution of aluminum during friction stir welding using liquid CO2 rapid cooling. Mater Des 2017;129:151–63.
[125] Liu FC, Nelson TW. In-situ material flow pattern around probe during friction stir welding of austenitic stainless steel. Mater Des 2016;110:354–64.
[126] Liu FC, Nelson TW. In-situ grain structure and texture evolution during friction stir welding of austenite stainless steel. Mater Des 2017;115:467–78.
[127] Dos Santos JF, Staron P, Fischer T, Robson JD, Kostka A, Colegrove P, et al. Understanding precipitate evolution during friction stir welding of Al-Zn-Mg-Cu alloy through in-situ measurement coupled with simulation. Acta Mater 2018;148:163–72.
[128] Dumont M, Steuwer A, Deschamps A, Peel M, Withers PJ. Microstructure mapping in friction stir welds of 7449 aluminium alloy using SAXS. Acta Mater 2006;54:4793–801.
[129] Steuwer A, Dumont M, Altenkirch J, Birosca S, Deschamps A, Prangnell P, et al. A combined approach to microstructure mapping of an Al–Li AA2199 friction stir weld. Acta Mater 2011;59:3002–11.
[130] De Geuser F, Malard B, Deschamps A. Microstructure mapping of a friction stir welded AA2050 Al–Li–Cu in the T8 state. Phil Mag 2014;94:1451–62.
[131] Malard B, De Geuser F, Deschamps A. Microstructure distribution in an AA2050 T34 friction stir weld and its evolution during post-welding heat treatment. Acta Mater 2015;101:90–100.
[132] Avettand-Fènoël M-N, De Geuser F, Deschamps A. Effect of the ageing on precipitation spatial distribution in stationary shoulder friction stir welded AA2050 alloys. Mater Charact 2019;154:193–9.
[133] Genevois C, Deschamps A, Denquin A, Doisneau-Cottignies B. Quantitative investigation of precipitation and mechanical behaviour for AA2024 friction stir welds. Acta Mater 2005;53:2447–58.
[134] Liu G, Murr LE, Niou CS, McClure JC, Vega FR. Microstructural aspects of the friction-stir welding of 6061–T6 aluminum. Scr Mater 1997;37:355–61.
[135] Su J-Q, Nelson TW, Mishra R, Mahoney M. Microstructural investigation of friction stir welded 7050–T651 aluminium. Acta Mater 2003;51:713–29.
[136] Fonda RW, Bingert JF. Precipitation and grain refinement in a 2195 Al friction stir weld. Metall Mater Trans A 2006;37:3593–604.
[137] Su J-Q, Nelson TW, Sterling CJ. Grain refinement of aluminum alloys by friction stir processing. Phil Mag 2006;86:1–24.
[138] Etter AL, Baudin T, Fredj N, Penelle R. Recrystallization mechanisms in 5251 H14 and 5251 O aluminum friction stir welds. Mater Sci Eng, A 2007;445:94–9.
[139] Arora KS, Pandey S, Schaper M, Kumar R. Microstructure evolution during friction stir welding of aluminum alloy AA2219. J Mater Sci Technol 2010;26:747–53.
[140] Khorrami MS, Kazeminezhad M, Kokabi AH. Microstructure evolutions after friction stir welding of severely deformed aluminum sheets. Mater Des 2012;40:364–72.
[141] Khodabakhshi F, Simchi A, Kokabi AH, Gerlich AP, Nosko M. Effects of stored strain energy on restoration mechanisms and texture components in an aluminum–magnesium alloy prepared by friction stir processing. Mater Sci Eng, A 2015;642:204–14.
[142] Moghaddam M, Zarei-Hanzaki A, Pishbin MH, Shafieizad AH, Oliveira VB. Characterization of the microstructure, texture and mechanical properties of 7075 aluminum alloy in early stage of severe plastic deformation. Mater Charact 2016;119:137–47.
[143] Vysotskiy I, Zhemchuzhnikova D, Malopheyev S, Mironov S, Kaibyshev R. Microstructure evolution and strengthening mechanisms in friction-stir welded Al–Mg–Sc alloy. Mater Sci Eng, A 2020;770:138540.
[144] Salih OS, Neate N, Ou H, Sun W. Influence of process parameters on the microstructural evolution and mechanical characterisations of friction stir welded Al-Mg-Si alloy. J Mater Process Technol 2020;275:116366.
[145] Yang C, Zhang JF, Ma GN, Wu LH, Zhang XM, He GZ, et al. Microstructure and mechanical properties of double-side friction stir welded 6082Al ultra-thick plates. J Mater Sci Technol 2020;41:105–16.
[146] Hu Y, Liu H, Fujii H, Ushioda K. Effect of ultrasound on microstructure evolution of friction stir welded aluminum alloys. J Manuf Processes 2020;56:362–71.
[147] Nayan N, Yadava M, Sarkar R, Murty SVSN, Gurao NP, Mahesh S, et al. Microstructure and tensile response of friction stir welded Al–Cu–Li (AA2198-T8) alloy. Mater Charact 2020;159:110002.
[148] Chhangani S, Masa SK, Mathew RT, Prasad MJNV, Sujata M. Microstructural evolution in Al–Mg–Sc alloy (AA5024): Effect of thermal treatment, compression deformation and friction stir welding. Mater Sci Eng, A 2020;772:138790.

[149] Tao Y, Zhang Z, Yu BH, Xue P, Ni DR, Xiao BL, et al. Friction stir welding of 2060–T8 AlLi alloy. Part I: Microstructure evolution mechanism and mechanical properties. Mater Charact 2020.
[150] Xu ZZ, Liu CY, Zhang B, Huang HF, Cheng W. Effects of base metal state on the microstructure and mechanical properties of Al–Mg–Si alloy friction stir-welded joints. J Manuf Processes 2020;56:248–57.
[151] Martinez N, Kumar N, Mishra RS, Doherty KJ. Microstructural comparison of friction-stir-welded aluminum alloy 7449 starting from different tempers. J Mater Sci 2018;53:9273–86.
[152] Wang T, Komarasamy M, Liu K, Mishra RS. Friction stir butt welding of strain-hardened aluminum alloy with high strength steel. Mater Sci Eng, A 2018;737:85–9.
[153] Sidhar H, Martinez NY, Mishra RS, Silvanus J. Friction stir welding of Al–Mg–Li 1424 alloy. Mater Des 2016;106:146–52.
[154] Jata KV, Semiatin SL. Continuous dynamic recrystallization during friction stir welding of high strength aluminum alloys. Scr Mater 2000;43:743–9.
[155] Mironov S, Sato YS, Kokawa H. Microstructural evolution during friction stir welding of Ti–15V–3Cr–3Al–3Sn alloy. Mater Sci Eng, A 2010;527:7498–504.
[156] Bay B, Hansen N, Hughes DA, Kuhlmann-Wilsdorf D. Overview no. 96 evolution of fcc deformation structures in polyslip. Acta Metall Mater 1992;40:205–19.
[157] Hughes DA, Hansen N. High angle boundaries formed by grain subdivision mechanisms. Acta Mater 1997;45:3871–86.
[158] Hansen N, Jensen DJ. Development of microstructure in FCC metals during cold work. Philos Trans R Soc London, Ser A 1999;357:1447–69.
[159] Park SHC, Sato YS, Kokawa H, Okamoto K, Hirano S, Inagaki M. Rapid formation of the sigma phase in 304 stainless steel during friction stir welding. Scr Mater 2003;49:1175–80.
[160] Park SHC, Sato YS, Kokawa H, Okamoto K, Hirano S, Inagaki M. Microstructural characterisation of stir zone containing residual ferrite in friction stir welded 304 austenitic stainless steel. Sci Technol Weld Joining 2005;10:550–6.
[161] Chen YC, Fujii H, Tsumura T, Kitagawa Y, Nakata K, Ikeuchi K, et al. Friction stir processing of 316L stainless steel plate. Sci Technol Weld Joining 2009;14:197–201.
[162] Jeon J, Mironov S, Sato Y, Kokawa H, Park SHC, Hirano S. Friction stir spot welding of single-crystal austenitic stainless steel. Acta Mater 2011;59:7439–49.
[163] Mironov S, Sato YS, Kokawa H, Inoue H, Tsuge S. Structural response of superaustenitic stainless steel to friction stir welding. Acta Mater 2011;59:5472–81.
[164] Jeon JJ, Mironov S, Sato YS, Kokawa H, Park SHC, Hirano S. Grain structure development during friction stir welding of single-crystal austenitic stainless steel. Metall Mater Trans A 2013;44:3157–66.
[165] Wang D, Ni DR, Xiao BL, Ma ZY, Wang W, Yang K. Microstructural evolution and mechanical properties of friction stir welded joint of Fe–Cr–Mn–Mo–N austenite stainless steel. Mater Des 2014;64:355–9.
[166] Li HB, Jiang ZH, Feng H, Zhang SC, Li L, Han PD, et al. Microstructure, mechanical and corrosion properties of friction stir welded high nitrogen nickel-free austenitic stainless steel. Mater Des 2015;84:291–9.
[167] Hajian M, Abdollah-Zadeh A, Rezaei-Nejad SS, Assadi H, Hadavi SMM, Chung K, et al. Microstructure and mechanical properties of friction stir processed AISI 316L stainless steel. Mater Des 2015;67:82–94.
[168] Sabooni S, Karimzadeh F, Enayati MH, Ngan AHW. Friction-stir welding of ultrafine grained austenitic 304L stainless steel produced by martensitic thermomechanical processing. Mater Des 2015;76:130–40.
[169] Cui HB, Xie GM, Luo ZA, Ma J, Wang GD, Misra RDK. Microstructural evolution and mechanical properties of the stir zone in friction stir processed AISI201 stainless steel. Mater Des 2016;106:463–75.
[170] Zhang H, Wang D, Xue P, Wu LH, Ni DR, Ma ZY. Microstructural evolution and pitting corrosion behavior of friction stir welded joint of high nitrogen stainless steel. Mater Des 2016;110:802–10.
[171] Li H, Yang S, Zhang S, Zhang B, Jiang Z, Feng H, et al. Microstructure evolution and mechanical properties of friction stir welding super-austenitic stainless steel S32654. Mater Des 2017;118:207–17.
[172] Torganchuk V, Vysotskiy I, Malopheyev S, Mironov S, Kaibyshev R. Microstructure evolution and strengthening mechanisms in friction-stir welded TWIP steel. Mater Sci Eng, A 2019;746:248–58.
[173] Mironov S, Inagaki K, Sato YS, Kokawa H. Development of grain structure during friction-stir welding of Cu–30Zn brass. Phil Mag 2014;94:3137–48.
[174] Heidarzadeh A, Saeid T, Klemm V. Microstructure, texture, and mechanical properties of friction stir welded commercial brass alloy. Mater Charact 2016;119:84–91.
[175] Rahimzadeh A, Heidarzadeh A, Mohammadzadeh A, Moeini G. Effect of friction stir welding heat input on the microstructure and tensile properties of Cu-Zn alloy containing disordered β phase. J Mater Res Technol 2020;9:11154–61.
[176] Heidarzadeh A. Tensile behavior, microstructure, and substructure of the friction stir welded 70/30 brass joints: RSM, EBSD, and TEM study. Arch Civ Mech Eng 2019;19:137–46.
[177] Heidarzadeh A, Motalleb-nejad P, Barenji RV, Khalili V, Güleryüz G. The origin of the maximum hardness of the friction stir welded single-phase Cu-Zn plates: RSM, EBSD, and TEM investigation. Mater Chem Phys 2019;223:9–15.
[178] Heidarzadeh A, Barenji RV, Khalili V, Güleryüz G. Optimizing the friction stir welding of the α/β brass plates to obtain the highest strength and elongation. Vacuum 2019;159:152–60.
[179] Heidarzadeh A, Saeid T. On the effect of β phase on the microstructure and mechanical properties of friction stir welded commercial brass alloys. Data in Brief 2015;5:1022–5.
[180] Heidarzadeh A, Saeid T. Correlation between process parameters, grain size and hardness of friction-stir-welded Cu–Zn alloys. Rare Met 2018;37:388–98.
[181] Heidarzadeh A, Paidar M, Güleryüz G, Vatankhah Barenji R. Application of nanoindentation to evaluate the hardness and yield strength of brass joints produced by FSW: microstructural and strengthening mechanisms. Arch Civ Mech Eng 2020;20:41.
[182] Nagira T, Liu XC, Ushioda K, Fujii H. Mechanism of grain structure development for pure Cu and Cu-30Zn with low stacking fault energy during FSW. Sci Technol Weld Joining 2020;1–10.
[183] Heidarzadeh A, Testik ÖM, Güleryüz G, Barenji RV. Development of a fuzzy logic based model to elucidate the effect of FSW parameters on the ultimate tensile strength and elongation of pure copper joints. J Manuf Processes 2020;53:250–9.
[184] Heidarzadeh A, Chabok A, Pei Y. Friction stir welding of Monel alloy at different heat input conditions: Microstructural mechanisms and tensile behavior. Mater Lett 2019;245:94–7.
[185] Deng H, Chen Y, Li S, Chen C, Zhang T, Xu M, et al. Microstructure, mechanical properties and transformation behavior of friction stir welded Ni50.7Ti49.3 alloy. Mater Des 2020.
[186] Nesterova EV, Rybin VV. Mechanical twinning and the fragmentation of commercial titanium at the stage of developed plastic deformation. Phys Met Metallogr(USSR) 1985;59:169–79.
[187] Salishchev G, Mironov S, Zherebtsov S, Belyakov A. Changes in misorientations of grain boundaries in titanium during deformation. Mater Charact 2010;61:732–9.
[188] Chang CI, Lee CJ, Huang JC. Relationship between grain size and Zener-Holloman parameter during friction stir processing in AZ31 Mg alloys. Scr Mater 2004;51:509–14.
[189] Chang C, Du XH, Huang JC. Producing nanograined microstructure in Mg–Al–Zn alloy by two-step friction stir processing. Scr Mater 2008;59:356–9.
[190] Suhuddin UFHR, Mironov S, Sato YS, Kokawa H, Lee C-W. Grain structure evolution during friction-stir welding of AZ31 magnesium alloy. Acta Mater 2009;57:5406–18.
[191] Mironov S, Motohashi Y, Kaibyshev R, Somekawa H, Mukai T, Tsuzaki K. Development of fine-grained structure caused by friction stir welding process of a ZK60A magnesium alloy. Mater Trans 2009;50:610–7.
[192] Mironov S, Yang Q, Takahashi H, Takahashi I, Okamoto K, Sato YS, et al. Specific character of material flow in near-surface layer during friction stir processing of AZ31 magnesium alloy. Metall Mater Trans A 2010;41:1016–24.
[193] Chen J, Fujii H, Sun Y, Morisada Y, Kondoh K, Hashimoto K. Effect of grain size on the microstructure and mechanical properties of friction stir welded non-combustive magnesium alloys. Mater Sci Eng, A 2012;549:176–84.

[194] Chen J, Fujii H, Sun Y, Morisada Y, Ueji R. Fine grained Mg–3Al–1Zn alloy with randomized texture in the double-sided friction stir welded joints. Mater Sci Eng, A 2013;580:83–91.
[195] Chai F, Zhang D, Li Y, Zhang W. Microstructure evolution and mechanical properties of a submerged friction-stir-processed AZ91 magnesium alloy. J Mater Sci 2015;50:3212–25.
[196] Xin R, Zheng X, Liu Z, Liu D, Qiu R, Li Z, et al. Microstructure and texture evolution of an Mg–Gd–Y–Nd–Zr alloy during friction stir processing. J Alloy Compd 2016;659:51–9.
[197] Li G, Zhou L, Luo S, Dong F, Guo N. Microstructure and mechanical properties of bobbin tool friction stir welded ZK60 magnesium alloy. Mater Sci Eng, A 2020;776:138953.
[198] Weng F, Liu Y, Chew Y, Lee BY, Ng FL, Bi G. Double-side friction stir welding of thick magnesium alloy: microstructure and mechanical properties. Sci Technol Weld Joining 2020;25:359–68.
[199] Zhou M, Morisada Y, Fujii H. Effect of Ca addition on the microstructure and the mechanical properties of asymmetric double-sided friction stir welded AZ61 magnesium alloy. J Magnesium Alloys 2020;8:91–102.
[200] Zhou M, Morisada Y, Fujii H, Wang J-Y. Microstructure and mechanical properties of friction stir welded duplex Mg–Li alloy LZ91. Mater Sci Eng, A 2020;773:138730.
[201] Yuan W, Mishra RS, Carlson B, Verma R, Mishra RK. Material flow and microstructural evolution during friction stir spot welding of AZ31 magnesium alloy. Mater Sci Eng, A 2012;543:200–9.
[202] Lee W-B, Lee C-Y, Chang W-S, Yeon Y-M, Jung S-B. Microstructural investigation of friction stir welded pure titanium. Mater Lett 2005;59:3315–8.
[203] Zhang Y, Sato YS, Kokawa H, Park SHC, Hirano S. Stir zone microstructure of commercial purity titanium friction stir welded using pcBN tool. Mater Sci Eng, A 2008;488:25–30.
[204] Sato YS, Nagahama Y, Mironov S, Kokawa H, Park SHC, Hirano S. Microstructural studies of friction stir welded Zircaloy-4. Scr Mater 2012;67:241–4.
[205] Sato YS, Nelson TW, Sterling CJ, Steel RJ, Pettersson C-O. Microstructure and mechanical properties of friction stir welded SAF 2507 super duplex stainless steel. Mater Sci Eng, A 2005;397:376–84.
[206] Mahmoudiniya M, Kokabi AH, Goodarzi M, Kestens LAI. Friction stir welding of advanced high strength dual phase steel: Microstructure, mechanical properties and fracture behavior. Mater Sci Eng, A 2020;769:138490.
[207] Pilchak AL, Juhas MC, Williams JC. Microstructural changes due to friction stir processing of investment-cast Ti-6Al-4V. Metall Mater Trans A 2007;38:401–8.
[208] Liu HJ, Zhou L, Liu QW. Microstructural characteristics and mechanical properties of friction stir welded joints of Ti–6Al–4V titanium alloy. Mater Des 2010;31:1650–5.
[209] Zhou L, Liu HJ, Liu P, Liu QW. The stir zone microstructure and its formation mechanism in Ti–6Al–4V friction stir welds. Scr Mater 2009;61:596–9.
[210] Kitamura K, Fujii H, Iwata Y, Sun YS, Morisada Y. Flexible control of the microstructure and mechanical properties of friction stir welded Ti–6Al–4V joints. Mater Des 2013;46:348–54.
[211] Pilchak AL, Williams JC. Microstructure and texture evolution during friction stir processing of fully lamellar Ti-6Al-4V. Metall Mater Trans A 2011;42:773–94.
[212] Wu LH, Wang D, Xiao BL, Ma ZY. Microstructural evolution of the thermomechanically affected zone in a Ti–6Al–4V friction stir welded joint. Scr Mater 2014;78:17–20.
[213] Yoon S, Ueji R, Fujii H. Microstructure and texture distribution of Ti–6Al–4V alloy joints friction stir welded below β-transus temperature. J Mater Process Technol 2016;229:390–7.
[214] Yoon S, Ueji R, Fujii H. Effect of rotation rate on microstructure and texture evolution during friction stir welding of Ti–6Al–4V plates. Mater Charact 2015;106:352–8.
[215] Liu H-J, Li Z. Microstructural zones and tensile characteristics of friction stir welded joint of TC4 titanium alloy. Trans Nonferrous Met Soc China 2010;20:1873–8.
[216] Zhou L, H-j LIU, L-z WU. Texture of friction stir welded To-6Al-4V alloy. Trans Nonferrous Met Soc China 2014;24:368–72.
[217] Farnoush H, Bastami AA, Sadeghi A, Mohandesi JA, Moztarzadeh F. Tribological and corrosion behavior of friction stir processed Ti-CaP nanocomposites in simulated body fluid solution. J Mech Behav Biomed Mater 2013;20:90–7.
[218] Pilchak AL, Norfleet DM, Juhas MC, Williams JC. Friction stir processing of investment-cast Ti-6Al-4V: Microstructure and properties. Metall Mater Trans A 2008;39:1519–24.
[219] Pasta S, Reynolds AP. Residual stress effects on fatigue crack growth in a Ti-6Al-4V friction stir weld. Fatigue Fract Eng Mater Struct 2008;31:569–80.
[220] Lippold JC, Livingston JJ. Microstructure evolution during friction stir processing and hot torsion simulation of Ti-6Al-4V. Metall Mater Trans A 2013;44:3815–25.
[221] Steuwer A, Hattingh DG, James MN, Singh U, Buslaps T. Residual stresses, microstructure and tensile properties in Ti–6Al–4V friction stir welds. Sci Technol Weld Joining 2012;17:525–33.
[222] Ma ZY, Pilchak AL, Juhas MC, Williams JC. Microstructural refinement and property enhancement of cast light alloys via friction stir processing. Scr Mater 2008;58:361–6.
[223] Esmaily M, Mortazavi SN, Todehfalah P, Rashidi M. Microstructural characterization and formation of α′ martensite phase in Ti–6Al–4V alloy butt joints produced by friction stir and gas tungsten arc welding processes. Mater Des 2013;47:143–50.
[224] Muzvidziwa M, Okazaki M, Suzuki K, Hirano S. Role of microstructure on the fatigue crack propagation behavior of a friction stir welded Ti–6Al–4V. Mater Sci Eng, A 2016;652:59–68.
[225] Zhou L, Liu HJ, Liu QW. Effect of rotation speed on microstructure and mechanical properties of Ti–6Al–4V friction stir welded joints. Mater Des (1980–2015) 2010;31:2631–6.
[226] Lauro A. Friction stir welding of titanium alloys. Weld Int 2012;26:8–21.
[227] Ji S, Li Z, Wang Y, Ma L. Joint formation and mechanical properties of back heating assisted friction stir welded Ti–6Al–4V alloy. Mater Des 2017;113:37–46.
[228] Atapour M, Pilchak A, Frankel GS, Williams JC. Corrosion behaviour of investment cast and friction stir processed Ti–6Al–4V. Corros Sci 2010;52:3062–9.
[229] Wang J, Su J, Mishra RS, Xu R, Baumann JA. Tool wear mechanisms in friction stir welding of Ti–6Al–4V alloy. Wear 2014;321:25–32.
[230] Fall A, Fesharaki M, Khodabandeh A, Jahazi M. Tool wear characteristics and effect on microstructure in Ti-6Al-4V friction stir welded joints. Metals 2016;6:275.
[231] Wu LH, Wang D, Xiao BL, Ma ZY. Tool wear and its effect on microstructure and properties of friction stir processed Ti–6Al–4V. Mater Chem Phys 2014;146:512–22.
[232] Singh AK, Kumar B, Jha K, Astarita A, Squillace A, Franchitti S, et al. Friction stir welding of additively manufactured Ti-6Al-4V: Microstructure and mechanical properties. J Mater Process Technol 2020;277:116433.
[233] Li J, Shen Y, Hou W, Qi Y. Friction stir welding of Ti-6Al-4V alloy: Friction tool, microstructure, and mechanical properties. J Manuf Processes 2020;58:344–54.
[234] Heidarzadeh A, Chabok A, Klemm V, Pei Y. A Novel Approach to Structure Modification of Brasses by Combination of Non-equilibrium Heat Treatment and Friction Stir Processing. Metall Mater Trans A 2019;50:2391–8.
[235] Li B, Shen Y, Luo L, Hu W. Fabrication of TiCp/Ti–6Al–4V surface composite via friction stir processing (FSP): Process optimization, particle dispersion-refinement behavior and hardening mechanism. Mater Sci Eng, A 2013;574:75–85.
[236] Wu LH, Xiao BL, Ni DR, Ma ZY, Li XH, Fu MJ, et al. Achieving superior superplasticity from lamellar microstructure of a nugget in a friction-stir-welded Ti–6Al–4V joint. Scr Mater 2015;98:44–7.
[237] Wu LH, Xue P, Xiao BL, Ma ZY. Achieving superior low-temperature superplasticity for lamellar microstructure in nugget of a friction stir welded Ti-6Al-4V joint. Scr Mater 2016;122:26–30.
[238] Pilchak AL, Williams JC. The effect of friction stir processing on the mechanical properties of investment cast and hot isostatically pressed Ti-6Al-4V. Metall Mater Trans A 2011;42:1630–45.

[239] Su J, Wang J, Mishra RS, Xu R, Baumann JA. Microstructure and mechanical properties of a friction stir processed Ti–6Al–4V alloy. Mater Sci Eng, A 2013;573:67–74.
[240] Edwards PD, Ramulu M. Comparative study of fatigue and fracture in friction stir and electron beam welds of 24 mm thick titanium alloy Ti-6Al-4 V. Fatigue Fract Eng Mater Struct 2016;39:1226–40.
[241] Mironov S, Zhang Y, Sato YS, Kokawa H. Development of grain structure in β-phase field during friction stir welding of Ti–6Al–4V alloy. Scr Mater 2008;59:27–30.
[242] Zhang Y, Sato YS, Kokawa H, Park SHC, Hirano S. Microstructural characteristics and mechanical properties of Ti–6Al–4V friction stir welds. Mater Sci Eng, A 2008;485:448–55.
[243] Atapour M, Pilchak AL, Frankel GS, Williams JC. Corrosion behavior of friction stir-processed and gas tungsten arc-welded Ti-6Al-4V. Metall Mater Trans A 2010;41:2318–27.
[244] Mironov S, Zhang Y, Sato YS, Kokawa H. Crystallography of transformed β microstructure in friction stir welded Ti–6Al–4V alloy. Scr Mater 2008;59:511–4.
[245] Li B, Shen Y, Hu W, Luo L. Surface modification of Ti–6Al–4V alloy via friction-stir processing: microstructure evolution and dry sliding wear performance. Surf Coat Technol 2014;239:160–70.
[246] Buffa G, Fratini L, Schneider M, Merklein M. Micro and macro mechanical characterization of friction stir welded Ti–6Al–4V lap joints through experiments and numerical simulation. J Mater Process Technol 2013;213:2312–22.
[247] Edwards P, Ramulu M. Peak temperatures during friction stir welding of Ti–6Al–4V. Sci Technol Weld Joining 2010;15:468–72.
[248] Wang J, Su J, Mishra RS, Xu R, Baumann JA. A preliminary study of deformation behavior of friction stir welded Ti-6Al-4V. J Mater Eng Perform 2014;23:3027–33.
[249] Fonda RW, Knipling KE. Texture development in near-α Ti friction stir welds. Acta Mater 2010;58:6452–63.
[250] Tiley JS, Shiveley AR, Pilchak AL, Shade PA, Groeber MA. 3D reconstruction of prior β grains in friction stir–processed Ti–6Al–4V. J Microsc 2014;255:71–7.
[251] Mironov S, Sato YS, Kokawa H. Evaluation of texture developed in high-temperature β-phase during friction stir welding of Ti-6Al-4V. Key Engineering Materials. Trans Tech Publ; 2012. p. 106–11.
[252] Reynolds AP, Tang W, Posada M, DeLoach J. Friction stir welding of DH36 steel. Sci Technol Weld Joining 2003;8:455–60.
[253] Sato YS, Yamanoi H, Kokawa H, Furuhara T. Microstructural evolution of ultrahigh carbon steel during friction stir welding. Scr Mater 2007;57:557–60.
[254] Lakshminarayanan AK, Balasubramanian V. An assessment of microstructure, hardness, tensile and impact strength of friction stir welded ferritic stainless steel joints. Mater Des 2010;31:4592–600.
[255] Hovanski Y, Santella ML, Grant GJ. Friction stir spot welding of hot-stamped boron steel. Scr Mater 2007;57:873–6.
[256] Ghosh M, Kumar K, Mishra RS. Analysis of microstructural evolution during friction stir welding of ultrahigh-strength steel. Scr Mater 2010;63:851–4.
[257] Ohashi R, Fujimoto M, Mironov S, Sato YS, Kokawa H. Effect of contamination on microstructure in friction stir spot welded DP590 steel. Sci Technol Weld Joining 2009;14:221–7.
[258] Ghosh M, Kumar K, Mishra RS. Friction stir lap welded advanced high strength steels: Microstructure and mechanical properties. Mater Sci Eng, A 2011;528:8111–9.
[259] Chen YC, Nakata K. Evaluation of microstructure and mechanical properties in friction stir processed SKD61 tool steel. Mater Charact 2009;60:1471–5.
[260] Chung YD, Fujii H, Ueji R, Nogi K. Friction stir welding of hypereutectoid steel (SK5) below eutectoid temperature. Sci Technol Weld Joining 2009;14:233–8.
[261] Barnes SJ, Bhatti AR, Steuwer A, Johnson R, Altenkirch J, Withers PJ. Friction stir welding in HSLA-65 steel: part I. Influence of weld speed and tool material on microstructural development. Metall Mater Trans A 2012;43:2342–55.
[262] Matsushita M, Kitani Y, Ikeda R, Ono M, Fujii H, Chung YD. Development of friction stir welding of high strength steel sheet. Sci Technol Weld Joining 2011;16:181–7.
[263] Xue P, Xiao BL, Wang WG, Zhang Q, Wang D, Wang QZ, et al. Achieving ultrafine dual-phase structure with superior mechanical property in friction stir processed plain low carbon steel. Mater Sci Eng, A 2013;575:30–4.
[264] Barnes SJ, Steuwer A, Mahawish S, Johnson R, Withers PJ. Residual strains and microstructure development in single and sequential double sided friction stir welds in RQT-701 steel. Mater Sci Eng, A 2008;492:35–44.
[265] Sato YS, Yamanoi H, Kokawa H, Furuhara T. Characteristics of microstructure in ultrahigh carbon steel produced during friction stir welding. ISIJ Int 2008;48:71–6.
[266] Mironov S, Sato YS, Yoneyama S, Kokawa H, Fujii HT, Hirano S. Microstructure and tensile behavior of friction-stir welded TRIP steel. Mater Sci Eng, A 2018;717:26–33.
[267] Hua P, Mironov S, Sato YS, Kokawa H, Park SHC, Hirano S. Crystallography of Martensite in Friction-Stir-Welded 12Cr Heat-Resistant Steel. Metall Mater Trans A 2019;1–6.
[268] Cui L, Fujii H, Tsuji N, Nakata K, Nogi K, Ikeda R, et al. Transformation in stir zone of friction stir welded carbon steels with different carbon contents. ISIJ Int 2007;47:299–306.
[269] Wei LY, Nelson TW. Correlation of microstructures and process variables in FSW HSLA-65 steel. Welding J 2011;90.
[270] Wei L, Nelson TW. Influence of heat input on post weld microstructure and mechanical properties of friction stir welded HSLA-65 steel. Mater Sci Eng, A 2012;556:51–9.
[271] Cho H-H, Kang SH, Kim S-H, Oh KH, Kim HJ, Chang W-S, et al. Microstructural evolution in friction stir welding of high-strength linepipe steel. Mater Des 2012;34:258–67.
[272] Aydin H, Nelson TW. Microstructure and mechanical properties of hard zone in friction stir welded X80 pipeline steel relative to different heat input. Mater Sci Eng, A 2013;586:313–22.
[273] Fujii H, Ueji R, Morisada Y, Tanigawa H. High strength and ductility of friction-stir-welded steel joints due to mechanically stabilized metastable austenite. Scr Mater 2014;70:39–42.
[274] Weinberger T, Enzinger N, Cerjak H. Microstructural and mechanical characterisation of friction stir welded 15–5PH steel. Sci Technol Weld Joining 2009;14:210–5.
[275] Tehrani-Moghadam HG, Jafarian HR, Heidarzadeh A, Eivani AR, Do H, Park N. Achieving extraordinary strength and ductility in TRIP steels through stabilization of austenite up to 99.8 % by friction stir welding. Mater Sci Eng, A 2020.
[276] Tehrani-Moghadam HG, Jafarian HR, Heidarzadeh A, Eivani AR, Do H, Park N. Superior mechanical properties in high-Ni transformation induced plasticity steels after friction stir welding. J Mater Res Technol 2020;9:5431–41.
[277] Steuwer A, Barnes SJ, Altenkirch J, Johnson R, Withers PJ. Friction stir welding of HSLA-65 steel: part II. The influence of weld speed and tool material on the residual stress distribution and tool wear. Metall Mater Trans A 2012;43:2356–65.
[278] Abbasi M, Nelson TW, Sorensen CD. Transformation and deformation texture study in friction stir processed API X80 pipeline steel. Metall Mater Trans A 2012;43:4940–6.
[279] Fabrègue D, Deschamps A, Suéry M, Drezet J-M. Non-isothermal tensile tests during solidification of Al–Mg–Si–Cu alloys: Mechanical properties in relation to the phenomenon of hot tearing. Acta Mater 2006;54:5209–20.
[280] Balasubramanian V, Ravisankar V, Reddy GM. Effect of postweld aging treatment on fatigue behavior of pulsed current welded AA7075 aluminum alloy joints. J Mater Eng Perform 2008;17:224–33.
[281] Fuller CB, Mahoney MW, Calabrese M, Micona L. Evolution of microstructure and mechanical properties in naturally aged 7050 and 7075 Al friction stir welds. Mater Sci Eng, A 2010;527:2233–40.
[282] Yuqing M, Liming K, Fencheng L, Yuhua C, Li X. Investigations on temperature distribution, microstructure evolution, and property variations along thickness in friction stir welded joints for thick AA7075-T6 plates. Int J Adv Manuf Technol 2016;86:141–54.
[283] Liu J, Kou S. Crack susceptibility of binary aluminum alloys during solidification. Acta Mater 2016;110:84–94.
[284] Liu J, Kou S. Susceptibility of ternary aluminum alloys to cracking during solidification. Acta Mater 2017;125:513–23.

[285] Biswas A, Siegel DJ, Wolverton C, Seidman DN. Precipitates in Al–Cu alloys revisited: Atom-probe tomographic experiments and first-principles calculations of compositional evolution and interfacial segregation. Acta Mater 2011;59:6187–204.
[286] Bourgeois L, Dwyer C, Weyland M, Nie J-F, Muddle BC. Structure and energetics of the coherent interface between the θ′ precipitate phase and aluminium in Al–Cu. Acta Mater 2011;59:7043–50.
[287] Liu C, Ma Z, Ma P, Zhan L, Huang M. Multiple precipitation reactions and formation of θ'-phase in a pre-deformed Al–Cu alloy. Mater Sci Eng, A 2018;733:28–38.
[288] Kang J, Feng Z-C, Frankel GS, Huang IW, Wang G-Q, Wu A-P. Friction stir welding of Al alloy 2219–T8: part I-evolution of precipitates and formation of abnormal Al 2 Cu agglomerates. Metall Mater Trans A 2016;47:4553–65.
[289] Chen YC, Feng JC, Liu HJ. Precipitate evolution in friction stir welding of 2219–T6 aluminum alloys. Mater Charact 2009;60:476–81.
[290] Starink MJ, Wang SC. The thermodynamics of and strengthening due to co-clusters: general theory and application to the case of Al–Cu–Mg alloys. Acta Mater 2009;57:2376–89.
[291] Genevois C, Fabregue D, Deschamps A, Poole WJ. On the coupling between precipitation and plastic deformation in relation with friction stir welding of AA2024 T3 aluminium alloy. Mater Sci Eng, A 2006;441:39–48.
[292] Gumbmann E, Lefebvre W, De Geuser F, Sigli C, Deschamps A. The effect of minor solute additions on the precipitation path of an AlCuLi alloy. Acta Mater 2016;115:104–14.
[293] Gumbmann E, De Geuser F, Sigli C, Deschamps A. Influence of Mg, Ag and Zn minor solute additions on the precipitation kinetics and strengthening of an Al-Cu-Li alloy. Acta Mater 2017;133:172–85.
[294] Wang SC, Starink MJ. Precipitates and intermetallic phases in precipitation hardening Al–Cu–Mg–(Li) based alloys. Int Mater Rev 2005;50:193–215.
[295] Dorin T, Deschamps A, De Geuser F, Sigli C. Quantification and modelling of the microstructure/strength relationship by tailoring the morphological parameters of the T1 phase in an Al–Cu–Li alloy. Acta Mater 2014;75:134–46.
[296] Decreus B, Deschamps A, de Geuser F, Sigli C. Influence of Natural Ageing and Deformation on Precipitation in an Al–C u–L i Alloy. Adv Eng Mater 2013;15:1082–5.
[297] Araullo-Peters V, Gault B, De Geuser F, Deschamps A, Cairney JM. Microstructural evolution during ageing of Al–Cu–Li–x alloys. Acta Mater 2014;66:199–208.
[298] Decreus B, Deschamps A, De Geuser F, Donnadieu P, Sigli C, Weyland M. The influence of Cu/Li ratio on precipitation in Al–Cu–Li–x alloys. Acta Mater 2013;61:2207–18.
[299] Gallais C, Denquin A, Bréchet Y, Lapasset G. Precipitation microstructures in an AA6056 aluminium alloy after friction stir welding: Characterisation and modelling. Mater Sci Eng, A 2008;496:77–89.
[300] Dong P, Li H, Sun D, Gong W, Liu J. Effects of welding speed on the microstructure and hardness in friction stir welding joints of 6005A–T6 aluminum alloy. Mater Des 2013;45:524–31.
[301] Sato YS, Kokawa H, Enomoto M, Jogan S. Microstructural evolution of 6063 aluminum during friction-stir welding. Metall Mater Trans A 1999;30:2429–37.
[302] Simar A, Bréchet Y, De Meester B, Denquin A, Pardoen T. Sequential modeling of local precipitation, strength and strain hardening in friction stir welds of an aluminum alloy 6005A–T6. Acta Mater 2007;55:6133–43.
[303] Simar A, Brechet Y, De Meester B, Denquin A, Pardoen T. Microstructure, local and global mechanical properties of friction stir welds in aluminium alloy 6005A–T6. Mater Sci Eng, A 2008;486:85–95.
[304] Dong P, Sun D, Li H. Natural aging behaviour of friction stir welded 6005A–T6 aluminium alloy. Mater Sci Eng, A 2013;576:29–35.
[305] Malopheyev S, Vysotskiy I, Kulitskiy V, Mironov S, Kaibyshev R. Optimization of processing-microstructure-properties relationship in friction-stir welded 6061–T6 aluminum alloy. Mater Sci Eng, A 2016;662:136–43.
[306] Rodrigues DM, Loureiro A, Leitao C, Leal RM, Chaparro BM, Vilaça P. Influence of friction stir welding parameters on the microstructural and mechanical properties of AA 6016–T4 thin welds. Mater Des 2009;30:1913–21.
[307] Olea CAW, Roldo L, Dos Santos JF, Strohaecker TR. A sub-structural analysis of friction stir welded joints in an AA6056 Al-alloy in T4 and T6 temper conditions. Mater Sci Eng, A 2007;454:52–62.
[308] Azarniya A, Taheri AK, Taheri KK. Recent advances in ageing of 7xxx series aluminum alloys: a physical metallurgy perspective. J Alloy Compd 2019;781:945–83.
[309] Martinez N, Kumar N, Mishra RS, Doherty KJ. Effect of tool dimensions and parameters on the microstructure of friction stir welded aluminum 7449 alloy of various thicknesses. Mater Sci Eng, A 2017;684:470–9.
[310] Zhang F, Su X, Chen Z, Nie Z. Effect of welding parameters on microstructure and mechanical properties of friction stir welded joints of a super high strength Al–Zn–Mg–Cu aluminum alloy. Mater Des 2015;67:483–91.
[311] Mahoney MW, Rhodes CG, Flintoff JG, Bingel WH, Spurling RA. Properties of friction-stir-welded 7075 T651 aluminum. Metall Mater Trans A 1998;29:1955–64.
[312] Kamp N, Sullivan A, Tomasi R, Robson JD. Modelling of heterogeneous precipitate distribution evolution during friction stir welding process. Acta Mater 2006;54:2003–14.
[313] Sullivan A, Robson JD. Microstructural properties of friction stir welded and post-weld heat-treated 7449 aluminium alloy thick plate. Mater Sci Eng, A 2008;478:351–60.
[314] Nie J-F. Precipitation and hardening in magnesium alloys. Metall Mater Trans A 2012;43:3891–939.
[315] Hutchinson CR, Nie J-F, Gorsse S. Modeling the precipitation processes and strengthening mechanisms in a Mg-Al-(Zn) AZ91 alloy. Metall Mater Trans A 2005;36:2093–105.
[316] Palanivel S, Mishra RS, Davis B, DeLorme R, Doherty KJ, Cho KC. Effect of initial microstructure on the microstructural evolution and joint efficiency of a WE43 alloy during friction stir welding. Friction Stir Welding and Processing VII. Springer; 2013. p. 253–61.
[317] Gao L, Chen RS, Han EH. Effects of rare-earth elements Gd and Y on the solid solution strengthening of Mg alloys. J Alloy Compd 2009;481:379–84.
[318] Johnson R. Friction stir welding of magnesium alloys. Materials Science Forum: Trans Tech Publications Ltd, Zurich-Uetikon, Switzerland 2003:365–70.
[319] Antion C, Donnadieu P, Perrard F, Deschamps A, Tassin C, Pisch A. Hardening precipitation in a Mg–4Y–3RE alloy. Acta Mater 2003;51:5335–48.
[320] Cao G, Zhang D, Zhang W, Qiu C. Microstructure evolution and mechanical properties of Mg–Nd–Y alloy in different friction stir processing conditions. J Alloy Compd 2015;636:12–9.
[321] Li J, Zhang D-T, Chai F, Zhang W. Microstructures and mechanical properties of WE43 magnesium alloy prepared by friction stir processing. Rare Met 2014;1–6.
[322] Robson JD, Cui S, Chen ZW. Incipient melting during friction stir processing of AZ91 magnesium castings. Mater Sci Eng, A 2010;527:7299–304.
[323] Kohn G, Antonsson S, Munitz A. Friction stir welding magnesium alloys. Automotive Alloys 1999;2000:285–92.
[324] Avettand-Fènoël M-N, Simar A. A review about Friction Stir Welding of metal matrix composites. Mater Charact 2016;120:1–17.
[325] Storjohann D, Barabash OM, David SA, Sklad PS, Bloom EE, Babu SS. Fusion and friction stir welding of aluminum-metal-matrix composites. Metall Mater Trans A 2005;36:3237–47.
[326] Uzun H. Friction stir welding of SiC particulate reinforced AA2124 aluminium alloy matrix composite. Mater Des 2007;28:1440–6.
[327] Nami H, Adgi H, Sharifitabar M, Shamabadi H. Microstructure and mechanical properties of friction stir welded Al/Mg2Si metal matrix cast composite. Mater Des 2011;32:976–83.
[328] Amirizad M, Kokabi AH, Gharacheh MA, Sarrafi R, Shalchi B, Azizieh M. Evaluation of microstructure and mechanical properties in friction stir welded A356+15% SiCp cast composite. Mater Lett 2006;60:565–8.
[329] Zhang Q, Xiao BL, Xue P, Ma ZY. Microstructural evolution and mechanical properties of ultrafine grained Al3Ti/Al–5.5 Cu composites produced via hot pressing and subsequent friction stir processing. Mater Chem Phys 2012;134:294–301.
[330] Huang C, Li W, Zhang Z, Fu M, Planche M-p, Liao H, et al. Modification of a cold sprayed SiCp/Al5056 composite coating by friction stir processing. Surf Coat Technol 2016;296:69–75.

[331] Ceschini L, Boromei I, Minak G, Morri A, Tarterini F. Effect of friction stir welding on microstructure, tensile and fatigue properties of the AA7005/10 vol.% Al2O3p composite. Compos Sci Technol 2007;67:605–15.
[332] Minak G, Ceschini L, Boromei I, Ponte M. Fatigue properties of friction stir welded particulate reinforced aluminium matrix composites. Int J Fatigue 2010;32:218–26.
[333] Periyasamy P, Mohan B, Balasubramanian V. Effect of heat input on mechanical and metallurgical properties of friction stir welded AA6061-10% SiCp MMCs. J Mater Eng Perform 2012;21:2417–28.
[334] Lee W-B, Lee C-Y, Kim M-K, Yoon J-I, Kim Y-J, Yoen Y-M, et al. Microstructures and wear property of friction stir welded AZ91 Mg/SiC particle reinforced composite. Compos Sci Technol 2006;66:1513–20.
[335] Ceschini L, Boromei I, Minak G, Morri A, Tarterini F. Microstructure, tensile and fatigue properties of AA6061/20 vol.% Al2O3p friction stir welded joints. Compos A Appl Sci Manuf 2007;38:1200–10.
[336] Jo M-G, Kim H-J, Kang M, Madakashira PP, Park ES, Suh J-Y, et al. Microstructure and mechanical properties of friction stir welded and laser welded high entropy alloy CrMnFeCoNi. Met Mater Int 2018;24:73–83.
[337] Park S, Park C, Na Y, Kim H-S, Kang N. Effects of (W, Cr) carbide on grain refinement and mechanical properties for CoCrFeMnNi high entropy alloys. J Alloy Compd 2019;770:222–8.
[338] Shaysultanov D, Stepanov N, Malopheyev S, Vysotskiy I, Sanin V, Mironov S, et al. Friction stir welding of a carbon-doped CoCrFeNiMn high-entropy alloy. Mater Charact 2018;145:353–61.
[339] Xu N, Song Q, Bao Y. Microstructure evolution and mechanical properties of friction stir welded FeCrNiCoMn high-entropy alloy. Mater Sci Technol 2019;35:577–84.
[340] Zherebtsov S, Stepanov N, Shaysultanov D, Malopheyev S, Vysotskiy I, Sanin V, et al. Use of Novel Welding Technologies for High-Entropy Alloys Joining. Materials Science Forum. Trans Tech Publ; 2018. p. 919–24.
[341] Li R, Wang M, Yuan T, Song B, Shi Y. Microstructural modification of laser-deposited high-entropy CrFeCoNiMoWC alloy by friction stir processing: Nanograin formation and deformation mechanism. Metall Mater Trans A 2017;48:841–54.
[342] Komarasamy M, Kumar N, Tang Z, Mishra RS, Liaw PK. Effect of microstructure on the deformation mechanism of friction stir-processed Al0. 1CoCrFeNi high entropy alloy. Mater Res Lett 2015;3:30–4.
[343] Kumar N, Komarasamy M, Nelaturu P, Tang Z, Liaw PK, Mishra RS. Friction stir processing of a high entropy alloy Al 0.1 CoCrFeNi. Jom 2015;67:1007–13.
[344] Choudhuri D, Komarasamy M, Ageh V, Mishra RS. Investigation of plastic deformation modes in Al0. 1CoCrFeNi high entropy alloy. Mater Chem Phys 2018;217:308–14.
[345] Wang T, Komarasamy M, Shukla S, Mishra RS. Simultaneous enhancement of strength and ductility in an AlCoCrFeNi2. 1 eutectic high-entropy alloy via friction stir processing. J Alloy Compd 2018;766:312–7.
[346] Wang T, Shukla S, Komarasamy M, Liu K, Mishra RS. Towards heterogeneous AlxCoCrFeNi high entropy alloy via friction stir processing. Mater Lett 2019;236:472–5.
[347] Zhu ZG, Sun YF, Goh MH, Ng FL, Nguyen QB, Fujii H, et al. Friction stir welding of a CoCrFeNiAl0. 3 high entropy alloy. Mater Lett 2017;205:142–4.
[348] Nene SS, Liu K, Frank M, Mishra RS, Brennan RE, Cho KC, et al. Enhanced strength and ductility in a friction stir processing engineered dual phase high entropy alloy. Sci Rep 2017;7:16167.
[349] Nene SS, Frank M, Liu K, Sinha S, Mishra RS, McWilliams B, et al. Reversed strength-ductility relationship in microstructurally flexible high entropy alloy. Scr Mater 2018;154:163–7.
[350] Liu K, Nene SS, Frank M, Sinha S, Mishra RS. Metastability-assisted fatigue behavior in a friction stir processed dual-phase high entropy alloy. Mater Res Lett 2018;6:613–9.
[351] Nene SS, Frank M, Liu K, Sinha S, Mishra RS, McWilliams BA, et al. Corrosion-resistant high entropy alloy with high strength and ductility. Scr Mater 2019;166:168–72.
[352] Sinha S, Nene SS, Frank M, Liu K, Mishra RS, McWilliams BA, et al. Revealing the microstructural evolution in a high entropy alloy enabled with transformation, twinning and precipitation. Materialia 2019;6:100310.
[353] Sinha S, Nene SS, Frank M, Liu K, Mishra RS, McWilliams BA, et al. Microstructural Evolution and Deformation Behavior of Ni-Si-and Co-Si-Containing Metastable High Entropy Alloys. Metall Mater Trans A 2019;50:179–90.
[354] Zhu ZG, Sun YF, Ng FL, Goh MH, Liaw PK, Fujii H, et al. Friction-stir welding of a ductile high entropy alloy: microstructural evolution and weld strength. Mater Sci Eng, A 2018;711:524–32.
[355] Simar A, Avettand-Fènoël M-N. State of the art about dissimilar metal friction stir welding. Sci Technol Weld Joining 2017;22:389–403.
[356] Patel V, Li W, Wang G, Wang F, Vairis A, Niu P. Friction stir welding of dissimilar aluminum alloy combinations: State-of-the-art. Metals 2019;9:270.
[357] Kalemba-Rec I, Kopyściański M, Miara D, Krasnowski K. Effect of process parameters on mechanical properties of friction stir welded dissimilar 7075–T651 and 5083–H111 aluminum alloys. Int J Adv Manuf Technol 2018;97:2767–79.
[358] İpekoğlu G, Çam G. Effects of initial temper condition and postweld heat treatment on the properties of dissimilar friction-stir-welded joints between AA7075 and AA6061 aluminum alloys. Metall Mater Trans A 2014;45:3074–87.
[359] Guo JF, Chen HC, Sun CN, Bi G, Sun Z, Wei J. Friction stir welding of dissimilar materials between AA6061 and AA7075 Al alloys effects of process parameters. Mater Des (1980–2015) 2014;56:185–92.
[360] Ouyang JH, Kovacevic R. Material flow and microstructure in the friction stir butt welds of the same and dissimilar aluminum alloys. J Mater Eng Perform 2002;11:51–63.
[361] Zhang C, Cao Y, Huang G, Zeng Q, Zhu Y, Huang X, et al. Influence of tool rotational speed on local microstructure, mechanical and corrosion behavior of dissimilar AA2024/7075 joints fabricated by friction stir welding. J Manuf Processes 2020;49:214–26.
[362] Jandaghi MR, Badini C, Pavese M. Dissimilar friction stir welding of AA2198 and AA7475: Effect of solution treatment and aging on the microstructure and mechanical strength. J Manuf Processes 2020;57:712–24.
[363] Zhang C, Huang G, Cao Y, Zhu Y, Huang X, Zhou Y, et al. Microstructure evolution of thermo-mechanically affected zone in dissimilar AA2024/7075 joint produced by friction stir welding. Vacuum 2020;179:109515.
[364] Dong J, Zhang D, Luo X, Zhang W, Zhang W, Qiu C. EBSD study of underwater friction stir welded AA7003-T4 and AA6060-T4 dissimilar joint. J Mater Res Technol 2020;9:4309–18.
[365] Niu PL, Li WY, Li N, Xu YX, Chen DL. Exfoliation corrosion of friction stir welded dissimilar 2024-to-7075 aluminum alloys. Mater Charact 2019;147:93–100.
[366] Zhang C, Huang G, Cao Y, Zhu Y, Li W, Wang X, et al. Microstructure and mechanical properties of dissimilar friction stir welded AA2024-7075 joints: Influence of joining material direction. Mater Sci Eng, A 2019;766:138368.
[367] Liu D, Nishio H, Nakata K. Anisotropic property of material arrangement in friction stir welding of dissimilar Mg alloys. Mater Des 2011;32:4818–24.
[368] Liu D, Xin R, Zheng X, Zhou Z, Liu Q. Microstructure and mechanical properties of friction stir welded dissimilar Mg alloys of ZK60–AZ31. Mater Sci Eng, A 2013;561:419–26.
[369] Sunil BR, Reddy GPK, Mounika ASN, Sree PN, Pinneswari PR, Ambica I, et al. Joining of AZ31 and AZ91 Mg alloys by friction stir welding. J Magnesium Alloys 2015;3:330–4.
[370] Luo C, Li X, Song D, Zhou N, Li Y, Qi W. Microstructure evolution and mechanical properties of friction stir welded dissimilar joints of Mg–Zn–Gd and Mg–Al–Zn alloys. Mater Sci Eng, A 2016;664:103–13.
[371] Zhang J, Huang G, Liu S, Xie Y, Wang G, Jiang B, et al. Microstructure evolution and mechanical properties of friction stir welded dissimilar joints of as-extruded AM60 and AZ31 alloys. Mater Sci Eng, A 2019;759:479–89.
[372] Zhang J, Chen X, Xia D, Huang G, Tang A, Jiang B, et al. Improving performance of friction stir welded AZ31/AM60 dissimilar joint by adjusting texture distribution and microstructure. Mater Sci Eng, A 2020;778:139088.

[373] Heidarzadeh A, Laleh HM, Gerami H, Hosseinpour P, Shabestari MJ, Bahari R. The origin of different microstructural and strengthening mechanisms of copper and brass in their dissimilar friction stir welded joint. Mater Sci Eng, A 2018;735:336–42.
[374] Murugan R, Thirumalaisamy N. Experimental and numerical analysis of friction stir welded dissimilar copper and bronze plates. Mater Today: Proc 2018;5:803–9.
[375] Liu H, Ushioda K, Fujii H. Elucidation of interface joining mechanism during friction stir welding through Cu/Cu-10Zn interfacial observations. Acta Mater 2019;166:324–34.
[376] İpekoğlu G, Küçükömeroğlu T, Aktarer SM, Sekban DM, Çam G. Investigation of microstructure and mechanical properties of friction stir welded dissimilar St37/St52 joints. Mater Res Express 2019;6:046537.
[377] Küçükömeroğlu T, Aktarer SM, İpekoğlu G, Çam G. Mechanical properties of friction stir welded St 37 and St 44 steel joints. Mater Test 2018;60:1163–70.
[378] Jafarzadegan M, Feng AH, Abdollah-Zadeh A, Saeid T, Shen J, Assadi H. Microstructural characterization in dissimilar friction stir welding between 304 stainless steel and st37 steel. Mater Charact 2012;74:28–41.
[379] Jafarzadegan M, Abdollah-Zadeh A, Feng AH, Saeid T, Shen J, Assadi H. Microstructure and mechanical properties of a dissimilar friction stir weld between austenitic stainless steel and low carbon steel. J Mater Sci Technol 2013;29:367–72.
[380] Logan BP, Toumpis AI, Galloway AM, McPherson NA, Hambling SJ. Dissimilar friction stir welding of duplex stainless steel to low alloy structural steel. Sci Technol Weld Joining 2016;21:11–9.
[381] Matlan MJB, Mohebbi H, Pedapati SR, Awang MB, Ismail MC, Kakooei S, et al. Dissimilar Friction Stir Welding of Carbon Steel and Stainless Steel: Some Observation on Microstructural Evolution and Stress Corrosion Cracking Performance. Trans Indian Inst Met 2018;71:2553–64.
[382] Wang H, Wang K, Wang W, Huang L, Peng P, Yu H. Microstructure and mechanical properties of dissimilar friction stir welded type 304 austenitic stainless steel to Q235 low carbon steel. Mater Charact 2019;155:109803.
[383] Sharma G, Dwivedi DK. Study on microstructure and mechanical properties of dissimilar steel joint developed using friction stir welding. Int J Adv Manuf Technol 2017;88:1299–307.
[384] He B, Cui L, Wang D, Liu Y, Liu C, Li H. The metallurgical bonding and high temperature tensile behaviors of 9Cr-1W steel and 316L steel dissimilar joint by friction stir welding. J Manuf Processes 2019;44:241–51.
[385] Chung YD, Fujii H, Sun Y, Tanigawa H. Interface microstructure evolution of dissimilar friction stir butt welded F82H steel and SUS304. Mater Sci Eng, A 2011;528:5812–21.
[386] Theodoro MC, Pereira VF, Mei PR, Ramirez AJ. Dissimilar friction stir welding between UNS S31603 austenitic stainless steel and UNS S32750 superduplex stainless steel. Metall Mater Trans B 2015;46:1440–7.
[387] Serizawa H, Murakami M, Morisada Y, Fujii H, Nogami S, Nagasaka T, et al. Influence of friction stir welding conditions on joinability of oxide dispersion strengthened steel/F82H ferritic/martensitic steel joint. Nucl Mater Energy 2016;9:367–71.
[388] Tang W, Yang X, Li S, Li H. Microstructure and properties of CLAM/316L steel friction stir welded joints. J Mater Process Technol 2019;271:189–201.
[389] Sato YS, Kokawa H, Fujii HT, Yano Y, Sekio Y. Mechanical properties and microstructure of dissimilar friction stir welds of 11Cr-Ferritic/Martensitic steel to 316 stainless steel. Metall Mater Trans A 2015;46:5789–800.
[390] Sarkar R, Sengupta S, Pal TK, Shome M. Microstructure and mechanical properties of friction stir spot-welded IF/DP dissimilar steel joints. Metall Mater Trans A 2015;46:5182–200.
[391] Derazkola HA, Khodabakhshi F, Simchi A. Evaluation of a polymer-steel laminated sheet composite structure produced by friction stir additive manufacturing (FSAM) technology. Polym Test 2020;90:106690.
[392] Wang W, Hu Y, Zhang M, Zhao H. Microstructure and mechanical properties of dissimilar friction stir welds in austenitic-duplex stainless steels. Mater Sci Eng, A 2020;787:139499.
[393] Argade GR, Shukla S, Liu K, Mishra RS. Friction stir lap welding of stainless steel and plain carbon steel to enhance corrosion properties. J Mater Process Technol 2018;259:259–69.
[394] Eyvazian A, Hamouda A, Tarlochan F, Derazkola HA, Khodabakhshi F. Simulation and experimental study of underwater dissimilar friction-stir welding between aluminium and steel. J Mater Res Technol 2020;9:3767–81.
[395] Han W, Chen D, Ha Y, Kimura A, Serizawa H, Fujii H, et al. Modifications of grain-boundary structure by friction stir welding in the joint of nano-structured oxide dispersion strengthened ferritic steel and reduced activation martensitic steel. Scr Mater 2015;105:2–5.
[396] Shi H, Chen K, Liang Z, Dong F, Yu T, Dong X, et al. Intermetallic compounds in the banded structure and their effect on mechanical properties of Al/Mg dissimilar friction stir welding joints. J Mater Sci Technol 2017;33:359–66.
[397] Sato YS, Park SHC, Michiuchi M, Kokawa H. Constitutional liquation during dissimilar friction stir welding of Al and Mg alloys. Scr Mater 2004;50:1233–6.
[398] Fu B, Qin G, Li F, Meng X, Zhang J, Wu C. Friction stir welding process of dissimilar metals of 6061–T6 aluminum alloy to AZ31B magnesium alloy. J Mater Process Technol 2015;218:38–47.
[399] Shah LH, Othman NH, Gerlich A. Review of research progress on aluminium–magnesium dissimilar friction stir welding. Sci Technol Weld Joining 2018;23:256–70.
[400] Kwon YJ, Shigematsu I, Saito N. Dissimilar friction stir welding between magnesium and aluminum alloys. Mater Lett 2008;62:3827–9.
[401] Firouzdor V, Kou S. Formation of liquid and intermetallics in Al-to-Mg friction stir welding. Metall Mater Trans A 2010;41:3238–51.
[402] Firouzdor V, Kou S. Al-to-Mg friction stir welding: effect of material position, travel speed, and rotation speed. Metall Mater Trans A 2010;41:2914–35.
[403] Mohammadi J, Behnamian Y, Mostafaei A, Izadi H, Saeid T, Kokabi AH, et al. Friction stir welding joint of dissimilar materials between AZ31B magnesium and 6061 aluminum alloys: Microstructure studies and mechanical characterizations. Mater Charact 2015;101:189–207.
[404] Paradiso V, Rubino F, Carlone P, Palazzo GS. Magnesium and aluminium alloys dissimilar joining by friction stir welding. Proc Eng 2017;183:239–44.
[405] Yong Y, Zhang D-T, Cheng Q, Zhang W. Dissimilar friction stir welding between 5052 aluminum alloy and AZ31 magnesium alloy. Trans Nonferrous Met Soc China 2010;20:s619–23.
[406] Aghajani Derazkola H, Eyvazian A, Simchi A. Submerged friction stir welding of dissimilar joints between an Al-Mg alloy and low carbon steel: Thermo-mechanical modeling, microstructural features, and mechanical properties. J Manuf Processes 2020;50:68–79.
[407] Chen W, Wang W, Liu Z, An D, Shi N, Zhang T, et al. Microstructure evolution mechanism of Al/Mg dissimilar joint during friction stir welding. Metall Res Technol 2020;117:311.
[408] Regev M, El Mehtedi M, Cabibbo M, Quercetti G, Ciccarelli D, Spigarelli S. High temperature plasticity of bimetallic magnesium and aluminum friction stir welded joints. Metall Mater Trans A 2014;45:752–64.
[409] Azizieh M, Alavijeh AS, Abbasi M, Balak Z, Kim HS. Mechanical properties and microstructural evaluation of AA1100 to AZ31 dissimilar friction stir welds. Mater Chem Phys 2016;170:251–60.
[410] Liang Z, Chen K, Wang X, Yao J, Yang Q, Zhang L, et al. Effect of tool offset and tool rotational speed on enhancing mechanical property of Al/Mg dissimilar FSW joints. Metall Mater Trans A 2013;44:3721–31.
[411] Morishige T, Kawaguchi A, Tsujikawa M, Hino M, Hirata T, Higashi K. Dissimilar welding of Al and Mg alloys by FSW. Mater Trans 2008.
[412] Simoncini M, Forcellese A. Effect of the welding parameters and tool configuration on micro-and macro-mechanical properties of similar and dissimilar FSWed joints in AA5754 and AZ31 thin sheets. Mater Des 2012;41:50–60.
[413] Pourahmad P, Abbasi M. Materials flow and phase transformation in friction stir welding of Al 6013/Mg. Trans Nonferrous Met Soc China 2013;23:1253–61.
[414] Sameer MD, Birru AK. Mechanical and metallurgical properties of friction stir welded dissimilar joints of AZ91 magnesium alloy and AA 6082–T6 aluminium alloy. J Magnesium Alloys 2019.
[415] Abdollahzadeh A, Shokuhfar A, Cabrera JM, Zhilyaev AP, Omidvar H. The effect of changing chemical composition on dissimilar Mg/Al friction stir welded butt joints using zinc interlayer. J Manuf Processes 2018;34:18–30.
[416] Chang W-S, Rajesh S, Chun C-K, Kim H-J. Microstructure and mechanical properties of hybrid laser-friction stir welding between AA6061-T6 Al alloy and AZ31 Mg alloy. J Mater Sci Technol 2011;27:199–204.

[417] Gao Y, Morisada Y, Fujii H, Liao J. Dissimilar friction stir lap welding of magnesium to aluminum using plasma electrolytic oxidation interlayer. Mater Sci Eng, A 2018;711:109–18.
[418] Springer H, Kostka A, Dos Santos JF, Raabe D. Influence of intermetallic phases and Kirkendall-porosity on the mechanical properties of joints between steel and aluminium alloys. Mater Sci Eng, A 2011;528:4630–42.
[419] Liu X, Lan S, Ni J. Electrically assisted friction stir welding for joining Al 6061 to TRIP 780 steel. J Mater Process Technol 2015;219:112–23.
[420] Mehta KP, Carlone P, Astarita A, Scherillo F, Rubino F, Vora P. Conventional and cooling assisted friction stir welding of AA6061 and AZ31B alloys. Mater Sci Eng, A 2019;759:252–61.
[421] Zhao Y, Lu Z, Yan K, Huang L. Microstructural characterizations and mechanical properties in underwater friction stir welding of aluminum and magnesium dissimilar alloys. Mater Des (1980–2015) 2015;65:675–81.
[422] Zhao Y, Jiang S, Yang S, Lu Z, Yan K. Influence of cooling conditions on joint properties and microstructures of aluminum and magnesium dissimilar alloys by friction stir welding. Int J Adv Manuf Technol 2016;83:673–9.
[423] Niu S, Ji S, Yan D, Meng X, Xiong X. AZ31B/7075-T6 alloys friction stir lap welding with a zinc interlayer. J Mater Process Technol 2019;263:82–90.
[424] Liu Z, Meng X, Ji S, Li Z, Wang L. Improving tensile properties of Al/Mg joint by smashing intermetallic compounds via ultrasonic-assisted stationary shoulder friction stir welding. J Manuf Processes 2018;31:552–9.
[425] Ji S, Meng X, Liu Z, Huang R, Li Z. Dissimilar friction stir welding of 6061 aluminum alloy and AZ31 magnesium alloy assisted with ultrasonic. Mater Lett 2017;201:173–6.
[426] Lv XQ, Wu CS, Padhy GK. Diminishing intermetallic compound layer in ultrasonic vibration enhanced friction stir welding of aluminum alloy to magnesium alloy. Mater Lett 2017;203:81–4.
[427] Lv X, Wu C, Yang C, Padhy GK. Weld microstructure and mechanical properties in ultrasonic enhanced friction stir welding of Al alloy to Mg alloy. J Mater Process Technol 2018;254:145–57.
[428] Huang EW, Chou HS, Tu KN, Hung WS, Lam TN, Tsai CW, et al. Element Effects on High-Entropy Alloy Vacancy and Heterogeneous Lattice Distortion Subjected to Quasi-equilibrium Heating. Sci Rep 2019;9:1–10.
[429] Ji S, Niu S, Liu J. Dissimilar Al/Mg alloys friction stir lap welding with Zn foil assisted by ultrasonic. J Mater Sci Technol 2019;35:1712–8.
[430] Xue P, Ni DR, Wang D, Xiao BL, Ma ZY. Effect of friction stir welding parameters on the microstructure and mechanical properties of the dissimilar Al–Cu joints. Mater Sci Eng, A 2011;528:4683–9.
[431] Murr LE, Flores RD, Flores OV, McClure JC, Liu G, Brown D. Friction-stir welding: microstructural characterization. Mater Res Innov 1998;1:211–23.
[432] Mehta KP, Badheka VJ. A review on dissimilar friction stir welding of copper to aluminum: process, properties, and variants. Mater Manuf Processes 2016;31:233–54.
[433] Sharma N, Siddiquee AN. Friction stir welding of aluminum to copper—an overview. Trans Nonferr Met Soc China 2017;27:2113–36.
[434] Galvao I, Leal RM, Loureiro A, Rodrigues DM. Material flow in heterogeneous friction stir welding of aluminium and copper thin sheets. Sci Technol Weld Joining 2010;15:654–60.
[435] Beygi R, Kazeminezhad M, Kokabi AH. Butt joining of Al–Cu bilayer sheet through friction stir welding. Trans Nonferrous Met Soc China 2012;22:2925–9.
[436] Xue P, Xiao BL, Ni DR, Ma ZY. Enhanced mechanical properties of friction stir welded dissimilar Al–Cu joint by intermetallic compounds. Mater Sci Eng, A 2010;527:5723–7.
[437] Carlone P, Astarita A, Palazzo GS, Paradiso V, Squillace A. Microstructural aspects in Al–Cu dissimilar joining by FSW. Int J Adv Manuf Technol 2015;79:1109–16.
[438] Zhang W, Shen Y, Yan Y, Guo R. Dissimilar friction stir welding of 6061 Al to T2 pure Cu adopting tooth-shaped joint configuration: Microstructure and mechanical properties. Mater Sci Eng, A 2017;690:355–64.
[439] Ouyang J, Yarrapareddy E, Kovacevic R. Microstructural evolution in the friction stir welded 6061 aluminum alloy (T6-temper condition) to copper. J Mater Process Technol 2006;172:110–22.
[440] Shojaeefard MH, Khalkhali A, Akbari M, Tahani M. Application of Taguchi optimization technique in determining aluminum to brass friction stir welding parameters. Mater Des (1980–2015) 2013;52:587–92.
[441] Muthu MFX, Jayabalan V. Tool travel speed effects on the microstructure of friction stir welded aluminum–copper joints. J Mater Process Technol 2015;217:105–13.
[442] Fotouhi Y, Rasaee S, Askari A, Bisadi H. Effect of transverse speed of the tool on microstructure and mechanical properties in dissimilar butt friction stir welding of al5083–copper sheets. Eng Solid Mech 2014;2:239–46.
[443] Fotoohi Y, Rasaee S, Bisadi H, Zahedi M. Effect of friction stir welding parameters on the mechanical properties and microstructure of the dissimilar Al5083–copper butt joint. Proc Inst Mech Eng, Part L: J Mater: Des Appl 2014;228:334-40.
[444] Bisadi H, Rasaee S, Fotoohi Y. Studying of tool rotation speed on mechanical properties of copper–Al5083 butt joint welded by friction stir welding. Proc Inst Mech Eng, Part B: J Eng Manuf 2015;229:1734–41.
[445] Liu P, Shi Q, Wang W, Wang X, Zhang Z. Microstructure and XRD analysis of FSW joints for copper T2/aluminium 5A06 dissimilar materials. Mater Lett 2008;62:4106–8.
[446] Galvao I, Oliveira JC, Loureiro A, Rodrigues DM. Formation and distribution of brittle structures in friction stir welding of aluminium and copper: influence of process parameters. Sci Technol Weld Joining 2011;16:681–9.
[447] Akinlabi ET, Akinlabi SA. Effect of heat input on the properties of dissimilar friction stir welds of aluminium and copper. Am J Mater Sci 2012;2:147–52.
[448] Sinha VC, Kundu S, Chatterjee S. Microstructure and mechanical properties of similar and dissimilar joints of aluminium alloy and pure copper by friction stir welding. Perspect Sci 2016;8:543–6.
[449] Bhattacharya TK, Das H, Pal TK. Influence of welding parameters on material flow, mechanical property and intermetallic characterization of friction stir welded AA6063 to HCP copper dissimilar butt joint without offset. Trans Nonferrous Met Soc China 2015;25:2833–46.
[450] Galvão I, Loureiro A, Verdera D, Gesto D, Rodrigues DM. Influence of tool offsetting on the structure and morphology of dissimilar aluminum to copper friction-stir welds. Metall Mater Trans A 2012;43:5096–105.
[451] Lee W-B, Jung S-B. Void free friction stir weld zone of the dissimilar 6061 aluminum and copper joint by shifting the tool insertion location. Mater Res Innovations 2004;8:93–6.
[452] Barekatain H, Kazeminezhad M, Kokabi AH. Microstructure and mechanical properties in dissimilar butt friction stir welding of severely plastic deformed aluminum AA 1050 and commercially pure copper sheets. J Mater Sci Technol 2014;30:826–34.
[453] Firouzdor V, Kou S. Al-to-Cu friction stir lap welding. Metall Mater Trans A 2012;43:303–15.
[454] Sahu PK, Pal S, Pal SK, Jain R. Influence of plate position, tool offset and tool rotational speed on mechanical properties and microstructures of dissimilar Al/Cu friction stir welding joints. J Mater Process Technol 2016;235:55–67.
[455] Li X-w, Zhang D-t, Cheng Q, Zhang W. Microstructure and mechanical properties of dissimilar pure copper/1350 aluminum alloy butt joints by friction stir welding. Trans Nonferrous Met Soc China 2012;22:1298–306.
[456] Tan CW, Jiang ZG, Li LQ, Chen YB, Chen XY. Microstructural evolution and mechanical properties of dissimilar Al–Cu joints produced by friction stir welding. Mater Des 2013;51:466–73.
[457] Esmaeili A, Givi MKB, Rajani HRZ. A metallurgical and mechanical study on dissimilar Friction Stir welding of aluminum 1050 to brass (CuZn30). Mater Sci Eng, A 2011;528:7093–102.
[458] Çakan A, Atmaca H, Uğurlu M. Analysis and joining of Al–Cu plates using friction-stir welding technique. Europ Mech Sci 2:1-8.
[459] Kumar N, Dhuria GK, Singh R. Evaluation of tensile strength in friction stir welded aluminum alloy 6101–T6 and commercially pure copper joints. Mater Today: Proc 2018;5:19230–6.
[460] Zhang Q-z, Gong W-b, Wei L. Microstructure and mechanical properties of dissimilar Al–Cu joints by friction stir welding. Trans Nonferrous Met Soc China 2015;25:1779–86.

[461] Muthu MFX, Jayabalan V. Effect of pin profile and process parameters on microstructure and mechanical properties of friction stir welded Al–Cu joints. Trans Nonferrous Met Soc China 2016;26:984–93.
[462] Mehta KP, Badheka VJ. Effects of tool pin design on formation of defects in dissimilar friction stir welding. Proc Technol 2016;23:513–8.
[463] Mehta KP, Badheka VJ. Influence of tool pin design on properties of dissimilar copper to aluminum friction stir welding. Trans Nonferrous Met Soc China 2017;27:36–54.
[464] Akinlabi ET, Andrews A, Akinlabi SA. Effects of processing parameters on corrosion properties of dissimilar friction stir welds of aluminium and copper. Trans Nonferrous Met Soc China 2014;24:1323–30.
[465] Beygi R, Kazeminezhad M, Kokabi AH, Loureiro A. Friction stir welding of Al-Cu bilayer sheet by tapered threaded pin: microstructure, material flow, and fracture behavior. Metall Mater Trans A 2015;46:2544–53.
[466] Mehta KP, Badheka VJ. Hybrid approaches of assisted heating and cooling for friction stir welding of copper to aluminum joints. J Mater Process Technol 2017;239:336–45.
[467] Al-Roubaiy AO, Nabat SM, Batako ADL. Experimental and theoretical analysis of friction stir welding of Al–Cu joints. Int J Adv Manuf Technol 2014;71:1631–42.
[468] Liu HJ, Shen JJ, Xie S, Huang YX, Cui F, Liu C, et al. Weld appearance and microstructural characteristics of friction stir butt barrier welded joints of aluminium alloy to copper. Sci Technol Weld Joining 2012;17:104–10.
[469] Girard M, Huneau B, Genevois C, Sauvage X, Racineux G. Friction stir diffusion bonding of dissimilar metals. Sci Technol Weld Joining 2010;15:661–5.
[470] Avettand-Fènoël MN, Taillard R, Ji G. Quality of interfaces in Cu/Al dissimilar friction-stirred welds. Materials Science Forum. Trans Tech Publ; 2012. p. 959–64.
[471] Genevois C, Girard M, Huneau B, Sauvage X, Racineux G. Interfacial reaction during friction stir welding of Al and Cu. Metall Mater Trans A 2011;42:2290.
[472] Safi SV, Amirabadi H, Kazem MBG. Formation and distribution of brittle structures in friction stir welding of AA 6061 to copper. Influence of preheat. Mech, Mater Sci Eng J 2016.
[473] Zhao X, Dong FB, Su GY, Guo LJ. Weld quality improvement with hybrid FSW technology assisted by preheating for copper T2/aluminium 5A06 dissimilar materials. Applied Mechanics and Materials. Trans Tech Publ; 2012. p. 1707–11.
[474] Muhammad NA, Wu CS. Ultrasonic vibration assisted friction stir welding of aluminium alloy and pure copper. J Manuf Processes 2019;39:114–27.
[475] Muhammad NA, Wu CS, Tian W. Effect of ultrasonic vibration on the intermetallic compound layer formation in Al/Cu friction stir weld joints. J Alloy Compd 2019;785:512–22.
[476] Liu W, Ma J, Atabaki MM, Kovacevic R. Joining of advanced high-strength steel to AA 6061 alloy by using Fe/Al structural transition joint. Mater Des 2015;68:146–57.
[477] Atabaki MM, Nikodinovski M, Chenier P, Ma J, Harooni M, Kovacevic R. Welding of aluminum alloys to steels: an overview. J Manuf Sci Prod 2014;14:59–78.
[478] Hussein SA, Tahir ASM, Hadzley AB. Characteristics of aluminum-to-steel joint made by friction stir welding: A review. Mater Today Commun 2015;5:32–49.
[479] Lee C-Y, Choi D-H, Yeon Y-M, Jung S-B. Dissimilar friction stir spot welding of low carbon steel and Al–Mg alloy by formation of IMCs. Sci Technol Weld Joining 2009;14:216–20.
[480] Lee W-B, Schmuecker M, Mercardo UA, Biallas G, Jung S-B. Interfacial reaction in steel–aluminum joints made by friction stir welding. Scr Mater 2006;55:355–8.
[481] Jiang WH, Kovacevic R. Feasibility study of friction stir welding of 6061–T6 aluminium alloy with AISI 1018 steel. Proc Inst Mech Eng, Part B: J Eng Manuf 2004;218:1323–31.
[482] Kimapong K, Watanabe T. Friction stir welding of aluminum alloy to steel. Welding J 2004;83:277.
[483] Uzun H, Dalle Donne C, Argagnotto A, Ghidini T, Gambaro C. Friction stir welding of dissimilar Al 6013–T4 to X5CrNi18-10 stainless steel. Mater Des 2005;26:41–6.
[484] Chen CM, Kovacevic R. Joining of Al 6061 alloy to AISI 1018 steel by combined effects of fusion and solid state welding. Int J Mach Tools Manuf 2004;44:1205–14.
[485] Watanabe T, Takayama H, Yanagisawa A. Joining of aluminum alloy to steel by friction stir welding. J Mater Process Technol 2006;178:342–9.
[486] Liu X, Lan S, Ni J. Analysis of process parameters effects on friction stir welding of dissimilar aluminum alloy to advanced high strength steel. Mater Des 2014;59:50–62.
[487] Dehghani M, Amadeh A, Mousavi SAAA. Investigations on the effects of friction stir welding parameters on intermetallic and defect formation in joining aluminum alloy to mild steel. Mater Des 2013;49:433–41.
[488] Shen Z, Chen Y, Haghshenas M, Gerlich AP. Role of welding parameters on interfacial bonding in dissimilar steel/aluminum friction stir welds. Eng Sci Technol, Int J 2015;18:270–7.
[489] Tanaka T, Morishige T, Hirata T. Comprehensive analysis of joint strength for dissimilar friction stir welds of mild steel to aluminum alloys. Scr Mater 2009;61:756–9.
[490] Zhao S, Ni J, Wang G, Wang Y, Bi Q, Zhao Y, et al. Effects of tool geometry on friction stir welding of AA6061 to TRIP steel. J Mater Process Technol 2018;261:39–49.
[491] Pourali M, Abdollah-Zadeh A, Saeid T, Kargar F. Influence of welding parameters on intermetallic compounds formation in dissimilar steel/aluminum friction stir welds. J Alloy Compd 2017;715:1–8.
[492] Yazdipour A, Heidarzadeh A. Effect of friction stir welding on microstructure and mechanical properties of dissimilar Al 5083–H321 and 316L stainless steel alloy joints. J Alloy Compd 2016;680:595–603.
[493] Ramachandran KK, Murugan N, Kumar SS. Influence of tool traverse speed on the characteristics of dissimilar friction stir welded aluminium alloy, AA5052 and HSLA steel joints. Arch Civ Mech Eng 2015;15:822–30.
[494] Ramachandran KK, Murugan N, Kumar SS. Effect of tool axis offset and geometry of tool pin profile on the characteristics of friction stir welded dissimilar joints of aluminum alloy AA5052 and HSLA steel. Mater Sci Eng: A 2015;639:219–33.
[495] Fei X, Jin X, Ye Y, Xiu T, Yang H. Effect of pre-hole offset on the property of the joint during laser-assisted friction stir welding of dissimilar metals steel and aluminum alloys. Mater Sci Eng, A 2016;653:43–52.
[496] Dehghani M, Mousavi SAAA, Amadeh A. Effects of welding parameters and tool geometry on properties of 3003–H18 aluminum alloy to mild steel friction stir weld. Trans Nonferrous Met Soc China 2013;23:1957–65.
[497] Coelho RS, Kostka A, Dos Santos JF, Kaysser-Pyzalla A. Friction-stir dissimilar welding of aluminium alloy to high strength steels: Mechanical properties and their relation to microstructure. Mater Sci Eng, A 2012;556:175–83.
[498] Kakiuchi T, Uematsu Y, Suzuki K. Evaluation of fatigue crack propagation in dissimilar Al/steel friction stir welds. Proc Struct Integrity 2016;2:1007–14.
[499] Hj AVAL, Loureiro A. Effect of reverse dual rotation process on properties of friction stir welding of AA7075 to AISI304. Trans Nonferrous Met Soc China 2019;29:964–75.
[500] Anaman SY, Cho H-H, Das H, Lee J-S, Hong S-T. Microstructure and mechanical/electrochemical properties of friction stir butt welded joint of dissimilar aluminum and steel alloys. Mater Charact 2019.
[501] Kundu S, Roy D, Bhola R, Bhattacharjee D, Mishra B, Chatterjee S. Microstructure and tensile strength of friction stir welded joints between interstitial free steel and commercially pure aluminium. Mater Des 2013;50:370–5.
[502] Tang J, Shen Y. Effects of preheating treatment on temperature distribution and material flow of aluminum alloy and steel friction stir welds. J Manuf Processes 2017;29:29–40.
[503] Wang H, Qin G, Geng P, Ma X. Interfacial microstructures and mechanical properties of friction welded Al/steel dissimilar joints. J Manuf Processes 2020;49:18–25.
[504] Tanaka T, Nezu M, Uchida S, Hirata T. Mechanism of intermetallic compound formation during the dissimilar friction stir welding of aluminum and steel. J Mater Sci 2020;55:3064–72.

[505] Yazdipour A, Heidarzadeh A. Dissimilar butt friction stir welding of Al 5083–H321 and 316L stainless steel alloys. Int J Adv Manuf Technol 2016;87:3105–12.
[506] Abbasi M, Dehghani M, Guim H-U, Kim D-I. Investigation of Fe-rich fragments in aluminum-steel friction stir welds via simultaneous Transmission Kikuchi Diffraction and EDS. Acta Mater 2016;117:262–9.
[507] Bang H, Bang H, Jeon G, Oh I, Ro C. Gas tungsten arc welding assisted hybrid friction stir welding of dissimilar materials Al6061-T6 aluminum alloy and STS304 stainless steel. Mater Des 2012;37:48–55.
[508] Merklein M, Giera A. Laser assisted Friction Stir Welding of drawable steel-aluminium tailored hybrids. Int J Mater Form 2008;1:1299–302.
[509] Derazkola HA, Khodabakhshi F. Underwater submerged dissimilar friction-stir welding of AA5083 aluminum alloy and A441 AISI steel. Int J Adv Manuf Technol 2019;102:4383–95.
[510] Thomä M, Wagner G, Strass B, Wolter B, Benfer S, Fuerbeth W. Ultrasound enhanced friction stir welding of aluminum and steel: Process and properties of EN AW 6061/DC04-Joints. J Mater Sci Technol 2018;34:163–72.
[511] Matsuda T, Owada K, Numata A, Shoji H, Sano T, Ohata M, et al. Influence of interfacial structure on the fracture behavior of friction stir spot welded dissimilar joints. Mater Sci Eng, A 2020;772:138743.
[512] Das H, Ghosh R, Pal T. Study on the formation and characterization of the intermetallics in friction stir welding of aluminum alloy to coated steel sheet lap joint. Metall Mater Trans A 2014;45:5098–106.
[513] Chen Y, Nakata K. Effect of the surface state of steel on the microstructure and mechanical properties of dissimilar metal lap joints of aluminum and steel by friction stir welding. Metall Mater Trans A 2008;39:1985.
[514] Wu A, Song Z, Nakata K, Liao J, Zhou L. Interface and properties of the friction stir welded joints of titanium alloy Ti6Al4V with aluminum alloy 6061. Mater Des 2015;71:85–92.
[515] Dressler U, Biallas G, Mercado UA. Friction stir welding of titanium alloy TiAl6V4 to aluminium alloy AA2024-T3. Mater Sci Eng, A 2009;526:113–7.
[516] Song Z, Nakata K, Wu A, Liao J, Zhou L. Influence of probe offset distance on interfacial microstructure and mechanical properties of friction stir butt welded joint of Ti6Al4V and A6061 dissimilar alloys. Mater Des 2014;57:269–78.
[517] Choi J-W, Liu H, Fujii H. Dissimilar friction stir welding of pure Ti and pure Al. Mater Sci Eng, A 2018;730:168–76.
[518] Li B, Zhang Z, Shen Y, Hu W, Luo L. Dissimilar friction stir welding of Ti–6Al–4V alloy and aluminum alloy employing a modified butt joint configuration: Influences of process variables on the weld interfaces and tensile properties. Mater Des 2014;53:838–48.
[519] Kar A, Choudhury SK, Suwas S, Kailas SV. Effect of niobium interlayer in dissimilar friction stir welding of aluminum to titanium. Mater Charact 2018;145:402–12.
[520] Kar A, Suwas S, Kailas SV. Two-pass friction stir welding of aluminum alloy to titanium alloy: A simultaneous improvement in mechanical properties. Mater Sci Eng, A 2018;733:199–210.
[521] Bang H, Bang H, Song H, Joo S. Joint properties of dissimilar Al6061-T6 aluminum alloy/Ti–6% Al–4% V titanium alloy by gas tungsten arc welding assisted hybrid friction stir welding. Mater Des 2013;51:544–51.
[522] Ma Z, Jin Y, Ji S, Meng X, Ma L, Li Q. A general strategy for the reliable joining of Al/Ti dissimilar alloys via ultrasonic assisted friction stir welding. J Mater Sci Technol 2019;35:94–9.
[523] Khodabakhshi F, Marzbanrad B, Yazdanmehr A, Jahed H, Gerlich AP. Tailoring the residual stress during two-step cold gas spraying and friction-stir surface integration of titanium coating. Surf Coat Technol 2019;380:125008.
[524] Yu M, Zhao H, Jiang Z, Guo F, Zhou L, Song X. Microstructure and mechanical properties of friction stir lap AA6061-Ti6Al4V welds. J Mater Process Technol 2019;270:274–84.
[525] Chen Y, Liu C, Liu G. Study on the joining of titanium and aluminum dissimilar alloys by friction stir welding. Open Mater Sci J 2011;5.
[526] Sadeghi-Ghogheri M, Kasiri-Asgarani M, Amini K. Friction stir welding of dissimilar joint of aluminum alloy 5083 and commercially pure titanium. Kovove Mater 2016;54:71–5.
[527] Pereira VF, Fonseca EB, Costa AM, Bettini J, Lopes ES. Nanocrystalline structural layer acts as interfacial bond in Ti/Al dissimilar joints produced by friction stir welding in power control mode. Scr Mater 2020;174:80–6.
[528] Kar A, Suwas S, Kailas SV. Multi-Length Scale Characterization of Microstructure Evolution and Its Consequence on Mechanical Properties in Dissimilar Friction Stir Welding of Titanium to Aluminum. Metall Mater Trans A 2019;50:5153–73.
[529] Chen YH, Yu L, Ni Q. Influence of zinc on the microstructure and brittle phases of friction stir welded joint of Al/Ti dissimilar alloys. Advanced Materials Research. Trans Tech Publ; 2012. p. 439–43.
[530] Yu M, Zhao H, Xu F, Chen T, Zhou L, Song X, et al. Influence of ultrasonic vibrations on the microstructure and mechanical properties of Al/Ti friction stir lap welds. J Mater Process Technol 2020;282:116676.
[531] Li S, Chen Y, Zhou X, Kang J, Huang Y, Deng H. High-strength titanium alloy/steel butt joint produced via friction stir welding. Mater Lett 2019;234:155–8.
[532] Li S, Chen Y, Kang J, Huang Y, Gianetto JA, Yin L. Interfacial microstructures and mechanical properties of dissimilar titanium alloy and steel friction stir butt-welds. J Manuf Processes 2019;40:160–8.
[533] Gotawala N, Shrivastava A. Microstructural analysis and mechanical behavior of SS 304 and titanium joint from friction stir butt welding. Mater Sci Eng, A 2020;789:139658.
[534] Ishida K, Gao Y, Nagatsuka K, Takahashi M, Nakata K. Microstructures and mechanical properties of friction stir welded lap joints of commercially pure titanium and 304 stainless steel. J Alloy Compd 2015;630:172–7.
[535] Kasai H, Morisada Y, Fujii H. Dissimilar FSW of immiscible materials: steel/magnesium. Mater Sci Eng, A 2015;624:250–5.
[536] Wang T, Shukla S, Gwalani B, Komarasamy M, Reza-Nieto L, Mishra RS. Effect of reactive alloy elements on friction stir welded butt joints of metallurgically immiscible magnesium alloys and steel. J Manuf Processes 2019;39:138–45.
[537] Xu R, Ni D, Yang Q, Xiao B, Liu C, Ma Z. Influencing mechanism of Al-containing Zn coating on interfacial microstructure and mechanical properties of friction stir spot welded Mg–steel joint. Mater Charact 2018;140:197–206.
[538] Jana S, Hovanski Y, Grant GJ. Friction stir lap welding of magnesium alloy to steel: a preliminary investigation. Metall Mater Trans A 2010;41:3173–82.
[539] Aonuma M, Nakata K. Effect of alloying elements on interface microstructure of Mg–Al–Zn magnesium alloys and titanium joint by friction stir welding. Mater Sci Eng, B 2009;161:46–9.
[540] Aonuma M, Nakata K. Effect of calcium on intermetallic compound layer at interface of calcium added magnesium–aluminum alloy and titanium joint by friction stir welding. Mater Sci Eng, B 2010;173:135–8.
[541] Aonuma M, Nakata K. Dissimilar metal joining of ZK60 magnesium alloy and titanium by friction stir welding. Mater Sci Eng, B 2012;177:543–8.
[542] Li Q, Ma Z, Ji S, Song Q, Gong P, Li R. Effective joining of Mg/Ti dissimilar alloys by friction stir lap welding. J Mater Process Technol 2020;278:116483.
[543] Choi J-W, Liu H, Ushioda K, Fujii H. Effect of an Al filler material on interfacial microstructure and mechanical properties of dissimilar friction stir welded Ti/Mg joint. Mater Charact 2019;155:109801.
[544] Khodabakhshi F, Marzbanrad B, Shah LH, Jahed H, Gerlich AP. Surface Modification of a Cold Gas Dynamic Spray-Deposited Titanium Coating on Aluminum Alloy by using Friction-Stir Processing. J Therm Spray Technol 2019;28:1185–98.
[545] Nascimento F, Santos T, Vilaça P, Miranda RM, Quintino L. Microstructural modification and ductility enhancement of surfaces modified by FSP in aluminium alloys. Mater Sci Eng, A 2009;506:16–22.
[546] Vaira Vignesh R, Padmanaban R, Govindaraju M, Suganya Priyadharshini G. Mechanical properties and corrosion behaviour of AZ91D-HAP surface composites fabricated by friction stir processing. Mater Res Express 2019;6:085401.
[547] Jamili AM, Zarei-Hanzaki A, Abedi HR, Mosayebi M, Kocich R, Kunčická L. Development of fresh and fully recrystallized microstructures through friction stir processing of a rare earth bearing magnesium alloy. Mater Sci Eng, A 2020;775:138837.
[548] Xiong F, Fu R-d, Li Y-J, Sang D-l. Effects of nitrogen alloying and friction stir processing on the microstructures and mechanical properties of CoCrFeMnNi high-entropy alloys. J Alloy Compd 2020.

[549] Vakili-Azghandi M, Roknian M, Szpunar JA, Mousavizade SM. Surface modification of pure titanium via friction stir processing: Microstructure evolution and dry sliding wear performance. J Alloy Compd 2020;816:152557.
[550] Liu K, Nene SS, Frank M, Mishra RS. Effect of Strain Rate on Deformation Response of Metastable High Entropy Alloys Upon Friction Stir Processing. Metall Mater Trans A 2020;51:5043–8.
[551] Sinha S, Nene SS, Frank M, Liu K, Lebensohn RA, Mishra RS. Deformation mechanisms and ductile fracture characteristics of a friction stir processed transformative high entropy alloy. Acta Mater 2020;184:164–78.
[552] Balachandran S, Mishra RS, Banerjee D. Friction stir processing of a metastable β titanium alloy in β and α+β phase fields. Mater Sci Eng, A 2020;772:138705.
[553] Sinha S, Komarasamy M, Thapliyal S, Gwalani B, Shukla S, Darling KA, et al. Immiscible nanostructured copper-aluminum-niobium alloy with excellent precipitation strengthening upon friction stir processing and aging. Scr Mater 2019;164:42–7.
[554] Nene SS, Zellner S, Mondal B, Komarasamy M, Mishra RS, Brennan RE, et al. Friction stir processing of newly-designed Mg-5Al-3.5Ca-1Mn (AXM541) alloy: Microstructure evolution and mechanical properties. Mater Sci Eng, A 2018;729:294–9.
[555] Freeney TA, Mishra RS. Effect of Friction Stir Processing on Microstructure and Mechanical Properties of a Cast-Magnesium–Rare Earth Alloy. Metall Mater Trans A 2009;41:73.
[556] Bhargava G, Yuan W, Webb SS, Mishra RS. Influence of Texture on Mechanical Behavior of Friction-Stir-Processed Magnesium Alloy. Metall Mater Trans A 2009;41:13.
[557] Jana S, Mishra RS, Baumann JB, Grant G. Effect of friction stir processing on fatigue behavior of an investment cast Al–7Si–0.6 Mg alloy. Acta Mater 2010;58:989–1003.
[558] Ma ZY, Liu FC, Mishra RS. Superplastic deformation mechanism of an ultrafine-grained aluminum alloy produced by friction stir processing. Acta Mater 2010;58:4693–704.
[559] Kumar N, Mishra RS, Huskamp CS, Sankaran KK. The effect of friction stir processing on the microstructure and mechanical properties of equal channel angular pressed 5052Al alloy sheet. J Mater Sci 2011;46:5527–33.
[560] Kumar N, Mishra RS, Huskamp CS, Sankaran KK. Microstructure and mechanical behavior of friction stir processed ultrafine grained Al–Mg–Sc alloy. Mater Sci Eng, A 2011;528:5883–7.
[561] Tungala V, Arora A, Gwalani B, Mishra RS, Brennan RE, Cho KC. Microstructure and mechanical properties of friction stir processed cast Eglin steel (ES-1). Mater Sci Eng, A 2018;709:105–14.
[562] Kumar N, Komarasamy M, Nelaturu P, Tang Z, Liaw PK, Mishra RS. Friction Stir Processing of a High Entropy Alloy Al0.1CoCrFeNi. JOM 2015;67:1007–13.
[563] Huang L, Wang K, Wang W, Peng P, Qiao K, Liu Q. Microstructural evolution and corrosion behavior of friction stir processed fine-grained AZ80 Mg alloy. Mater Corros.
[564] Patel V, Li W, Vairis A, Badheka V. Recent Development in Friction Stir Processing as a Solid-State Grain Refinement Technique: Microstructural Evolution and Property Enhancement. Crit Rev Solid State Mater Sci 2019;44:378–426.
[565] Balakrishnan M, Dinaharan I, Palanivel R, Sathiskumar R. Effect of friction stir processing on microstructure and tensile behavior of AA6061/Al3Fe cast aluminum matrix composites. J Alloy Compd 2019;785:531–41.
[566] Saini N, Dwivedi DK, Jain PK, Singh H. Surface Modification of Cast Al-17%Si Alloys Using Friction Stir Processing. Procedia Eng 2015;100:1522–31.
[567] Ma ZY, Mishra RS, Mahoney MW. Superplastic deformation behaviour of friction stir processed 7075Al alloy. Acta Mater 2002;50:4419–30.
[568] Liu FC, Tan MJ, Liao J, Ma ZY, Meng Q, Nakata K. Microstructural evolution and superplastic behavior in friction stir processed Mg–Li–Al–Zn alloy. J Mater Sci 2013;48:8539–46.
[569] Yazdipour A, Shafiei MA, Dehghani K. Modeling the microstructural evolution and effect of cooling rate on the nanograins formed during the friction stir processing of Al5083. Mater Sci Eng, A 2009;527:192–7.
[570] Reed-Hill RE, Abbaschian R. Physical metallurgy principles. Van Nostrand 1973.
[571] Santella ML, Engstrom T, Storjohann D, Pan TY. Effects of friction stir processing on mechanical properties of the cast aluminum alloys A319 and A356. Scr Mater 2005;53:201–6.
[572] Wang Y, Huang Y, Meng X, Wan L, Feng J. Microstructural evolution and mechanical properties of MgZnYZr alloy during friction stir processing. J Alloy Compd 2017;696:875–83.
[573] Khodabakhshi F, Ghasemi Yazdabadi H, Kokabi AH, Simchi A. Friction stir welding of a P/M Al–Al2O3 nanocomposite: Microstructure and mechanical properties. Mater Sci Eng, A 2013;585:222–32.
[574] Khodabakhshi F, Simchi A, Kokabi AH, Gerlich AP, Nosko M, Švec P. Influence of hard inclusions on microstructural characteristics and textural components during dissimilar friction-stir welding of an PM Al–Al_2O_3–SiC hybrid nanocomposite with AA1050 alloy. Sci Technol Weld Joining 2017;22:412–27.
[575] Nadammal N, Kailas SV, Szpunar J, Suwas S. Development of microstructure and texture during single and multiple pass friction stir processing of a strain hardenable aluminium alloy. Mater Charact 2018;140:134–46.
[576] Pradeep S, Pancholi V. Superplastic Forming of Multipass Friction Stir Processed Aluminum-Magnesium Alloy. Metall Mater Trans A 2014;45:6207–16.
[577] Ajay Kumar P, Madhu HC, Pariyar A, Perugu CS, Kailas SV, Garg U, et al. Friction stir processing of squeeze cast A356 with surface compacted graphene nanoplatelets (GNPs) for the synthesis of metal matrix composites. Mater Sci Eng, A 2020;769:138517.
[578] Singh SK, Immanuel RJ, Babu S, Panigrahi SK, Janaki Ram GD. Influence of multi-pass friction stir processing on wear behaviour and machinability of an Al-Si hypoeutectic A356 alloy. J Mater Process Technol 2016;236:252–62.
[579] Guru PR, Khan MdF, Panigrahi SK, Ram GDJ. Enhancing strength, ductility and machinability of a Al-Si cast alloy by friction stir processing. J Manuf Processes 2015;18:67–74.
[580] Meenia S, Khan MdF, Babu S, Immanuel RJ, Panigrahi SK, Janaki Ram GD. Particle refinement and fine-grain formation leading to enhanced mechanical behaviour in a hypo-eutectic Al-Si alloy subjected to multi-pass friction stir processing. Mater Charact 2016;113:134–43.
[581] Kopysciański M, Węglowski MS, Dziadosz M, Małyszko M, Dymek S. Electron microscopy investigation of a cast AlSi9Mg aluminum alloy subjected to friction stir processing with overlapping passes. Int J Mater Res 2015;106:813–7.
[582] Malopheyev S, Kulitskiy V, Mironov S, Zhemchuzhnikova D, Kaibyshev R. Friction-stir welding of an Al-Mg-Sc-Zr alloy in as-fabricated and work-hardened conditions. Mater Sci Eng, A 2014;600:159–70.
[583] Malopheyev S, Mironov S, Kulitskiy V, Kaibyshev R. Friction-stir welding of ultra-fine grained sheets of Al-Mg-Sc-Zr alloy. Mater Sci Eng, A 2015;624:132–9.
[584] Ebrahimi M, Par MA. Twenty-year uninterrupted endeavor of friction stir processing by focusing on copper and its alloys. J Alloy Compd 2019;781:1074–90.
[585] Leal RM, Galvão I, Loureiro A, Rodrigues DM. Effect of friction stir processing parameters on the microstructural and electrical properties of copper. Int J Adv Manuf Technol 2015;80:1655–63.
[586] Cao G, Zhang L, Zhang D, Liu Y, Gao J, Li W, et al. Microstructure and properties of nano-hydroxyapatite reinforced WE43 alloy fabricated by friction stir processing. Materials 2019;12.
[587] Lipscomb CA, Fortier A, Kong F, Das S, Kumar N, Mishra RS. Evaluation of plastic zone development in WE43 magnesium alloy upon friction stir processing using finite element modeling. Mater Sci Eng, A 2016;673:178–84.
[588] Darras B, Kishta E. Submerged friction stir processing of AZ31 Magnesium alloy. Mater Des 2013;47:133–7.
[589] Luo XC, Zhang DT, Cao GH, Qiu C, Chen DL. High-temperature tensile behavior of AZ61 magnesium plate prepared by multi-pass friction stir processing. Mater Sci Eng, A 2019;759:234–40.
[590] Luo XC, Zhang DT, Cao GH, Qiu C, Chen DL. Multi-pass submerged friction stir processing of AZ61 magnesium alloy: strengthening mechanisms and fracture behavior. J Mater Sci 2019;54:8640–54.
[591] Liu Q, Ma QX, Chen GQ, Cao X, Zhang S, Pan JL, et al. Enhanced corrosion resistance of AZ91 magnesium alloy through refinement and homogenization of surface microstructure by friction stir processing. Corros Sci 2018;138:284–96.
[592] Raja A, Biswas P, Pancholi V. Effect of layered microstructure on the superplasticity of friction stir processed AZ91 magnesium alloy. Mater Sci Eng, A 2018;725:492–502.

[593] Liu FC, Tan MJ, Liao J, Ma ZY, Meng Q, Nakata K. Microstructural evolution and superplastic behavior in friction stir processed Mg-Li-Al-Zn alloy. J Mater Sci 2013;48:8539–46.
[594] Grewal HS, Arora HS, Singh H, Agrawal A. Surface modification of hydroturbine steel using friction stir processing. Appl Surf Sci 2013;268:547–55.
[595] Nagaoka T, Kimoto Y, Watanabe H, Fukusumi M, Morisada Y, Fujii H. Friction stir processing of a D2 tool steel layer fabricated by laser cladding. Mater Des 2015;83:224–9.
[596] Yasavol N, Abdollah-Zadeh A, Vieira MTF, Jafarian HR. Microstructure evolution and texture development in a friction stir-processed AISI D2 tool steel. Appl Surf Sci 2014;293:151–9.
[597] Khodabakhshi F, Rahmati R, Nosko M, Orovčík L, Nagy Š, Gerlich AP. Orientation structural mapping and textural characterization of a CP-Ti/HA surface nanocomposite produced by friction-stir processing. Surf Coat Technol 2019;374:460–75.
[598] Mironov S, Sato YS, Kokawa H. Friction-stir welding and processing of Ti-6Al-4V titanium alloy: A review. J Mater Sci Technol 2018;34:58–72.
[599] Nandan R, DebRoy T, Bhadeshia HKDH. Recent advances in friction-stir welding – Process, weldment structure and properties. Prog Mater Sci 2008;53:980–1023.
[600] Abbas A, Huang SJ, Ballóková B, Sülleiová K. Tribological effects of carbon nanotubes on magnesium alloy AZ31 and analyzing aging effects on CNTs/AZ31 composites fabricated by stir casting process. Tribol Int 2020;142.
[601] Arokiasamy S, Anand Ronald B. Experimental investigations on the enhancement of mechanical properties of magnesium-based hybrid metal matrix composites through friction stir processing. Int J Adv Manuf Technol 2017;93:493–503.
[602] Ashok Kumar G, Dinaharan I, Vijay SJ, Murugan N. Friction stir processing of intermetallic particulate reinforced aluminum matrix composite. Adv Mater Lett 2013;4:230–4.
[603] Balakrishnan M, Dinaharan I, Palanivel R, Sathiskumar R. Influence of friction stir processing on microstructure and tensile behavior of AA6061/Al3Zr cast aluminum matrix composites. J Manuf Processes 2019;38:148–57.
[604] Bauri R, Yadav D, Suhas G. Effect of friction stir processing (FSP) on microstructure and properties of Al-TiC in situ composite. Mater Sci Eng, A 2011;528:4732–9.
[605] Chelliah NM, Singh H, Raj R, Surappa MK. Processing, microstructural evolution and strength properties of in-situ magnesium matrix composites containing nano-sized polymer derived SiCNO particles. Mater Sci Eng, A 2017;685:429–38.
[606] Dinaharan I, Ashok Kumar G, Vijay SJ, Murugan N. Development of Al3Ti and Al3Zr intermetallic particulate reinforced aluminum alloy AA6061 in situ composites using friction stir processing. Mater Des 2014;63:213–22.
[607] Dinaharan I, Balakrishnan M, David Raja Selvam J, Akinlabi ET. Microstructural characterization and tensile behavior of friction stir processed AA6061/Al_2Cu cast aluminum matrix composites. J Alloy Compd 2019;781:270–9.
[608] Golmohammadi M, Atapour M, Ashrafi A. Fabrication and wear characterization of an A413/Ni surface metal matrix composite fabricated via friction stir processing. Mater Des 2015;85:471–82.
[609] Huang Y, Li J, Wan L, Meng X, Xie Y. Strengthening and toughening mechanisms of CNTs/Mg-6Zn composites via friction stir processing. Mater Sci Eng, A 2018;732:205–11.
[610] Juang SH, Xue CS. Investigation of mechanical properties and microstructures of aluminum-fly ash composite processed by friction stirring. Mater Sci Eng, A 2015;640:314–9.
[611] Karbalaei Akbari M, Rajabi S, Shirvanimoghaddam K, Baharvandi HR. Wear and friction behavior of nanosized TiB_2 and TiO_2 particle-reinforced casting A356 aluminum nanocomposites: A comparative study focusing on particle capture in matrix. J Compos Mater 2015;49:3665–81.
[612] Prabakaran RK, Sait AN, Senthilkumar V. Synthesis and Characterization of High Entropy Alloy (CrMnFeNiCu) Reinforced AA6061 Aluminium Matrix Composite. Mech Mech Eng 2017;21:823–32.
[613] Rajeshkumar R, Udhayabanu V, Srinivasan A, Ravi KR. Microstructural evolution in ultrafine grained Al-Graphite composite synthesized via combined use of ultrasonic treatment and friction stir processing. J Alloy Compd 2017;726:358–66.
[614] Sarmadi H, Kokabi AH, Seyed Reihani SM. Friction and wear performance of copper-graphite surface composites fabricated by friction stir processing (FSP). Wear 2013;304:1–12.
[615] Sharma S, Nanda T, Pandey OP. Investigation of T4 and T6 heat treatment on the wear properties of sillimanite reinforced LM30 aluminium alloy composites. Wear 2019;426–427:27–36.
[616] Singh S, Pal K. Influence of surface morphology and UFG on damping and mechanical properties of composite reinforced with spinel MgAl<inf>2</inf>O<inf>4</inf>-SiC core-shell microcomposites. Mater Charact 2017;123:244–55.
[617] Sun N, Apelian D. Friction stir processing of aluminum cast alloys for high performance applications. JOM 2011;63:44–50.
[618] Venkatesh C, Venkatesan R. Optimization of process parameters of hot extrusion of SiC/Al 6061 composite using Taguchi's technique and upper bound technique. Mater Manuf Processes 2015;30:85–92.
[619] Vijayavel P, Balasubramanian V. Effect of pin profile volume ratio on microstructure and tensile properties of friction stir processed aluminum based metal matrix composites. J Alloy Compd 2017;729:828–42.
[620] Yadav D, Bauri R. Friction Stir Processing of Al-TiB2 In Situ Composite: Effect on Particle Distribution, Microstructure and Properties. J Mater Eng Perform 2015;24:1116–24.
[621] Yang R, Zhang Z, Zhao Y, Chen G, Guo Y, Liu M, et al. Effect of multi-pass friction stir processing on microstructure and mechanical properties of Al_3Ti/A356 composites. Mater Charact 2015;106:62–9.
[622] Gangil N, Siddiquee AN, Maheshwari S. Aluminium based in-situ composite fabrication through friction stir processing: A review. J Alloy Compd 2017;715:91–104.
[623] Sharma P, Khanduja D, Sharma S. Tribological and mechanical behavior of particulate aluminum matrix composites. J Reinf Plast Compos 2014;33:2192–202.
[624] Sunil BR, Reddy GPK, Patle H, Dumpala R. Magnesium based surface metal matrix composites by friction stir processing. J Magnesium Alloys 2016;4:52–61.
[625] Khodabakhshi F, Derazkola HA, Gerlich AP. Monte Carlo simulation of grain refinement during friction stir processing. J Mater Sci 2020;55:13438–56.
[626] Heidarzadeh A, Pouraliakbar H, Mahdavi S, Jandaghi MR. Ceramic nanoparticles addition in pure copper plate: FSP approach, microstructure evolution and texture study using EBSD. Ceram Int 2018;44:3128–33.
[627] Heidarzadeh A, Taghizadeh B, Mohammadzadeh A. Microstructure and mechanical properties of CuZn-Al2O3 nanocomposites produced by friction stir processing. Arch Civ Mech Eng 2020;20:98.
[628] Khodabakhshi F, Ghasemi Yazdabadi H, Kokabi AH, Simchi A. Friction stir welding of a P/M Al-Al2O3 nanocomposite: Microstructure and mechanical properties. Mater Sci Eng, A 2013;585:222–32.
[629] Khodabakhshi F, Simchi A, Kokabi AH, Gerlich AP. Similar and dissimilar friction-stir welding of an PM aluminum-matrix hybrid nanocomposite and commercial pure aluminum: Microstructure and mechanical properties. Mater Sci Eng, A 2016;666:225–37.
[630] Khodabakhshi F, Gerlich AP, Švec P. Fabrication of a high strength ultra-fine grained Al-Mg-SiC nanocomposite by multi-step friction-stir processing. Mater Sci Eng, A 2017;698:313–25.
[631] Khodabakhshi F, Nosko M, Gerlich AP. Dynamic restoration and crystallographic texture of a friction-stir processed Al–Mg–SiC surface nanocomposite. Mater Sci Technol (United Kingdom) 2018;34:1773–91.
[632] Khodabakhshi F, Gerlich AP, Simchi A, Kokabi AH. Cryogenic friction-stir processing of ultrafine-grained Al-Mg-TiO_2 nanocomposites. Mater Sci Eng, A 2014;620:471–82.
[633] Khodabakhshi F, Gerlich AP, Švec P. Reactive friction-stir processing of an Al-Mg alloy with introducing multi-walled carbon nano-tubes (MW-CNTs): Microstructural characteristics and mechanical properties. Mater Charact 2017;131:359–73.
[634] Khodabakhshi F, Nosko M, Gerlich AP. Influence of CNTs decomposition during reactive friction-stir processing of an Al–Mg alloy on the correlation between microstructural characteristics and microtextural components. J Microsc 2018;271:188–206.

[635] Khodabakhshi F, Arab SM, Švec P, Gerlich AP. Fabrication of a new Al-Mg/graphene nanocomposite by multi-pass friction-stir processing: Dispersion, microstructure, stability, and strengthening. Mater Charact 2017;132:92–107.
[636] Khodabakhshi F, Nosko M, Gerlich AP. Effects of graphene nano-platelets (GNPs) on the microstructural characteristics and textural development of an Al-Mg alloy during friction-stir processing. Surf Coat Technol 2018;335:288–305.
[637] Morisada Y, Fujii H, Nagaoka T, Nogi K, Fukusumi M. Fullerene/A5083 composites fabricated by material flow during friction stir processing. Compos A Appl Sci Manuf 2007;38:2097–101.
[638] Yang M, Xu C, Wu C, Lin KC, Chao YJ, An L. Fabrication of AA6061/Al_2O_3 nano ceramic particle reinforced composite coating by using friction stir processing. J Mater Sci 2010;45:4431–8.
[639] Shafiei-Zarghani A, Kashani-Bozorg SF, Hanzaki AZ. Wear assessment of Al/Al2O3 nano-composite surface layer produced using friction stir processing. Wear 2011;270:403–12.
[640] Shafiei-Zarghani A, Kashani-Bozorg SF, Zarei-Hanzaki A. Microstructures and mechanical properties of Al/Al2O3 surface nano-composite layer produced by friction stir processing. Mater Sci Eng, A 2009;500:84–91.
[641] Al-Ghamdi KA, Hussain G, Hashemi R. Fabrication of metal-matrix AL7075T651/TiN nano composite employing friction stir process. Proc Inst Mech Eng, Part B: J Eng Manuf 2017;231:1319–31.
[642] Huang Y, Wang T, Guo W, Wan L, Lv S. Microstructure and surface mechanical property of AZ31 Mg/SiCp surface composite fabricated by Direct Friction Stir Processing. Mater Des 2014;59:274–8.
[643] Morisada Y, Fujii H, Nagaoka T, Fukusumi M. Effect of friction stir processing with SiC particles on microstructure and hardness of AZ31. Mater Sci Eng, A 2006;433:50–4.
[644] Azizieh M, Kokabi AH, Abachi P. Effect of rotational speed and probe profile on microstructure and hardness of AZ31/Al_2O_3 nanocomposites fabricated by friction stir processing. Mater Des 2011;32:2034–41.
[645] Hanas T, Sampath Kumar TS, Perumal G, Doble M, Ramakrishna S. Electrospun PCL/HA coated friction stir processed AZ31/HA composites for degradable implant applications. J Mater Process Technol 2018;252:398–406.
[646] Ratna Sunil B, Sampath Kumar TS, Chakkingal U, Nandakumar V, Doble M. Nano-hydroxyapatite reinforced AZ31 magnesium alloy by friction stir processing: A solid state processing for biodegradable metal matrix composites. J Mater Sci - Mater Med 2014;25:975–88.
[647] Lee CJ, Huang JC. High strain rate superplasticity of Mg based composites fabricated by friction stir processing. Mater Trans 2006;47:2773–8.
[648] Lee CJ, Huang JC, Hsieh PL. Using friction stir processing to fabricate Mg based composites with nano fillers. Key Eng Mater 2006:69–76.
[649] Asadi P, Faraji G, Besharati MK. Producing of AZ91/SiC composite by friction stir processing (FSP). Int J Adv Manuf Technol 2010;51:247–60.
[650] Asadi P, Givi MKB, Rastgoo A, Akbari M, Zakeri V, Rasouli S. Predicting the grain size and hardness of AZ91/SiC nanocomposite by artificial neural networks. Int J Adv Manuf Technol 2012;63:1095–107.
[651] Rahmati R, Khodabakhshi F. Microstructural evolution and mechanical properties of a friction-stir processed Ti-hydroxyapatite (HA) nanocomposite. J Mech Behav Biomed Mater 2018;88:127–39.
[652] McNelley TR, Swaminathan S, Su JQ. Recrystallization mechanisms during friction stir welding/processing of aluminum alloys. Scr Mater 2008;58:349–54.
[653] Mousavizade SM, Pouranvari M, Malek Ghaini F, Fujii H, Sun YF. Dynamic recrystallization phenomena during laser-assisted friction stir processing of a precipitation hardened nickel base superalloy. J Alloy Compd 2016;685:806–11.
[654] Murr LE, Pizaña C. Dynamic recrystallization: The dynamic deformation regime. Metall Mater Trans A 2007;38A:2611–28.
[655] Singh Yadav RK, Sharma V, Venkata Manoj Kumar B. On the role of sliding load and heat input conditions in friction stir processing on tribology of aluminium alloy–alumina surface composites. Tribol Mater Surf Interfaces 2019;13:88–101.
[656] Roy P, Singh S, Pal K. Enhancement of mechanical and tribological properties of SiC- and CB-reinforced aluminium 7075 hybrid composites through friction stir processing. Adv Compos Mater 2019;28:1–18.
[657] Owa T, Shimizu Y, Kaiume S, Hashimoto Y. Effect of sintered reinforcement on characteristics of MWCNT-reinforced aluminum alloy composite via friction stir processing. Mater Trans 2019;60:1018–25.
[658] Mehta KM, Badheka VJ. Wear behavior of boron-carbide reinforced aluminum surface composites fabricated by Friction Stir Processing. Wear 2019;426–427:975–80.
[659] Mahesh VP, Arora A. Effect of tool shoulder diameter on the surface hardness of aluminum-molybdenum surface composites developed by single and double groove friction stir processing. Metall Mater Trans A: Phys Metall Mater Sci 2019.
[660] Kumar JR, Jayaraman M, Kumar TS, Priyadharshini GS, Kumar JS. Characterization of Y2O3 particles reinforced AA6082 aluminum matrix composites produced using friction stir processing. Mater Res Express 2019;6.
[661] Ikumapayi OM, Akinlabi ET, Majumdar JD, Akinlabi SA. Characterization of high strength aluminium-based surface matrix composite reinforced with low-cost PKSA fabricated by friction stir processing. Mater Res Express 2019;6.
[662] Huang GQ, Yan YF, Wu J, Shen YF, Gerlich AP. Microstructure and mechanical properties of fine-grained aluminum matrix composite reinforced with nitinol shape memory alloy particulates produced by underwater friction stir processing. J Alloy Compd 2019;786:257–71.
[663] Balakrishnan M, Dinaharan I, Palanivel R, Sathiskumar R. Influence of friction stir processing on microstructure and tensile behavior of AA6061/Al <inf>3</inf> Zr cast aluminum matrix composites. J Manuf Processes 2019;38:148–57.
[664] Balakrishnan M, Dinaharan I, Palanivel R, Sathiskumar R. Effect of friction stir processing on microstructure and tensile behavior of AA6061/Al<inf>3</inf>Fe cast aluminum matrix composites. J Alloy Compd 2019;785:531–41.
[665] Acuña R, Cristóbal MJ, Abreu CM, Cabeza M. Microstructure and Wear Properties of Surface Composite Layer Produced by Friction Stir Processing (FSP) in AA2024-T351 Aluminum Alloy. Metall Mater Trans A 2019;50:2860–74.
[666] Abraham SJ, Dinaharan I, Raja Selvam JD, Akinlabi ET. Microstructural characterization of vanadium particles reinforced AA6063 aluminum matrix composites via friction stir processing with improved tensile strength and appreciable ductility. Compos Commun 2019;12:54–8.
[667] Zhang ZW, Liu ZY, Xiao BL, Ni DR, Ma ZY. High efficiency dispersal and strengthening of graphene reinforced aluminum alloy composites fabricated by powder metallurgy combined with friction stir processing. Carbon 2018;135:215–23.
[668] Thapliyal S, Dwivedi DK. Barium titanate reinforced nickel aluminium bronze surface composite by friction stir processing. Mater Sci Technol (United Kingdom) 2018;34:366–77.
[669] Sadeghi B, Shamanian M, Ashrafizadeh F, Cavaliere P, Rizzo A. Friction stir processing of spark plasma sintered aluminum matrix composites with bimodal micro- and nano-sized reinforcing Al<inf>2</inf>O<inf>3</inf> particles. J Manuf Processes 2018;32:412–24.
[670] Kishan V, Devaraju A, Prasanna Lakshmi K. Tribological Properties of nano TiB2 particle reinforced 6061-T6 aluminum alloy surface composites via friction stir processing. Mater Today: Proc 2018;1:1615–9.
[671] Huang G, Wu J, Hou W, Shen Y. Microstructure, mechanical properties and strengthening mechanism of titanium particle reinforced aluminum matrix composites produced by submerged friction stir processing. Mater Sci Eng, A 2018;734:353–63.
[672] Huang G, Hou W, Shen Y. Evaluation of the microstructure and mechanical properties of WC particle reinforced aluminum matrix composites fabricated by friction stir processing. Mater Charact 2018;138:26–37.
[673] Dinaharan I, Akinlabi ET. Low cost metal matrix composites based on aluminum, magnesium and copper reinforced with fly ash prepared using friction stir processing. Compos Commun 2018;9:22–6.
[674] Cao X, Shi Q, Liu D, Feng Z, Liu Q, Chen G. Fabrication of in situ carbon fiber/aluminum composites via friction stir processing: Evaluation of microstructural, mechanical and tribological behaviors. Compos B Eng 2018;139:97–105.
[675] Yuvaraj N, Aravindan S, Vipin. Comparison studies on mechanical and wear behavior of fabricated aluminum surface nano composites by fusion and solid state processing. Surf Coat Technol 2017;309:309–19.
[676] Selvakumar S, Dinaharan I, Palanivel R, Ganesh Babu B. Characterization of molybdenum particles reinforced Al6082 aluminum matrix composites with improved ductility produced using friction stir processing. Mater Charact 2017;125:13–22.

[677] Selvakumar S, Dinaharan I, Palanivel R, Babu BG. Development of stainless steel particulate reinforced AA6082 aluminum matrix composites with enhanced ductility using friction stir processing. Mater Sci Eng, A 2017;685:317–26.
[678] Saravanakumar S, Gopalakrishnan S, Dinaharan I, Kalaiselvan K. Assessment of microstructure and wear behavior of aluminum nitrate reinforced surface composite layers synthesized using friction stir processing on copper substrate. Surf Coat Technol 2017;322:51–8.
[679] Khan M, Rehman A, Aziz T, Naveed K, Ahmad I, Subhani T. Cold formability of friction stir processed aluminum composites containing carbon nanotubes and boron carbide particles. Mater Sci Eng, A 2017.
[680] Khan M, Rehman A, Aziz T, Naveed K, Ahmad I, Subhani T. Cold formability of friction stir processed aluminum composites containing carbon nanotubes and boron carbide particles. Mater Sci Eng, A 2017;696:552–7.
[681] Dinaharan I, Kalaiselvan K, Murugan N. Influence of rice husk ash particles on microstructure and tensile behavior of AA6061 aluminum matrix composites produced using friction stir processing. Compos Commun 2017;3:42–6.
[682] Verdera D, Rey P, García F, Saldaña R. Manufacturing a surface composite material made of nanoceramic particles of TiC and aluminum alloy 7075 by means of friction stir processing. Friction Stir Welding Proc VIII 2016:199–206.
[683] Palanivel R, Dinaharan I, Laubscher RF, Davim JP. Influence of boron nitride nanoparticles on microstructure and wear behavior of AA6082/TiB<inf>2</inf> hybrid aluminum composites synthesized by friction stir processing. Mater Des 2016;106:195–204.
[684] Mahmoud ERI, Tash MM. Characterization of aluminum-based-surface matrix composites with iron and iron oxide fabricated by friction stir processing. Materials 2016;9.
[685] Ma ZY, Liu ZY, Xiao BL, Wang WG. Fabrication of carbon nanotube reinforced aluminum matrix composites via friction stir processing. Friction Stir Welding Processing VII 2016:21–8.
[686] Kurt HI, Oduncuoglu M, Asmatulu R. Wear Behavior of Aluminum Matrix Hybrid Composites Fabricated through Friction Stir Welding Process. J Iron Steel Res Int 2016;23:1119–26.
[687] Kurt HI. Influence of hybrid ratio and friction stir processing parameters on ultimate tensile strength of 5083 aluminum matrix hybrid composites. Compos B Eng 2016;93:26–34.
[688] Joyson Abraham S, Chandra Rao Madane S, Dinaharan I, John Baruch L. Development of quartz particulate reinforced AA6063 aluminum matrix composites via friction stir processing. J Asian Ceram Soc 2016;4:381–9.
[689] Huang G, Shen Y, Guo R, Guan W. Fabrication of tungsten particles reinforced aluminum matrix composites using multi-pass friction stir processing: Evaluation of microstructural, mechanical and electrical behavior. Mater Sci Eng, A 2016;674:504–13.
[690] Dinaharan I, Nelson R, Vijay SJ, Akinlabi ET. Microstructure and wear characterization of aluminum matrix composites reinforced with industrial waste fly ash particulates synthesized by friction stir processing. Mater Charact 2016;118:149–58.
[691] Dinaharan I, Murugan N, Thangarasu A. Development of empirical relationships for prediction of mechanical and wear properties of AA6082 aluminum matrix composites produced using friction stir processing. Eng Sci Technol, Int J 2016;19:1132–44.
[692] Dinaharan I. Influence of ceramic particulate type on microstructure and tensile strength of aluminum matrix composites produced using friction stir processing. J Asian Ceram Soc 2016;4:209–18.
[693] Sarkari Khorrami M, Samadi S, Janghorban Z, Movahedi M. In-situ aluminum matrix composite produced by friction stir processing using FE particles. Mater Sci Eng, A 2015;641:380–90.
[694] Khodabakhshi F, Simchi A, Kokabi AH, Gerlich AP. Friction stir processing of an aluminum-magnesium alloy with pre-placing elemental titanium powder: In-situ formation of an Al<inf>3</inf>Ti-reinforced nanocomposite and materials characterization. Mater Charact 2015;108:102–14.
[695] Khodabakhshi F, Gerlich AP, Simchi A, Kokabi AH. Hot deformation behavior of an aluminum-matrix hybrid nanocomposite fabricated by friction stir processing. Mater Sci Eng, A 2015;626:458–66.
[696] Arab SM, Karimi S, Jahromi SAJ, Javadpour S, Zebarjad SM. Fabrication of novel fiber reinforced aluminum composites by friction stir processing. Mater Sci Eng, A 2015;632:50–7.
[697] Wójcicka A, Mroczka K, Kurtyka P, Binkowski M, Wróbel Z. X-ray microtomography analysis of the aluminum alloy composite reinforced by SiC after friction stir processing. J Mater Eng Perform 2014;23:3215–21.
[698] Liu ZY, Xiao BL, Wang WG, Ma ZY. Effect of carbon nanotube orientation on mechanical properties and thermal expansion coefficient of carbon nanotube-reinforced aluminum matrix composites. Acta Metall Sin (Engl Lett) 2014;27:901–8.
[699] Liu ZY, Xiao BL, Wang WG, Ma ZY. Tensile strength and electrical conductivity of carbon nanotube reinforced aluminum matrix composites fabricated by powder metallurgy combined with friction stir processing. J Mater Sci Technol 2014;30:649–55.
[700] Liu ZY, Xiao BL, Wang WG, Ma ZY. Analysis of carbon nanotube shortening and composite strengthening in carbon nanotube/aluminum composites fabricated by multi-pass friction stir processing. Carbon 2014;69:264–74.
[701] Jeon CH, Jeong YH, Seo JJ, Tien HN, Hong ST, Yum YJ, et al. Material properties of graphene/aluminum metal matrix composites fabricated by friction stir processing. Int J Precis Eng Manuf 2014;15:1235–9.
[702] You GL, Ho NJ, Kao PW. Aluminum based in situ nanocomposite produced from Al-Mg-CuO powder mixture by using friction stir processing. Mater Lett 2013;100:219–22.
[703] Liu ZY, Xiao BL, Wang WG, Ma ZY. Developing high-performance aluminum matrix composites with directionally aligned carbon nanotubes by combining friction stir processing and subsequent rolling. Carbon 2013;62:35–42.
[704] Liu Q, Ke L, Liu F, Huang C, Xing L. Microstructure and mechanical property of multi-walled carbon nanotubes reinforced aluminum matrix composites fabricated by friction stir processing. Mater Des 2013;45:343–8.
[705] Liu P, Sun QZ, Liu Y, Sun QL. Microstructure and corrosion properties of 5A06 aluminum matrix surface composite fabricated by friction stir processing. Sci Eng Compos Mater 2013;20:123–7.
[706] Devaraju A, Kumar A, Kumaraswamy A, Kotiveerachari B. Influence of reinforcements (SiC and Al2O3) and rotational speed on wear and mechanical properties of aluminum alloy 6061–T6 based surface hybrid composites produced via friction stir processing. Mater Des 2013;51:331–41.
[707] Devaraju A, Kumar A, Kotiveerachari B. Influence of rotational speed and reinforcements on wear and mechanical properties of aluminum hybrid composites via friction stir processing. Mater Des 2013;45:576–85.
[708] Devaraju A, Kumar A, Kotiveerachari B. Influence of addition of Grp/Al2O3p with SiCp on wear properties of aluminum alloy 6061–T6 hybrid composites via friction stir processing. Trans Nonferrous Met Soc China (Engl Ed) 2013;23:1275–80.
[709] Aruri D, Adepu K, Adepu K, Bazavada K. Wear and mechanical properties of 6061–T6 aluminum alloy surface hybrid composites [(SiC + Gr) and (SiC + Al<inf>2</inf>O<inf>3</inf>)] fabricated by friction stir processing. J Mater Res Technol 2013;2:362–9.
[710] Sohn YH, Patterson T, Hofmeister C, Kammerer C, Mohr W, Van Den Bergh M, et al. Tailoring microstructure and properties of hierarchical aluminum metal matrix composites through friction stir processing. JOM 2012;64:234–8.
[711] Rejil CM, Dinaharan I, Vijay SJ, Murugan N. Microstructure and sliding wear behavior of AA6360/(TiC+B4C) hybrid surface composite layer synthesized by friction stir processing on aluminum substrate. Mater Sci Eng, A 2012;552:336–44.
[712] Qian J, Li J, Xiong J, Zhang F, Lin X. In situ synthesizing Al 3Ni for fabrication of intermetallic-reinforced aluminum alloy composites by friction stir processing. Mater Sci Eng, A 2012;550:279–85.
[713] Liu ZY, Xiao BL, Wang WG, Ma ZY. Singly dispersed carbon nanotube/aluminum composites fabricated by powder metallurgy combined with friction stir processing. Carbon 2012;50:1843–52.
[714] Izadi H, Gerlich AP. Distribution and stability of carbon nanotubes during multi-pass friction stir processing of carbon nanotube/aluminum composites. Carbon 2012;50:4744–9.
[715] Hodder KJ, Izadi H, McDonald AG, Gerlich AP. Fabrication of aluminum-alumina metal matrix composites via cold gas dynamic spraying at low pressure followed by friction stir processing. Mater Sci Eng, A 2012;556:114–21.

[716] Hassan AM, Almomani M, Qasim T, Ghaithan A. Effect of processing parameters on friction stir welded aluminum matrix composites wear behavior. Mater Manuf Processes 2012;27:1419–23.
[717] Lee IS, Hsu CJ, Chen CF, Ho NJ, Kao PW. Particle-reinforced aluminum matrix composites produced from powder mixtures via friction stir processing. Compos Sci Technol 2011;71:693–8.
[718] Wang W, Qy Shi, Liu P, Hk Li, Li T. A novel way to produce bulk SiCp reinforced aluminum metal matrix composites by friction stir processing. J Mater Process Technol 2009;209:2099–103.
[719] Hsu CJ, Kao PW, Ho NJ. Intermetallic-reinforced aluminum matrix composites produced in situ by friction stir processing. Mater Lett 2007;61:1315–8.
[720] Berbon PB, Bingel WH, Mishra RS, Bampton CC, Mahoney MW. Friction stir processing: A tool to homogenize nanocomposite aluminum alloys. Scr Mater 2001;44:61–6.
[721] Khodabakhshi F, Gerlich AP. Potentials and strategies of solid-state additive friction-stir manufacturing technology: A critical review. J Manuf Processes 2018;36:77–92.
[722] Khodabakhshi F, Marzbanrad B, Jahed H, Gerlich AP. Interfacial bonding mechanisms between aluminum and titanium during cold gas spraying followed by friction-stir modification. Appl Surf Sci 2018;462:739–52.
[723] Khodabakhshi F, Marzbanrad B, Shah LH, Jahed H, Gerlich AP. Friction-stir processing of a cold sprayed AA7075 coating layer on the AZ31B substrate: Structural homogeneity, microstructures and hardness. Surf Coat Technol 2017;331:116–28.
[724] Khodabakhshi F, Gerlich AP. On the correlation between indentation hardness and tensile strength in friction stir processed materials. Mater Sci Eng, A 2020;139682.
[725] Mazaheri Y, Karimzadeh F, Enayati MH. A novel technique for development of A356/Al2O3 surface nanocomposite by friction stir processing. J Mater Process Technol 2011;211:1614–9.
[726] Mazaheri Y, Karimzadeh F, Enayati MH. Tribological behavior of A356/Al2O3 surface nanocomposite prepared by friction stir processing. Metall Mater Trans A 2014;45:2250–9.
[727] Derazkola HA, Khodabakhshi F. A novel fed friction-stir (FFS) technology for nanocomposite joining. Sci Technol Weld Joining 2019;1–12.
[728] Nosko M, Štepánek M, Zifčák P, Orovčík L, Nagy Š, Dvorák T, et al. Solid-state joining of powder metallurgy Al-Al2O3 nanocomposites via friction-stir welding: Effects of powder particle size on the weldability, microstructure, and mechanical property. Mater Sci Eng, A 2019;754:190–204.
[729] Ambigai R, Prabhu S. Experimental and ANOVA analysis on tribological behavior of Al/B_4C micro and nanocomposite. Aust J Mech Eng 2017;1–11.
[730] You GL, Ho NJ, Kao PW. In-situ formation of Al2O3 nanoparticles during friction stir processing of AlSiO2 composite. Mater Charact 2013;80:1–8.
[731] Abraham SJ, Madane SCR, Vettive SC. Mechanical behavior of SiO_2 particulate reinforced AA 6063 surface composites using friction stir processing. Int J Appl Eng Res 2015;10:43934–8.
[732] Du Z, Tan MJ, Guo JF, Wei J. Friction stir processing of Al-CNT composites. Proc Inst Mech Eng, Part L: J Mater: Des Appl 2016;230:825-33.
[733] Lim DK, Shibayanagi T, Gerlich AP. Synthesis of multi-walled CNT reinforced aluminium alloy composite via friction stir processing. Mater Sci Eng, A 2009;507:194–9.
[734] Kotiyani MZM, Ranjbar K, Dehmolaei R. In-situ fabrication of Al3Zr aluminide reinforced AA3003 alloy composite by friction stir processing. Mater Charact 2017;131:78–90.
[735] Khodabakhshi F, Kokabi AH, Simchi A. Reactive friction-stir processing of nanocomposites: effects of thermal history on microstructure–mechanical property relationships. Mater Sci Technol 2017;33:1776–89.
[736] Khodabakhshi F, Simchi A, Kokabi AH, Sadeghahmadi M, Gerlich AP. Reactive friction stir processing of AA 5052-TiO2 nanocomposite: Process-microstructure-mechanical characteristics. Mater Sci Technol (United Kingdom) 2015;31:426–35.
[737] Shyam Kumar CN, Yadav D, Bauri R, Janaki Ram GD. Effects of ball milling and particle size on microstructure and properties 5083 Al-Ni composites fabricated by friction stir processing. Mater Sci Eng, A 2015;645:205–12.
[738] Yuvaraj N, Aravindan S, Vipin. Wear characteristics of Al5083 surface hybrid nano-composites by friction stir processing. Trans Indian Inst Met 2017;70:1111–29.
[739] Rollett A, Humphreys F, Rohrer GS, Hatherly M. Recrystallization and Related Annealing Phenomena: Second Edition; 2004.
[740] Sharma V, Prakash U, Kumar BVM. Surface composites by friction stir processing: A review. J Mater Process Technol 2015;224:117–34.
[741] Shafiei-Zarghani A, Kashani-Bozorg SF, Gerlich AP. Texture Analyses of Ti/Al2O3 Nanocomposite Produced Using Friction Stir Processing. Metall Mater Trans A 2016;47:5618–29.
[742] Khodabakhshi F, Gerlich AP, Simchi A, Kokabi AH. Cryogenic friction-stir processing of ultrafine-grained Al–Mg–TiO_2 nanocomposites. Mater Sci Eng, A 2015;620:471–82.
[743] Du Z, Tan MJ, Guo JF, Bi G, Wei J. Fabrication of a new Al-Al_2O_3-CNTs composite using friction stir processing (FSP). Mater Sci Eng, A 2016;667:125–31.
[744] Jafari J, Givi MKB, Barmouz M. Mechanical and microstructural characterization of Cu/CNT nanocomposite layers fabricated via friction stir processing. Int J Adv Manuf Technol 2015;78:199–209.
[745] Daud M, Kamal MS, Shehzad F, Al-Harthi MA. Graphene/layered double hydroxides nanocomposites: A review of recent progress in synthesis and applications. Carbon 2016;104:241–52.
[746] Dorri Moghadam A, Omrani E, Menezes PL, Rohatgi PK. Mechanical and tribological properties of self-lubricating metal matrix nanocomposites reinforced by carbon nanotubes (CNTs) and graphene – A review. Compos B Eng 2015;77:402–20.
[747] Geim AK. Graphene: Status and prospects. Science 2009;324:1530–4.
[748] Hu Z, Lu X. Chapter 8 - Mechanical Properties of Carbon Nanotubes and Graphene A2 - Tanaka, K. In: Iijima S, editor. Carbon Nanotubes and Graphene. Second Edition. Oxford: Elsevier; 2014. p. 165–200.
[749] Kumar HGP, Xavior MA. Graphene Reinforced Metal Matrix Composite (GRMMC): A Review. Procedia Eng 2014;97:1033–40.
[750] Nieto A, Bisht A, Lahiri D, Zhang C, Agarwal A. Graphene reinforced metal and ceramic matrix composites: a review. Int Mater Rev 2016;1–62.
[751] Tachibana M, Yamada S. Two-dimensional nanocarbon materials called carbon nanowalls—Structure, physical properties and applications. Carbon 2013;55:373–4.
[752] Khodabakhshi F, Simchi A, Kokabi A, Nosko M, Švec P. Strain rate sensitivity, work hardening, and fracture behavior of an Al-Mg TiO2 nanocomposite prepared by friction stir processing. Metall Mater Trans A 2014;45:4073–88.
[753] Azizieh M, Iranparast D, Dezfuli MAG, Balak Z, Kim HS. Fabrication of Al/Al2Cu in situ nanocomposite via friction stir processing. Trans Nonferrous Met Soc China (Engl Ed) 2017;27:779–88.
[754] Bauri R. Optimization of process parameters for friction stir processing (FSP) of Al-TiC in situ composite. Bull Mater Sci 2014;37:571–8.
[755] Chen CF, Kao PW, Chang LW, Ho NJ. Effect of processing parameters on microstructure and mechanical properties of an Al-Al11Ce3-Al2O3 in-situ composite produced by friction stir processing. Metall Mater Trans A 2010;41:513–22.
[756] Chen Z, Li J, Borbely A, Ji G, Zhong SY, Wu Y, et al. The effects of nanosized particles on microstructural evolution of an in-situ TiB2/6063Al composite produced by friction stir processing. Mater Des 2015;88:999–1007.
[757] Hosseini Zeidabadi SR, Daneshmanesh H. Fabrication and characterization of in-situ Al/Nb metal/intermetallic surface composite by friction stir processing. Mater Sci Eng, A 2017;702:189–95.
[758] Hsu CJ, Kao PW, Ho NJ. Ultrafine-grained Al-Al2Cu composite produced in situ by friction stir processing. Scr Mater 2005;53:341–5.
[759] Ke L, Huang C, Xing L, Huang K. Al-Ni intermetallic composites produced in situ by Friction Stir Processing. J Alloy Compd 2010;503:494–9.
[760] Lee IS, Kao PW, Ho NJ. Microstructure and mechanical properties of Al-Fe in situ nanocomposite produced by friction stir processing. Intermetallics 2008;16:1104–8.
[761] Lee IS, Kao PW, Ho NJ. Microstructure and mechanical properties of an Al-Mo in situ nanocomposite produced by friction stir processing. TMS Annual Meeting 2009:141–7.
[762] Madhu HC, Kailas SV. In-Situ Aluminothermal Reduction Synthesis of Ti3AlC2 Aluminium Composite by Friction Stir Processing. Proc Manuf 2017;7:157–62.

[763] Rajan HBM, Dinaharan I, Ramabalan S, Akinlabi ET. Influence of friction stir processing on microstructure and properties of AA7075/TiB2 in situ composite. J Alloy Compd 2016;657:250–60.
[764] Shahi A, Sohi MH, Ahmadkhaniha D, Ghambari M. In situ formation of Al–Al3Ni composites on commercially pure aluminium by friction stir processing. Int J Adv Manuf Technol 2014;75:1331–7.
[765] Yang Y, Zhao Y, Kai X, Tao R. Superplasticity behavior and deformation mechanism of the in-situ Al3Zr/6063Al composites processed by friction stir processing. J Alloy Compd 2017;710:225–33.
[766] You GL, Ho NJ, Kao PW. The microstructure and mechanical properties of an Al-CuO in-situ composite produced using friction stir processing. Mater Lett 2013;90:26–9.
[767] Zhang Q, Xiao BL, Wang QZ, Ma ZY. In situ Al3Ti and Al2O3 nanoparticles reinforced Al composites produced by friction stir processing in an Al-TiO2 system. Mater Lett 2011;65:2070–2.
[768] Zhang Q, Xiao BL, Wang QZ, Ma ZY. Effects of processing parameters on the microstructures and mechanical properties of in situ (Al3Ti + Al2O3)/Al composites fabricated by hot pressing and subsequent friction-stir processing. Metall Mater Trans A 2014;45:2776–91.
[769] Zhang Q, Xiao BL, Wang WG, Ma ZY. Reactive mechanism and mechanical properties of in situ composites fabricated from an Al-TiO <inf>2</inf> system by friction stir processing. Acta Mater 2012;60:7090–103.
[770] Zhao Y, Kai X, Chen G, Lin W, Wang C. Effects of friction stir processing on the microstructure and superplasticity of in situ nano-ZrB2/2024Al composite. Prog Nat Sci: Mater Int 2016;26:69–77.
[771] Khodabakhshi F, Simchi A, Kokabi AH. Surface modifications of an aluminum-magnesium alloy through reactive stir friction processing with titanium oxide nanoparticles for enhanced sliding wear resistance. Surf Coat Technol 2017;309:114–23.
[772] Khodabakhshi F, Simchi A, Kokabi AH, Gerlich AP, Nosko M. Effects of post-annealing on the microstructure and mechanical properties of friction stir processed Al–Mg–TiO2 nanocomposites. Mater Des 2014;63:30–41.
[773] Khodabakhshi F, Simchi A, Kokabi AH, Sadeghahmadi M, Gerlich AP. Reactive friction stir processing of AA 5052–TiO2 nanocomposite: process–microstructure–mechanical characteristics. Mater Sci Technol 2015;31:426–35.
[774] Azimi-Roeen G, Kashani-Bozorg SF, Nosko M, Švec P. Reactive mechanism and mechanical properties of in-situ hybrid nano-composites fabricated from an Al–Fe2O3 system by friction stir processing. Mater Charact 2017;127:279–87.
[775] Eskandari H, Taheri R, Khodabakhshi F. Friction-stir processing of an AA8026-TiB2-Al2O3 hybrid nanocomposite: Microstructural developments and mechanical properties. Mater Sci Eng, A 2016;660:84–96.
[776] Vatankhah Barenji R, Khojastehnezhad VM, Pourasl HH, Rabiezadeh A. Wear properties of Al-Al2O3/TiB2 surface hybrid composite layer prepared by friction stir process. J Compos Mater 2015;50:1457–66.
[777] Narimani M, Lotfi B, Sadeghian Z. Evaluation of the microstructure and wear behaviour of AA6063-B4C/TiB2 mono and hybrid composite layers produced by friction stir processing. Surf Coat Technol 2016;285:1–10.
[778] Sharifitabar M, Kashefi M, Khorshahian S. Effect of friction stir processing pass sequence on properties of Mg-ZrSiO4-Al2O3 surface hybrid micro/nano-composites. Mater Des 2016;108:1–7.
[779] Hosseini SA, Ranjbar K, Dehmolaei R, Amirani AR. Fabrication of Al5083 surface composites reinforced by CNTs and cerium oxide nano particles via friction stir processing. J Alloy Compd 2015;622:725–33.
[780] Almomani M, Hassan AM, Qasim T, Ghaithan A. Effect of process parameters on corrosion rate of friction stir welded aluminium SiC-Gr hybrid composites. Corros Eng, Sci Technol 2013;48:346–53.
[781] Mostafapour Asl A, Khandani ST. Role of hybrid ratio in microstructural, mechanical and sliding wear properties of the Al5083/Graphitep/Al2O3p a surface hybrid nanocomposite fabricated via friction stir processing method. Mater Sci Eng, A 2013;559:549–57.
[782] Prakash T, Sivasankaran S, Sasikumar P. Mechanical and Tribological Behaviour of Friction-Stir-Processed Al 6061 Aluminium Sheet Metal Reinforced with Al2O3/0.5 Gr Hybrid Surface Nanocomposite. Arab J Sci Eng 2014;40:559–69.
[783] Nazari M, Eskandari H, Khodabakhshi F. Production and characterization of an advanced AA6061-Graphene-TiB2 hybrid surface nanocomposite by multi-pass friction stir processing. Surf Coat Technol 2019;377:124914.
[784] Abbasi M, Bagheri B, Dadaei M, Omidvar HR, Rezaei M. The effect of FSP on mechanical, tribological, and corrosion behavior of composite layer developed on magnesium AZ91 alloy surface. Int J Adv Manuf Technol 2015;77:2051–8.
[785] Abdollahi SH, Karimzadeh F, Enayati MH. Development of surface composite based on Mg-Al-Ni system on AZ31 magnesium alloy and evaluation of formation mechanism. J Alloy Compd 2015;623:335–41.
[786] Ahmadkhaniha D, Fedel M, Heydarzadeh Sohi M, Zarei Hanzaki A, Deflorian F. Corrosion behavior of magnesium and magnesium-hydroxyapatite composite fabricated by friction stir processing in Dulbecco's phosphate buffered saline. Corros Sci 2016;104:319–29.
[787] Ahmadkhaniha D, Heydarzadeh Sohi M, Salehi A, Tahavvori R. Formations of AZ91/Al2O3 nano-composite layer by friction stir processing. J Magnesium Alloys 2016;4:314–8.
[788] Arokiasamy S, Anand Ronald B. Experimental investigations on the enhancement of mechanical properties of magnesium-based hybrid metal matrix composites through friction stir processing. Int J Adv Manuf Technol 2017;1–11.
[789] Asadi P, Faraji G, Masoumi A, Givi MKB. Experimental investigation of magnesium-base nanocomposite produced by friction stir processing: Effects of particle types and number of friction stir processing passes. Metall Mater Trans A 2011;42:2820–32.
[790] Balakrishnan M, Dinaharan I, Palanivel R, Sivaprakasam R. Synthesize of AZ31/TiC magnesium matrix composites using friction stir processing. J Magnesium Alloys 2015;3:76–8.
[791] Bhadouria N, Kumar P, Thakur L, Dixit S, Arora N. A Study on Micro-hardness and Tribological Behaviour of Nano-WC–Co–Cr/Multi-walled Carbon Nanotubes Reinforced AZ91D Magnesium Matrix Surface Composites. Trans Indian Inst Met 2017;1–7.
[792] Chen YH, Mao YQ, Xie JL, Zhan ZL, Yu L. Microstructure and microwave absorption properties of MWCNTs reinforced magnesium matrix composites fabriccated by FSP. Optoelectron Lett 2017;13.
[793] Das S, Mishra RS, Doherty KJ, Cho KC, Davis B, DeLorme R. Magnesium based composite via friction stir processing. Friction Stir Welding Process VII 2016:245–52.
[794] Liao H, Chen J, Peng L, Han J, Yi H, Zheng F, et al. Fabrication and characterization of magnesium matrix composite processed by combination of friction stir processing and high-energy ball milling. Mater Sci Eng, A 2017;683:207–14.
[795] Lu D, Jiang Y, Zhou R. Wear performance of nano-Al2O3 particles and CNTs reinforced magnesium matrix composites by friction stir processing. Wear 2013;305:286–90.
[796] Ratna Sunil B, Sampath Kumar TS, Chakkingal U, Nandakumar V, Doble M. Friction stir processing of magnesium-nanohydroxyapatite composites with controlled in vitro degradation behavior. Mater Sci Eng, C 2014;39:315–24.
[797] Zhao Y, Ding Z, Shen C, Chen Y. Interfacial microstructure and properties of aluminum-magnesium AZ31B multi-pass friction stir processed composite plate. Mater Des 2016;94:240–52.
[798] Vigneshkumar M, Padmanaban G, Balasubramanian V. Influence of Tool Tilt Angle on the Formation of Friction Stir Processing Zone in Cast Magnesium Alloy ZK60/SiCp Surface Composites. Metall, Microstruct, Analy 2019;8:58–66.
[799] Vignesh Kumar M, Padamanaban G, Balasubramanian V. Effect of tool pin profile on microstructure and hardness of magnesium alloy ZK60/ SiCp surface composites fabricated by friction stir processing. J Test Eval 2019;47.
[800] Vaira Vignesh R, Padmanaban R, Govindaraju M, Suganya Priyadharshini G. Investigations on the corrosion behaviour and biocompatibility of magnesium alloy surface composites AZ91D-ZrO2 fabricated by friction stir processing. Trans Inst Met Finish 2019;97:261–70.
[801] Vaira Vignesh R, Padmanaban R, Govindaraju M. Synthesis and Characterization of Magnesium Alloy Surface Composite (AZ91D - SiO<inf>2</inf>) by Friction Stir Processing for Bioimplants. Silicon 2019.

[802] Ram B, Deepak D, Bala N. Microstructural Refinement and Enhancement in Mechanical Properties of Magnesium/SiC as-Cast Composites via Friction Stir Processing Route. Trans Indian Inst Met 2019.
[803] Vigneshkumar M, Padmanaban G, Balasubramanian V. Influence of tool rotational speed on the formation of friction stir processing zone in cast Zk60/SiCp magnesium alloy surface composites. Mater Perform Charact 2018;7.
[804] Vedabouriswaran G, Aravindan S. Development and characterization studies on magnesium alloy (RZ 5) surface metal matrix composites through friction stir processing. J Magnesium Alloys 2018;6:145–63.
[805] Arokiasamy S, Anand Ronald B. Enhanced properties of Magnesium based metal matrix composites via Friction Stir Processing. Materials Today: Proceedings. 2 ed. 2018:6934-9.
[806] Afrinaldi A, Kakiuchi T, Nakagawa S, Moritomi H, Kumabe K, Nakai A, et al. Fabrication of recycled carbon fiber reinforced magnesium alloy composite by friction stir processing using 3-flat pin tool and its fatigue properties. Mater Trans 2018;59:475–81.
[807] Dinaharan I, Zhang S, Chen G, Shi Q. Titanium particulate reinforced AZ31 magnesium matrix composites with improved ductility prepared using friction stir processing. Mater Sci Eng, A 2020;772:138793.
[808] Ratna Sunil B, Sampath Kumar TS, Chakkingal U, Nandakumar V, Doble M. Friction stir processing of magnesium–nanohydroxyapatite composites with controlled in vitro degradation behavior. Mater Sci Eng, C 2014;39:315–24.
[809] Zhu C, Lv Y, Qian C, Ding Z, Jiao T, Gu X, et al. Microstructures, mechanical, and biological properties of a novel Ti-6V-4V/zinc surface nanocomposite prepared by friction stir processing. Int J Nanomed 2018;13:1881–98.
[810] Zhu C, Lv Y, Qian C, Qian H, Jiao T, Wang L, et al. Proliferation and osteogenic differentiation of rat BMSCs on a novel Ti/SiC metal matrix nanocomposite modified by friction stir processing. Sci Rep 2016;6.
[811] Shafiei-Zarghani A, Kashani-Bozorg SF, Gerlich AP. Strengthening analyses and mechanical assessment of Ti/Al2O3 nano-composites produced by friction stir processing. Mater Sci Eng, A 2015;631:75–85.
[812] Shamsipur A, Kashani-Bozorg SF, Zarei-Hanzaki A. Surface modification of titanium by producing Ti/TiN surface composite layers via FSP. Acta Metall Sinica (Engl Lett) 2017;30:550–7.
[813] Wang T, Gwalani B, Shukla S, Frank M, Mishra RS. Development of in situ composites via reactive friction stir processing of Ti–B4C system. Compos B Eng 2019;172:54–60.
[814] Dinaharan I, Sathiskumar R, Murugan N. Effect of ceramic particulate type on microstructure and properties of copper matrix composites synthesized by friction stir processing. J Mater Res Technol 2016;5:302–16.
[815] Sathiskumar R, Murugan N, Dinaharan I, Vijay SJ. Characterization of boron carbide particulate reinforced in situ copper surface composites synthesized using friction stir processing. Mater Charact 2013;84:16–27.
[816] Sathiskumar R, Murugan N, Dinaharan I, Vijay SJ. Prediction of mechanical and wear properties of copper surface composites fabricated using friction stir processing. Mater Des 2014;55:224–34.
[817] Suvarna Raju L, Kumar A. Influence of Al2O3 particles on the microstructure and mechanical properties of copper surface composites fabricated by friction stir processing. Defence Technol 2014;10:375–83.
[818] Thankachan T, Prakash KS. Microstructural, mechanical and tribological behavior of aluminum nitride reinforced copper surface composites fabricated through friction stir processing route. Mater Sci Eng, A 2017;688:301–8.
[819] Thankachan T, Soorya Prakash K, Loganathan M. WEDM process parameter optimization of FSPed copper-BN composites. Mater Manuf Processes 2017;1–9.
[820] Shamsipur A, Asadkarami S. Microstructure and mechanical properties of copper surface composite layers reinforced by nano and microscale SiC particles via friction stir processing. Adv Compos Mater 2019.
[821] Kumar H, Khan MZ, Vashista M. Microstructure, mechanical and electrical characterization of zirconia reinforced copper based surface composite by friction stir processing. Mater Res Express 2018;5.
[822] Huang CW, Aoh JN. Friction stir processing of copper-coated SiC particulate-reinforced aluminum matrix composite. Materials 2018;11.
[823] Dinaharan I, Akinlabi ET, Hattingh DG. Microstructural Characterization and Sliding Wear Behavior of Cu/TiC Copper Matrix Composites Developed Using Friction Stir Processing. Metallogr, Microstruct, Analy 2018;7:464–75.
[824] Dinaharan I, Kalaiselvan K, Akinlabi ET, Davim JP. Microstructure and wear characterization of rice husk ash reinforced copper matrix composites prepared using friction stir processing. J Alloy Compd 2017;718:150–60.
[825] Abbasi-Khazaei B, Keshavarz S. Nickel-aluminum-bronze/Al2O3 surface nanocomposite produced by friction-stir processing: Corrosion properties and microstructure. Mater Corros 2017.
[826] Thapliyal S, Dwivedi DK. Microstructure evolution and tribological behavior of the solid lubricant based surface composite of cast nickel aluminum bronze developed by friction stir processing. J Mater Process Technol 2016;238:30–8.
[827] Ghasemi-Kahrizsangi A, Kashani-Bozorg SF. Microstructure and mechanical properties of steel/TiC nano-composite surface layer produced by friction stir processing. Surf Coat Technol 2012;209:15–22.
[828] Ghasemi-Kahrizsangi A, Kashani-Bozorg SF, Moshref-Javadi M, Sharififar M. Friction Stir Processing of Mild Steel/Al2O3 Nanocomposite: Modeling and Experimental Studies. Metallogr, Microstruct, Analy 2015;4:122–30.

Akbar Heidarzadeh is currently an assistant professor at Faculty of Engineering, Department of Materials Engineering, Azarbaijan Shahid Madani University, Tabriz, Iran. He earned a BSc degree in Materials Science in autumn 2007. He obtained his MSc degree in Advanced Engineering Materials in autumn 2010. He received his Ph.D. degree in Materials Science, working on the FSW of copper-based alloys, in Feb. 2016. Akbar's PhD studies resulted in more than 25 papers in the field of microstructural evolution during FSW/FSP. His achievements in the field of FSW have been appreciated by the society and he received several awards and research grants. He is currently an author of more than 70 papers (Google Scholar (2020), h-index= 24), 5 book chapter and more than 35 communications to national and international conferences.

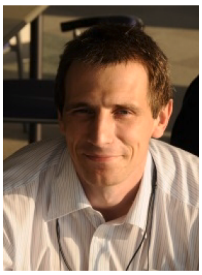

Sergey Mironov is currently senior researcher at Belgorod National Research University, Russia. He earned his PhD degree in Solid State Physics from Institute for Materials Superplasticity Problems in 2004. He has authored or coauthored 192 journal articles and 4 book chapters. His publications have been cited more than 3900 times (Google Scholar (2020), h-index = 34). Research interests include friction-stir welding/processing, severe plastic deformation, ultrafine-grained materials, electron backscatter diffraction.

Rustam Kaibyshev is currently a full professor at the Department of Material Science and Nanotechnology, Belgorod State University, Belgorod, Russia. He earned his PhD degree in Materials Science from Moscow Institute of Steels and Alloys, Moscow, in 1991. He has authored or coauthored more than 500 publications, including about 250 journal articles, 250 proceeding papers, 2 book chapters, and 33 patents of Russian Federation. His publications have been cited more than 11500 times (Google Scholar (2020), h-index = 52). His research interests include dynamic Recrystallization, evolution of ultrafine grains during intense plastic straining, mechanisms of plastic deformation, creep and superplasticity of metal matrix composite, aluminum alloys and fossil power steels, TWIP and TRIP steels, Cu-Cr-Zr, Cu-Mg and Al conductors, Phase transformation in none-ferrous alloys. He was awarded in 2000 JSPS scientific fellowship. He was a member of several International Conference Committee Memberships.

Gürel Çam is currently a full professor at the Department of Mechanical Engineering of Iskenderun Technical University, İskenderun-Hatay, Turkey. He earned his PhD degree in Materials Science from Imperial College of Science, Technology, and Medicine, University of London, U. K., in 1990. He has authored or coauthored 76 journal articles, 66 proceeding papers, 7 keynote presentations (invited lectures) and one book chapter. His publications have been cited more than 3500 times (Google Scholar (2020), h-index = 33). His research interests include welding technologies including friction stir welding, diffusion bonding, electron beam welding and laser beam welding, characterization of welded joints, and low transformation temperature (LTT) filler materials. He is a member of AWS (American Welding Society), USA, and DVS (Deutsche Verband für Schweisstechnik), Germany. He is also a member of the General Board, Institute of Turkish Welding Technologies, İstanbul, Turkey.

Aude Simar is professor, the University of Louvain (UCLouvain) in Louvain-la-Neuve, Belgium. She earned her PhD degree in the same university in 2006 and treated the FSW of 6xxx series Al alloys leading to a paper in 2012 in Progress in Materials Science cited 167 times. She is also authors of two review papers on FSW and one book chapter about FSP. She performed a post-doc at University of California at Berkeley in 2007-2008. She is an associate editor for the journal Elsevier Materials Characterization. She is the main organizer of the international conference on FSW/FSP in September 2019. She was awarded in 2016 the prestigious European Research Council (ERC) grant for working on new materials processed by FSP. She is currently author of 60 papers referenced on scopus (Google Scholar (2020), h-index = 26).

Adrian Gerlich has been an Associate Professor at Waterloo since 2012 and has been appointed the NSERC/TransCanada Industrial Research Chair in Welding for Energy Infrastructure in 2014. His research focuses on welding metallurgy of ferrous and non-ferrous materials and characterization of microstructures using electron microscopy, with a strong focus on solid-state joining techniques, such as friction stir welding and joining of dissimilar materials. To date he has published 120 journal papers and more than 30 conference papers, along with one book chapter, which together have garnered more than 6300 citations (Google Scholar (2020), h-index = 45). He has attracted over $1.9M in operating funding and more than $6M in capital as a principal investigator, and has trained more than 32 graduate, post-doctoral researchers, and undergraduate students.

Farzad Khodabakhshi is an Assistant Professor at the University of Tehran since 2018. He has received his Ph.D. degree as a joint between the Sharif University of Technology and the University of Waterloo on the field of materials science and engineering with the major on metal matrix nanocomposites by friction stir processing at 2014. His current research focuses on welding metallurgy and microstructure-property correlation during friction stir welding and processing, additive manufacturing, and severe plastic deformation. He has published more than 80 journal articles and 20 conference papers, an Google Scholar (2020) h-index of 29 and an i10-index of 58 with the total number of citations of 2122.

Amir Mostafaei is an Assistant Professor in the Department of Materials, Mechanical and Aerospace Engineering at the Illinois Institute of Technology, Chicago, since January 2020, with a Ph.D. in Materials Science and Engineering from the University of Pittsburgh, PA, USA, a post-doc research fellow at the Manufacturing Futures Initiatives (MFI) Center at Carnegie Mellon University between September 2018 and December 2019 and an M.Sc. degree in Corrosion and Materials Protection (Sahand University of Technology, Iran). His Ph.D. research was primary on binder jet 3D printing of structural, bio-compatible, metal matrix composites and magnetic shape memory alloys. Effects of print processing optimization during binder jetting as well as post-processing development including sintering and surface treatment of the 3D printed parts were investigated on the microstructural evolution, phase formation, and resulting properties of binder jetted parts. Additionally, he has been working on laser powder bed fusion of metallic materials and evaluation of the processing parameters on the microstructure, porosity distribution, mechanical properties, and corrosion behavior of various additive manufactured parts from aluminum, stainless steel, and nickel-based alloys. Dr. Mostafaei has published literature in high temperature corrosion and failure analysis of stainless steels and nickel-based superalloys used in petroleum and nuclear power plants, multi-functional organic coatings, welding metallurgy, and nanomaterials fabrication. Finally, Dr. Mostafaei's research mainly focuses on applying fundamental aspects of materials science and engineering to address the demands of various manufacturing industries via additive manufacturing. His publications have been cited more than 1500 times (Google Scholar (2020), h-index = 20).

David Field is Professor and Associate Dean for Research in the Voiland College of Engineering and Architecture at Washington State University. He received his Ph.D. in Mechanical Engineering in 1991 from Yale University. From 1990 to 2000 he was employed as Sr. Engineer at Alcoa Technical Center and Director of Technology at TexSEM Laboratories. He joined the School of Mechanical and Materials Engineering at Washington State University in August, 2000. His research interests include physical and mechanical metallurgy, deformation and recrystallization, anisotropy of materials, and advanced experimental and characterization techniques. Field is the author or co-author of 200 technical articles and has given more than 80 invited presentations at national or international meetings, universities, and national laboratories. In addition, he has lectured and taught workshops on electron backscatter diffraction in several venues worldwide. His publications have been cited more than 7000 times (Google Scholar (2020), h-index = 37).

Joseph Robson is currently Professor of Physical Metallurgy, University of Manchester. He earned his PhD in Metallurgy from the University of Cambridge in 1996. Since then he has worked at Cambridge, Swansea, and Manchester universities, being appointed a Chair in 2016. His research interests are focussed on microstructure and property evolution in industrial alloys, with a particular emphasis on light alloys (aluminium and magnesium) and metallurgically complex processes, such as friction stir welding. He has published over 145 papers on these topics and was awarded the Grunfeld prize of the UK Institute of Materials, Minerals, and Mining (IoM3) in 2011, The Hume Rothery Prize of the IoM3 in 2015 and the Champion H Matthewson Prize (published work) of TMS in 2017. His publications have been cited more than 6100 times (Google Scholar (2020), h-index = 42).

Alexis Deschamps is currently University Professor, Grenoble Institute of Technology, France. He earned his PhD degree in Materials Science and Engineering from INPG. His research interests include Microstructure control at the nanoscale in metallic materials, precipitation kinetics, microstructure/properties relationships, physical metallurgy of welding, use of large scale facilities for the study of microstructures in metals, and combinatorial methods for microstructure characterization in metals and alloy development. He has authored or coauthored more than 300 publications. His publications have been cited more than 10000 times (Google Scholar (2020), h-index = 56).

Philip Withers obtained his PhD in Metallurgy at Cambridge University and took up a lectureship there, before taking up a Chair in Manchester in 1998. His interests lie in applying advanced techniques to follow the behaviour of engineering and natural materials in real time and in 3D. In 2005 he was elected to the Royal Academy of Engineering and in 2008 set up the Henry Moseley X-ray Imaging Facility, which is now one of the most extensive suites of 3D X-ray Imaging facilities in the world. Awarded the Royal Society Armourers & Brasiers' Company Prize for pioneering use of neutron and X-ray beams to map stresses and image components in 2010, his work underpins the scientific basis by which we can predict component failure. In 2012, he became the inaugural Director of the BP International Centre for Advanced Materials. In 2014, the University of Manchester was awarded the Queen's Anniversary Prize, recognising the Manchester X-ray Imaging Facility's work. He was elected a Fellow of the Royal Society in 2016. In 2017 he became the inaugural Regius Professor of Materials and Chief Scientist of the newly founded Henry Royce Institute for Advanced Materials. He has authored or coauthored more than 850 publications, which have been cited more than 32000 times (Google Scholar (2020), h-index = 80).